Schlumberger

Fundamentals of Production Logging

Colin Whittaker

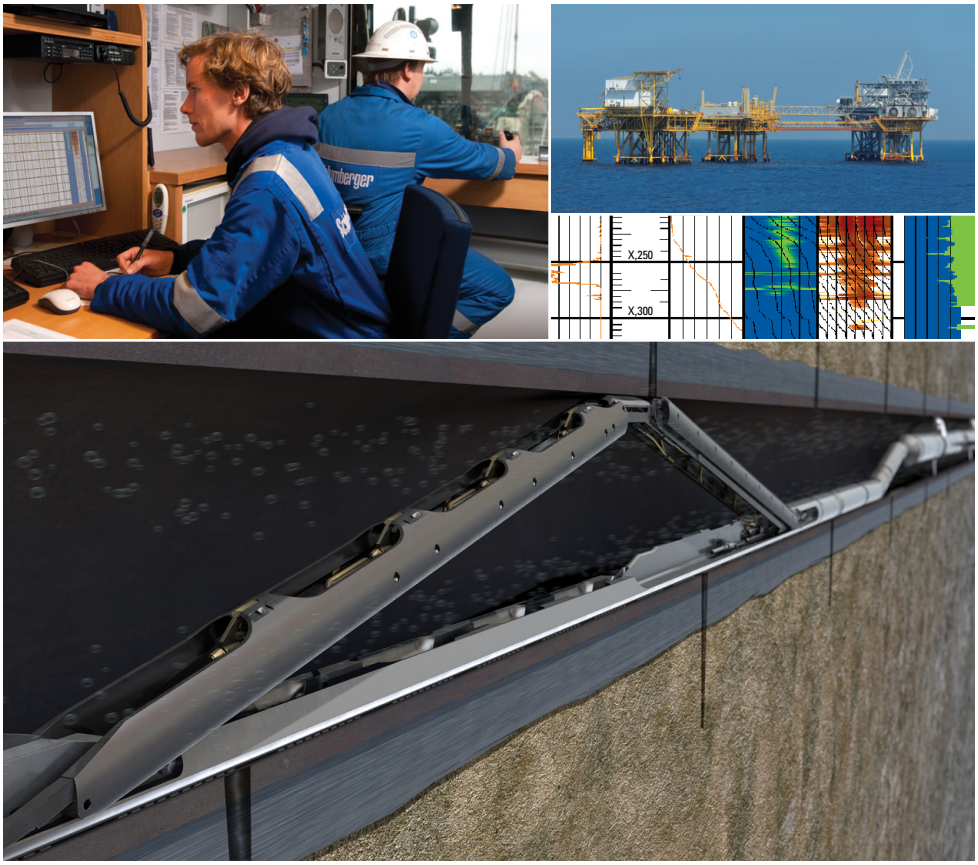

This book's aim is to provide the reader with a comprehensive understanding of production logging sensors, interpretation techniques, applications, and job planning.

Links are provided on each page to ease navigation. The PDF may also be browsed normally.

From the Contents pages, any of the listed items may be accessed by clicking either the entry or page number. This eBook is also bookmarked and indexed.

Click **here** for the table of contents.

For help using Adobe Acrobat Reader, press the **F1** key or click **here** to access Adobe Acrobat online help.

For optimal viewing of this document, it is recommended that you install the latest version of Acrobat Reader software. Click the icon to download the appropriate version:

Schlumberger
3750 Briarpark Drive
Houston, Texas 77042

slb.com

Produced by Schlumberger Digital Marketing

Second printing: 2016

16-PR-0001

ISBN-13: 978-1-937949-07-5

Contents

Foreword

From a few basic sensors, production logging tools have evolved to a family of tools each with sensors designed to make measurements that, once interpreted together, provide accurate flow rates for multiple phases and determine precisely where the various fluids are entering (or exiting) the borehole. This development and application of new production logging technologies is much needed, as well trajectories continue to grow in complexity, progressing from vertical to deviated and horizontal and posing new challenges in completion design and flow assurance.

The aim of this book is to provide the reader with a comprehensive understanding of the production logging sensors, interpretation techniques, applications, and job planning. From the most basic wells through intelligent completions with three-phase flow, the goal remains the same: to achieve an accurate interpretation.

Fundamentals of Production Logging is the third in a series of Schlumberger reference books produced for current and future oilfield technical experts.

Catherine MacGregor
President, Wireline
Clamart, France
January 2013

1 Introduction

Although most people picking up this book will have a good idea what "production logging" means, by literary convention and for the minority who are coming completely fresh to the subject, the definition is supplied in this introduction.

The aim of production logging is to determine where the oil and gas and water are coming from in a producing well or to determine where the gas or water is going to in an injection well. Because the radial influx (or outflux) of these phases into the borehole cannot be directly measured, production logging looks for intervals of stable or unchanging flow rate (q) and then calculates the differences between adjacent stable intervals.

Downhole separators and positive displacement meters are not used to measure the stable downhole flow rates; instead, velocities, areas, void fractions, and other indirect attributes of the flow rate must be measured. Most of the measurements available have limited ranges within which a calibrated response can be expected. It would be fair to say that the task of converting downhole measurements into a multiphase flow rate and then accurately determining where the various fluids are entering the borehole presents a challenge, a nontrivial task, or to use plain, noneuphemistic language, a problem. The objective of this book is to help readers address this problem and, if possible, succeed in making an acceptably accurate production log interpretation.

Therefore, this book reviews the downhole flow conditions to be quantified, a selection of standard and advanced sensors used to generate measurements, and the interpretation techniques used to convert measurements into flow rates. Examples of production logging measurements are presented to demonstrate operational and interpretation techniques.

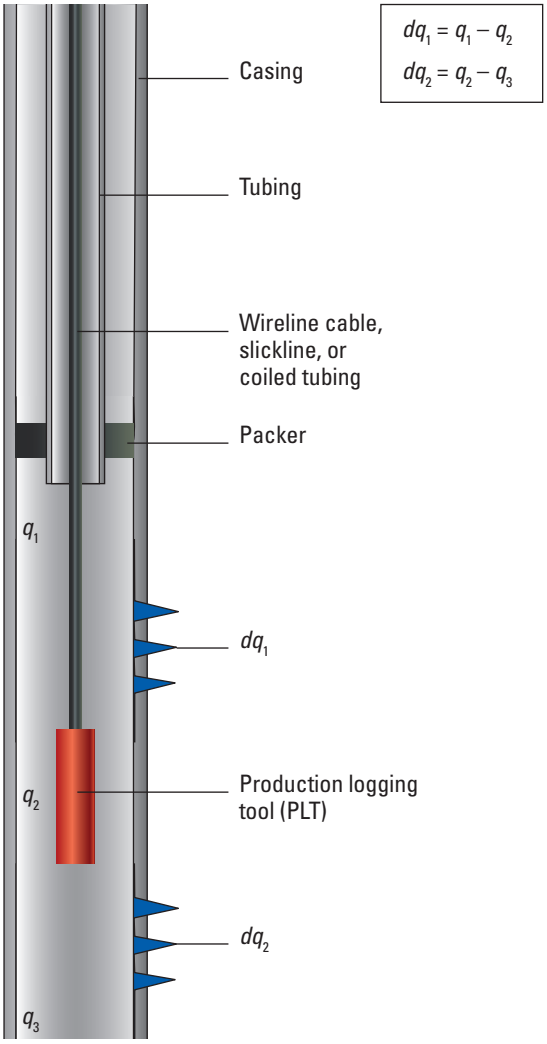

Figure 1-1. The principle of production logging.

2 The Downhole Environment

This chapter begins by considering what is happening inside a flowing well at the depth of the reservoir. For the simplest case of an oil well with no water or free gas present, the inertial forces

$$\frac{\rho v^2}{d} \tag{2-1}$$

within the flowing oil are competing against the viscous forces

$$\frac{\mu v}{d^2} \tag{2-2}$$

within the oil, where ρ is the oil density, v is the average axial velocity, d is the pipe diameter, and μ is the dynamic viscosity.

Dividing the inertial forces by the viscous forces ends up with $\rho vd/\mu$ (or vd/υ, where υ is the kinematic viscosity) otherwise known as the Reynolds number:

$$N_{\mathrm{Re}} = \frac{\rho vd}{\mu}. \tag{2-3}$$

The Reynolds number is dimensionless and successfully predicts the flow regime in round pipes from the size of a drinking straw to the largest concrete pipe, from atmospheric gas densities up to the density of mercury, and for viscosities from the heaviest tar or treacle down to the slipperiest gas. With a slight modification it can be extended to rectangular troughs and even rivers. Empirical analysis of flow in pipes shows that for Reynolds numbers less than 2,000 there is laminar flow, for Reynolds numbers above 4,000 there is turbulent flow, and for Reynolds numbers between 2,000 and 4,000 there is a high degree of uncertainty (Fig. 2-1). This degree of fuzziness cannot be tolerated in most interpretation software, so a hard transition from laminar to turbulent is used at a Reynolds number of 2,000. In some situations a lower transition of 1,500 is used to correct for the turbulence-creating presence of a moving logging tool.

Working in SI units the density is measured in kilograms per cubic meter (kg/m³), the velocity in meters per second (m/s), the diameter in meters (m), and the viscosity in pascal-seconds (Pa.s).

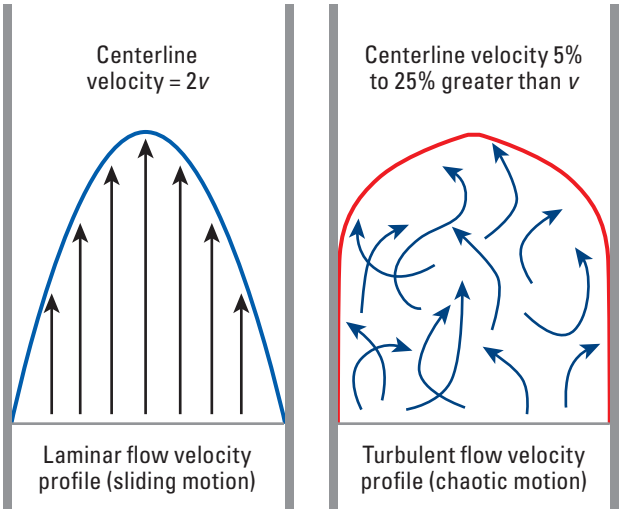

Figure 2-1. Laminar and turbulent flow.

For an example 5½-in pipe with an ID of 4.9 in, the diameter in SI units is 0.12 m. Water at surface pressure and temperature has a density of 1,000 kg/m³ and a viscosity of 0.001 Pa.s. Assuming an arbitrary flow rate of 500 bbl/d gives a velocity of 0.076 m/s:

$$N_{\mathrm{Re}} = 1{,}000 \times 0.076 \times 0.12/0.001 = 9{,}120.$$

This is a case of turbulent flow, and in the majority of oil and gas and water wells, turbulent flow dominates. Only in the case of heavy oils for which the downhole viscosity is greater than 100 cP should laminar flow routinely occur.

In customary oilfield units the equation for the Reynolds number becomes

$$N_{\mathrm{Re}} = \frac{1.48q\rho}{d\mu}, \tag{2-4}$$

where
q = flow rate, bbl/d
ρ = fluid density, lbm/ft³
d = pipe inside diameter, in
μ = dynamic viscosity, cP.

Laminar flow can be described completely by a relatively simple formula:

$$v(r) = v_{max}\left[1 - \left(\frac{r}{R}\right)^2\right], \quad (2\text{-}5)$$

$$v = \frac{1}{A}\int_0^R v(r)2\pi r\partial r = \frac{v_{max}}{2}, \quad (2\text{-}6)$$

where

$v(r)$ = axial velocity at radius r
v_{max} = centerline velocity
R = internal radius of the pipe
v = average pipe velocity
A = pipe area.

Turbulent flow is less easily described, and a number of models have been proposed to capture the velocity variation across the pipe (Fig. 2-2). One of these models is the Prandtl relationship:

$$v(r) = v_{max}\left[1 - \left(\frac{r}{R}\right)\right]^m, \quad (2\text{-}7)$$

$$v = \frac{1}{A}\int_0^R v(r)2\pi r\partial r = \frac{2v_{max}}{(m+1)(m+2)}, \quad (2\text{-}8)$$

where

m = exponent weakly dependent on the degree of turbulence, normally with a value of 1/7 (Fig. 2-3).

Flow inside a pipe has an associated frictional pressure drop. In the majority of wells worldwide, this frictional pressure drop is insignificant, but for high-velocity wells this effect may need to be calculated.

The frictional pressure gradient is

$$\frac{dp}{dL} = \frac{1}{2}fv^2\frac{\rho}{d}, \quad (2\text{-}9)$$

where

f = Moody friction factor.

For laminar flow the Moody friction factor f is given by $64/N_{Re}$, but for turbulent flow the situation is more complicated because the interaction of the pipe roughness with the viscous sublayer on the pipe wall comes into play. For low Reynolds numbers the viscous sublayer is generally thicker than the pipe roughness, making the pipe roughness irrelevant, but as the Reynolds number increases, the viscous sublayer becomes thinner, and the pipe roughness begins to poke through the viscous sublayer into the turbulent flow with a significant increase in the frictional pressure drop.

The Moody friction factor is a function of the Reynolds number and the relative roughness of the pipe (e/d, where e is the pipe roughness measured in the same units as the pipe diameter) (Fig. 2-4).

New steel casing has a nominal surface roughness of 0.0006 in, which gives a relative roughness of 0.0001 for a 6-in-ID casing. However, after a period of months or years downhole, corrosion and abrasion can be expected to significantly increase the surface roughness of

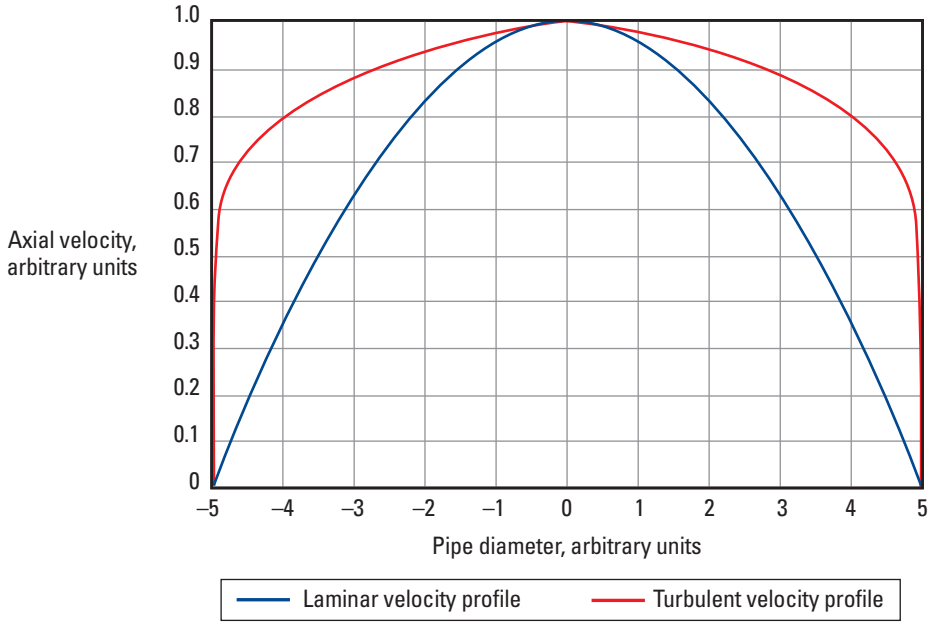

Figure 2-2. Velocity distribution in laminar and turbulent flow.

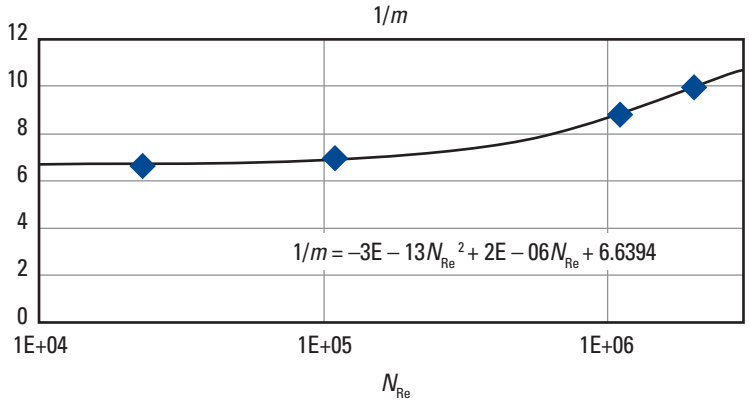

Figure 2-3. Prandtl exponent as a function of N_{Re} from Schlumberger Cambridge Research Center (renamed Schlumberger Gould Research Center in 2012) flow loop experiments.

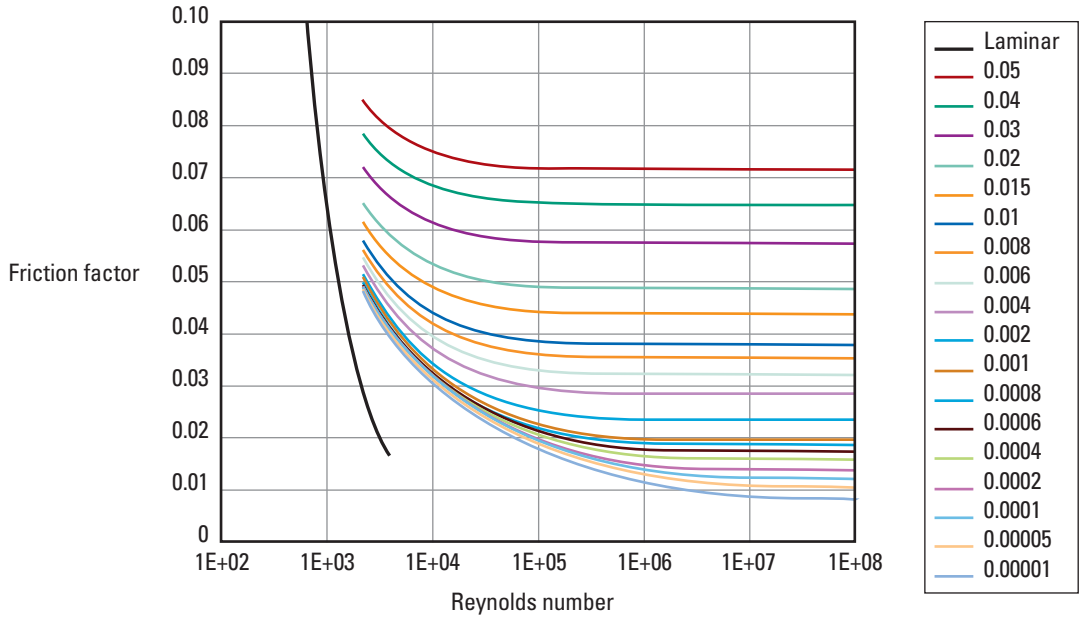

Figure 2-4. Moody friction factor as a function of N_{Re} and *e/d*.

a steel pipe. In practice the surface roughness of a pipe is computed from the observed pressure drop along a pipe when supplied with a known flow rate of water. In the case of a steel tubular, thousands of feet down in the Earth, this calibrated pressure drop technique is not available and only educated guesses can be used for the pipe roughness.

The preceding theory is sufficient to explain monophasic flow. However, multiphase mixtures of two or more immiscible phases—the phases being water, oil, and gas—often occur.

Oil-water flow regimes

For the relatively simple case of oil and water flowing in a vertical pipe, buoyancy causes the oil bubbles to rise through the slower moving water (Fig. 2-5). The assumptions and models of monophasic flow are no longer strictly valid, but in the absence of any better model the same models are applied but now use the mixture density, mixture viscosity, and mixture velocity to calculate the Reynolds number and velocity profile.

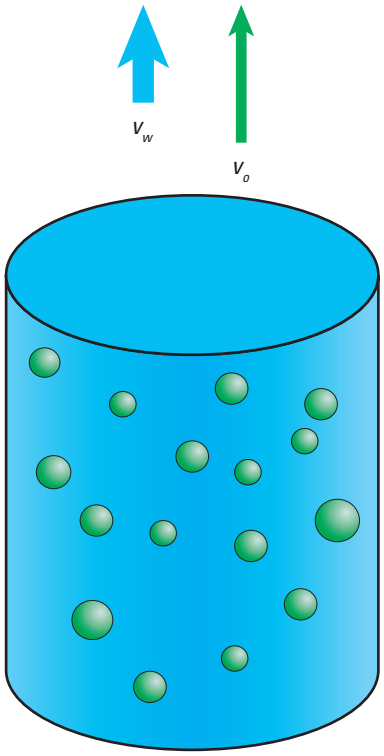

Figure 2-5. Two-phase oil and water flow.

The average velocity of the oil bubbles is called the oil-phase velocity (v_o). The average velocity of the continuous water phase is called the water-phase velocity (v_w).

If the motion is frozen at some arbitrary point in time, the volume fraction of the pipe occupied by water is called the water holdup (Y_w). Similarly, the volume fraction of the pipe occupied by oil is called the oil holdup (Y_o).

In the case of two-phase oil and water flow,

$$Y_w + Y_o = 1. \tag{2-10}$$

The flow rates of water and oil are, respectively,

$$q_w = v_w Y_w A, \tag{2-11}$$

$$q_o = v_o Y_o A. \tag{2-12}$$

The average volumetric mixture velocity is provided by

$$v_m = \left(v_w Y_w\right) + \left(v_o Y_o\right) \tag{2-13}$$

and can be used to drive the Reynolds number computation.

The mixture density for the Reynolds number calculation can be calculated as

$$\rho_m = \left(Y_w \rho_w\right) + \left(Y_o \rho_w\right), \tag{2-14}$$

or, correcting for the differing phase velocities, as

$$\rho_m = \frac{\left(v_w Y_w \rho_w + v_o Y_o \rho_o\right)}{\left(v_w Y_w + v_o Y_o\right)}, \tag{2-15}$$

where

ρ_m = average or mixture density
ρ_w = water density
ρ_o = oil density.

Neither approach strictly satisfies the bulk approximations built into the use of the Reynolds number, but neither is too far away from the truth. Therefore, the simpler expression of Eq. 2-14 is normally used.

Finally, a mixture viscosity is needed, but the linear approximations previously introduced are no longer valid. The continuous-phase viscosity normally dominates, except in the case of emulsions, where the water content of the oil is also important. For a water-continuous phase, the mixture viscosity is safely approximated by the water viscosity. For an oil-continuous phase, the mixture viscosity is approximated by the oil viscosity, unless surfactants are present and there is a degree of mixing, in which case the viscosity rises as an emulsion begins to form.

The point at which the transition from a water-continuous to an oil-continuous phase occurs is poorly defined, lying somewhere between a water holdup of 0.4 to 0.6 (Fig. 2-6). The degree of mixing is still more poorly defined. Fortunately, a lot of crude oils have low downhole viscosities of a similar magnitude to water and without the complications of emulsion-forming surfactants. In these cases a linear combination of the water and oil viscosities is as good as any other method:

$$\mu_m = \left(Y_w \mu_w\right) + \left(Y_o \mu_o\right), \tag{2-16}$$

where

μ_m = mixture viscosity
μ_w = downhole water viscosity
μ_o = downhole oil viscosity.

In this manner a multiphase mixture of oil and water in a vertical pipe can be treated as though it were a monophasic fluid for computing the Reynolds number and an expected velocity profile.

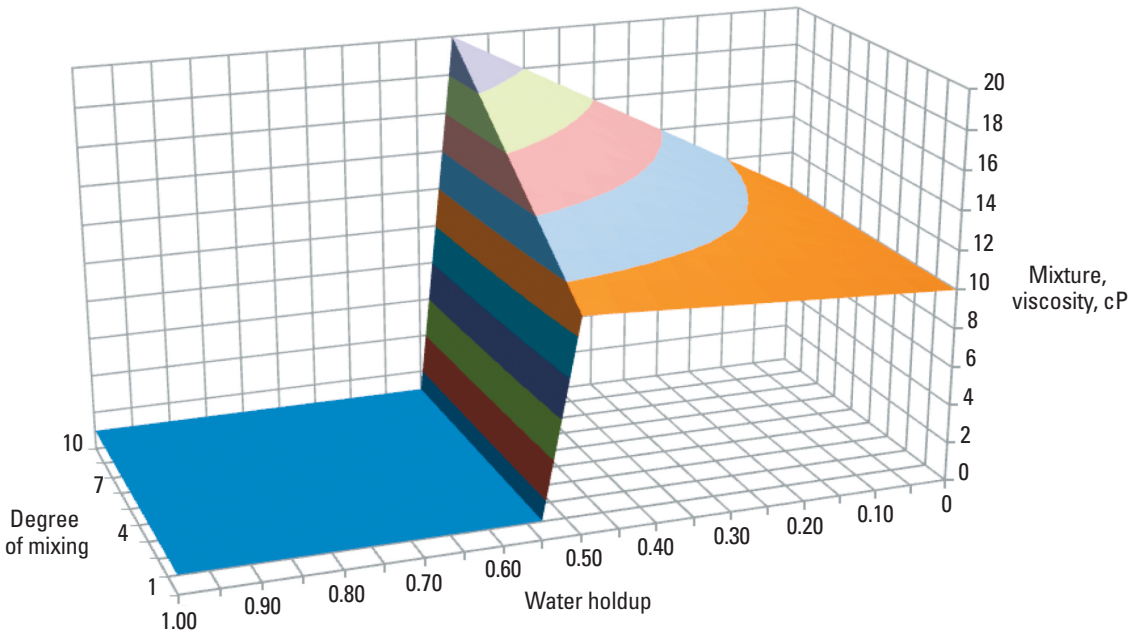

Figure 2-6. Typical water-oil mixture viscosity map.

Sidebar 2A. Superficial velocities

Superficial velocities can be used to conveniently sidestep the problem of predicting the difference in velocity between different phases. The superficial velocity of a phase is calculated as if the phase were filling the entire pipe. Superficial velocities are most commonly encountered as the axes of flow regime maps for predicting the downhole flow regime.

$$v_{wsup} = \frac{q_w}{A}, \quad \text{(2A-1)}$$

$$v_{osup} = \frac{q_o}{A}, \quad \text{(2A-2)}$$

$$v_{gsup} = \frac{q_g}{A}, \quad \text{(2A-3)}$$

$$v_m = v_{wsup} + v_{osup} + v_{gsup}, \quad \text{(2A-4)}$$

where

v_{wsup} = superficial water velocity, m/s
v_{osup} = superficial oil velocity, m/s
v_{gsup} = superficial gas velocity, m/s
q_w = downhole water flow rate, m^3/s
q_o = downhole oil flow rate, m^3/s
q_g = downhole gas flow rate, m^3/s
A = pipe area, m^2.

The velocity difference between the oil and the water, known as the slip velocity (v_s), can be modeled relatively successfully. Droplet rise experiments, which measure the rise velocity of a single oil droplet in a stagnant column of water, can be extended to the case of increasingly large numbers of oil droplets and large oil holdups. However, the modeling becomes more approximate when deviated wells are encountered and still more approximate when gas is introduced.

Sidebar 2B. The need for slip velocities

The slip velocity of oil through water or of gas through liquid is something that can almost never be measured with production logging toolstrings. Because the slip velocity is an important input to the computation of downhole fluid rates, slip models or correlations must be used to supply what cannot be measured. Unfortunately, the accuracy of the various slip models ranges from acceptable to wildly wrong.

For oil-water flow the slip velocity is strongly influenced by the density difference between the oil and water and less strongly by the relative proportions of oil and water. Figure 2-7 shows the Choquette (1975) model for slip.

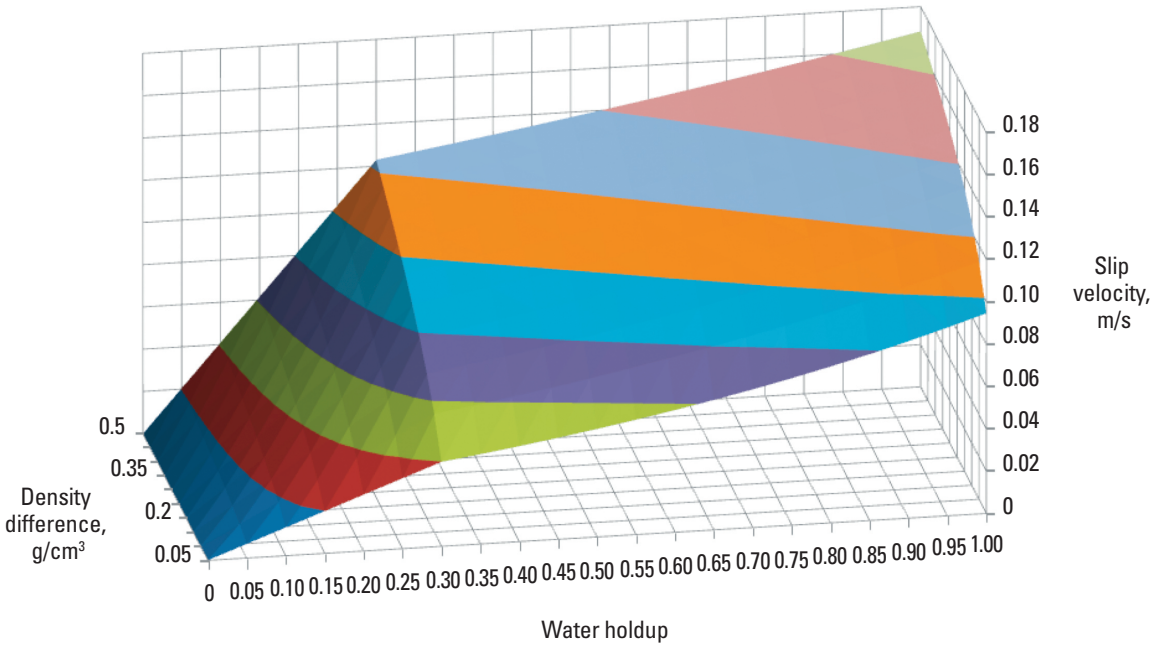

Figure 2-7. Choquette slip velocity (vertical pipe).

Maximum slip velocity occurs with a single droplet of oil rising through a continuous phase of water. Adding more oil helps to lift the water and thus reduce the slip velocity. Increasing the density difference also increases the slip velocity but not in a linear fashion.

The equation used is

$$v_s = 0.2\Delta\rho^{0.25} e^{-0.788\ln\left(1.85/\Delta\rho\right)Y_o}, \qquad (2\text{-}17)$$

where

$\Delta\rho$ = density difference between the oil and water, g/cm^3
v_s = slip velocity, m/s (a positive number for $v_o > v_w$).

Below water holdups of about 0.3 the situation is confused, with droplets of water carried by a continuous oil phase; the droplet rise models no longer work properly. However, because very high mixture velocities are needed to achieve this situation, resulting in $v_m >> v_s$, any errors in computing v_s have little impact on the calculations. A common approximation for v_s in this scenario is to linearly interpolate v_s from the value at $Y_w = 0.3$ to $v_s = 0$ at $Y_w = 0$.

Once the well is deviated, some curious things happen. Buoyancy moves the oil bubbles to the high side of the pipe, where they are able to travel faster despite a reduced buoyancy vector along the pipe axis (Fig. 2-8). The fast-moving oil drags some water along with it, more water than is actually flowing up the pipe, so a downflow of water on the low side of the pipe is required to balance the net flux.

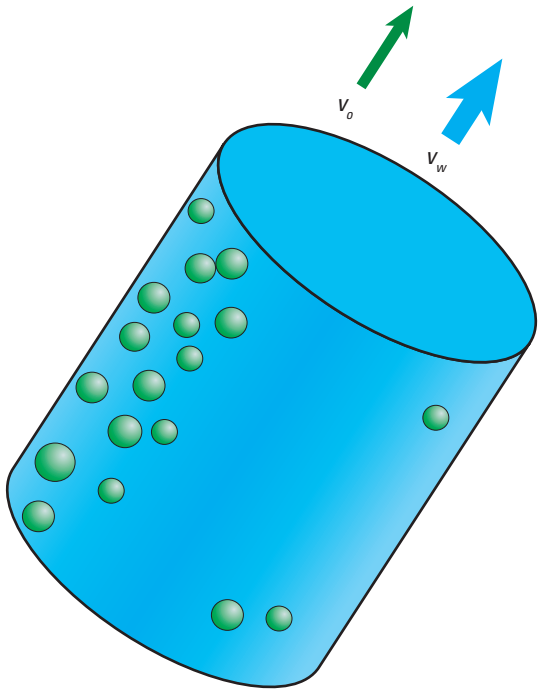

Figure 2-8. Effect of pipe deviation on oil-water flow.

Computer simulations of these conditions show a complicated structure of holdup and velocity across the pipe (Fig. 2-9).

Although it is possible to build an empirical model that predicts the velocity and holdup distribution for a limited number of cases, the general solution of all pipe diameters, all well deviations, all density contrasts, all flow rates, etc., is too difficult to model.

At low mixture velocities, where $v_s >> v_m$, the velocity profile looks like Fig. 2-10, with complicated counter currents and challenges for velocity measurements.

At higher velocities, where $v_m > v_s$, the scenario is much closer to the vertical pipe and monophasic velocity profile, with a more subtle velocity variation from top to bottom (Fig. 2-11).

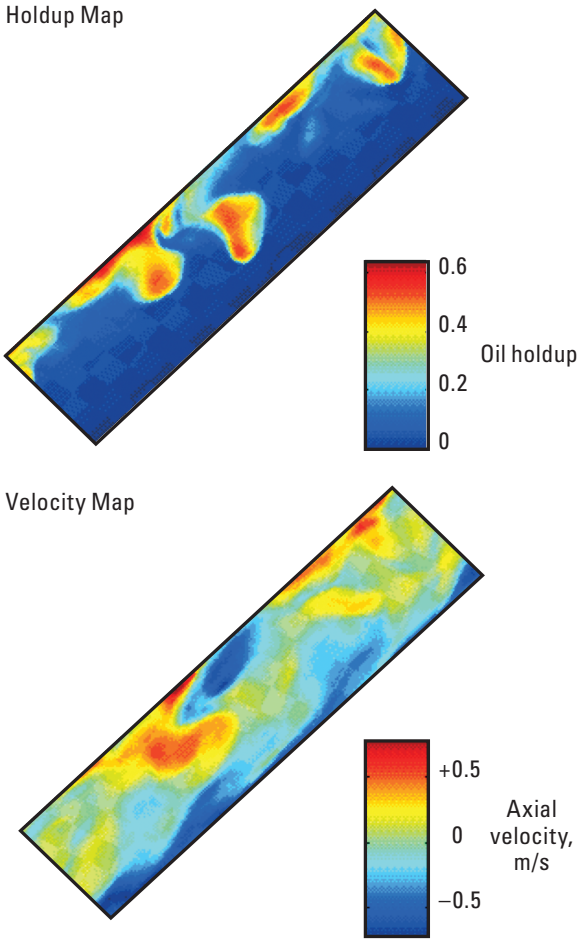

Figure 2-9. Numerical simulation of recirculation (8-in ID, 1,000 bbl/d, 85% water cut, 45° deviation).

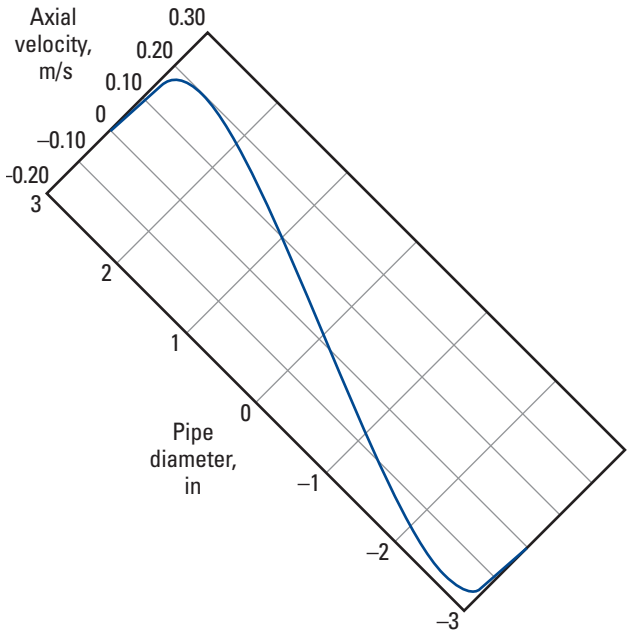

Figure 2-10. Velocity distribution across the vertical pipe diameter for low velocities.

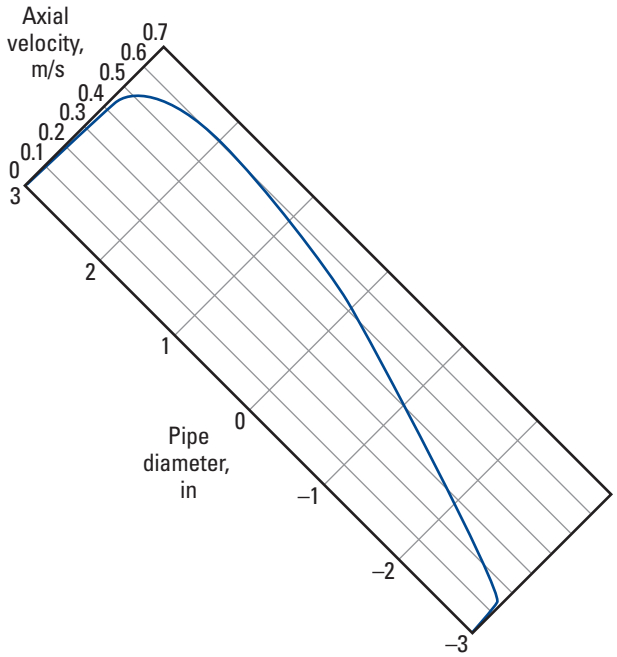

Figure 2-11. Velocity distribution across the vertical pipe diameter for high velocities.

Although the slip velocity increases with increasing deviation from the vertical, the physics and models developed for vertical-pipe slip velocities do not offer any solution for deviated pipes. Therefore, the following empirical correction is often applied:

$$v_{s\_deviated} = v_s(1+0.04\delta), \qquad (2\text{-}18)$$

where

$v_{s\_deviated}$ = deviated-pipe slip velocity

δ = pipe deviation in degrees from the vertical.

A further refinement has been inspired by Ding et al. (1993) to reduce the slip velocity above 50° to correct for the reducing buoyancy vector acting up the pipe axis as horizontal conditions are approached (Fig. 2-12). The original 4th-order polynomial multiplier is normally approximated to a slope reversal at 45° deviation.

Increasing the pipe deviation to the near horizontal results in the oil and water separating into two layers with an interface that can be flat, wavy, or bubbly (Fig. 2-13). The axial velocity distribution within the water has returned to something approaching the monophasic case except where the water is in contact with oil (Fig. 2-14).

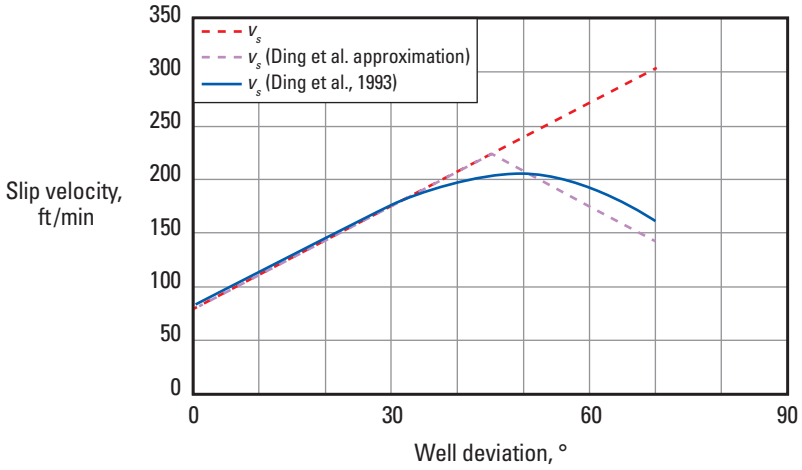

Figure 2-12. Deviation corrections for vertical slip models.

Figure 2-13. Stratified oil-water flow.

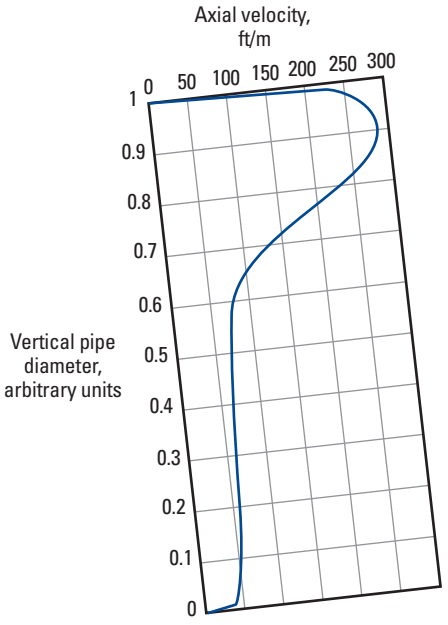

Figure 2-14. Velocity distribution across vertical pipe diameter at near horizontal.

Expanding the plot in Fig. 2-14 to fill the entire pipe gives the 3D velocity image in Fig. 2-16.

Taking the pipe deviation past 90° returns a mirror image Fig. 2-16 with large oil holdups and faster moving water.

The series of images in Fig. 2-15 show yellow water and brown oil traveling from right to left through a 5½-in-equivalent transparent plastic pipe. In each of the 12 cross sections the water cut is 50% (each image shows an equal flow rate of oil and water). At the lower flow rates gravity and the buoyancy difference between the oil and water dominate the partition of the holdup. However, as the flow rate is increased the wall friction pressure drop becomes more significant and at 6,000 bbl/d [about 1 m/s] the wall friction is more important than a change in deviation of a few degrees.

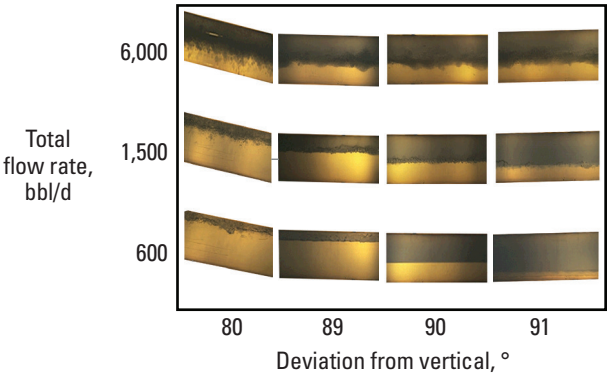

Figure 2-15. Variations in horizontal water and oil holdup for a constant 50% water cut.

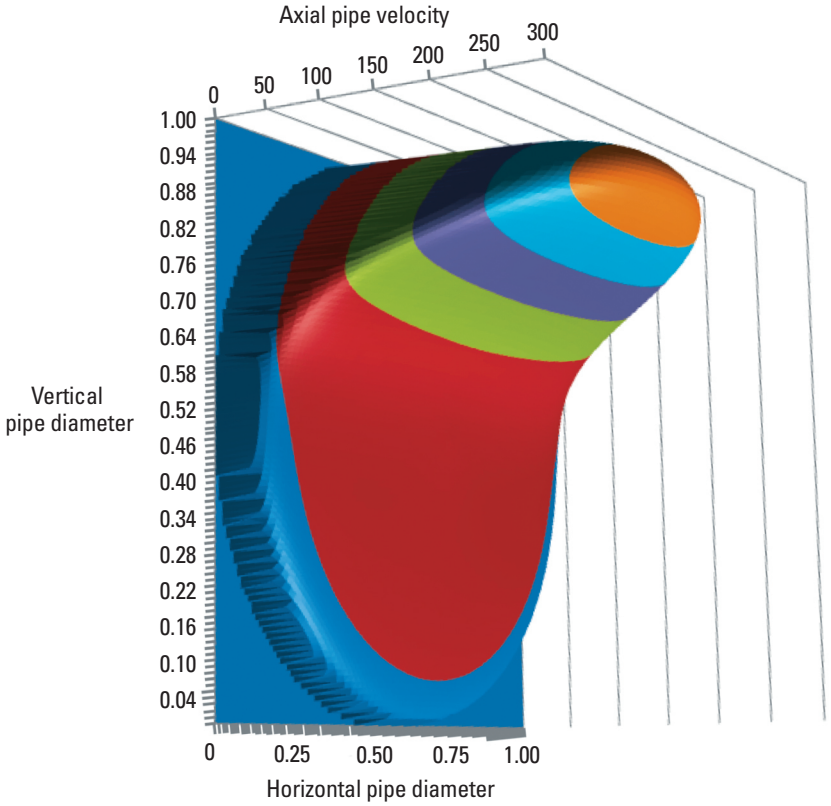

Figure 2-16. Typical velocity distribution in horizontal oil-water flow below 90° deviation. Arbitrary units are used.

Schlumberger proprietary Stratflo software is an oil-water slip model for these horizontal conditions. It uses a force balance within the water and oil layers to predict the slip velocity (in the absence of gas) (Fig. 2-17). The Stratflo model has been used in the Schlumberger BorFlow* production log interpretation package and more recently in KAPPA Engineering's Emeraude production modeling software on a user-controlled basis.

Conventional bubble models such as from Choquette (1975) can be pushed to about 70° whereas the Stratflo model works well in stratified oil-water flows of 85° to 95° and can be pushed to 80° to 100° (Fig. 2-18). This leaves a gray area from 70° to 80°, where the flow regime or the slip velocity cannot be predicted with confidence.

Computer interpretation models have to supply some slip velocity, no matter what the pipe deviation is, and therefore use some original and unphysical methods to fill the gap from 70° to 80°.

There are some exceptional wells where the deviation rises to about 135°. In these cases the oil-water slip velocity models from 45° deviation upflow seem to work well at 45° deviation downflow, with water bubbles falling through an oil-continuous phase. A more common case of water bubbles falling through a continuous phase of oil is often observed when a well is shut and water that was being carried to the surface falls back through a column of oil to the wellbore oil/water contact.

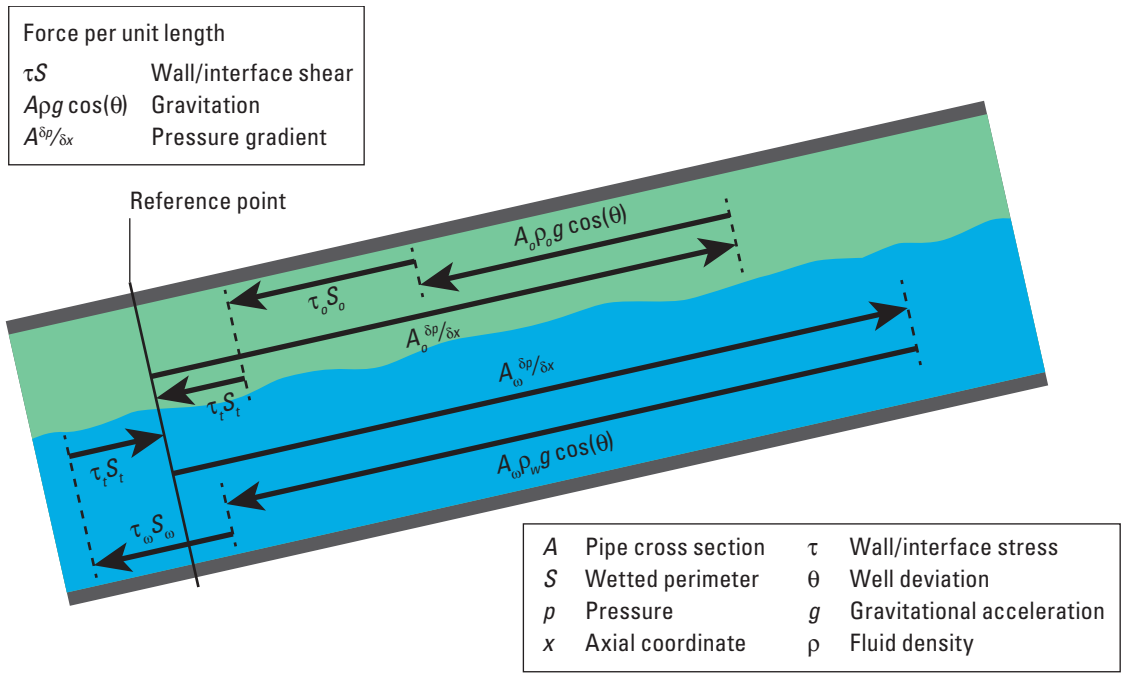

Figure 2-17. Force balance within the Stratflo slip model.

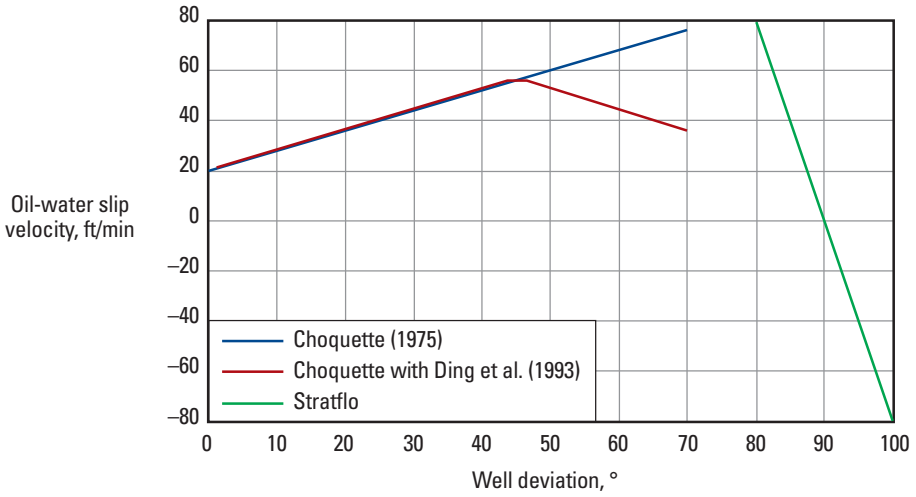

Figure 2-18. Variations of slip velocity for an arbitrary oil-water mixture.

Gas-liquid flow regimes

The situation of gas-liquid flow (Fig. 2-19) is a lot more complicated than that of oil-water flow, with many more flow regimes. Dukler and coworkers (Taitel et al., 1980) identified four flow regimes for vertical pipes, and more recent work in horizontal pipes has identified another five regimes.

The story, in brief, begins with small bubbles of homogeneously distributed gas moving up through oil or water at a relative velocity governed by the density contrast and the viscosity of the liquid. This is bubble flow. Another version of bubble flow occurs at high liquid rates where the gas bubbles are prevented from aggregating. This is sometimes called dispersed flow.

Farther up the well the pressure has dropped, more gas has come out of solution, and the preexisting gas has expanded. Some of the gas bubbles begin to aggregate and the resulting larger gas bubbles begin to move faster, capturing smaller gas bubbles in their path. Eventually the gas bubbles reach the size of the pipe diameter and are called gas slugs. This is slug flow.

As the pressure falls still lower the slugs tend to unite and move up the center of the pipe. The gas carries a few drops of liquid but most of the liquid flows up the pipe walls. This is froth or churn flow.

At still higher gas rates the flow either stabilizes with a gas core and a thin liquid film on the pipe walls, called annular flow, or the gas rips the liquid off the pipe walls and carries it along as a series of microdroplets, called mist flow. It is not clear whether annular flow and mist flow are really separate flow regimes.

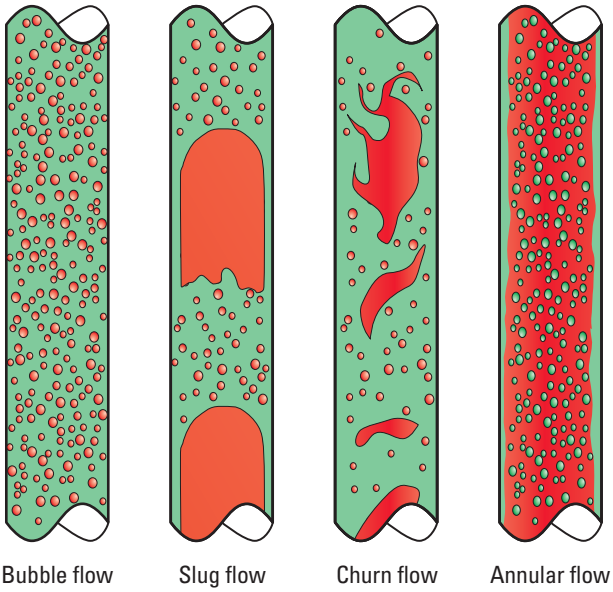

Figure 2-19. Basic vertical gas-liquid flow regimes.

Sidebar 2C. Where do gas-liquid slip correlations come from?

When a well is being completed, someone has to choose the tubing size. Small tubings cost less but may restrict the well's production. Big tubings cost more and may result in insufficient velocity for the produced gas to lift the liquids to surface.

The problem becomes one of describing the inflow performance of the well and the vertical lift performance of the tubing and finding where the two curves cross because this gives the reservoir drawdown and surface flow rate.

The vertical lift performance (VLP) curve provides a pressure drop for a given flow rate of gas and liquid. This pressure drop can be converted into a mixture density and hence a liquid holdup (Y_l):

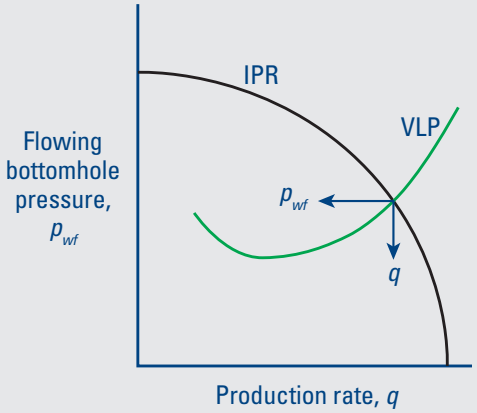

Figure 2C-1. The inflow performance rate (IPR) relates the production rate to the flowing bottomhole pressure.

$$dp/dL = \cos(\delta) g \left(Y_l \rho_l + (1 - Y_l) \rho_g \right), \quad (2C\text{-}1)$$

$$Y_l = \frac{dp/dL \, \frac{1}{g \cos\delta} - \rho_g}{\rho_l - \rho_g}, \quad (2C\text{-}2)$$

where

dp/dL = local pressure gradient, Pa/m
g = acceleration due to gravity, m/s^2
δ = local pipe deviation, degrees
ρ_g = gas density from the appropriate pressure-volume-temperature (PVT) model, kg/m^3
ρ_l = liquid density from the appropriate PVT model, kg/m^3.

Taking the phase flow rates and liquid holdup, the phase velocities can be written as

$$v_l = \frac{q_l}{(A \times Y_l)}, \quad (2C\text{-}3)$$

$$v_g = \frac{q_g}{\left[A \times (1 - Y_l) \right]}. \quad (2C\text{-}4)$$

And the slip velocity becomes

$$v_s = v_g - v_l = \left(\frac{q_g}{1 - Y_l} - \frac{q_l}{Y_l} \right) \frac{1}{A}, \quad (2C\text{-}5)$$

where

v_l = mean liquid velocity, m/s
v_g = mean gas velocity, m/s
q_l = local downhole liquid rate, m^3/d
q_g = local downhole gas rate, m^3/d
A = pipe internal cross-sectional area, m^2
v_s = slip velocity, m/s.

In this manner a VLP curve is coaxed into delivering a slip velocity for use in production log interpretation. However, this approach neglects to make any correction for the frictional pressure drop. Where the frictional pressure drop is significant, the mixture density and viscosity need to be modeled or approximated and pipe roughness guessed. Significant errors can be expected.

Gas-liquid pressure drop models use different methods and approximations to predict the flow regime, calculate the degree of gas-liquid interaction, and correct for the pipe frictional pressure drops. This often results in amazingly different slip velocities under the same downhole conditions of gas rate and liquid rate.

Duns and Ross (1963) used an experimental (empirical) model from laboratory data with a single flow map to divide the flow into bubble, slug, froth, or mist flow. The flow map plots a liquid number versus a gas number, where the number is a function of superficial velocity, liquid density, and interfacial friction. The absence of gas density is probably a limitation of the low-pressure laboratory experiments. In 1963 deviated wells were a rarity, so this model is probably designed for vertical wells.

If the Duns and Ross model is used on a deviated well, the following multiplier is needed:

$$v_s = v_s \times (1 + 0.04\delta), \quad (2\text{-}19)$$

with the option to invoke Ding et al. (1993) for deviations greater than 45°.

It would be surprising to find this model working as well as some of the more recent developments.

Hagedorn and Brown (1965) is based on experimental data from a 1,500-ft-deep vertical well completed with small tubings of 1-, 1¼-, and 1½-in internal diameter. No flow map was used. Deviation corrections are again of the form in Eq. 2-19.

It would be surprising to find this model working as well as some of the more recent developments.

Aziz et al. (1972) built a mechanistic model using a single flow map to divide the flow into bubble, slug, froth, or mist flow by using the superficial velocities of liquid and gas as well as the densities of the phases present together with their interfacial tension.

As Aziz produced another mechanistic model (Petalas and Aziz, 1996) it should be assumed that he regarded the later work as an improvement over his model from 24 years earlier.

Beggs and Brill (1973) produced a model-based correlation using Froude numbers versus the liquid fraction to determine a flow regime and hence a suitable equation for slip. The Froude (pronounced like prude) number is a dimensionless number based on the ratio of intertial to gravitational forces:

$$N_{\mathrm{Fr}} = \frac{v_m}{\sqrt{gd}}, \qquad (2\text{-}20)$$

where

N_{Fr} = Froude number
v_m = mixture velocity
d = pipe diameter.

The model was tuned using experiments on pipes at various inclinations of flowing water and air.

The author speculates that this model from over 30 years ago is unlikely to be as accurate as more modern work but is open to correction.

Sidebar 2D. Modeling considerations

Mechanistic models apply physics and not just empirical correlations to the task of predicting the pressure drop and hence the slip velocity in a gas-liquid well. Typically a mechanistic model first predicts the flow regime and then uses physical models to predict the holdup and pressure drop under these conditions.

Changes from one flow regime to the next are sharp and commonly discontinuous. To a production engineer choosing the tubing size these discontinuities are irrelevant. But to a production log analyst or a reservoir simulator these discontinuities are, respectively, awkward and unusable.

Gas-liquid slip correlations in use today

Dukler and his associates (Taitel et al., 1980) published their model in 1980. This mechanistic model divided up the flow into finely dispersed bubble, bubble, slug, froth or churn, and annular or mist flow and identified the different flow regimes based on the superficial velocities of gas and liquid (Fig. 2-20). Experimental data was used from vertical small-diameter pipes flowing water and air.

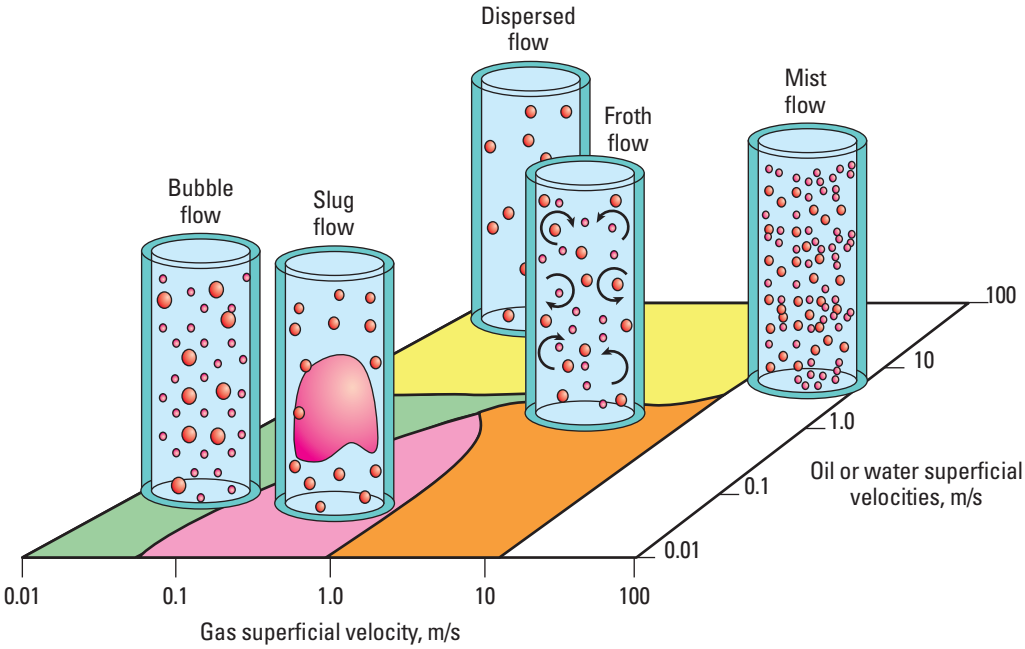

Figure 2-20. Dukler vertical flow regime map.

This paper provides an excellent and very easily read introduction to modeling flow regimes in gas-liquid flows.

Earlier primitive applications of Dukler and coworkers (Taitel et al., 1980) within Schlumberger wellsite answer products reduced the world of gas-liquid flow to exclusively bubble flow and then used the following algorithms.

In oilfield units of ft/min:

$$v_s = \left(60\sqrt{0.95 - Y_g^2} + 1.5 \right)\left(1 + 0.04\delta\right), \qquad (2\text{-}21)$$

whereas in SI units of m/min:

$$v_s = \left(60\sqrt{0.95 - Y_g^2} + 1.5 \right)\left(1 + 0.04\delta\right) / 3.281. \qquad (2\text{-}21)$$

If $Y_g^2 > 0.95$ the equation cannot be solved, but at very high gas holdup values the flow is not bubble flow and a different slip correlation should be used.

Properly implemented, Dukler's model works well in low-pressure (<1,000 psi), low-deviation (<10°) gas wells.

The Association de Recherche sur les Techniques d'Exploitation du Petrole (ARTEP) (Ferschneider et al., 1988) provided another mechanistic model tuned to flow loop measurements made between 0° and 90° and using water, natural gas, condensate, and oil. Pressures extended up to 725 psi [50 bar] and pipe diameters of 3 and 6 in [7.62 and 15.24 cm] were used.

In the conclusion of their paper, the authors state that they created and used a flow pattern prediction model, in which mechanistically based relations determine transitions, and a hydrodynamic model for each flow pattern (i.e., bubble, slug, and annular flow).

Large experimental data banks, generated in conditions similar to oil production conditions, ensure a good physical basis to the proposed model. The resulting computer program performs calculations of pressure and temperature profiles in wells. Tested against field data gathered from 90 wells in a broad range of production conditions, the WELLSIM model has shown an increased accuracy in multiphase flow calculations for wells.

Although the objective of simulation has been to predict pressure drops, the derived gas-liquid slip velocities should work better than the old empirical correlations. Because the gas-liquid flow regime changes significantly at 90° deviation, no attempt should be made to use this model beyond 90° deviation.

Petalas and Aziz (1996) also provided another mechanistic model that uses 10 different flow regimes based on 20,000 laboratory measurements and 1,800 measurements from wells:

- elongated bubble
- bubble
- stratified smooth
- stratified wavy
- slug
- annular
- mist
- dispersed bubble
- froth 1 (transition between dispersed bubble and annular-mist)
- froth 2 (transition between slug flow and annular-mist).

This is the first model to handle all pipe deviations, including >90°.

Tests of this model in the flow loop at the Schlumberger Gould Research Center in Cambridge, England, show a high-accuracy prediction of the flow regime and a good prediction of the holdup (and hence slip velocity) for liquid holdups greater than 50%.

Away from the world of vertical low-pressure gas-water wells (best suited for the Dukler model), this slip model is probably a good default slip correlation to start with.

Kaya et al. (2001) produced another mechanistic model using bubbly, dispersed-bubble, slug, churn, and annular flows in vertical and deviated wells. However, this model is not designed for and makes no predictions about pressure drops in near-horizontal wells.

The authors tested the model against its peers on a very large database of well measurements and compared the predicted and measured pressure drops from tubing end to surface. To reduce the effect of self-canceling errors in differing flow regimes, the model was separately tested on datasets in which one particular flow regime dominated. Comparison with the models of Hagedorn and Brown (1965), Chokshi (1994), Tengesdal (1998), Aziz et al. (1972), Hasan and Kabir (1988), and Ansari et al. (1994) showed that the Kaya et al. model was superior in most cases.

In the absence of a similar comparison that includes Dukler (Taitel et al., 1980) and Petalas and Aziz (1996), the Kaya et al. model is assumed to be of comparable quality.

Other gas-liquid models

When encountering a new gas-liquid slip correlation (e.g., Barnea, 1987; Zhang et al., 2003; Chokshi, 1994; Tengesdal, 1998; and Ansari et al., 1994), the author's rule of thumb is to put more trust in modern mechanistic models using large databases than in empirical correlations matched to a limited set of local conditions.

References

Ansari, A.M., Sylvester, N.D., Sarica, C., Shoham, O., and Brill, J.P.: "A Comprehensive Mechanistic Model for Upward Two-Phase Flow in Wellbores," *SPE Production & Facilities* (May 1994), 143–152.

Aziz, K., Govier, G., and Fogarasi, M.J.: "Pressure Drop in Wells Producing Oil and Gas," *Journal of Canadian Petroleum Technology* (July–September 1972), 38–48.

Barnea, D.: "A Unified Model for Predicting Flow-Pattern Transitions for the Whole Range of Pipe Inclinations," *International Journal of Multiphase Flow* (1987) 13, No. 1, 1–12.

Beggs, H., and Brill, J.: "A Study of Two-Phase Flow in Inclined Pipes," *Journal of Petroleum Technology* (May 1973), 607–617.

Chokshi, R.N.: "Prediction of Pressure Drop and Liquid Holdup in Vertical Two-Phase Flow Through Large Diameter Tubing," PhD dissertation, University of Tulsa, Tulsa, Oklahoma, USA (1994).

Choquette, S.P.: "Vertical Two-Phase Flow Systems and Interpretation of the Flowmeter and the Gradiomanometer Production Logs," MS thesis, Stanford University, Stanford, California, USA (1975).

Ding, Z.X., Flecker, M.J., and Anderson, C.: "Improved Multiphase Flow Analysis Using an Expert System for Slip Velocity Determination," *Transactions of the SPWLA 34th Annual Logging Symposium*, Calgary, Alberta, Canada (June 13–16, 1993), paper YY.

Duns, H. Jr., and Ros, N.C.J.: "Vertical Flow of Gas and Liquid Mixtures in Wells," *Proceedings of the Sixth World Petroleum Congress*, Frankfurt (1963), 10, paper 22, 451–465.

Ferschneider, G., Ozon, P.M., and Duchet-Suchaux, P.: "Models for Multiphase Flow in Oil Wells," Offshore Multiphase Production Conference, London, England, British Hydromechanics Research Association (September 14–15, 1988).

Hagedorn, A.R., and Brown, K.E.: "Experimental Study of Pressure Gradients Occurring During Continuous Two-Phase Flow in Small Diameter Vertical Conduits," *Journal of Petroleum Technology* (April 1965) 17, 475–484.

Hasan, A.R., and Kabir, C.S.: "Predicting Multiphase Flow Behavior in a Deviated Well," *SPE Production Engineering* (November 1988), 474–482.

Kaya, A.S., Sarica, C., and Brill, J.P.: "Mechanistic Modeling of Two-Phase Flow in Deviated Wells," *SPE Production & Facilities* (August 2001), 156–165.

Petalas, N., and Aziz, K.: "Development and Testing of a New Mechanistic Model for Multiphase Flow in Pipes," *ASME Fluids Engineering Division Second International Symposium on Numerical Methods for Multiphase Flows*, San Diego, California, USA (July 7–11, 1996).

Taitel, Y., Barnea, D., and Dukler, A.E.: "Modelling Flow Pattern Transitions for Steady Upward Gas-Liquid Flow in Vertical Tubes," *AIChe Journal* (1980) 26, No. 3, 345–354.

Tengesdal, J.O.: "Predictions of Flow Patterns, Pressure Drop, and Liquid Holdup in Vertical Upward Two-Phase Flow," MS thesis, University of Tulsa, Tulsa, Oklahoma, USA (1998).

Théron, B.E., and Unwin, T.: "Stratified Flow Model and Interpretation in Horizontal Wells," paper SPE 36560 presented at the SPE Annual Technical Conference and Exhibition, Denver, Colorado, USA (October 6–9, 1996).

Zhang, H.-Q., Wang, Q., Sarica, C., and Brill, J.P.: "A Unified Mechanistic Model for Slug Liquid Holdup and Transition Between Slug and Dispersed Bubble Flows," *International Journal of Multiphase Flow* (2003) 29, No. 2, 271–289.

3 PVT for Production Logging

Reservoir engineers and completions engineers have their uses for PVT models and PVT analyses; production logging interpreters have a slightly different set of needs. These needs and their resolution are reviewed in this chapter.

What are PVT properties?

In the oil and gas world, PVT properties refer to the change in physical properties of oil, water, and gas with changing pressure and temperature.

Shrinkage factors provide the ratio of downhole volumes to surface volumes. Shrinkage can be due to the compressibility of a phase, phase changes as solution gas is evolved or condensate drops out, or both.

Density varies with pressure and temperature, with gas showing the most extreme behavior and water the least affected by shrinkage. To a first-order approximation, shrinkage factors and density changes are inversely proportional to each other, but the high solubility of gas in oil complicates the story for oil.

Viscosity has a strong dependency on temperature for liquids, whereas gas viscosity is more affected by pressure.

PVT of water

Water density and viscosity change only slightly with pressure and temperature. The biggest factor affecting the density of water comes from dissolved salts, primarily sodium chloride (NaCl). Sodium chloride concentrations are normally quoted in parts per million (ppm), but some are in milligrams per liter (mg/L) or even moles per liter. To add a little confusion, chemists sometimes quote just the chloride concentration and ignore the sodium. Table 3-1 shows these different measurement systems for a typical seawater concentration.

The last number in the table—30,000 ppm—is the one used by most production logging interpretation software packages. When working with very salty formation waters, it is essential to know what system has been used for measuring the water salinity if significant errors are to be avoided.

Table 3-1. Typical Seawater NaCl and Chlorides Concentrations in Different Units

Compound	Value	Unit
NaCl	0.51274	mole/liter
Chlorides	18,202	mg/liter
Chlorides	18,205	ppm
NaCl	29,996	mg/liter
NaCl	30,000	ppm

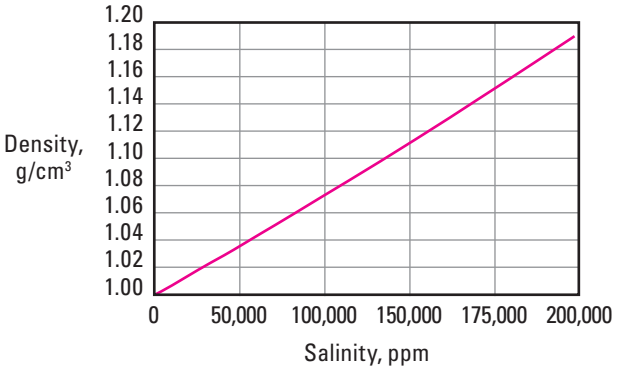

Figure 3-1. Density versus salinity for NaCl solutions in water at standard temperature and pressure.

Water salinity can also be supplied as a surface water density at standard conditions. In this case Fig. 3-1 can be used to convert back to ppm NaCl (the presence of a weak square law relationship precludes the use of a conversion factor) or the salinity can be guessed until the PVT software replicates the supplied surface density.

Any methane present has some solubility in water (Fig. 3-2):

$$R_{sw} = \frac{\text{volume of gas at standard conditions}}{\text{volume of water at standard conditions}}, \quad (3\text{-}1)$$

where the solution gas ratio (R_{sw}) can be measured in standard cubic feet per barrel (scf/bbl) or cubic meter per cubic meter (m^3/m^3). The choice of unit system changes the value of the ratio.

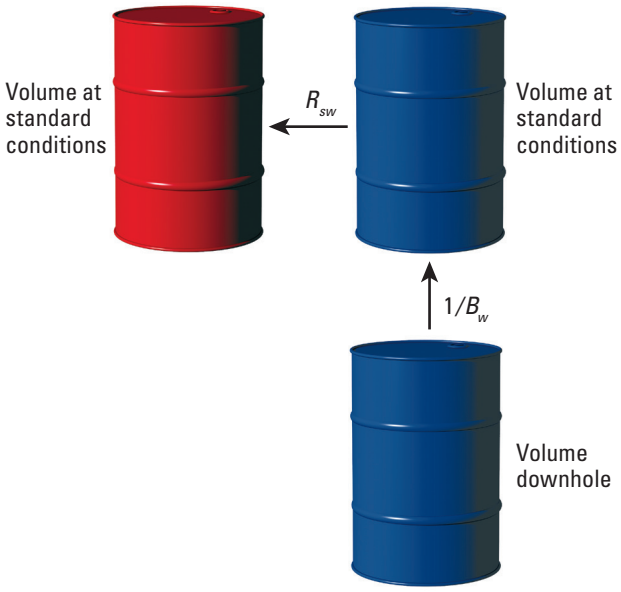

Figure 3-2. Water shrinkage factor (B_w) and solution gas ratio (R_{sw}). Blue indicates water, red indicates gas.

Based on gas solubility data of Culberson and McKetta (1951), the McCain, Spivey, and Lenn (McCain et al., 2011) correlation predicts methane solubility in water with an average error of about 1%. The correlation of Kobayashi and Katz (1993) has errors of about 5%.

The compressibility of water changes with pressure and temperature, but this is only of importance to pressure transient interpretation and reservoir modeling.

The water shrinkage factor (B_w, also called the water formation volume factor) is defined as

$$B_w = \frac{\text{volume of water and dissolved gas leaving the reservoir at the downhole pressure and temperature}}{\text{volume of water at standard conditions}}. \quad (3\text{-}2)$$

Three common models for the shrinkage factor and density of water come from Gould (1974), McCain (1990), and Meehan and Ramey (Meehan, 1980a). Errors from McCain are within 1% of the graphical correlation of Long and Chierici (1961). Similar errors are expected from Gould and from Meehan and Ramey.

Water viscosity is most often supplied by Kestin et al. (1978), van Wingen (1950), or Meehan and Ramey (Meehan, 1980b). Typical errors with Meehan and Ramey are less than 5% whereas using Kestin et al. takes the average errors below 1%. However, errors in the value used for water viscosity have only a weak effect on the frictional pressure drop corrections and an even weaker effect on the shape of the velocity profile across a pipe.

PVT of gas

The PVT of gas is dominated by the modified ideal gas law:

$$pV = nzRT, \quad (3\text{-}3)$$

where

p = absolute pressure, atm
V = volume, L
n = number of moles (the molar volume at standard temperature and pressure [STP] is 22.414 L)
R = universal gas constant, 0.08206 L.atm/mol.K
z = gas compressibility factor, accounting for deviation from the ideal gas law
T = temperature, Kelvin.

In SI units the universal gas constant is 8.3145 J/mol.K, whereas in oilfield units the gas constant is 10.732 scf.psia/lbm.mol.R. McCain (1990) provides a table of 22 different values of the universal gas constant in his book *The Properties of Petroleum Fluids*.

Sidebar 3A. Standard temperature and pressure

Standard temperature and pressure (STP) is defined as 0 degC and 10^5 Pa by the International Union of Pure and Applied Chemistry (IUPAC).

Normal temperature and pressure (NTP) is defined as 20 degC and 1 atm or 1.01325×10^5 Pa by the National Institute of Standards and Technology (NIST).

Standard Ambient Temperature and Pressure (SATP) is often used in chemistry and is defined as 15 degC and 1.01×10^5 Pa. This is the standard for natural gas companies in Europe and South America.

The International Standard Atmosphere (ISA) is 1.01325×10^5 Pa, 15 degC, and 0% humidity.

The International Civil Aviation Organization (ICAO) Standard Atmosphere uses 15 degC and 760 mmHg or 14.7 psia.

In the oil industry, the Society for Petroleum Engineers (SPE) uses 60 degF and 14.696 psia for STP.

Curiously, McCain's *The Properties of Petroleum Fluids* (1990) uses 60 degF and 14.65 psia for standard conditions.

Which standard are you using?

Natural gas is almost never pure methane and contains significant fractions of ethane, propane, and other hydrocarbons. These fractions must be known to accurately model the gas PVT properties. However, acceptable accuracies are obtained by measuring the gas density relative to air and estimating the probable gas fractions that would match this density. Pure methane has a gas specific gravity of 0.5537 whereas extremely rich gases can exceed a gas specific gravity of 1.0.

When the surface gas density is supplied in SI units of kilogram per cubic meter at the NIST normal temperature and pressure, the gas density must be divided by 1.2041 kg/m^3 to deliver the gas gravity. However, if the IUPAC standard pressure and temperature and pressure are being used the gas density must be divided by 1.2754 kg/m^3, and for the SATP a value of 1.2217 kg/m^3 is used.

It is also possible to model gas behavior based on its equation of state (EOS) or composition, which refers to the hydrocarbon compounds expressed as the number of carbon atoms C_1, C_2, through C_n together with small degrees of contamination by N_2, CO_2, and H_2S. However, use of a standard natural gas EOS model on CO_2 disposal wells or wells with a very high H_2S content leads to large errors.

Predicting the nonideal gas behavior deviation factor (z) is the only step at which errors can creep into the modeling of the downhole shrinkage factor and density. However, typical errors in computing z are less than 2%, so the choice of the z correlation does not make a significant difference to production log interpretation.

The law of corresponding states observes that the plots of z versus pressure at a number of different temperatures for a number of different gases and gas compositions show a very similar behavior. Normalizing these plots by the pressure and temperature of the critical point allows the value of z from one to be applied to any of the others. Therefore, the aim of most gas PVT models is to predict the pressure and temperature at the critical point as accurately as possible. This is done by taking the volume-weighted sum of all of the critical pressures and temperatures of the components of the produced gas, known as the pseudo-critical pressure and temperature:

$$T_{pc} = \Sigma_n Y_n T_{cn}, \tag{3-4}$$

$$p_{pc} = \Sigma_n Y_n p_{cn}, \tag{3-5}$$

where

T_{pc} = pseudo-critical temperature of the gas mixture
Y_n = volumetric fraction of component n of the gas
T_{cn} = critical temperature of component n of the gas
p_{pc} = pseudo-critical pressure of the gas mixture
p_{cn} = critical pressure of component n of the gas.

At a given pressure and temperature of the gas mixture, the pseudo-reduced pressure (p_{pr}) and temperature (T_{pr}) are computed from the pseudo-critical pressure and temperature:

$$T_{pr} = \frac{T}{T_{pc}}, \tag{3-6}$$

$$p_{pr} = \frac{p}{p_{pc}}. \tag{3-7}$$

These computations are generally hidden from the production log analyst. The only choice the analyst has to make is deciding which algorithm of z factors versus pseudo-reduced pressures and pseudo-reduced temperatures should be selected. Common options are Brill and Beggs (1974), Standing and Katz (1942) (Fig. 3-3), and the well-respected Hall and Yarborough (1973).

Two possible models for gas viscosity come from Lee et al. (1966) and Carr et al. (1954). Because the calculations of production log interpretation are only very weakly dependent on gas viscosity, the choice of correlation is somewhat arbitrary.

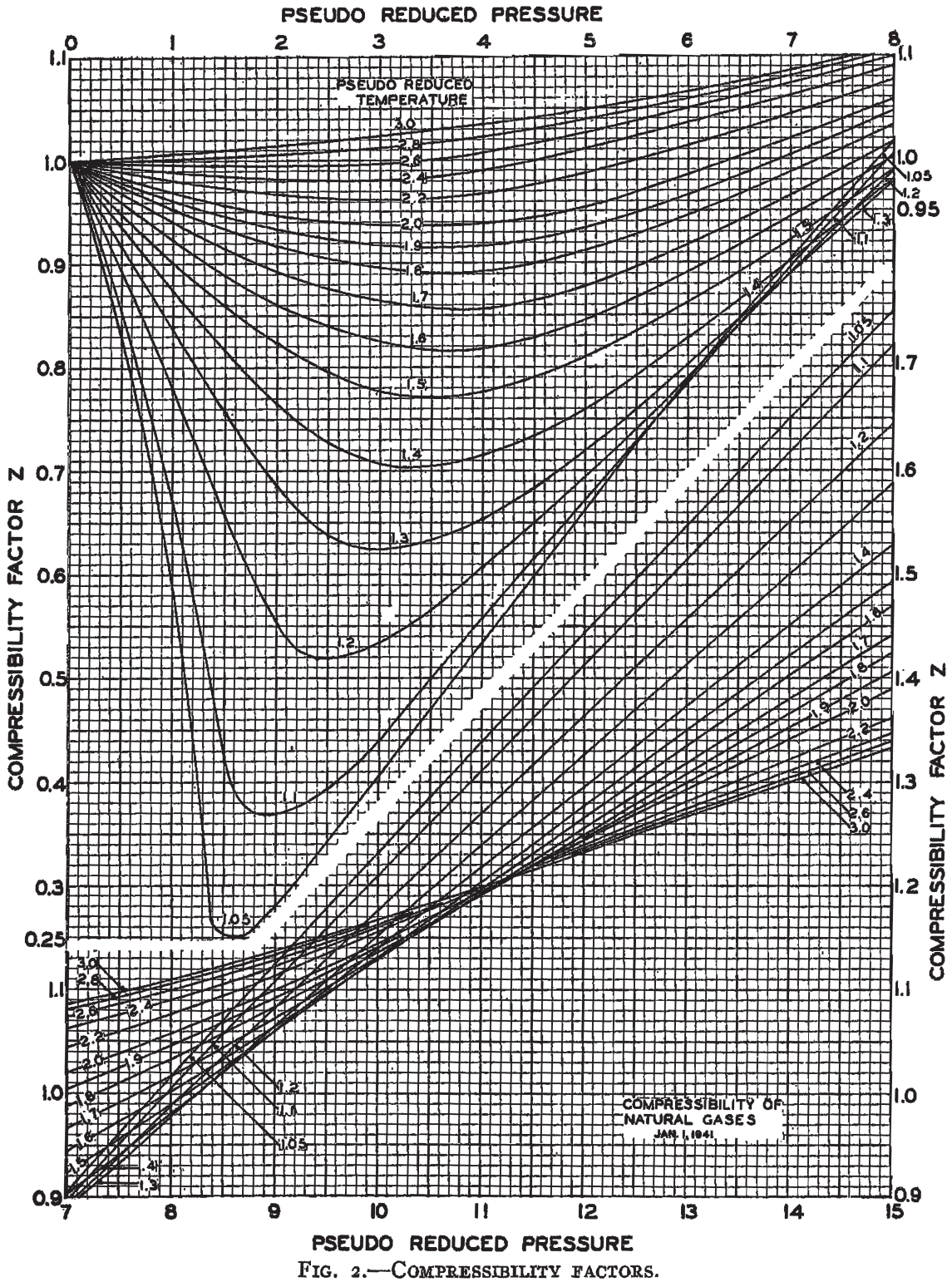

Figure 3-3. Standing and Katz (1942) chart for the *z* factor.

The shrinkage factor for gas (B_g) (Fig. 3-4) is defined similarly to that for water:

$$B_g = \frac{\text{volume of gas leaving the reservoir at the downhole pressure and temperature}}{\text{volume of gas at standard conditions}}. \quad (3\text{-}8)$$

In SI units B_g is normally dimensionless (m^3/m^3) whereas in oilfield units B_g is measured in reservoir barrels per standard cubic foot (bbl/scf). Common oilfield practice is to use $1/B_g$ (scf/bbl) to avoid working with very small numbers.

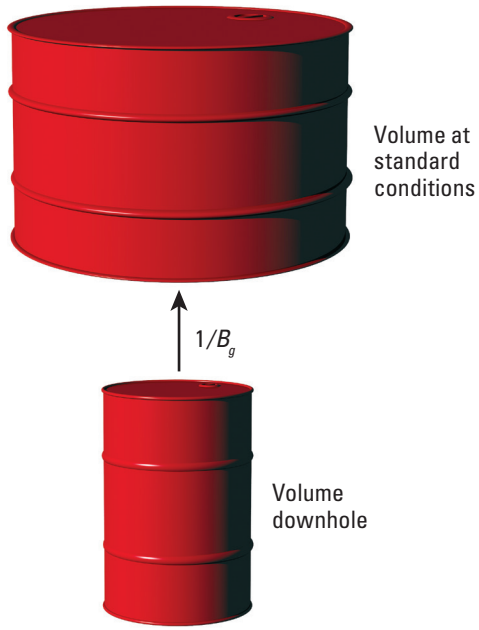

Figure 3-4. Gas shrinkage factor.

PVT of oil

Similar to PVT models for water and gas, PVT oil models are driven by the surface density of oil (measured in specific gravity or API gravity), the associated solution gas gravity, and the solution gas/oil ratio (R_{so}). The specific gravity of oil is calculated as

$$\gamma_o = \frac{\rho_o}{\rho_w}, \quad (3\text{-}9)$$

$$\text{API gravity} = \frac{141.5}{\gamma_o} - 131.5, \quad (3\text{-}10)$$

Sidebar 3B. API gravity

The curious relationship used for calculating the API gravity was chosen to deliver a linear scale on a hydrometer used to make the measurement.

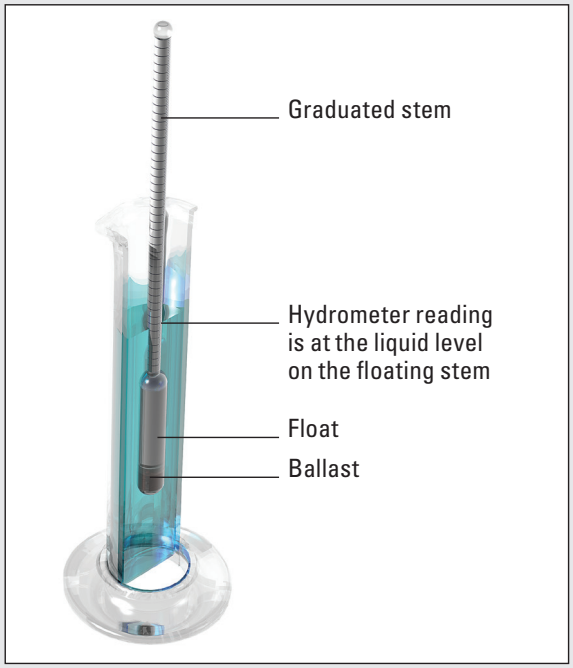

Figure 3B-1. Hydrometer reading for API gravity.

where
γ_o = specific gravity of oil
ρ_o = density of oil at standard conditions
ρ_w = density of freshwater at standard conditions
and the temperature is 60 degF.

The shrinkage factor for oil (B_o) and solution gas/oil ratio (R_{so}) are, respectively (Fig. 3-5),

$$B_o = \frac{\text{volume of oil and dissolved gas leaving the reservoir at the downhole pressure and temperature}}{\text{volume of oil at standard conditions}}, \quad (3\text{-}11)$$

$$R_{so} = \frac{\text{volume of dissolved gas at standard conditions}}{\text{volume of oil at standard conditions}}. \quad (3\text{-}12)$$

The oil shrinkage factor is always dimensionless. The solution gas/oil ratio (GOR) can be measured in standard cubic feet per stock-tank barrel (scf/bbl) or m^3/m^3. Significant errors result from confusing the units for GOR.

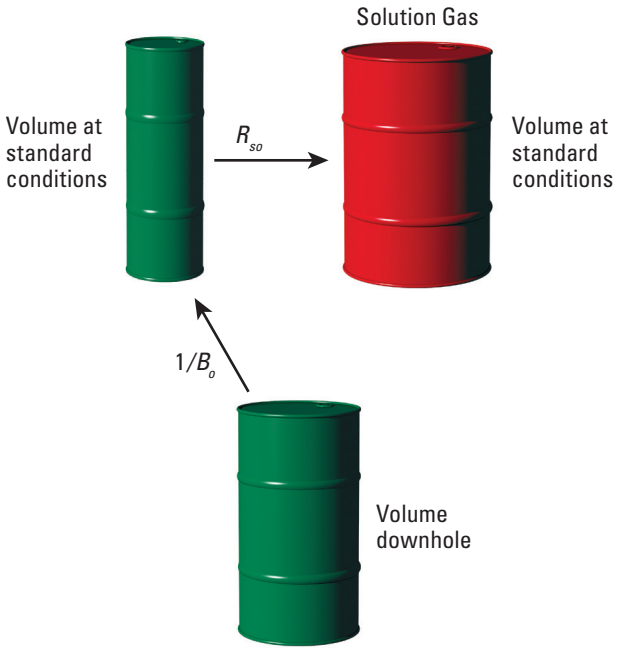

Figure 3-5. Shrinkage factors and solution gas/oil ratio for oil. Green indicates oil.

While the PVT behavior of water is straightforward and that of gas only a little more complicated, the PVT behavior of oil is much more complicated and uncertain. Historically, Standing's (1947) California Black Crude correlation has been the standard; however, the study of oil PVT has been enriched by Lasater (1958), Vazquez and Beggs (1980), Glasø (1980), Petrosky and Farshad (1998), Beggs and Robinson (1975), Beal (1946), and many more.

The presence of so many correlations indicates that most of them are wrong in some conditions and none of them is right all the time. Before deciding on the best correlation to use it is important to consider what production log interpretation needs from a PVT correlation and what effect errors have.

- Downhole oil density (ρ_o) is used for the Gradiomanometer* derived holdup. A 5% to 10% error in calculating ρ_o introduces significant nonuniform errors in the computed zonal oil splits.
- Downhole density difference between water and oil ($\rho_w - \rho_o$) is used for slip velocity calculations. A 5% to 10% error in calculating ρ_o introduces a small and relatively uniform error in the slip velocity and hence the zonal water cuts. The zonal split of oil is not significantly affected.
- ρ_o is used for computing the Reynolds number and hence the velocity profile correction. Any resulting errors are insignificant.
- ρ_o is used for computing the oil shrinkage factor (B_o). A 5% to 10% error in calculating B_o introduces an error in the surface-computed flow rates, but the zonal oil splits are not affected.
- Bubblepoint pressure (p_{bp}) is used to determine whether free gas is present and if so, how much. It is also used to determine the downhole oil density. A 5% to 10% error in p_{bp} creates a similar error in ρ_o. Working with a downhole pressure close to an unknown bubblepoint pressure typically introduces major errors.
- Oil viscosity (μ_o) has a weak effect on the velocity profile correction factor and a similarly weak effect on the frictional pressure drop calculations.
- Downhole compressibility of oil (c_o) is important for pressure transient analysis but has no effect on production log interpretation.

It therefore follows that the largest errors, resulting from unknown bubblepoint pressure and unknown oil density, are eliminated by using direct measurements of holdup such as obtained with water holdup probes and gas holdup probes.

Where there is a PVT analysis of the reservoir hydrocarbons, p_{bp}, ρ_o, and B_o no longer need to be estimated as long as the flowing bottomhole pressure and temperature match the conditions used for the PVT analysis. Where the PVT analysis does not match the logging conditions, perhaps because the flowing bottomhole pressure is well below the reservoir pressure, the basic PVT models accept a user-defined p_{bp} to improve the accuracy of the B_o, ρ_o, and μ_o estimations. Advanced PVT models calibrate a generic PVT model (such as that of Standing, 1947) to all the important PVT values of a PVT report.

In older fields, where most production logs are run, PVT analysis is further complicated by production over time. Consider Fields A and B in Sidebar 3C.

In certain parts of the world a PVT analysis is the exception rather than the rule. The best that can be hoped for is a surface GOR including oil and gas gravity. In these cases the log analyst looks for a column of pure oil and pure water (most commonly found when the well is shut in). The Gradiomanometer density is slightly shifted to match the expected produced water density, then a PVT model is tuned to match the

measured downhole oil density. A PVT model can be picked to match local preferences, but where a free choice is offered, the best practice is to ignore the older and regionally specific PVT models and choose the more modern correlations based on the biggest number of samples and improved computer selection of the correlation coefficients.

Sidebar 3C. PVT in producing fields

Field A was drilled and put into production. The following PVT properties were measured:

- gas gravity = 0.75
- oil gravity = 0.82
- R_{so} = 100 m^3/m^3
- p_{bp} = 180 bar
- reservoir temperature (T_r) = 95 degC
- B_o at bubblepoint = 1.35
- ρ at bubble point = 0.62 g/cm^3.

It is now 15 years later, and water has been injected to maintain pressure. Produced gas has been reinjected to maintain pressure and conserve the gas against the day that the field is turned into a gas field and blown down. Owing to compartmentalization and dipping high-permeability streaks, the gas cap is now in contact with some open perforations. A production log has been recorded on a well with an oil rate of 200 m^3/d, water cut of 70%, and GOR of 500 m^3/m^3.

Although the gas gravity and oil gravity are probably unchanged, the GOR has increased significantly. Different layers in the well today have different values of GOR and hence different bubblepoint pressures and other fluid properties. The PVT analysis from the beginning of field production can no longer be used and the situation has returned to one of relying on correlations and their associated errors.

Imposing the PVT bubblepoint pressure from a GOR of 100 m^3/m^3 on a well that is flowing with a GOR of 500 m^3/m^3 would result in downhole oil densities and shrinkage factors that are very wrong.

When Field B was drilled and put in production, the desire to produce oil immediately coupled with the delay in drilling water injectors and then finding poor communication from the injectors to the producers resulted in portions of the field falling 1,000 psi below the bubblepoint. Gas bubbled out of solution and formed a new gas cap. Even when water injection succeeded in raising the reservoir pressure above the bubblepoint, the gas cap remained. The produced oil now has a lower solution GOR and a different bubblepoint pressure and downhole density. The original PVT analysis is no longer valid.

Bubblepoint pressures have an average error of 10% for the best correlations, rising to 12.7% for Standing's (1947) California correlation and up to errors of 45% for the worst correlations.

If the bubblepoint pressure is known, then the best correlations for the shrinkage factors are good to errors of less than 2%. Standing's California correlation achieved about a 3% error. The worst correlations still have an error of about 9%. In the case of an unknown bubblepoint pressure, the shrinkage factor errors tend toward the bubblepoint error.

With the bubblepoint pressure known, most correlations predict the downhole density at the bubblepoint with better than a 1% error. At pressures below a known bubblepoint, the errors rise to 2%.

The prediction of oil viscosity at pressures below the bubblepoint is quite poor, with errors starting at about 20% and rising to over 50%. The prediction of oil viscosity above the bubblepoint pressure is even worse. Fortunately, oil viscosity is a very minor input to a production log interpretation.

Sidebar 3D. Bubblepoint correlation

An in situ determination of the bubblepoint can be supplied by a production logging tool containing gas holdup probes in a well with a flowing bottomhole pressure above the bubblepoint (Fig. 3D-1).

While running in hole, the production logging tool records the gas holdup and the gas bubble count as well as the flowing temperature and pressure. The bubble counts reach zero at the bubblepoint pressure.

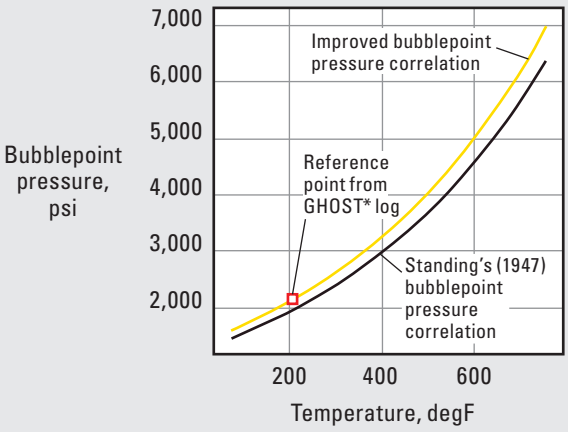

Figure 3D-1. Bubblepoint pressure imposed on a correlation.

Gas-condensate PVT

The theory of gas-condensate phase behavior and PVT models is not too difficult—until it comes to practice.

Ideally the dewpoint pressure at reservoir temperatures is not encountered until the reservoir fluids have exited the perforations and are flowing to surface (Fig. 3-6). Under these conditions either downhole samples or surface recombination samples can be analyzed to deliver an accurate PVT model.

BorFlow and Emeraude PVT models for gas condensate try to fit a second-order polynomial curve through properties at the dewpoint, standard temperature and pressure, and high-pressure first-stage separator (Fig. 3-7). This curve is primarily designed to predict the liquid condensate drop out from downhole to surface, but it can also be used to predict the downhole density of condensate for a rich gas.

The complete set of inputs to these gas-condensate PVT models is rarely available to the log analyst, and the temptation is to use the default inputs and trust to luck. Obviously the resulting computations of PVT properties relating to the condensate are quite arbitrary.

If the falling pressure from the reservoir to the borehole passes through the dewpoint, then condensate drops out in the formation, impairing the permeability and increasing the produced fraction of lean gas. Under these conditions a PVT model developed for an earlier stage in the reservoir, when the dewpoint occurred in the casing or tubing, is no longer valid because the gas/condensate ratio has changed. In some new fields the dewpoint is already found in the formation and the problems become still more intractable.

Current production logging technology in a gas-condensate reservoir can measure a downhole volumetric rate with a spinner, but there is no holdup sensor to discriminate between condensate-carrying rich gas and lean gas. Downhole fluid samples acquired with a production logging tool and subjected to a complete PVT analysis offer a possible solution to the problem of identifying where the condensate-rich gas is being produced from.

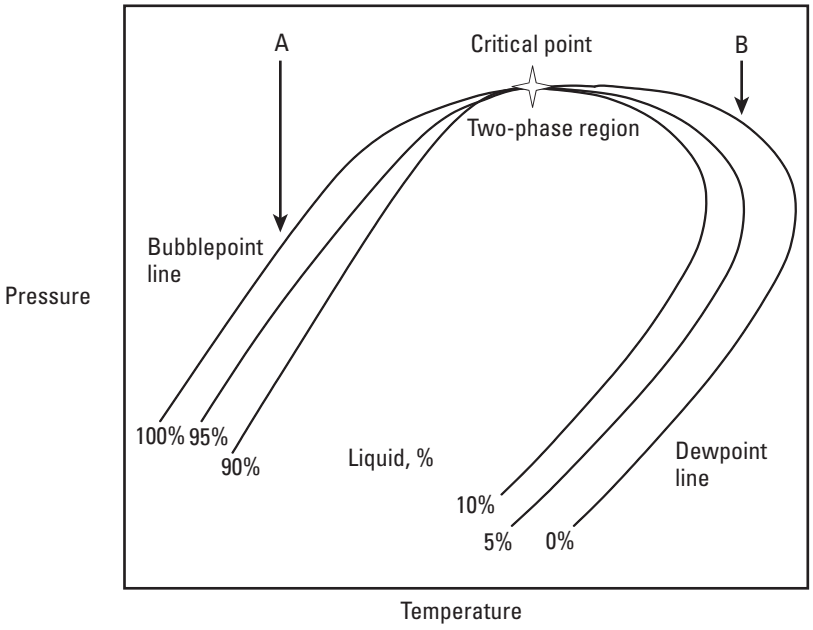

Figure 3-6. Phase diagram of a retrograde gas-condensate reservoir.

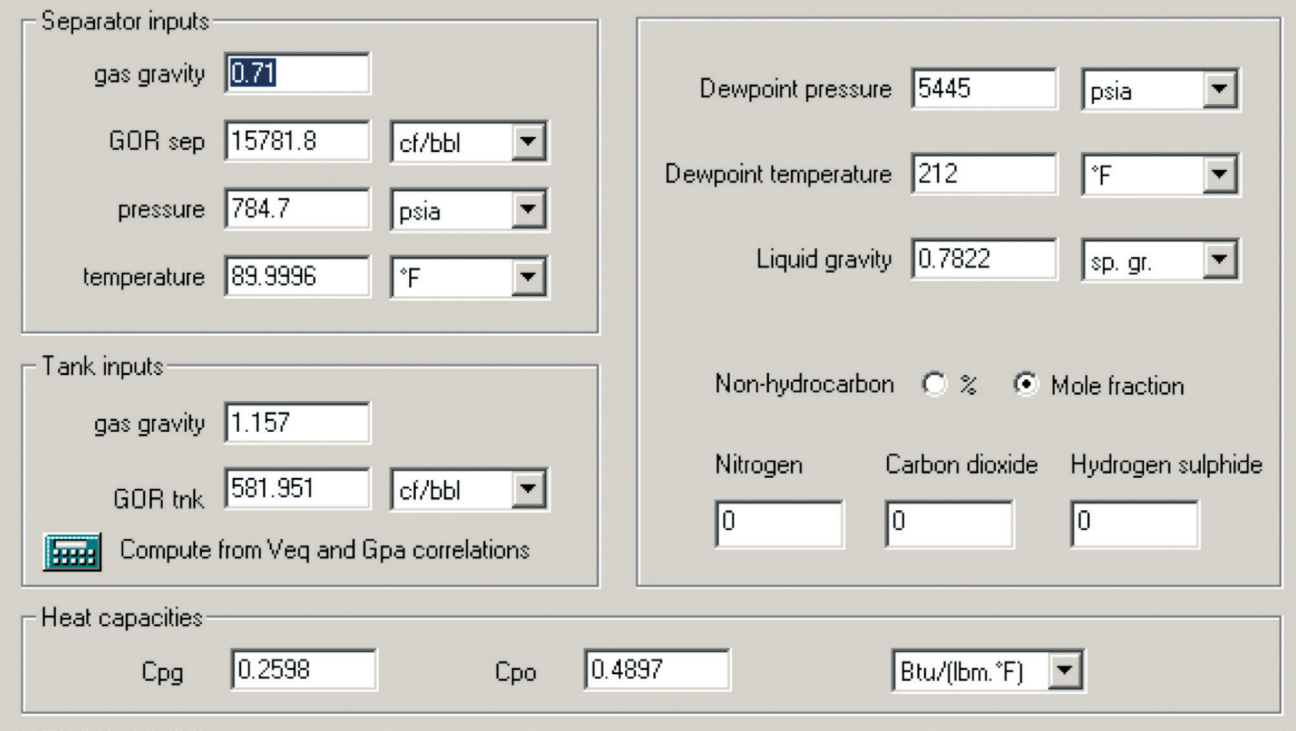

Figure 3-7. Gas-condensate PVT model inputs (Kleyweg, 1989).

References

Beal, C.: "The Viscosity of Air, Water, Natural Gas, Crude Oil and Its Associated Gases at Oilfield Temperatures and Pressures," *Trans*., AIME (1946) 165, 94–115.

Beggs, H.D., and Robinson, J.R.: "Estimating the Viscosity of Crude Oil Systems," *Journal of Petroleum Technology* (September 1975), 1140–1141.

Brill, J.P., and Beggs, H.D.: "Two-Phase Flow in Pipes," INTERCOMP Course, The Hague (1974).

Carr, N.L., Kobayashi, R., and Burrows, D.B.: "Viscosity of Hydrocarbon Gases Under Pressure," *Trans*., AIME (1954) 201, 264–272.

Culbertson, O.L., and McKetta, J.J., Jr.: "Phase Equilibria in Hydrocarbon-Water Systems III—The Solubility of Methane in Water at Pressures to 10,000 psia," *Trans.*, AIME (1951) 192, 223–226.

Glasø, Ø.: "Generalized Pressure-Volume-Temperature Correlations," *Journal of Petroleum Technology* (May 1980), 785–795.

Gould, T.L.: "Vertical Two-Phase Steam-Water Flow in Geothermal Wells," *Journal of Petroleum Technology* (August 1974), 833–842.

Hall, K.R., and Yarborough, L.: "A New Equation of State for Z-Factor Calculations," *Oil and Gas Journal* (June 18, 1973), 82–92.

Kestin, J., Khalifa, H.E., Abe, Y., Grimes, C.E., Sookiazian, H., and Wakeham, W.A.: "Effect of Pressure on the Viscosity of Aqueous NaCl Solutions in the Temperature Range 20–150°C," *Journal of Chemical Engineering Data* (1978) 23, No. 4, 328–336.

Kleyweg, D.: "A Set of Consistent PVT-Correlations for Gas/Condensate Systems," paper SPE 19509 available from SPE, Richardson, Texas, USA (1989).

Kobayashi, R.; and Katz, D.L.: "Vapor-Liquid Equilibria for Binary Hydrocarbon-Water Systems," *Industrial Engineering and Chemistry* (February 1993), 440–451.

Lasater, J.A.: "Bubble-Point Pressure Correlation," *Trans.*, AIME (1958) 213, 379–381.

Lee, A.L., Gonzalez, M.H., and Eakin, B.E.: "The Viscosity of Natural Gases," *Journal of Petroleum Technology* (August 1966), 997–1000.

Long, G., and Chierici, G.: "Salt Content Changes Compressibility of Reservoir Brines," *Petroleum Engineer* (July 1961), B-25–B-32.

McCain, W.D., Jr.: *The Properties of Petroleum Fluids* (2nd ed.), Tulsa, Oklahoma, USA, PennWell Books (1990).

McCain, W.D., Jr., Spivey, J.P., and Lenn, C.P.: *Petroleum Reservoir Fluid Property Correlations*, Tulsa, Oklahoma, USA, PennWell Books (2011).

Meehan, D.N.: "A Correlation for Water Compressibility," *Petroleum Engineer* (November 1980a), 125–126.

————: "Estimating Water Viscosity at Reservoir Conditions," *Petroleum Engineer International* (November 1980b), 117–118.

Petrosky, G.E., and Farshad, F.F.: "Pressure-Volume-Temperature Correlations for Gulf of Mexico Crude Oils," *SPE Reservoir Evaluation & Engineering* (October 1998), 416–420.

Standing, M.B.: "A Pressure-Volume-Temperature Correlation for Mixtures of California Oils and Gases," *API Drilling and Production Practice* (1947), 275–287.

Standing, M.B., and Katz, D.L.: "Density of Natural Gases," *Trans*., AIME (1942) 146, 140–149.

van Wingen, N.: "Viscosity of Air, Water, Natural Gas, and Crude Oil at Varying Pressures and Temperatures," *Secondary Recovery of Oil in the United States* (2nd ed.), Dallas, Texas, USA, API (1950), 126–132.

Vazquez, M.E., and Beggs, H.D.: "Correlations for Fluid Physical Property Prediction," *Journal of Petroleum Technology* (June 1980), 968–970.

4 Spinner Velocity Tools

Although turbine, or spinner, flowmeters are used extensively within industry with small to negligible errors, the situation is very different in oilfield applications.

The fullbore spinner does not, as its name suggests, cover the entire pipe cross section (Fig. 4-1). Typically a fullbore spinner sweeps only about 40% of the casing's cross-sectional area. In addition, the blades do not have a progressive pitch (as on a ship's propellers and in gas turbines) because the requirement to collapse down to a diameter of $1\frac{1}{16}$ in precludes anything more complicated than a flat spinner blade.

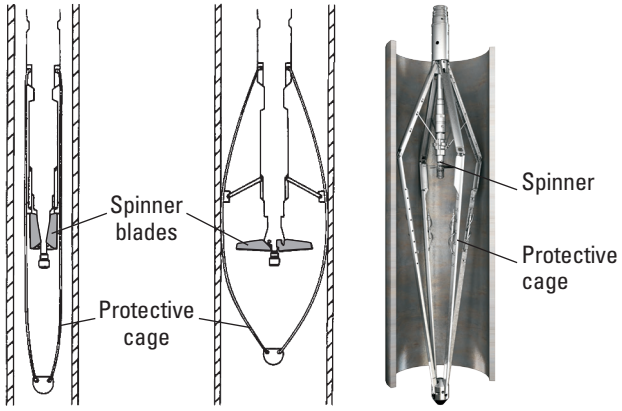

Figure 4-1. Fullbore spinner schematic.

The continuous, or tubing, spinner has a progressive-pitch spinner, which is more effective at extracting energy from the well fluids (and therefore reducing the spinner threshold, which is the minimum velocity needed to start the spinner turning) (Fig. 4-2). Unfortunately, the much reduced spinner diameter more than negates the effect of the improved blade profile, and the threshold velocity of a standard tubing spinner is about 3 times higher than that of a fullbore spinner.

The Flow Scanner* minispinner (Fig. 4-3) is used in an array of five minispinners recording velocities on the vertical axis of the pipe, from the bottom to the top. This arrangement is discussed in detail for the Flow Scanner horizontal and deviated well production logging system (see the "Flow Scanner Interpretation" chapter). A change of bearing technology together with the progressive pitch of a tubing spinner delivers a spinner threshold comparable to that of a fullbore spinner.

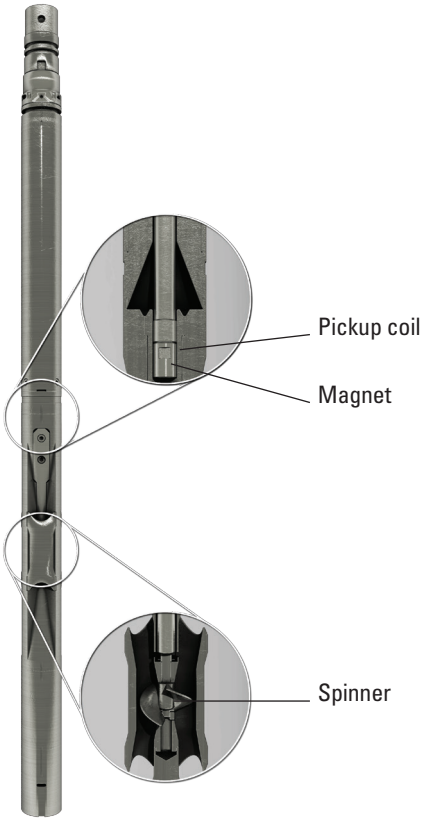

Figure 4-2. Continuous, or tubing, spinner.

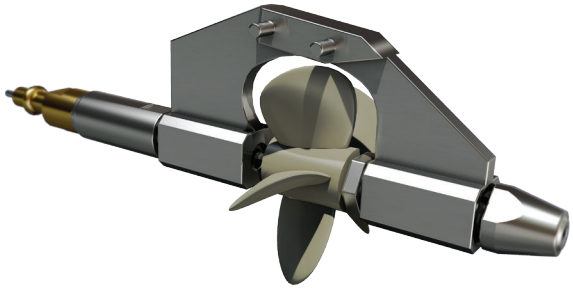

Figure 4-3. Flow Scanner minispinner.

Theoretical spinner response model

Consider the response of an ideal spinner flowmeter (Fig. 4-4). The spinner speed in revolutions per second (rps) is directly proportional to the fluid velocity passing through the spinner. The slope of the response curve, measured in rps/ft/min [rps/m/min], comes directly from the spinner pitch measured in inches [centimeters].

Once friction in the bearings is included, the response becomes a little more complicated, with two response lines, one for positive spinner readings and a second for negative spinner readings. There is now a range of low fluid velocities where the spinner does not turn because the spinner torque is smaller than the bearing friction. Close inspection of the response lines in Fig. 4-4 shows a small curve at low spinner speeds owing to the action of static friction (stiction), viscosity effects, or both. To avoid the complications arising from nonlinear spinner response, near-zero spinner readings are discarded if they look at all suspicious.

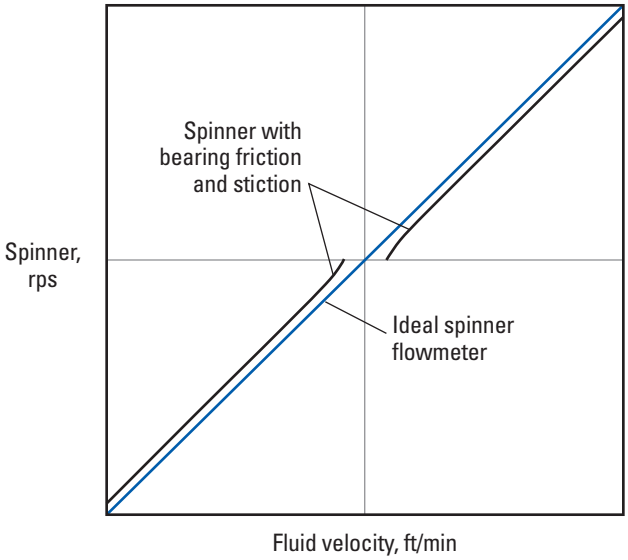

Figure 4-4. Spinner response with friction and stiction.

Increasing the viscosity of the fluid passing through the spinner produces some unusual results. The threshold first increases and then decreases while the spinner slope changes by about a factor of 5 or more. Figures 4-5 and 4-6 show the results of previously unpublished experimental data from the Schlumberger Gould Research Center.

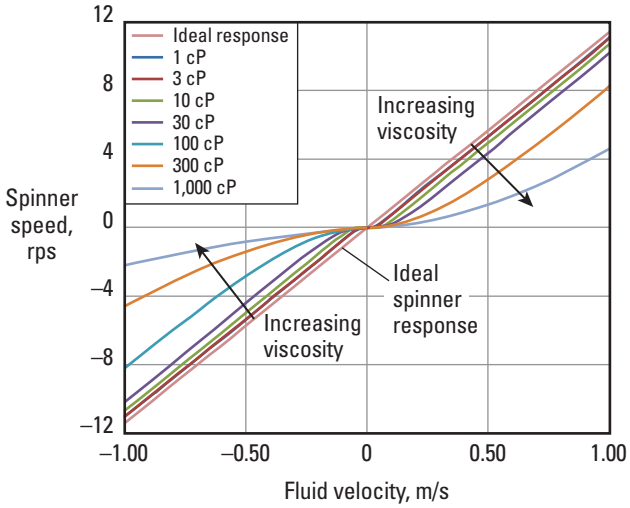

Figure 4-5. Spinner response to increasing viscosity.

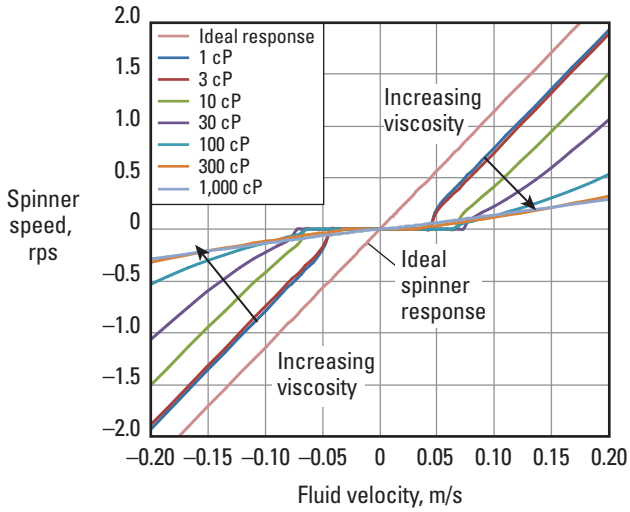

Figure 4-6. Spinner response to increasing viscosity, amplified scale.

Changing the density of the fluid passing through the spinner (e.g., from liquid to gas) also increases the size of the low-velocity region where the spinner does not turn but should not significantly change the spinner response slope (Fig. 4-7).

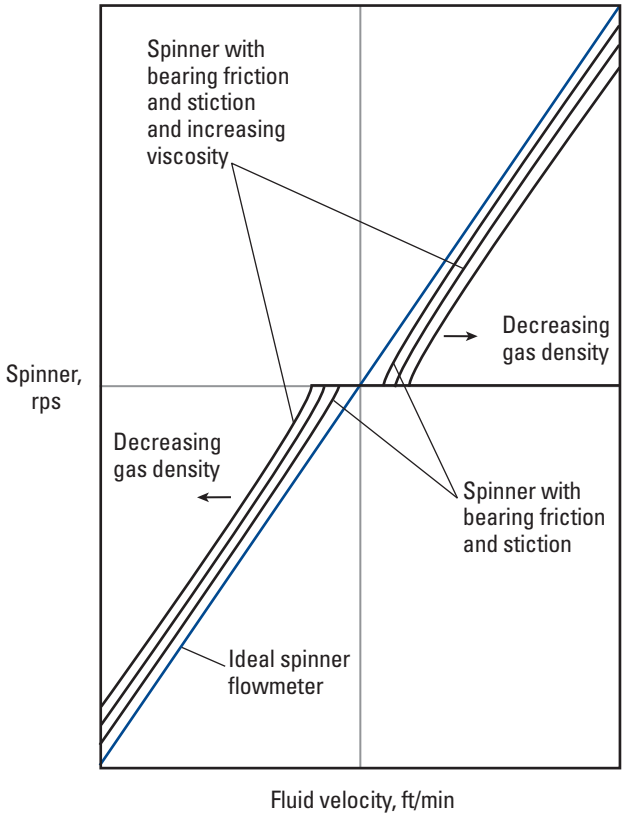

Figure 4-7. Spinner response to decreasing density.

However, changing the fluid from liquid to gas causes a big change in the pseudo-Reynolds number (created using the tool velocity) and makes the creation of turbulence and vortices much easier, thus leading to the situation of Fig. 4-8:

$$N_{\mathrm{Re\_pseudo}} = \frac{v\rho d}{\mu}, \qquad (4\text{-}1)$$

where

v = tool velocity, m/s

ρ = gas density, kg/m^3

d = hydraulic diameter, m (this number is a little larger than the pipe internal diameter)

μ = dynamic viscosity, Pa.s.

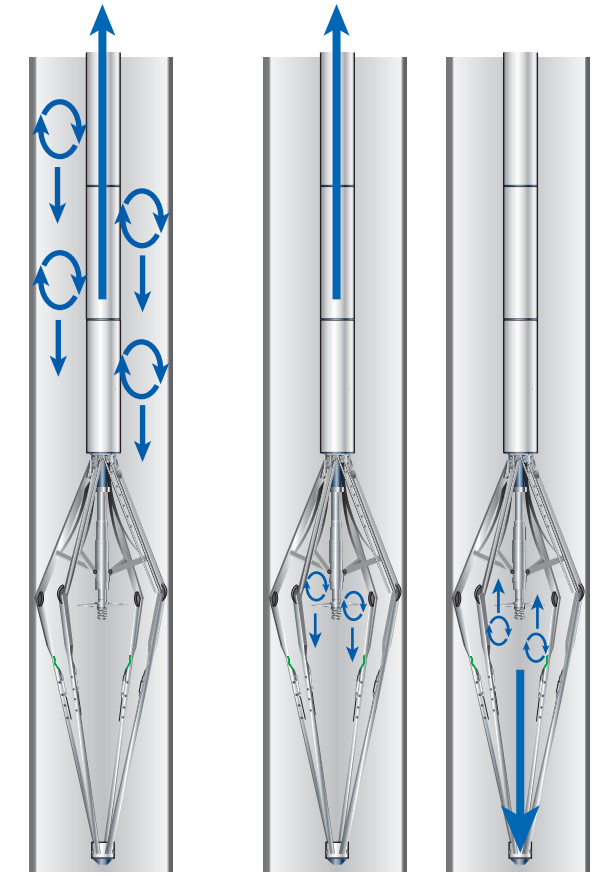

Figure 4-8. Fluid turbulence and the fullbore spinner.

On the left of Fig. 4-8 is an upward-moving tool (equivalent to a negative fluid velocity) generating vortices that travel down and confuse the spinner. Behavior like this creates asymmetric spinner slopes and thresholds. The effect can be expected to be bigger in gas wells, but it is still present in water and the lighter oils.

In the middle and on the right of Fig. 4-8 is the effect of the spinner cage stirring up the flow. To a first-order approximation the effects seem to be equal for flow from above and flow from below.

Practical spinner response model

The theoretical spinner response model described in the previous section is too complicated for everyday use. Instead, some approximations are introduced until the model of Fig. 4-9 is reached. This shows a spinner in an unknown fluid as having a positive and negative spinner slope and a positive and negative spinner threshold. Because these four parameters can change with velocity, fluid density, fluid viscosity, casing diameter, and other conditions, the model needs judicious updating over an interpretation interval.

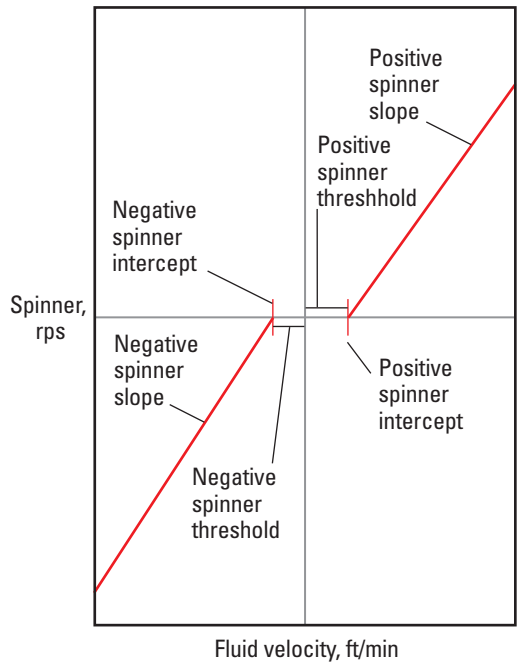

Figure 4-9. Approximation to a spinner response.

Spinner interpretation—Initial laboratory characterization

The first approach (Meunier et al., 1971) to calibrating the spinner involved laboratory characterization and the creation of interpretation nomograms (Fig. 4-10).

The laboratory-determined spinner threshold and spinner pitch were combined with a stationary spinner reading, velocity-profile viscosity model, and the pipe internal diameter to deliver a downhole flow rate.

Unfortunately, the log analyst did not often have reliable downhole viscosity information, so measurements of the spinner threshold in the laboratory were rarely representative of the field, and logs versus depth could not easily be processed.

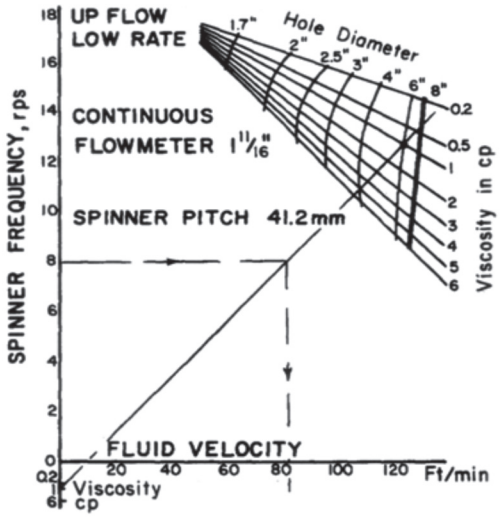

Figure 4-10. Spinner interpretation nomogram (Meunier et al., 1971).

Sidebar 4A. Downhole tool speed

Because tool speed cannot be measured downhole, as a proxy the cable velocity at surface is used. Typically cable speeds of 30, 60, and 90 ft/min [10, 20, and 30 m/min] are used, but for unstable wells additional speeds are added to average out the variations. For high-velocity gas wells, top speeds of 120–150 ft/min [40–50 m/min] are used to better define the positive spinner intercept.

In situ spinner calibration

Fortunately, the in situ spinner calibration technique was developed. The earliest reference to this technique dates back to Peebler (1982).

Because it is impractical to vary the downhole fluid velocity while measuring the spinner rps, the problem of spinner characterization (usually known as calibration) is approached from a different direction. Instead of varying the fluid velocity, the tool is moved up and down at different speeds and the spinner rps plotted versus tool speed.

Sidebar 4B. Downhole tool velocity measurement

In the absence of any kind of downhole velocity or downhole depth measurement, the tool velocity is inferred from the cable velocity as it leaves the drum at surface. Fortunately, under steady-state conditions the velocity at surface is very close to the downhole tool velocity. However, under transient conditions as the tool accelerates from rest or slows to a halt, the tool velocity cannot be expected to accurately match the cable velocity at surface. As a rule of thumb, traversing a 30-ft [10-m] interval above the top perforation and below the deepest perforation allows the tool to achieve a steady velocity before logging the zone of interest.

In a zero-flow environment it is possible to determine the positive and negative spinner slopes and the positive and negative spinner thresholds (Fig. 4-11). But where does a zero-flow environment exist? Shutting in the well at surface does not guarantee zero flow because there may be crossflow between zones. Above the top perforation, after the well has been shut in for many hours, there should be no flow, but in the time available for production logging there may be wellbore storage (unlikely) or liquid fallback from the tubing that extends to surface. Although it is safer to assume that there is no flow below the deepest perforation (in the absence of casing plugs isolating deeper zones), the fluid density and viscosity below the deepest perforation are often unrepresentative of the fluid density and viscosity flowing in the well (the fluid for which the spinner calibration is intended). Usually the best way to identify a zero-flow region is to refer to the temperature log and identify what appears to be a geothermal gradient because geothermal gradients are incompatible with fluid movement. The spinner calibration in Fig. 4-12 corresponds to a small positive velocity (downflow) but this analysis can be delivered with confidence only after inspecting the temperature log in Fig. 4-13.

The log in Fig. 4-13 shows cable velocity, depth, spinner rps, the extent of the perforated intervals in red, spinner calibration zone in yellow, rate calibration zones in gray, pressure, temperature, and density (indicating a water-filled borehole). The steep change in temperature at about 3,900 ft shows where the cooler crossflowing water is lost into a perforation (indicated in red) and the geothermal gradient is recovered.

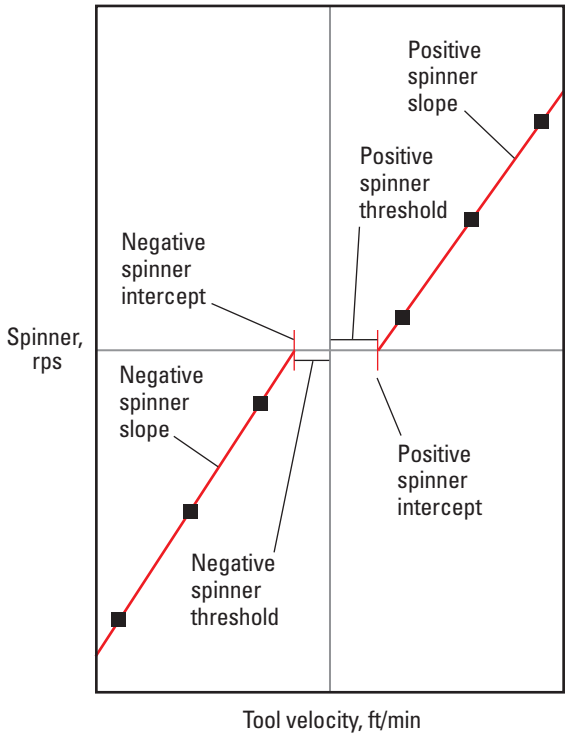

Figure 4-11. Zero-flow spinner calibration.

Sidebar 4C. Positive velocity, positive rps

Why is a cable velocity positive when running in the hole? Differentiating depth with respect to time gives a positive velocity for increasing depth and a negative velocity for decreasing depth. Therefore, flow to surface has a negative cable velocity on the spinner cable velocity crossplot. Somewhat arbitrarily, it has been decided that a spinner should return positive rps when driven by a positive cable velocity in zero-flow conditions.

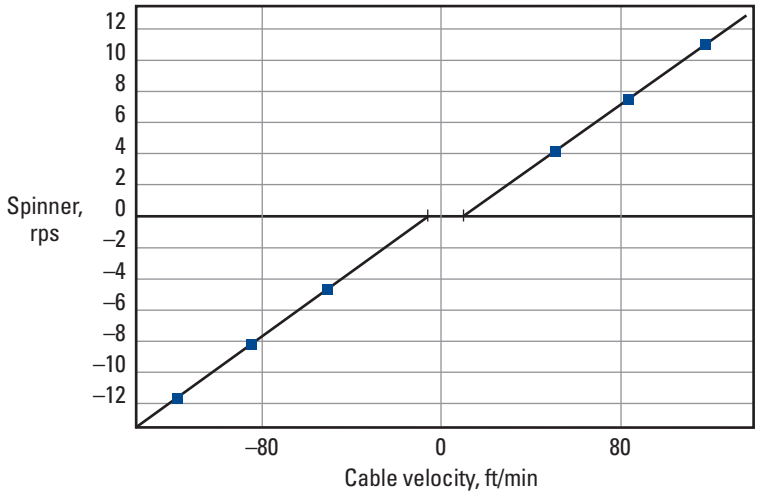

Figure 4-12. Ambiguous near-zero spinner calibration.

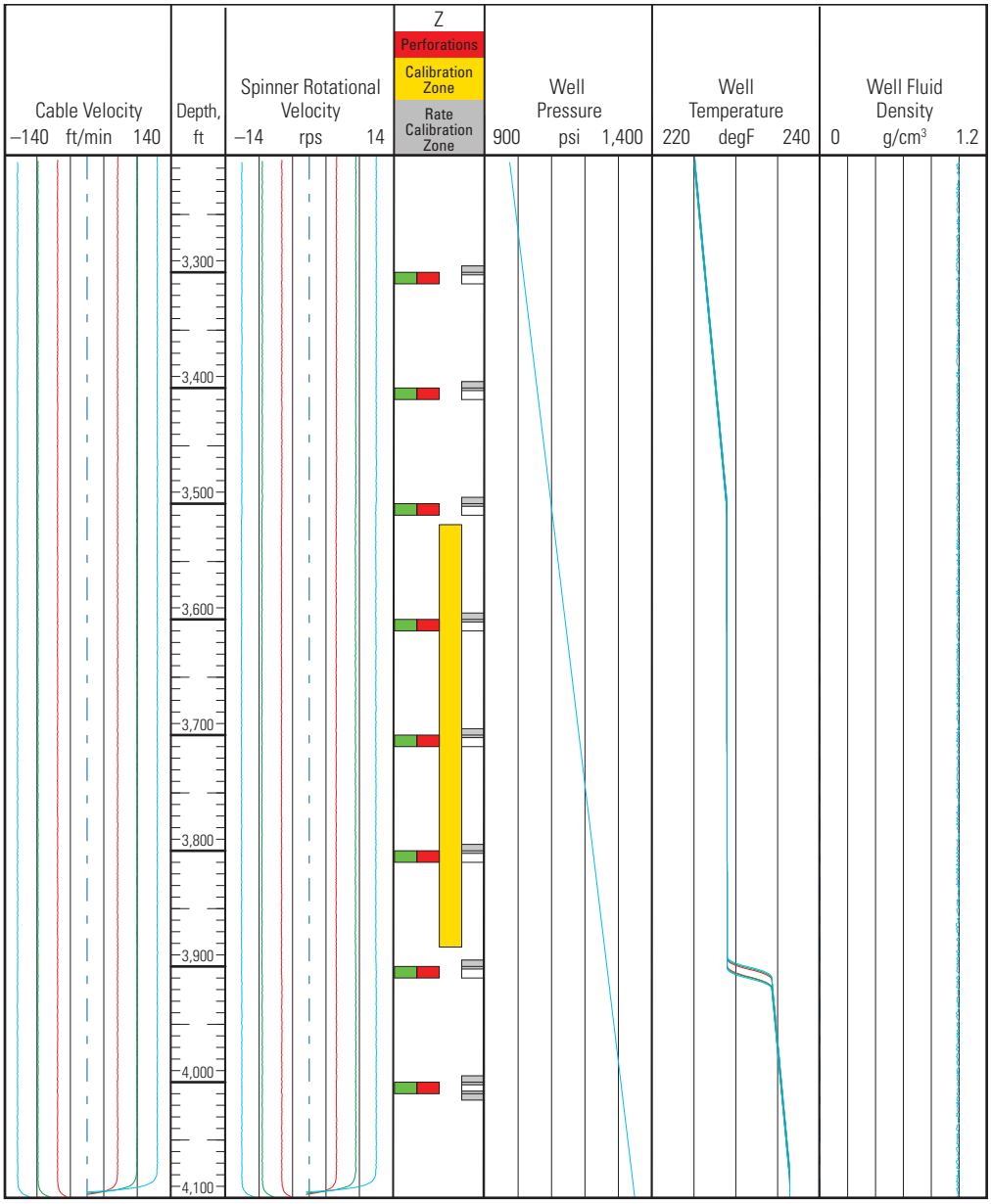

Figure 4-13. Near-zero spinner calibration plot data.

Will the positive and negative spinner thresholds be of equal magnitude? To a first-order approximation, the answer is yes, but more precisely the answer is generally no. It is normal to see a positive threshold that is between 40% and 60% of the distance from the negative intercept to the positive intercept, but a range of 30% to 70% is still acceptable. Only when values of less than 30% or more than 70% are encountered should the validity of the spinner calibration or spinner measurements be questioned.

When the well is flowing, the same spinner response is translated to the left, with the measured velocity found by subtracting the positive spinner threshold from the positive intercept (Fig. 4-14).

Zero spinner readings have an associated uncertainty on the cable velocity axis no matter how accurately the cable velocity is measured. Consequently a zero (or near zero, say less than 0.5 rps) spinner reading should never be used to calculate a spinner slope or fluid velocity.

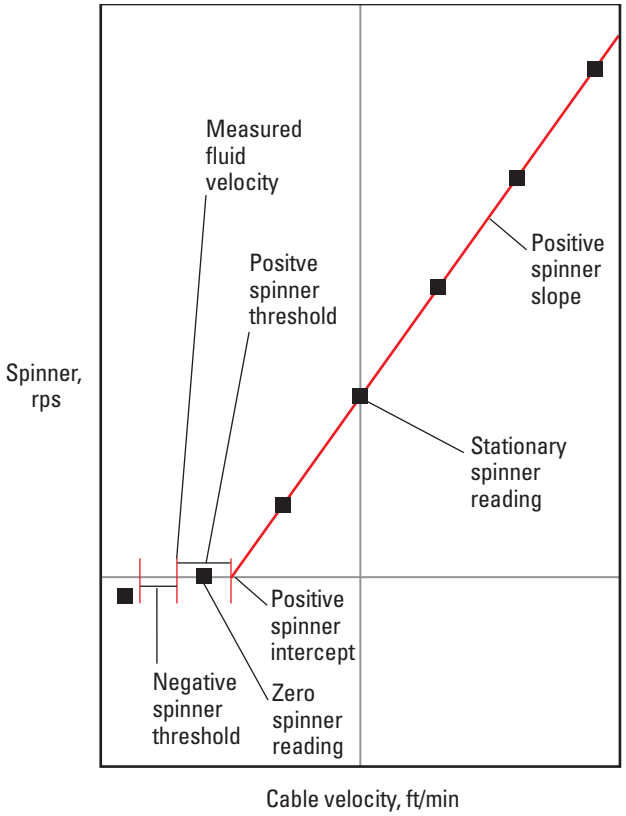

Figure 4-14. Spinner calibration in a flowing well.

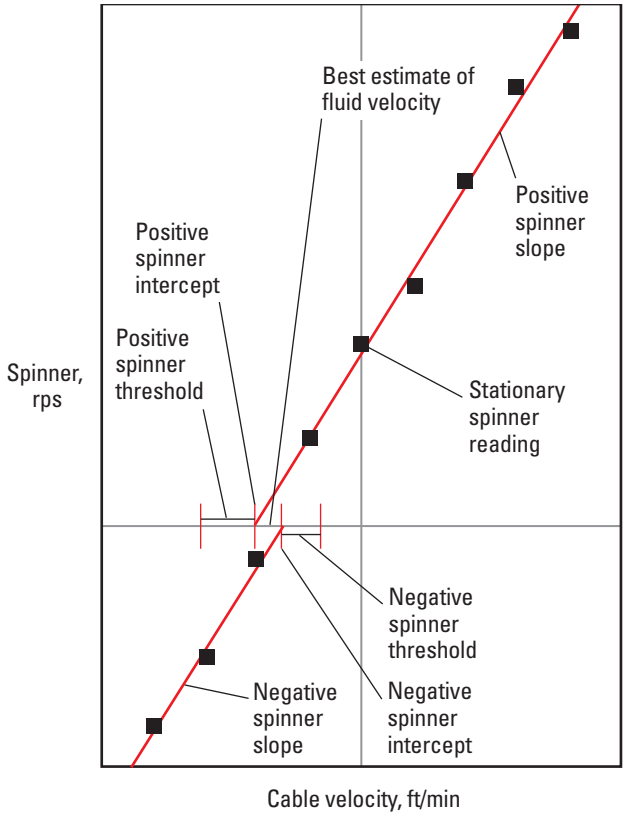

Figure 4-15. Crossed intercepts on a spinner calibration.

Stationary spinner readings, which are spinner readings with a cable velocity of zero, can be added to the crossplot, where they complement the pass data.

Note that the data quality of the flowing crossplot in Fig. 4-14 occurs only in stable monophasic flowing conditions. Multiphase flow has more scatter on the data points and more ambiguity in choosing the appropriate spinner slope and threshold.

Where the fluid velocity is about 60 ft/min [20 m/min] or faster, it is not be possible to determine the negative spinner intercept with any degree of confidence if at all. Therefore, the positive spinner threshold has to be assumed from lower speed measurements deeper in the well. There are errors in this assumption of the order of 10% to 20% of the positive spinner threshold. Taking a typical fullbore spinner threshold of 5 ft/min, the expected error in the assumed threshold is about 0.5 to 1.0 ft/min. However, compared with a fluid velocity of 60 ft/min or higher, an error of 0.5 to 1.0 ft/min is not significant.

In deviated wells with multiphase flow it is not uncommon to see the positive and negative intercepts move closer to each other and finally move past each other, resulting in an overlapping intercept (Fig. 4-15). In this case there are no physical models to allow any correction to be applied; therefore, averaging the positive and negative intercepts and calling this the spinner velocity is a simple and not too bad way of creating a fluid velocity.

The log in Fig. 4-16 is from a deviated well under shut-in conditions and possibly with a little bit of water fallback and oil bubbling upward. Track 1 shows the cable velocity followed by the depth, fullbore spinner rps, perforation interval in red, spinner calibration zones in yellow, rate calibration zones in gray, pressure, temperature, mixture density, X caliper, Y caliper, cable tension, and formation gamma ray.

Above 2,815 m there is 9⅝-in casing and below 2,817 m there is a 7-in liner. The wellbore oil/water contact is at 2,820.5 m. The temperature response at 2,821.5 m is opposite a perforation and may indicate some inflow.

Three spinner calibration zones were chosen. The top zone is in the 9⅝-in casing in the oil column that may have some water falling back from the tubing when the well was shut in. The second zone is in similar conditions except for a reduction in the casing size. The third zone is in the water leg in the 7-in liner.

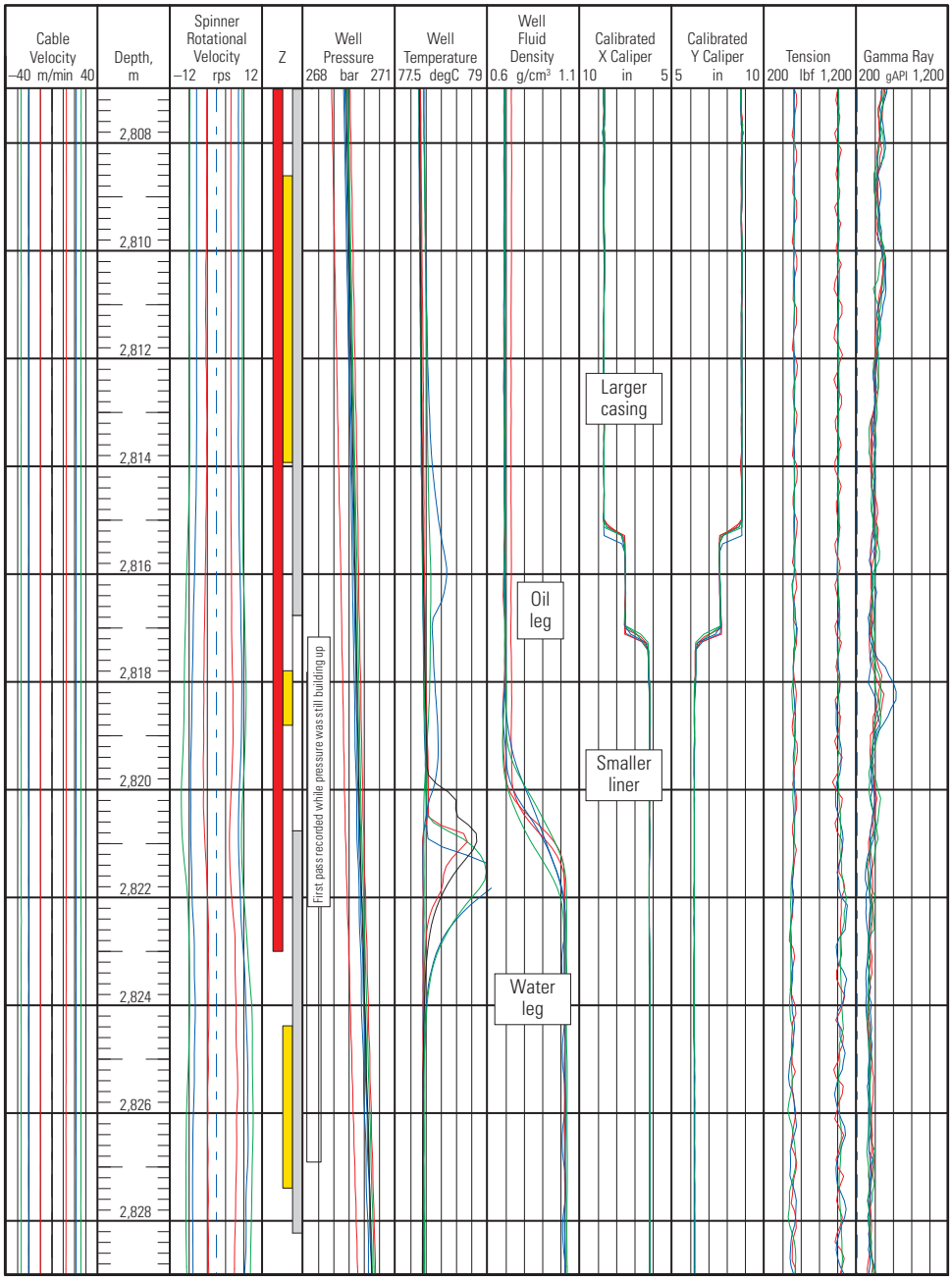

Figure 4-16. Effect of changing diameter, changing density, and recirculation.

In Fig. 4-17 it can be observed that the top two zones have crossed intercepts. Each calibration zone has a different slope as the spinner responds to changes in mixture density and casing ID. No one slope is correct, and the log analyst must choose where the slopes (and thresholds) are calculated and where the interpolation between zones should occur.

On occasion it is impossible to calibrate the spinner downhole with a series of up and down passes at different speeds. Perhaps the tool failed after the first logging pass or well conditions changed. In these cases a default spinner slope and threshold must be applied. The table in the Appendix to this book contains the theoretical spinner slopes (and pitches) and reasonable estimates of spinner thresholds for all current and most historical Schlumberger spinners.

Because it is normal to see some changes in slope and threshold over the logged interval, the use of a default slope and threshold is deprecated as it often results in an inferior interpretation answer.

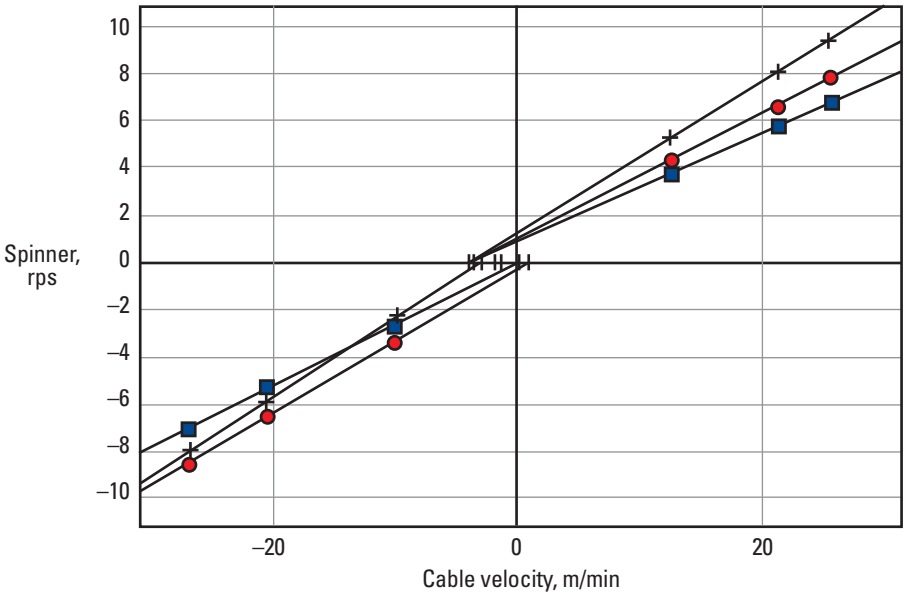

Threshold/Interval = 0.5

Calibration Zone, m	Positive Slope	Negative Slope	Positive Intercept, m/min	Negative Intercept, m/min	Intercept Difference, m/min
2,808.3–2,813.0	0.229	0.259	–3.98	0.18	–4.16
2,818.1–2,818.7	0.266	0.305	–3.65	0.90	–4.55
2,824.5–2,828.3	0.319	0.334	–4.09	–3.03	–1.06

Figure 4-17. Spinner calibration from data of Fig. 4-16.

Spinner velocity to mixture velocity

The spinner measures a fluid velocity but this is not the same as an average mixture velocity. Across the pipe there are faster moving fluids in the center and slower moving fluids closer to the pipe wall. The centralized spinner reads some kind of average of the faster moving fluid velocities swept by the spinner blade (Fig. 4-18).

A correction factor is required to reduce the spinner velocity to the average velocity. The first approach (Nicolas and Meunier, 1970) to this problem was entirely empirical, based on a survey of 45 wells where surface separator rates could be compared with downhole velocity measurements (Fig. 4-19). The spinner diameter used for these surveys was probably about 1.5 in [3.8 cm], thus requiring a smaller correction coefficient than a more modern spinner of 2½-in or 3½-in [6.4- to 8.9-cm] diameter.

Despite the lack of scientific rigor (the correction factor should increase from the bottom to the top of the well as the velocity increases and the velocity profile becomes flatter), the correction factor of 0.83 is still widely used today and does not introduce unmanageable errors.

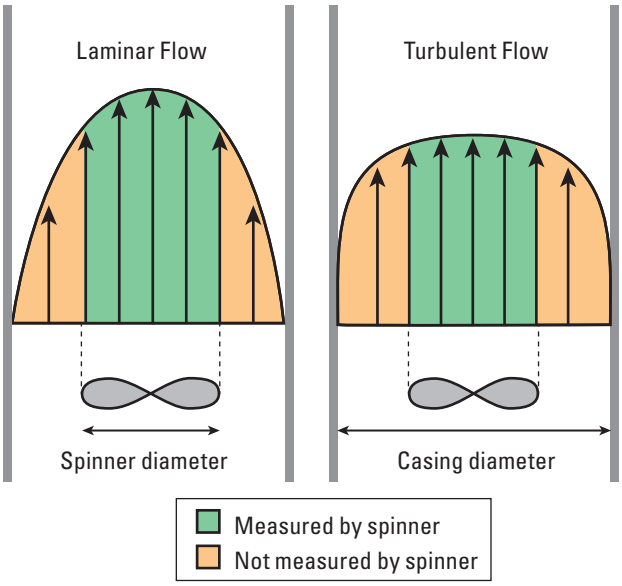

Figure 4-18. Effect of velocity profile on apparent spinner velocity.

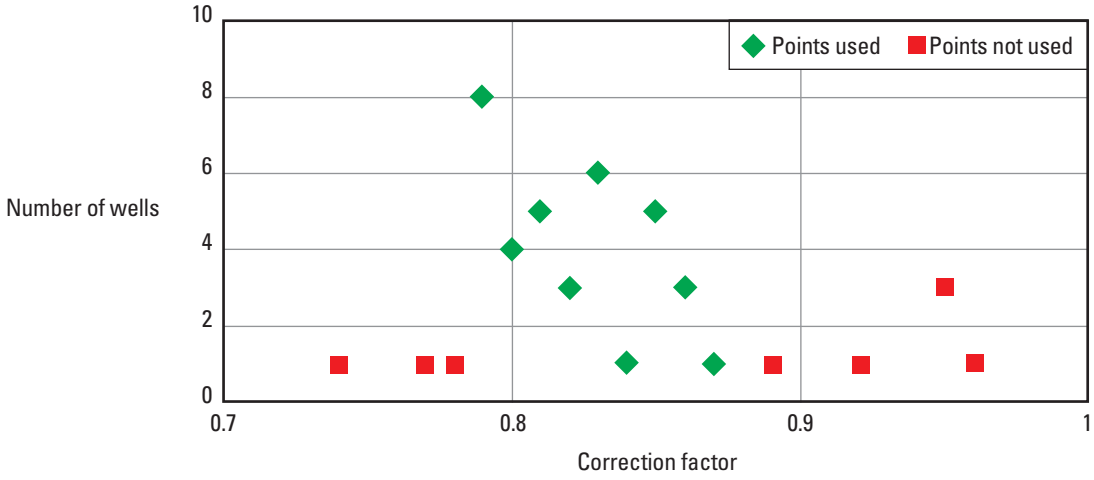

Figure 4-19. Empirical study of 45 wells to determine a spinner correction factor (Nicolas and Meunier, 1970).

Most modern computer-based interpretation techniques use a model for the velocity profile across the pipe and then average the velocity that would be seen by the swept area of the spinner.

For a spinner (Fig. 4-20) with blades of external radius R_2, internal radius R_1, and in laminar flow, the average velocity seen by the spinner is

$$v_{ave\_spinner} = \frac{2v_{max}}{\left(R_2^2 - r_1^2\right)}\left[\frac{r^2}{2} - \frac{r^4}{4R^2}\right]_{R_1}^{R_2}, \qquad (4\text{-}2)$$

with

$$v_{ave} = \frac{v_{max}}{2}, \qquad (4\text{-}3)$$

making the correction factor

$$F_{vpc} = \frac{v_{ave}}{v_{ave\_spinner}}, \qquad (4\text{-}4)$$

where

$v_{ave\_spinner}$ = average velocity measured in the swept area of the spinner
v_{max} = pipe centerline velocity
r = radial distance from the pipe centerline
R = pipe internal radius
v_{ave} = average pipe velocity
F_{vpc} = spinner correction factor (more commonly known as the velocity profile correction factor [VPCF]).

In turbulent flow and using the Prandtl relationship,

$$v_{ave\_spinner} = \frac{2R^2 v_{max}}{\left(R_2^2 - R_1^2\right)}\left[\frac{z^{m+2}}{m+2} - \frac{z^{m+1}}{m+1}\right]_{1-\frac{R_1}{R}}^{1-\frac{R_2}{R}}, \qquad (4\text{-}5)$$

where z comes from the following substitution:

$$z = 1 - \frac{r}{R}, \qquad (4\text{-}6)$$

and

$$v_{ave} = \frac{2v_{max}}{(m+1)(m+2)}. \qquad (4\text{-}7)$$

F_{vpc} is still calculated using Eq. 4-4.

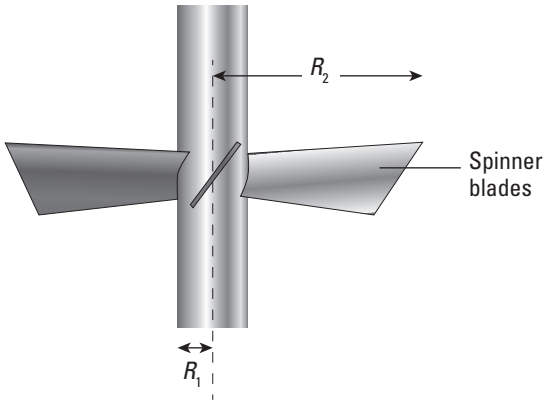

Figure 4-20. Spinner blade dimensions.

In the case of two- or three-phase flow, the same correction algorithms developed for monophasic flow are used. Where the multiphase velocity profile looks similar to a monophasic velocity (in vertical wells or high-velocity deviated wells) this approximation is acceptable. However, in deviated wells with low-velocity multiphase-flow, recirculation occurs.

Recirculation and the spinner

In anywhere from 5° to 75° deviation, a low mixture velocity combined with a high slip velocity produces gravity segregation of the phases, giving rise to large high-side velocities, significant shear between light and heavy phases in the pipe, and finally a downflow of the heavy phase on the low side of the pipe (Fig. 4-21). A centered spinner tries to average the mixture of velocities passing through the swept area of the blades but generally returns a velocity that is too low if not actually negative. A poorly centralized spinner, lying closer to the low side of the pipe, returns an answer still more heavily weighted for heavy-phase recirculation.

Increasing the diameter of the spinner blades reduces the size of the errors and is the simplest way of improving data quality under these conditions. The data in Fig. 4-22 shows the effect of increasing the spinner swept area (however, the use of heavy dead oil has greatly reduced the slip velocity and the recirculation effect).

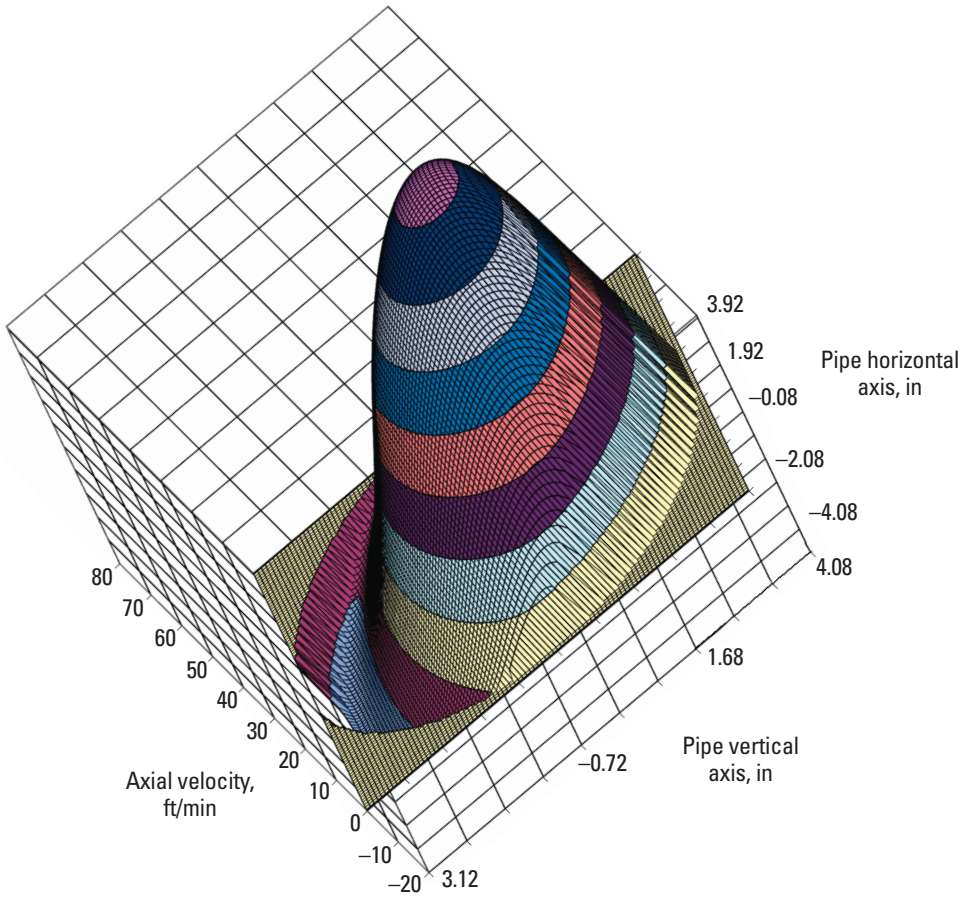

Figure 4-21. Three-dimensional axial velocity distribution in recirculation.

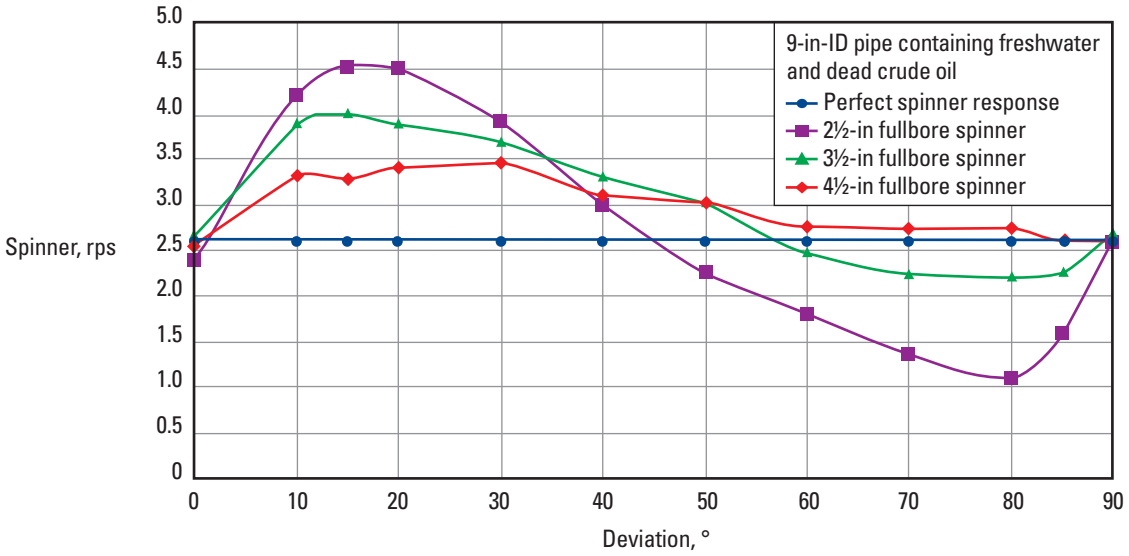

Figure 4-22. Effect of increasing spinner deviation at a constant oil–water flow rate on recirculation errors.

While recirculation normally occurs with gas or oil bubbling up through water, the inverse situation, of water falling back through oil or gas, is often seen when a well has just been shut in. In these cases the spinner sees an erroneous uphole flow rate.

Diverter flowmeters

Another approach to handling the problems of recirculation is use of the diverter flowmeter. Because recirculation requires a low mixture velocity, the diverter, or petal basket (Fig. 4-23), flowmeter funnels the flow of the well through a 1- to 1½-in diameter tube in which a spinner velocity is recorded. If run in a 7-in completion the diverter flowmeter increases the velocity by about 20 times and therefore reduces the poorly defined threshold for recirculation effects to one twentieth. However, once the diverter is deployed the diverter flowmeter tool can only be used to make stationary measurements. This means that the accelerated flow passing through the diverter must exceed the spinner threshold (which is of the order of 15 ft/min for the small spinner used). In addition, the in situ spinner calibration of the slope and threshold must be made with the flowmeter closed and in a different flow regime from that being used for the station measurements. Nevertheless, the diverter flowmeter is currently the least bad approach to measuring velocity in the presence of recirculation.

Sidebar 4D. Petal baskets

The original diverter flowmeter tool used a series of metal petals that slid over each other and unfortunately provided an interesting nonlinear leak path around the turbine. More modern designs use a better sealing fabric diverter, but the old and technically incorrect name of petal basket flowmeter is still in common usage.

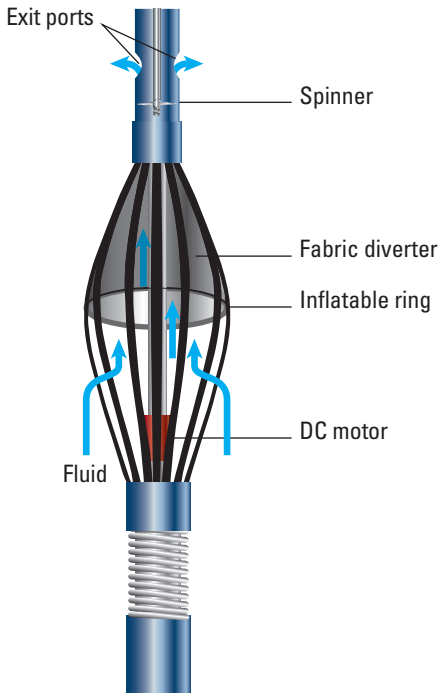

Figure 4-23. Diverter, or petal basket, flowmeter.

Graphical interpretation techniques

In the past, graphical techniques for interpreting spinner data were very popular. One elegant approach is still seen in production log interpretation manuals. In Fig. 4-24, after the various stable interval responses are plotted together with a zero-flow response, the reading line for the zero tool velocity spinner is projected right, across to the zero-flow line, from which a vertical line is dropped down to the horizontal axis, which delivers the fluid velocity. Increasing the slope of the zero-flow line by the reciprocal of the velocity profile correction factor automatically corrects for the velocity profile across the pipe.

This technique assumes that the zero-flow spinner response slope and threshold are applicable to all the stable intervals above. In practice this is true only for well-behaved monophasic wells with a clean, uncontaminated zero-flow region at the bottom. This plotting technique is no longer used commercially.

Computer processing algorithms

Computer-based interpretation techniques tend to use one of two approaches for delivering a velocity to the flow rate interpretation engine.

In the first approach, a spinner calibration is performed above and below every production zone of interest. The velocity computed by the spinner calibration is delivered directly to the interpretation engine. No flow rates are computed outside of the spinner calibration zones. (This technique is used by BorFlow software.)

In the second, a spinner calibration is performed every time the spinner calibration slope or threshold is suspected of changing. In a monophasic well this requires a single spinner calibration, whereas in a multiphase well with changing holdup and velocity a series of spinner calibrations are made.

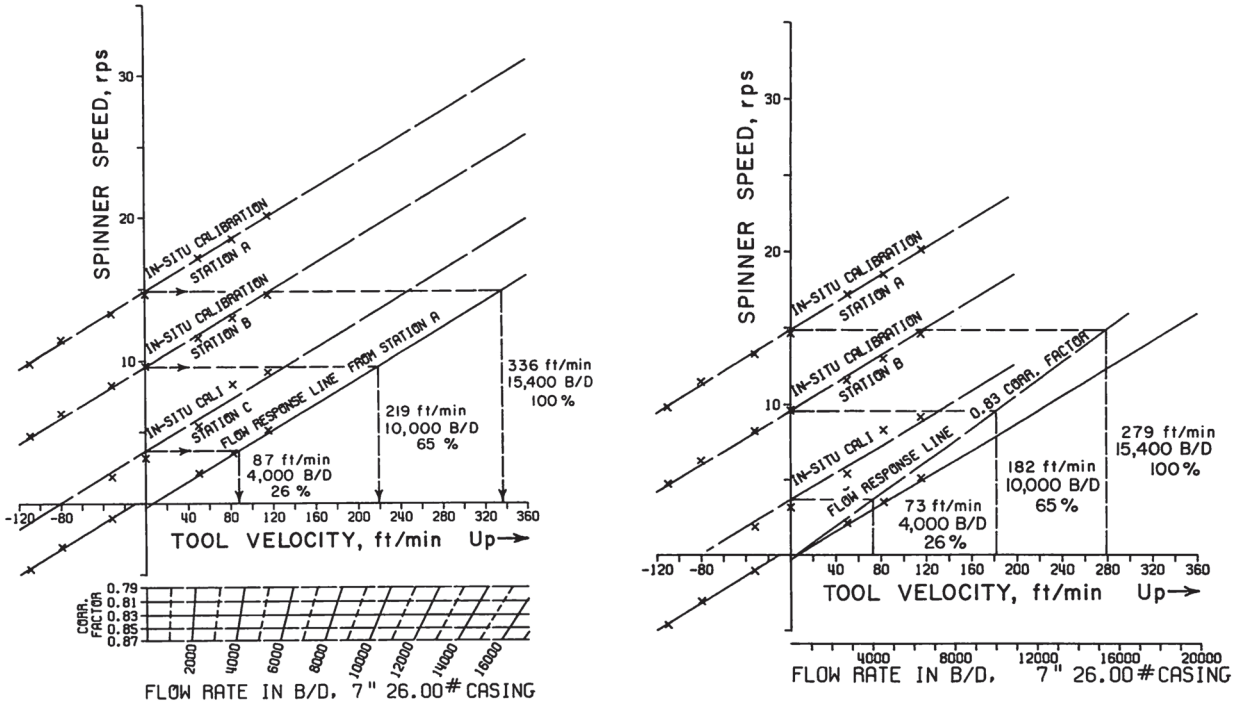

Figure 4-24. Graphical techniques for computing the mixture velocity (*Production Log Interpretation*, 1973).

From each calibration zone only the slopes and thresholds are used (the computed spinner velocity is ignored). Each spinner pass is converted into a spinner velocity pass using the following equation for positive spinner readings:

$$v_{\text{spinner}} = \frac{\omega_{\text{spinner}}}{\gamma_{\text{positive}}} + v_{+\text{threshold}} - v_{\text{cable}}, \quad (4\text{-}8)$$

and this equation for negative spinner readings:

$$v_{\text{spinner}} = \frac{\omega_{\text{spinner}}}{\gamma_{\text{negative}}} + v_{-\text{threshold}} - v_{\text{cable}}, \quad (4\text{-}9)$$

where

v_{spinner} = spinner velocity, ft/min [m/min]
ω_{spinner} = spinner reading, rps
γ_{positive} = spinner slope for positive spinner readings, rps/ft/min [rps/m/min]
γ_{negative} = negative slope for negative spinner readings, rps/ft/min [rps/m/min]
$v_{+\text{threshold}}$ = spinner threshold for positive spinner readings, ft/min [m/min]
$v_{-\text{threshold}}$ = spinner threshold for negative spinner readings, ft/min [m/min]
v_{cable} = cable (or tool) velocity, ft/min [m/min].

Different spinner calibration zones have different values of slopes and thresholds. For depths between spinner calibration zones, the slopes and thresholds are normally interpolated from the adjacent calibration zones.

A survey of three up and three down passes delivers six velocity curves. It is a good quality control practice to inspect the multiple velocity curves for repeatability and either discard bad velocity sections or revisit the spinner calibration and correct the slopes and thresholds before averaging the resulting velocities and loading them into the interpretation solver.

Spinner response in the presence of local slip

In bubble flow the spinner encounters the continuous phase, typically water traveling slowly, and the discontinuous bubble phase, typically oil traveling quicker. The traditional spinner interpretation approach is based on the following equations, to which subscripts identifying monophasic and multiphase have been added for clarity. This approach is known as volumetric averaging.

$$q_{t\_\text{monophasic}} = v_{\text{spinner}} F_{vpc} A, \quad (4\text{-}10)$$

$$q_{t\_\text{multiphase}} = q_o + q_w, \quad (4\text{-}11)$$

$$q_o = v_o Y_o A, \quad (4\text{-}12)$$

$$q_w = v_w Y_w A. \quad (4\text{-}13)$$

If

$$q_{t\_\text{multiphase}} = q_{t\_\text{monophasic}} = v_{\text{spinner}} F_{vpc} A, \quad (4\text{-}14)$$

then

$$v_{\text{spinner}} F_{vpc} = v_o Y_o + v_w Y_w, \quad (4\text{-}15)$$

where

$q_{t\_\text{monophasic}}$ = single-phase pipe flow rate
$q_{t\_\text{multiphase}}$ = multiphase pipe flow rate
v_{spinner} = velocity from the spinner calibration plot
A = pipe internal cross-sectional area
q_o = oil flow rate
q_w = water flow rate
v_w = water-phase velocity
Y_w = water holdup (void fraction)
v_o = oil-phase velocity
Y_o = oil holdup (void fraction).

Volumetric averaging has been the default model used in production log interpretation for many years and it works reasonably well where there is only a small density difference between the phases present or the slip velocity is quite small. Where a large density difference exists between two flowing phases, the velocity of the denser phase has significantly more weight in the average velocity the spinner reads. (An extreme example is a paddle steamer that can move only because the paddle in the water creates more thrust than the paddle in the air.) To correct for the effects of differing density, Whittaker et al. (2006) propose using the mass-fraction average:

$$v_{\text{spinner}} F_{vpc} = \frac{v_o Y_o \rho_o + v_w Y_w \rho_w}{Y_o \rho_o + Y_w \rho_w}, \quad (4\text{-}16)$$

where

ρ_o = oil density
ρ_w = water density.

In the presence of a high density contrast between the oil and water and a high slip velocity between the oil and water there is a large difference in the resulting spinner velocity depending on which mixing model is applied. For gas and water the differences are still larger, but in many cases there is no bubble flow and the mass-fraction model is applicable only to bubble flow.

Sidebar 4E. Spinner models and slip

As of 2012, there is no rigorous physical model for what a turbine or spinner averages in the presence of local slip. Of the number of proposed empirical models, just the volumetric and mass-fraction ones are in common use within production logging interpretation. The nuclear power industry also has a multiphase metering need focused on the flow rate of saturated steam around a reactor. Steam metering using volumetric, mass-fraction, and other techniques has been investigated.

Minimum velocities registered by multipass spinner surveys

Most of the turbine flowmeters in the world are fixed within the pipe work and have a lower threshold velocity below which they do not turn. Because this threshold velocity is an important quality measurement for any turbine or flowmeter, we also measure the thresholds for our production logging flowmeters. However, although the threshold describes the lower velocity limit for a fixed spinner, a multispeed in situ calibration of a spinner takes the quantifiable velocity limit significantly lower.

Figure 4-25 shows the modeled spinner response in a 7-in liner flowing a total of 1,000 bbl/d of water. A typical spinner with a slope of 0.091 rps/ft/min and a threshold of 6 ft/min was simulated at a number of logging speeds (ft/min) and also as station measurements.

Of the five station measurements, only the last two stations, in 800- and 1,000-bbl/d flow, had sufficient water velocity to start turning the spinner. This indicates that a survey comprising just station measurements would be unsatisfactory. A lower spinner threshold would be required to monitor the smaller flow rates. However, if a series of logging passes were recorded, the spinner would be rotating over the entire interval to indicate the complete flow profile. It therefore follows that the spinner threshold cannot be used to indicate the minimum flow velocity detectable by a production logging spinner.

If the spinner threshold does not indicate the minimum mixture velocity that a spinner can quantify, then what does? The following factors affect the minimum detectable fluid velocity measurable by a spinner.

- A bigger spinner diameter is able to detect lower fluid velocities.
- Spinner pitch has an impact, as does the blade profile (is it flat or with a progressive pitch?).
- The logging speed must be fast enough to make the spinner turn but not so fast that the blades deform.
- High-density, low-viscosity fluids improve the sensitivity.
- Shallow vertical wells with smooth tool movement allow smaller velocities to be detected than in deeper, more highly deviated wells.
- The flowmeter bearing design and the maintenance the bearing has received are also important.
- Single-phase flow is much easier to measure than multiphase flow.

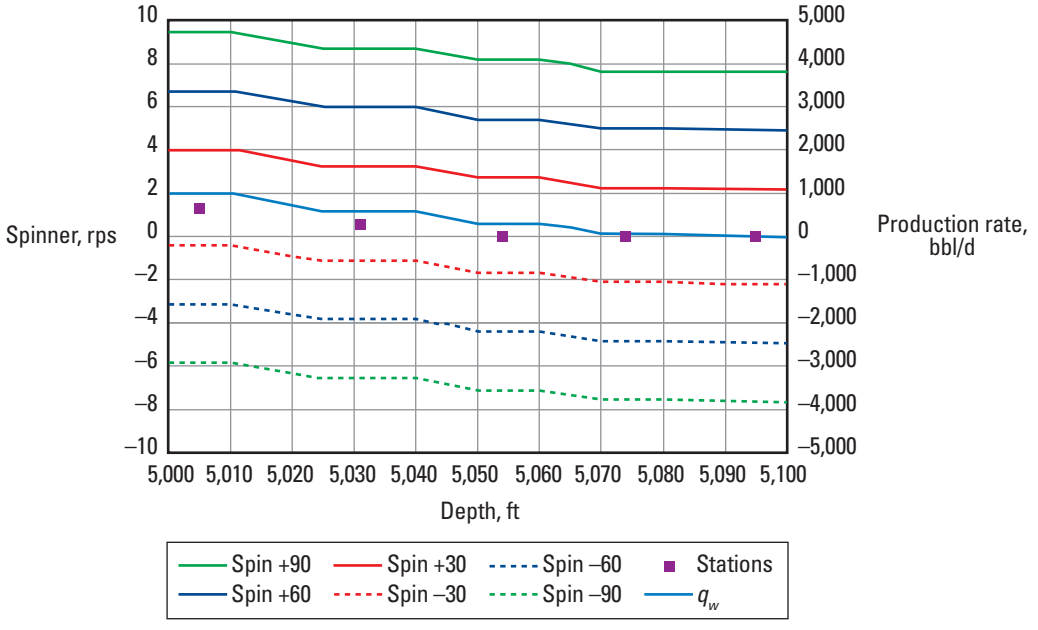

Figure 4-25. Effect of a threshold on a spinner response.

The complexity is such that models must be abandoned and reliance put on empiricism and experience. For the log analyst lacking experience, the following observations may help.

- A modern well-designed fullbore flowmeter should be able to resolve down to about 3 ft/min in a water-filled borehole of 45° deviation and 9,000-ft depth.
- In a shallow vertical well filled with water it is possible to resolve down to about 1.5 ft/min.

What is the upper viscosity limit for spinner operations?

Highly viscous crude oils may not allow the spinner flowmeter to turn. Work in the Schlumberger Gould Research Center shows that a local Reynolds number can be used to determine the cutoff point:

$$N_{\mathrm{Re\_local}} = \frac{v_{\mathrm{local}} \rho d_{\mathrm{local}}}{\mu} \qquad (4\text{-}17)$$

and

- if $N_{\mathrm{Re\_local}} > 1{,}000$, then the spinner just begins to turn
- if $N_{\mathrm{Re\_local}} > 10{,}000$, then the spinner is operating in its linear region,

where

v_{local} = velocity difference between the mixture velocity and the tool velocity, m/s
d_{local} = spinner diameter, m
ρ = downhole fluid density, kg/m^3
μ = downhole dynamic fluid viscosity, Pa.s.

Because fullbore spinners collapse or deform under the stresses experienced in highly viscous fluids, this computation should be limited to rigid turbine spinners and the minispinners.

Unfortunately this method cannot be used for the newer highly viscous non-Newtonian polymers, for which the spinner situation may be worse (Zheng and Liu, 2006).

References

Meunier, D., Tixier, M.P., and Bonnet, J.L.: "The Production Combination Tool—A New System for Production Monitoring," *Journal of Petroleum Technology* (May 1971), 603–613.

Nicolas, Y., and Meunier, D.: "From Memos by Y. Nicholas [*sic*], EPS, and D. Meunier, STS," *Technical Review* (October 1970), 18, No. 5, 21–25.

Peebler, B.: *Multipass Interpretation of the Full Bore Spinner*, Houston, Texas, USA, Schlumberger Well Services (1982).

Production Log Interpretation, Houston, Texas, USA, Schlumberger Well Surveying Corporation (1973).

Whittaker, A.C., Lenn, C.P., and Hammond, P.: "Improving Multiphase Production Logging Answers with the Mass-Fraction Spinner Response Model for Gas-Liquid Flows," *Petrophysics* (April 2006) 47, No. 2, 120–128; originally presented at the SPWLA 46th Annual Logging Symposium, New Orleans, Louisiana, USA (June 26–29, 2005), paper NN.

Zheng, H., and Liu, X.-B.: "Injection Profiling in Polymer Injectors in Daqing Oilfield," paper SPE 103703 presented at the 2006 SPE International Oil & Gas Conference and Exhibition, Beijing, China (December 5–7, 2006).

5 Pressure and Temperature

Pressure sensors

Downhole pressure data can be acquired with a number of different technologies. Amerada® mechanical chart recorders with Bourdon gauges came first and were followed by Wheatstone bridge strain gauges, capacitance strain gauges, quartz pressure gauges, sapphire crystal strain gauges, and more recently Bragg grating optical strain gauges.

In modern production logging toolstrings, the choice of pressure gauge is limited to

- strain
- sapphire strain
- quartz

listed in order of increasing accuracy, resolution, and price. Choosing the appropriate gauge technology for a production log requires considering the use that will be made of the pressure measurement.

Pressure data for well stability identification

In the example in Fig. 5-1, the pressure is slowly dropping while the production log is being made. The change in drawdown from the start to the end of the survey is 75 psi. If the overall drawdown from static reservoir pressure to flowing pressure is 1,000 psi or larger, then a variation of 75 psi can safely be ignored. However, if the drawdown is only 200 psi, then the downhole flow rate has significantly changed during logging. In this latter case, it may be necessary to discard all but the last two fast passes, where the well drawdown seems to have stabilized.

Pressure used in this manner does not need to be very accurate, merely stable, and any of the three technologies mentioned previously is sufficient.

Pressure data for PVT properties

A typical 10,000-psi strain gauge has an accuracy of about 10 psi whereas the corresponding quartz gauge has an accuracy of 1 psi. A 10-psi pressure change at standard temperature and pressure has significant effects on gas density, but downhole a 10-psi change on a bottomhole pressure of 2,000 psi has negligible effect on the PVT properties of gas, oil, or water. Pressures used to predict downhole PVT properties do not need to be quartz accurate.

Pressure data for reservoir pressures

One of the simplest tasks performed with a production logging tool is to record the shut-in pressure at a reference depth opposite the reservoir. In a stable well this pressure should correspond to the reservoir pressure, which is an important variable for reservoir simulation and reservoir depletion. Usually a pressure used in this way must be as accurate as possible, and a quartz gauge is used.

Pressure data for fluid density calculations

The pressure gradient dp/dZ delivers the fluid density; for more information, see the "Density Measurements" chapter. When used in this way, the absolute accuracy of the pressure gauge is unimportant as long as the pressure errors remain constant over the logging interval. Almost any pressure gauge can successfully be used to compute a fluid density.

Pressure data for transient analysis

The pressure gauge requirements for pressure transient analysis are covered in the Schlumberger *Fundamentals of Formation Testing* book.

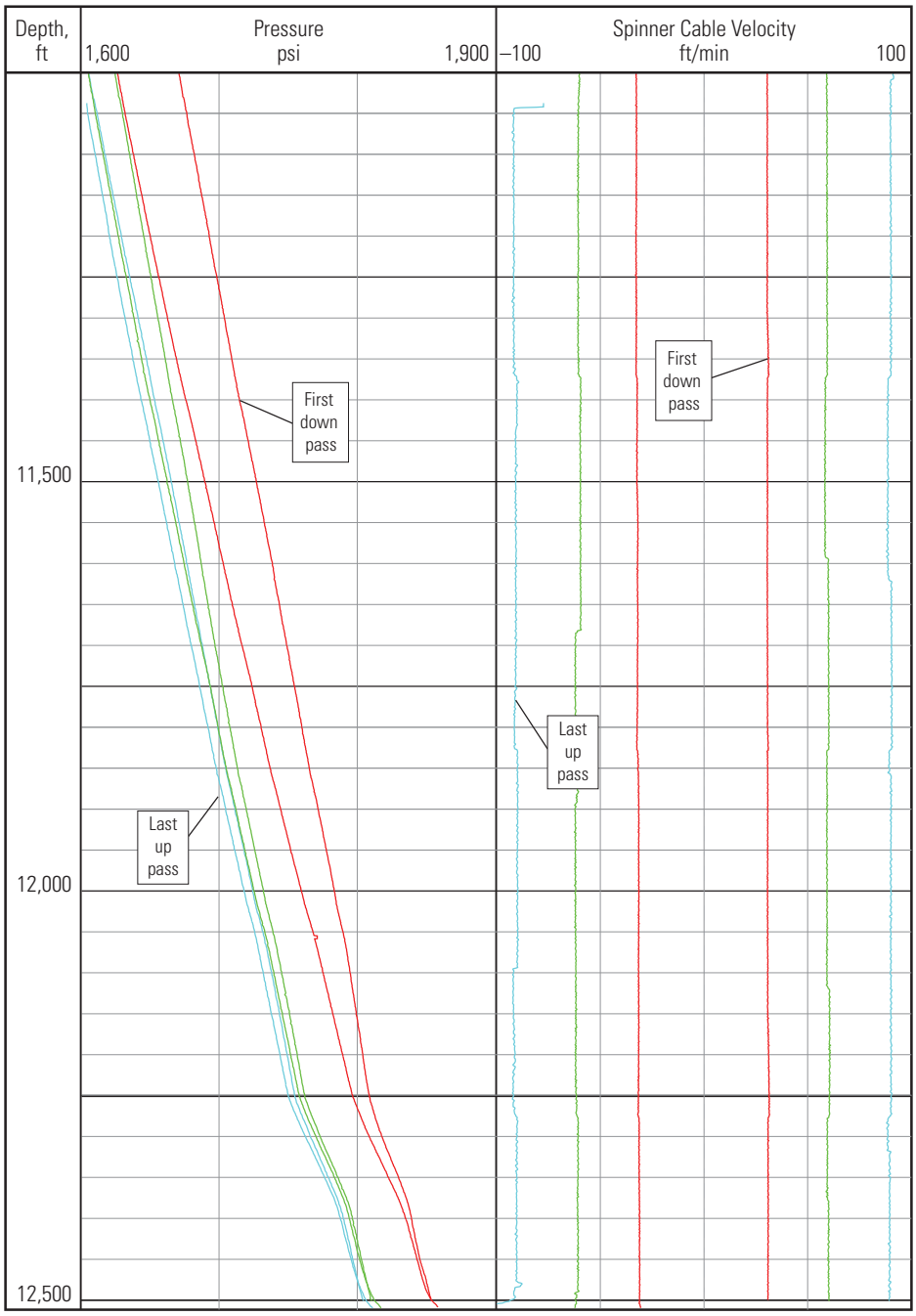

Figure 5-1. Drawdown still stabilizing while logging.

Temperature sensors

The Schlumberger PS Platform* new-generation production services platform has a temperature sensor in the Platform Basic Measurement Sonde (PBMS). The sensor is a 500-ohm (at 32 degF [0 degC]) platinum resistance temperature detector (RTD). The sensor is designed to work from –15 to 350 degF [–25 to 175 degC] with an accuracy of ±1.8 degF [±1 degC] in the range 75 to 300 degF [25 to 150 degC] and a resolution of 0.01 degF [0.006 degC] using 1-s samples.

In practice the resolution of the temperature sensor is much smaller than the thermal time constant of the platinum probe; normally the temperature gauge resolution is limited by the thermal time constant, with the best log data acquired while slowly running in the hole, at less than 1,000 ft/h [300 m/h].

Temperature data for PVT properties

An accuracy of ±1.8 degF [±1 degC] is more than sufficient to drive any PVT model or PVT correlation.

An unconventional logging technique can be used to identify the bubblepoint pressure using the temperature log. The example in Fig. 5-2 shows an increase in the temperature gradient that occurs opposite an increase in the spinner noise. This temperature gradient changes because of the extra heat needed to vaporize gas coming out of solution while the spinner noise is caused by the onset of multiphase bubbly flow.

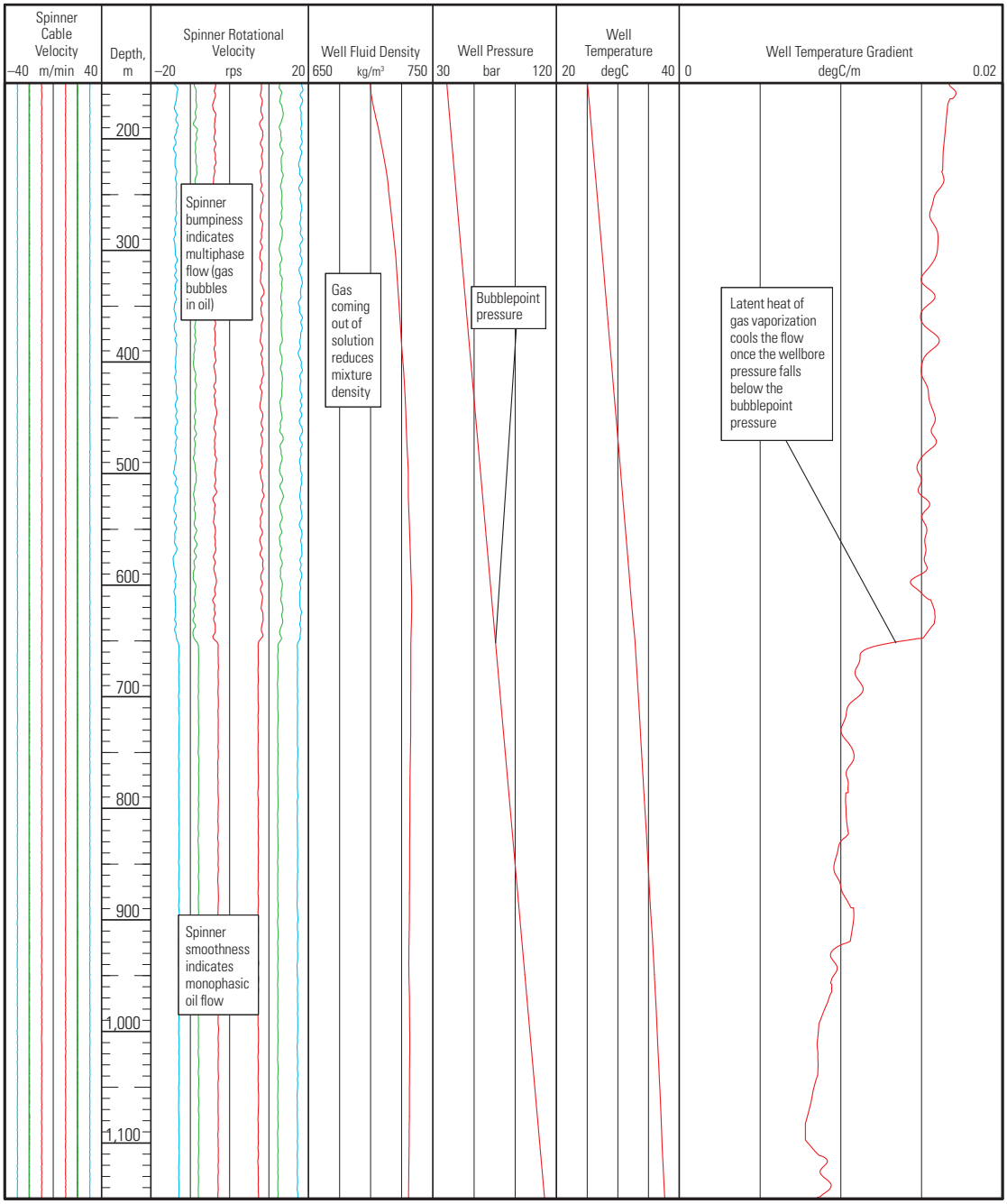

Figure 5-2. Identifying the bubblepoint in a flowing well.

Temperature data for qualitative flow analysis

In an undisturbed geologic sequence there is a monotonic increase in temperature with increasing depth (once the surface diurnal and annual temperature cycles have been left behind).

Changes in the thermal conductivity of different rock layers change the local temperature gradient, but there is still a monotonic increase in temperature with depth. Typical geothermal gradients are on the order of 1.5 to 3 degF/100 ft [0.8 to 1.7 degC/30 m].

Fluid movement, either up or down, equalizes the temperatures of the surrounding casing, cement, and formation. This leads to a reduction in the temperature gradient, making the temperature curve gradient shallower (i.e., closer to vertical on a wireline log) than the geothermal gradient. Fluid movement up- or downward also leads to a reduction in character of the temperature log as local details are smeared away.

One of the best production logging uses for temperature is in low-flow conditions, where the spinner velocity may be ambiguous but the temperature can clearly identify the location of fluid flow. Flow within the well takes the fluid and surroundings to some near-constant value with a temperature gradient that is much smaller than the geothermal gradient. Regions of no flow normally show the geothermal gradient or some asymptotic curve tending toward the geothermal gradient.

A simple thermal model (with no vertical thermal conductivity) has been used to create nine standard temperature signatures in Fig. 5-3. The small heat rate entry corresponds to either a low volumetric liquid flow rate or a medium volumetric gas flow rate; the medium and high heat rate entries are 1 and 2 orders of magnitude larger, respectively. Zero-flow regions show the geothermal temperature whereas entries, whether warm, cool, or geothermal, show an asymptotic trend toward

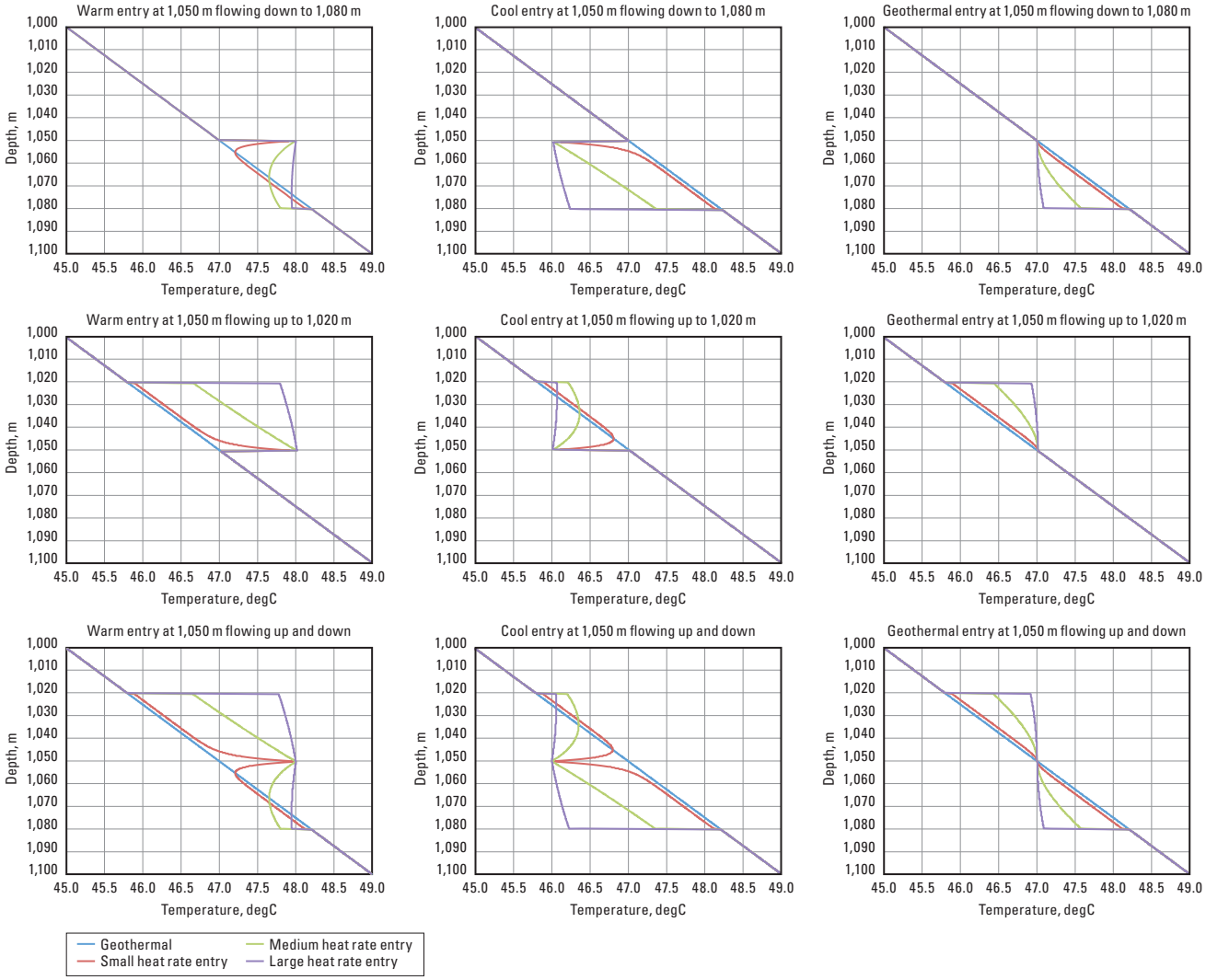

Figure 5-3. A library of standard thermal signatures.

a line parallel to the geothermal gradient. Cool entries flowing upward and warm entries flowing downward can be difficult to identify on temperature logs.

The example in Fig. 5-4 has a series of small downward crossflows. Each crossflow shows a subgeothermal temperature before decaying back to the geothermal gradient as thermal conductivity through the casing to the formation restores equilibrium. At the bottom of

Sidebar 5A. Temperature and pressure display

Normally temperature and pressure are shown increasing from left to right. However, in horizontal wells the true vertical depth (TVD) is normally shown increasing from right to left. Therefore, in a horizontal well the temperature and pressure are often displayed on reversed scales so that they can correlate with changes in TVD.

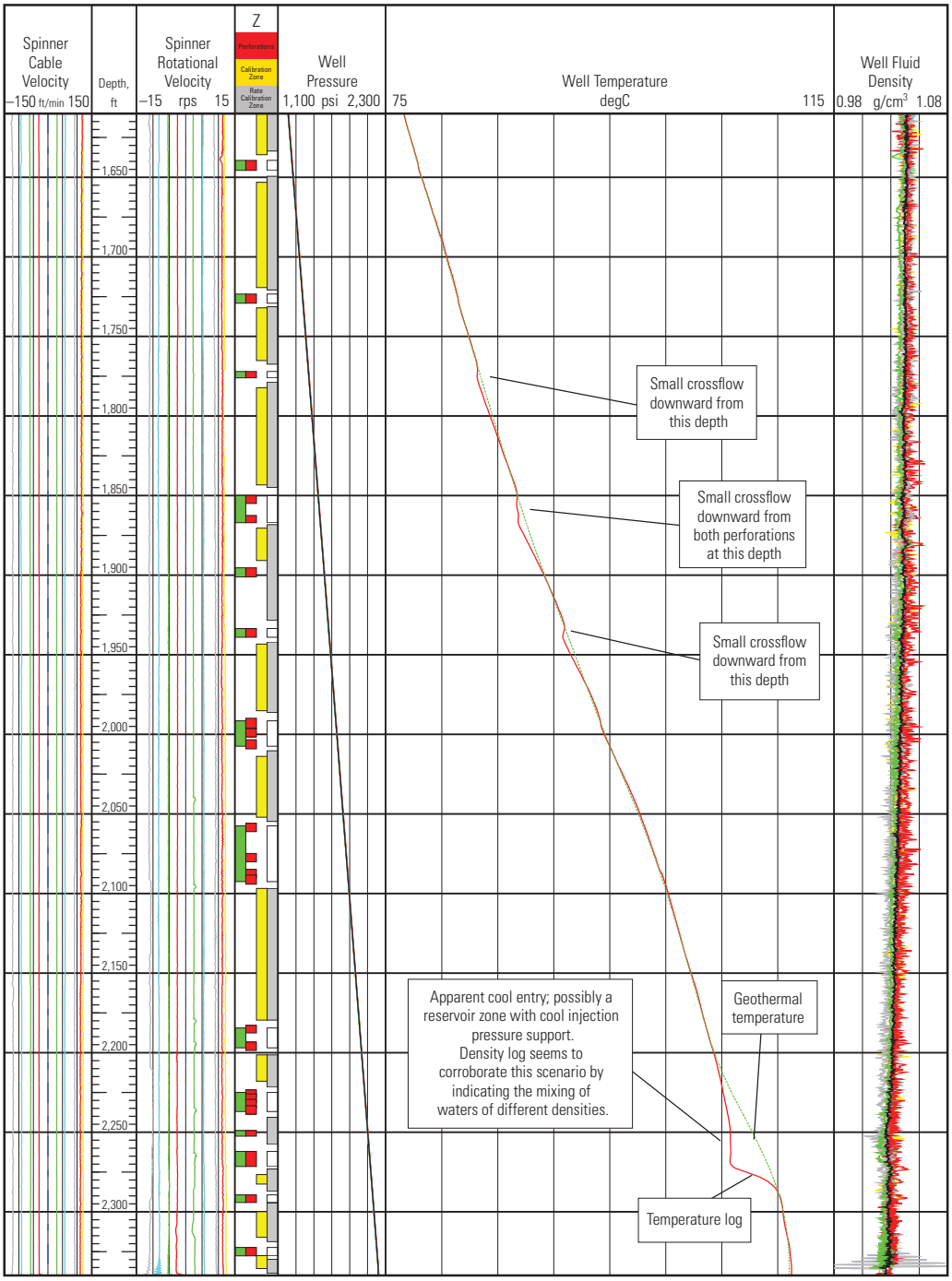

Figure 5-4. Use of temperature to identify crossflow and flow direction. (Puesto Zorro field, Argentina, courtesy of Pan American Energy LLC)

the log there is a cool entry at 2,263 m that is mainly crossflowing into a perforation at 2,250 m with a weak crossflow up to the next perforation at 2,195 m.

Amplifying the density scale shows a change in the water density over the logged interval that suggests waters of different salinities, densities, and sources are being mixed. Key to understanding temperature logs is comparison with the geothermal temperature. Unfortunately, the geothermal temperature usually is an artificial creation by the log analyst.

In the next example in Fig. 5-5, the interpretation of the wireline tractor-conveyed production logging tool shows no production from the toe of the well but does show an unusually warm point just above the bottom of the logging interval. After many inflow scenarios were explored, the toolstring length was checked and the hot

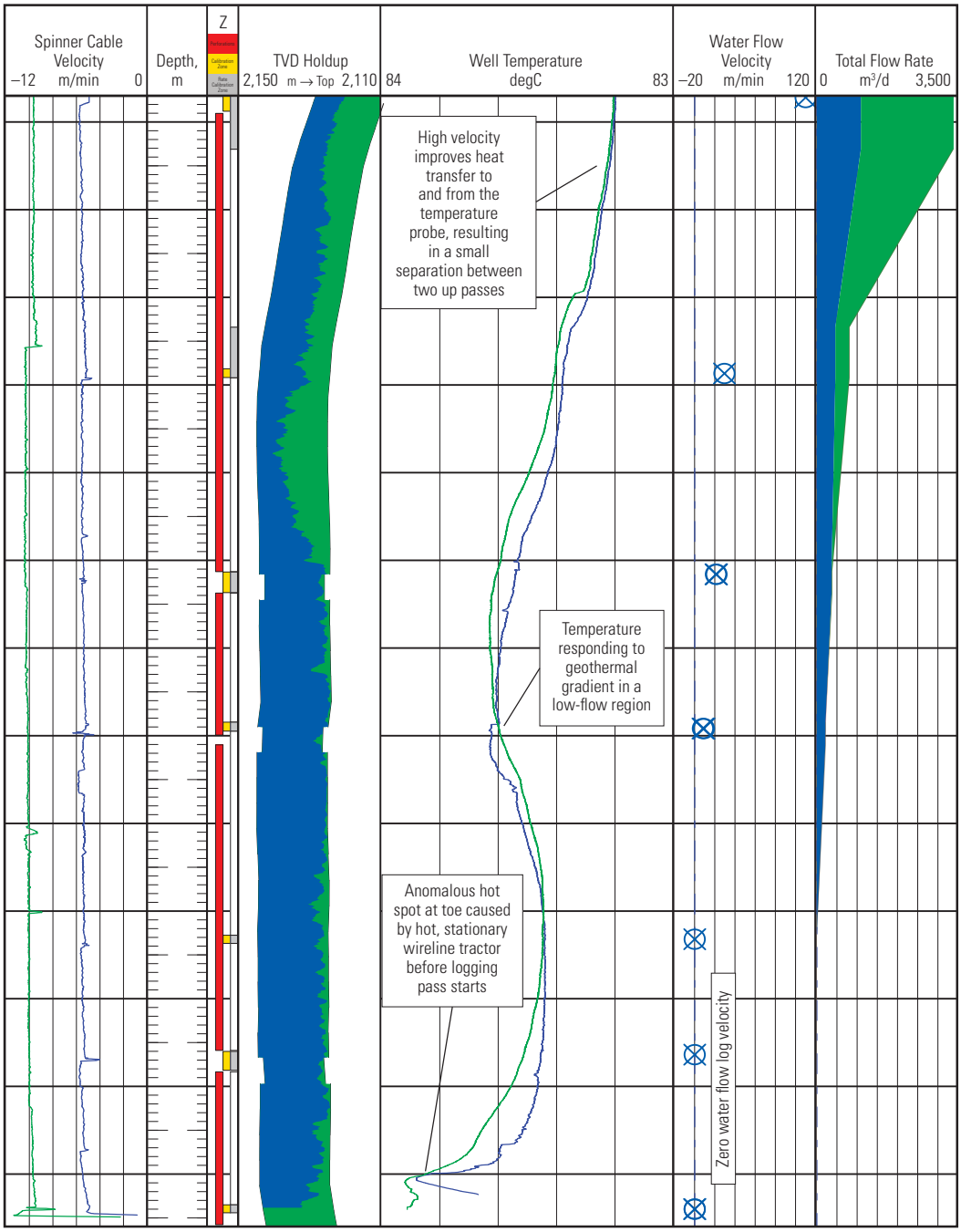

Figure 5-5. Anomalous temperature event created by wireline intervention.

spot was found to correspond to the position of the stationary wireline tractor while power was being rerouted from the tractor to the tool. The hot tractor was temporarily elevating the wellbore temperature and there really was no flow from the toe.

When the surface injection is turned off on an injector, the wellbore warms back to the geothermal temperature. Zones that have taken a large volume of cool injection fluid warm back slowly, whereas zones with only near-wellbore cooling warm back more quickly. Figure 5-6 shows a warm-back survey on a water injection well. In this example the temperature only serves to confirm the picture painted by the spinner-derived injection rates, but in wells where a spinner cannot be run, either because of the corrosive nature of the fluid being injected or because injection is occurring in the short string of a dual-completion well, temperature may provide the only indication of which zones are taking fluid.

Using temperature data in a qualitative way is one of the less natural tasks for the novice production log analyst to learn.

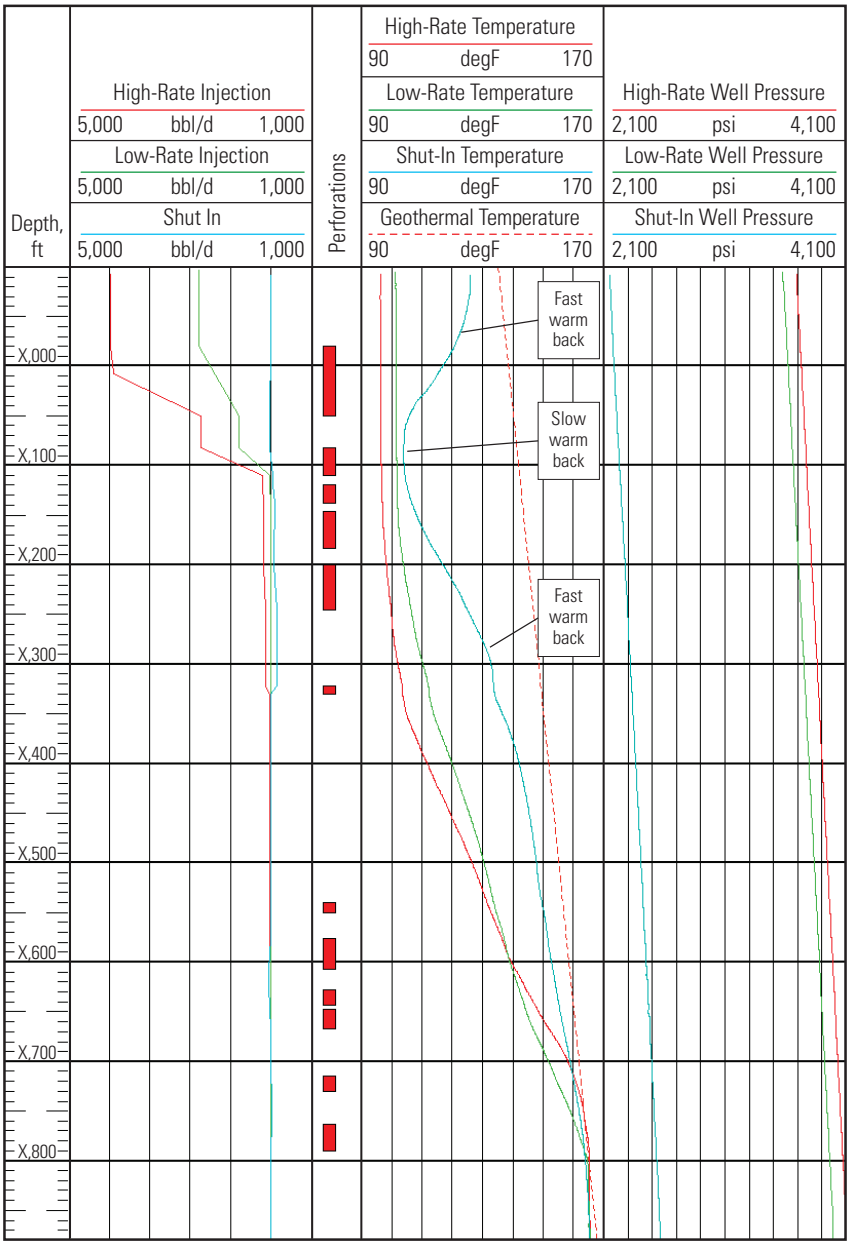

Figure 5-6. Warm back on a water injector after being shut in.

Temperature data for quantitative flow analysis

This subject is covered in the “Production Logging Interpretation Equations and Techniques” chapter.

Temperature data for leak detection

This subject is covered in the “Leak Detection and Localization” chapter.

6 Density Measurements

After the spinner the second most important measurement of a production logging string is normally density. Density is used to compute the holdup of two phases in a two-phase system and as one of the holdup inputs for a three-phase system.

Holdups from density

The density of a two-phase mixture is given by the sum of the holdups multiplied by the phase densities:

$$\rho = Y_{lp}\rho_l + Y_{hp}\rho_h. \quad (6\text{-}1)$$

The sum of the holdups must be one:

$$1 = Y_{lp} + Y_{hp}, \quad (6\text{-}2)$$

so the equations can be combined:

$$Y_{hp} = \frac{\rho - \rho_l}{\rho_h - \rho_l}, \quad (6\text{-}3)$$

$$Y_{lp} = \frac{\rho_h - \rho}{\rho_h - \rho_l}, \quad (6\text{-}4)$$

where

ρ = mixture density
ρ_l = light-phase density
ρ_h = heavy-phase density
Y_{lp} = light-phase holdup
Y_{hp} = heavy-phase holdup.

Accurate determination of the holdup requires not only an accurate measurement of the mixture density but also accurate reference densities for the light phase and heavy phase:

- Water density—The PVT properties of water at a known salinity are very well understood and accurate downhole densities can be predicted.
- Gas density—Gas PVT is well understood and accurate downhole densities are expected.
- Oil density—Taking an oil density directly from a PVT correlation is usually inaccurate. The standard procedure is to either
  - under well shut-in conditions look for a column of oil and use the measured density to adjust the PVT correlation
  - use a PVT analysis of the oil and gas from the well or field to calibrate a general PVT correlation.

Commingled waters, oils, and, to a lesser extent, gases result in a range of values for each referenced phase and therefore holdup can no longer be calculated this way.

There are a number of ways to measure a mixture density.

Gradiomanometer measurements

Bellows technique

The original Schlumberger Gradiomanometer tool was based on a bellows system that measured the average density within the pipe and between the two upper bellows (Fig. 6-1). It had a poor resolution and a worse accuracy. A simple deviation correction could be applied:

$$\rho_{dev\_corr} = \frac{\rho_{measured}}{\cos\delta}, \quad (6\text{-}5)$$

where

ρ_{dev_corr} = density corrected for deviation
$\rho_{measured}$ = tool density reading
δ = well deviation.

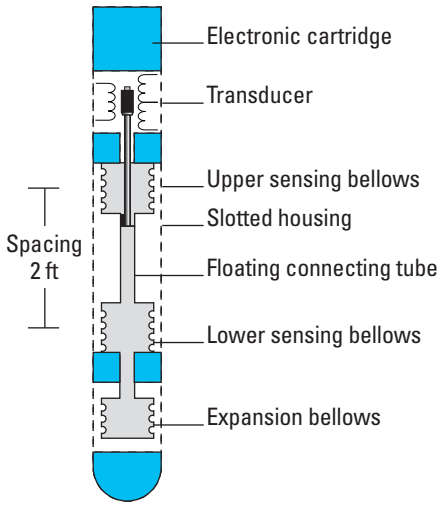

Figure 6-1. Bellows-based Gradiomanometer tool.

Differential pressure technique

The differential pressure Gradiomanometer uses a sensitive and relatively fragile differential pressure sensor to measure a pressure difference $(p_2 - p_1)$ across a diaphragm containing a strain gauge (Fig. 6-2).

The differential pressure sensor is connected to the well fluids (and the hydrostatic pressure gradient) by two silicone-oil-filled tubes. To slightly simplify the mathematics, one external pressure port (p_b) is at the same depth as the differential strain gauge and the second external pressure port (p_a) is a distance h meters higher up the toolstring:

$$p_1 = p_a + \rho_{so} g h, \tag{6-6}$$

$$p_2 = p_b, \tag{6-7}$$

$$p_b - p_a = \rho_m g h. \tag{6-8}$$

Therefore,

$$p_m = \frac{p_2 - p_1}{gh} + \rho_{so}, \tag{6-9}$$

and in a deviated well (Fig. 6-3)

$$p_m = \frac{p_2 - p_1}{gh \cos\delta} + \rho_{so}, \tag{6-10}$$

where

p = pressure, Pa

ρ_{so} = density of silicone oil at the downhole pressure and temperature, kg/m^3

g = gravitational constant, 9.81 ms^{-2}

h = separation of the two pressure ports, 0.538 m

ρ_m = unknown density of the well fluids mixture.

Silicone oil is used for its chemical inertness, not for its density stability with changing pressure and temperature. Therefore, an algorithm is used to model the downhole silicone oil density (Fig. 6-4).

For reasons of historical continuity some different units are used in Fig. 6-4:

p = downhole pressure, psia

T = temperature, degC

ρ_{so} = density of silicone oil, g/cm^3.

Unlike the uncorrected bellows Gradiomanometer tool, which reads 0 g/cm^3 at 90° deviation, the uncorrected differential pressure Gradiomanometer tool reads the density of the silicone oil when placed horizontally. Care must be taken when making a computer interpretation to ensure that the correct deviation correction is applied and is applied only once.

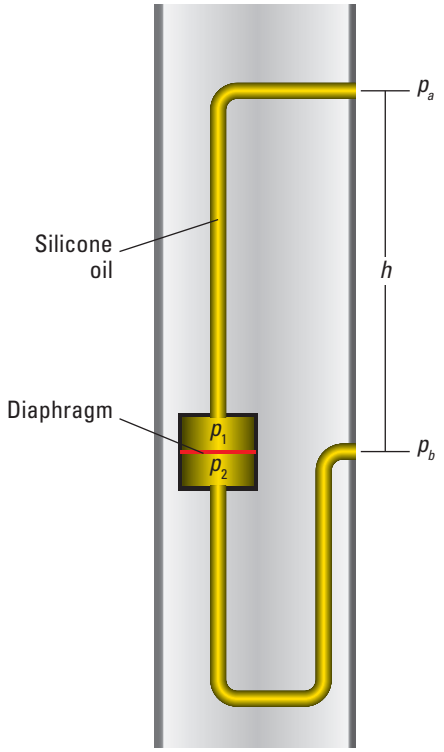

Figure 6-2. Differential pressure Gradiomanometer schematic.

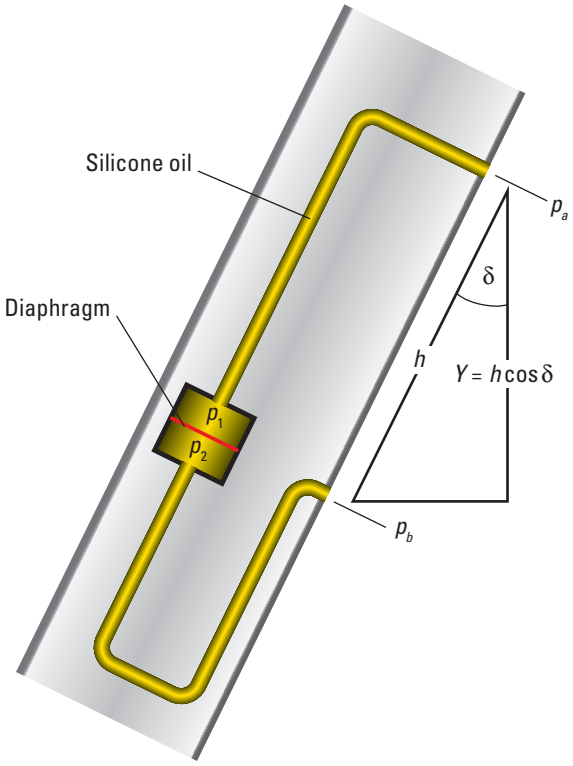

Figure 6-3. Differential pressure Gradiomanometer in a deviated well.

$$G = 9.8112950\times10^{-1} + 7.3927070\times10^{-6}\times P - 2.0766910\times10^{-10}\times P^2 + 3.1127790\times10^{-15}\times P^3$$
$$H = -7.4131230\times10^{-4} + 7.7043930\times10^{-9}\times P - 9.8239830\times10^{-13}\times P^2 + 4.2406710\times10^{-17}\times P^3$$
$$I = -1.2768390\times10^{-6} + 3.1979650\times10^{-10}\times P - 1.3299140\times10^{-14}\times P^2 + 1.6182250\times10^{-19}\times P^3$$
$$J = 3.9837600\times10^{-9} - 7.4403430\times10^{-13}\times P + 2.1716300\times10^{-17}\times P^2$$
$$\rho_{so} = G + H\times T + I\times T^2 + J\times T^3$$

Figure 6-4. Rhodorsil® silicone oil density algorithm.

Sidebar 6A. Accuracy of the PSOI sensor in the Gradiomanometer sonde

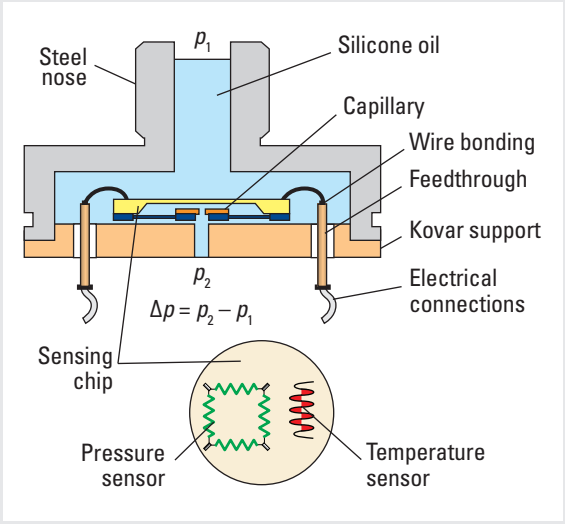

Figure 6A-1. PSOI sensor architecture.

For the Schlumberger Gradiomanometer sonde (PGMS) using a polycrystalline silicon on insulator (PSOI) sensor, the Gradiomanometer resolution is 0.002 g/cm³ with a 1-s sample time (longer stable intervals between inflow zones deliver longer sample times and hence superior density resolution). The accuracy of the Gradiomanometer sonde is ±0.02 g/cm³ in a vertical hole; the accuracy in a deviated well is $\pm^{0.02}/_{\cos\delta}$ g/cm³. Although the resolution of the gauge can be regarded as a random error, the accuracy is essentially a systematic error, amenable to correction by applying a block shift. On every interpretation using a Gradiomanometer tool, the log analyst looks for a reliable downhole reference density and nudges the density curve to match it. A downhole reference may be

- water column above the deepest inflow zone
- density derived from a pressure gradient (assuming a vertical well and negligible friction corrections)

but may not be the fluid that has collected in the sump below the deepest inflow zone because of its unknown origin and properties.

As the deviation increases, the dynamic range of the Gradiomanometer measurement decreases. It therefore follows that depending on the accuracy and resolution of the strain gauge and the density contrast between the light and heavy phase, there is a maximum deviation at which the Gradiomanometer tool can be used.

Consider the case in Fig. 6-5, with oil of 0.65 g/cm³ and water of 1.0 g/cm³. The dynamic range from 0 to 100% water holdup is 0.35 g/cm³. The polycrystalline silicon on insulator (PSOI) sensor can resolve the holdup to 0.002/0.35 = 0.5% of the holdup or better but with an accuracy of only ±6% of the holdup. Because the accuracy error is typically systematic, most experienced interpretation analysts start by determining the size of the Gradiomanometer offset to apply.

As a rule of thumb, water-oil holdup measurements can be made up to 60°–65° deviation whereas gas-liquid holdup measurements can be made to slightly higher deviations because of the increased dynamic range of density between water and gas.

The Gradiomanometer sonde (PGMS) for the modular PS Platform production services platform generates the following channels:

- filtered density (2-ft sliding average) corrected for deviation (WFDE)
- filtered density (2-ft sliding average) uncorrected for deviation (UWFD)
- deviation measured by an accelerometer in the PGMS tool (PGMS_DEVI).

There is no channel for friction-corrected density. Friction corrections can be computed only by making a complete multiphase interpretation.

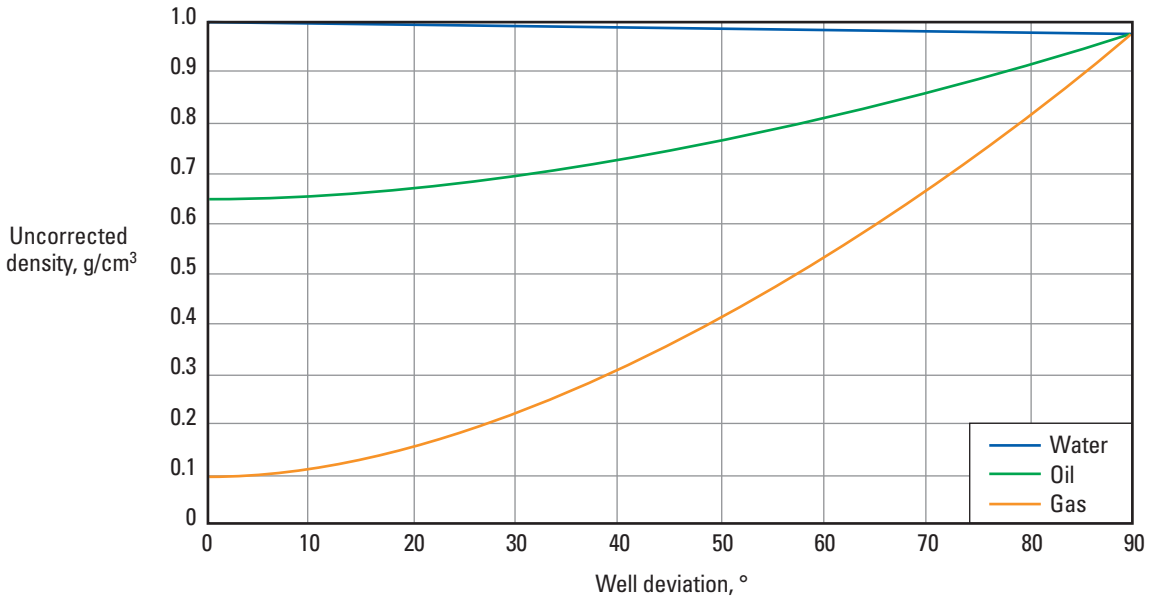

Figure 6-5. Differential pressure Gradiomanometer response to increasing deviation.

Sidebar 6B. PGMS-B accelerometer accuracy

The Schlumberger differential pressure Gradiomanometer sonde (PGMS-B) contains an accelerometer with an accuracy of ±28 mg. Conversion into a deviation error band produces the chart in Fig. 6B-1. The large errors around the near vertical correspond to a region where the deviation corrections for the density are very slight, thus the near-vertical computed density is more accurate than the near-vertical computed deviation would suggest.

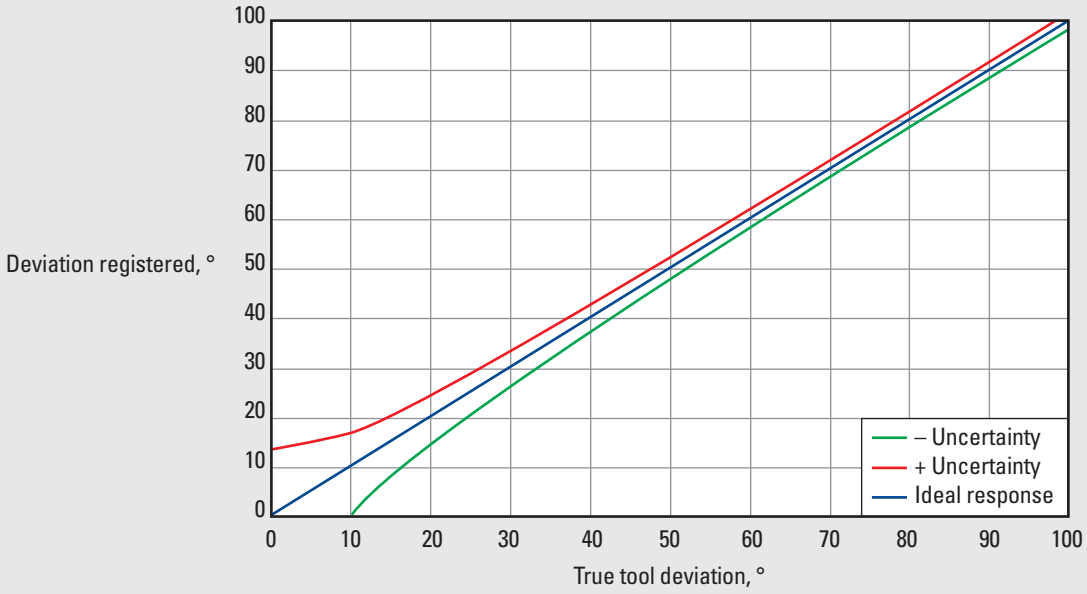

Figure 6B-1. Accuracy of the PGMS-B accelerometer mounted on the tool axis.

The excellent response of the deviation-measuring accelerometer near the horizontal has led to inclusion of the PGMS-B in horizontal production logging toolstrings to deliver an accurate and continuous measurement of well deviation.

Friction corrections

Above about 2.5 m/s [8.2 ft/s] in liquid flow in common oilfield pipe diameters, the frictional pressure drop in the casing starts to appear as a significant increase in the apparent density of the liquid. Friction corrections then need to be applied:

$$\rho = \frac{p_2 - p_1 - dp_{\text{friction}}}{gh\cos\delta} + \rho_{so}. \quad (6\text{-}11)$$

The frictional pressure drop in an empty pipe is given by

$$dp_{\text{friction}}/dL = \tfrac{1}{2}\frac{fv^2\rho}{d}, \quad (6\text{-}12)$$

but Gradiomanometer friction has to be considered as well, and the frictional pressure drop becomes

$$dp_{\text{friction}}/dL = \tfrac{1}{2} f_p v^2 \rho \frac{d}{\left(d^2 d_t^2\right)} + \tfrac{1}{2} f_t v_t^2 \rho \frac{d_t}{\left(d^2 d_t^2\right)}, \quad (6\text{-}13)$$

where

$$f_p = \frac{1.325}{\left[\ln\left(\frac{e}{3.7d} + \frac{5.74}{N_{\text{Re}}^{0.9}}\right)\right]^2}, \quad (6\text{-}14)$$

$$f_t = \frac{1.325}{\left[\ln\left(\frac{e_t}{3.7d_t} + \frac{5.74}{N_{\text{Re}}^{0.9}}\right)\right]^2}, \quad (6\text{-}15)$$

$$N_{\text{Re}} = \frac{\rho v d}{\mu}, \quad (6\text{-}16)$$

where

f = Moody friction factor
f_p = pipe Moody friction factor
f_t = tool Moody friction factor
dL = length between the two pressure ports, 0.54 m
d = pipe internal diameter, m
d_t = Gradiomanometer outside diameter, m
ρ = mixture density
dp_{friction} = frictional pressure drop
v = mixture velocity of the tool to casing annulus, m/s
v_t = relative velocity between the tool and flow, m/s
e = surface roughness of the pipe, m
e_t = surface roughness of the tool, m
N_{Re} = Reynolds number
μ = mixture viscosity, Pa.s.

Sidebar 6C. How not to correct for friction

Historical charts from the 1970s, developed for friction corrections in manual interpretations, contain a number of undocumented assumptions, including the well deviation, Gradiomanometer type (bellows or differential pressure or pressure gradient), tool position, and casing roughness, and should not be used for any interpretation.

Because the friction-corrected density is an input to the computation of frictional pressure drop, an iterative computation approach is needed.

This model is valid for a coaxially positioned logging tool and casing. However, in practice the Gradiomanometer tool is often run eccentred to reduce the tool lift forces and incidentally reduce the friction corrections. Proprietary algorithms correct for this effect.

Because the casing roughness e in all but the newest of wells is unknown and unmeasurable, a typical approach in an interpretation is to adjust the roughness opposite the maximum downhole flow rate until the computed interpretation's surface rates match the measured surface rates. This value of roughness is then propagated to all deeper zones in the well.

Liquid flow rates above 4 m/s [13 ft/s] normally have too large a friction correction to permit extracting a usable density.

Yo-yo or kinetic corrections

Particularly on fast logging passes and under shut-in conditions, the logging toolstring may start to bounce, with the armored logging cable or slickline behaving like a long piece of elastic. This results in vertical sinusoidal motion superimposed on the steady logging speed. When the tool is accelerating upward the weight of the silicone oil in the tool's buffer tubes increases, whereas tool deceleration upward reduces the weight of the silicone oil. This can be observed on a log as a sinusoidal density signal superimposed on the true mixture density. The application of a depth filter with the same length as the wavelength of the oscillations eliminates the sinusoidal noise while minimizing the loss of depth resolution.

The example in Fig. 6-6 from a shut-in well shows a minor degree of yo-yoing with a periodicity of about 4 to 5 ft. A number of filter lengths need to tried on each of the logging passes because the periodicity usually changes with the logging speed. Curiously, yo-yo effects are much reduced once the well is flowing.

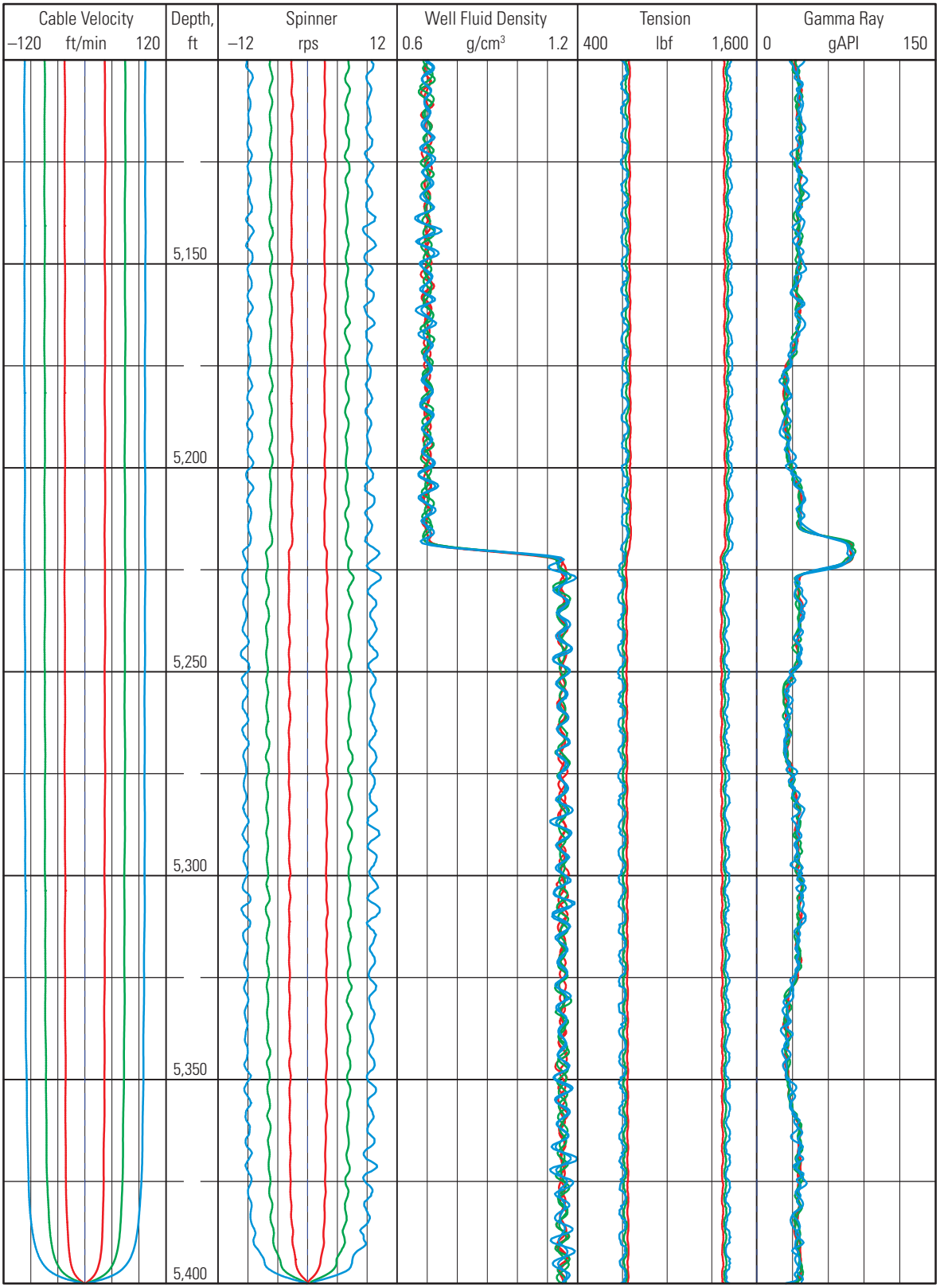

Figure 6-6. Yo-yo effect on spinner, Gradiomanometer, and surface tension measurements.

The gamma ray track shows a peak coincident with the wellbore oil/water contact. This peak disappears once the well is flowing. It is caused by some weak, naturally occurring radioactive material that is acting as a surfactant or is attracted to a naturally occurring surfactant. This behavior is not uncommon but it can be hard to explain.

Jetting entries

A strong radial entry from a high-permeability zone acts first on one Gradiomanometer pressure port and then on the second pressure port. This is observed as an unusually low density (maybe even negative) next to an unusually high density. No corrections are possible beyond the obvious approach of only using data from above and below the jetting entry.

The Schlumberger inverted Gradiomanometer tool moves the pressure ports from the outside face of the logging tool to an inside passage to avoid jetting entries that can overstress and destroy the delicate differential pressure gauge. Unfortunately, protecting the Gradiomanometer gauge in this way creates some additional acceleration corrections resulting from significant changes in the cross section of the tool.

Acceleration effects

Changes in the cross-sectional area available for flow that result from changes in the borehole diameter or the tool diameter cause the fluid velocity to rise and fall. A changing velocity requires an acceleration or deceleration that makes the well fluids appear heavier or lighter, respectively. Changes in the borehole diameter cannot normally be corrected for, but the acceleration effects owing to changes in the cross-sectional area of the Schlumberger inverted Gradiomanometer tool have been modeled and are applied if the interpretation software is correctly set up. BorFlow, Emeraude, and Interpretive Software Products' PLATO production logging software all have the necessary switches for the Schlumberger "inverted" pressure ports.

The log fragment in Fig. 6-7 shows a very high-velocity fluid traveling from a liner up into casing. Velocities in the casing are about 3 m/s while in the liner the peak velocity reaches almost 4 m/s. The density curve has been corrected for deviation but not friction and therefore can be viewed only qualitatively. The change in the average density readings from below to above the liner hanger is caused by the velocity reduction as the cross-sectional area is increased. The deceleration of the fluid at the liner hanger gives a large density transient as first one Gradiomanometer port and then the other encounters the deceleration zone. At these velocities, even casing collars have a significant ID upset and a consequent acceleration effect on the Gradiomanometer measurement.

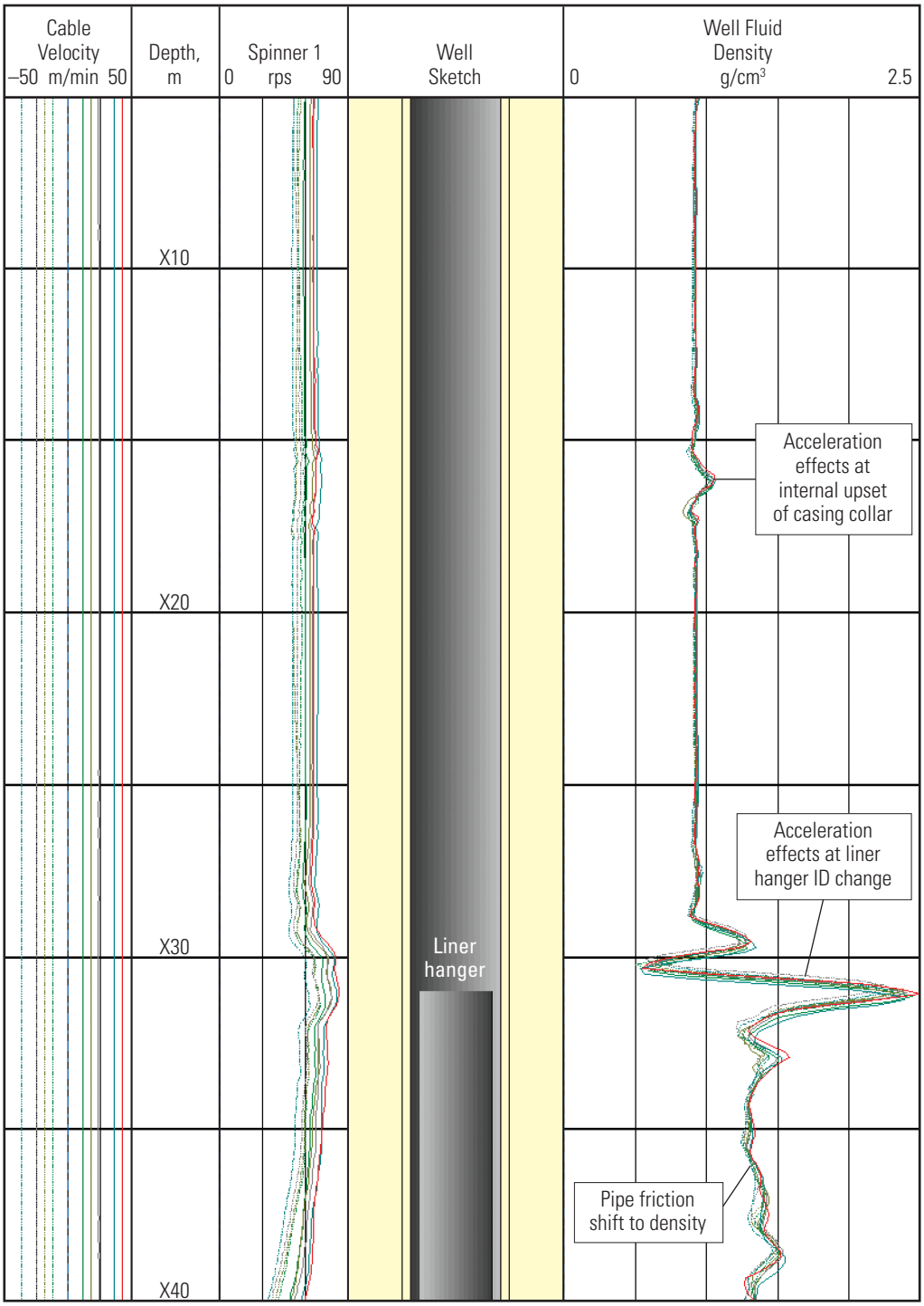

Figure 6-7. Gradiomanometer friction and acceleration effects.

Pressure gradient measurements

Differentiating a pressure curve with respect to depth delivers a density curve. To correct for irregularities in the tool's smooth movement, quite a large depth window is normally used; computing the average density across a 10- or 20-ft [3- or 6-m] window is quite typical.

If the well is still stabilizing or slugging or if the tool movement is not smooth, then the pressure gradient density is probably unusable. However, if the well is stable and the pressure curves from pass to pass are repeating well, then the resulting pressure gradient density is very accurate, albeit with poor depth resolution. After the correct deviation corrections have been applied, the pressure gradient makes a good downhole reference for the Gradiomanometer density:

$$\rho_{dev\_corr} = \frac{1}{0.433}\frac{dp}{dZ}\frac{1}{\cos\delta}, \qquad (6\text{-}17)$$

where

ρ_{dev_corr} = deviation-corrected density, g/cm^3
dp/dZ = pressure gradient, psi/ft
δ = well deviation from vertical.

When friction corrections are required they are applied as

$$\rho_{corr} = \frac{1}{0.433}\frac{\left(dp - dp_{friction}\right)}{dZ}\frac{1}{\cos\delta}. \qquad (6\text{-}18)$$

In SI units, this becomes

$$\rho_{corr} = \frac{1}{9{,}810}\frac{\left(dp - dp_{friction}\right)}{dZ}\frac{1}{\cos\delta}, \qquad (6\text{-}19)$$

where

ρ_{corr} = deviation and friction corrected density, g/cm^3
dp/dZ = pressure gradient, Pa/m
$dp_{friction}$ = frictional pressure drop from Eq. 6-12.

Friction corrections for the pressure gradient-derived density need to take into account only the pipe wall frictional pressure drop. No correction should be applied for the decreased cross-sectional area and increased velocity around the pressure gauge, nor for the tool body roughness or tool velocity.

Sidebar 6D. Computing pressure-derived density

MaxWell* and other Schlumberger proprietary wellsite acquisition software compute a pressure gradient-derived density curve, labeled the manometer well fluid density (MWFD). Depending on the logging tool and surface acquisition system, the MWFD curve may be recorded on depth or off depth and corrected for deviation using a tool measurement or just a fixed deviation parameter. Log analysts are encouraged to disregard the MWFD curve and compute their own pressure-derived density curve to ensure that the corrections are applied correctly.

Nuclear fluid density measurements

There are two main types of nuclear density measurements (Figs. 6-8 and 6-9). Both techniques do not require deviation, friction, yo-yo, or acceleration corrections, but unfortunately there are compensating deficiencies.

The scattering approach, as used in the Schlumberger nuclear fluid density (NFDC) tool, separates the gamma ray source and gamma ray crystal detector with a tungsten shield to avoid direct coupling of the source to detector (Fig. 6-8). A relatively powerful gamma ray source scatters and attenuates gamma rays off the wellbore contents and receives a gamma ray flux at the detector that is inversely proportional to the density of the wellbore contents. Unfortunately the gamma rays also penetrate the casing, and the log responds not only to the wellbore density but also to the annulus and formation density. To correct for these unwanted density signals, the difference in density between shut-in and flowing conditions is computed and added to an independently calculated shut-in density. Because the annulus and formation density should be essentially unchanged with changing flow rates, the difference signal comes only from changes in the wellbore holdup:

$$\Delta\rho = \rho_{nuclear\_flowing} - \rho_{nuclear\_shutin}, \qquad (6\text{-}20)$$

$$\rho_{flowing} = \rho_{shutin} + \Delta\rho, \qquad (6\text{-}21)$$

where

$\Delta\rho$ = density difference
$\rho_{nuclear\_flowing}$ = nuclear density from the flowing well
$\rho_{nuclear\_shutin}$ = nuclear density from the shut-in well
$\rho_{flowing}$ = corrected density from the flowing well
ρ_{shutin} = independently measured shut-in density.

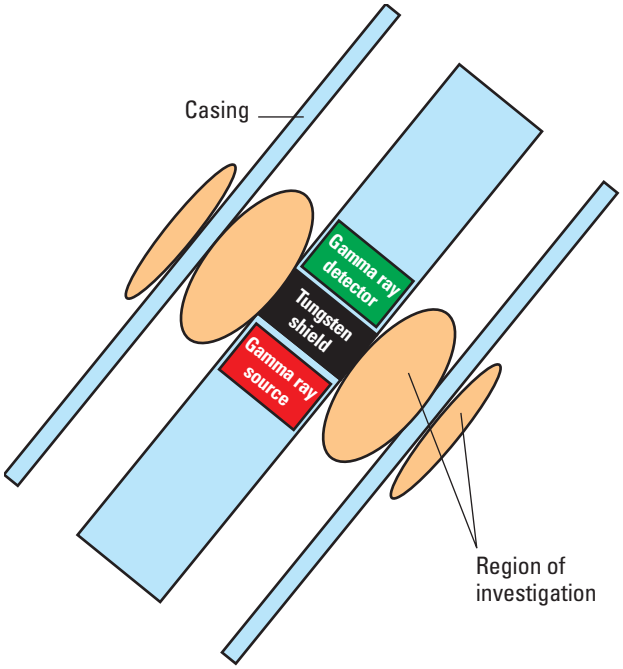

Figure 6-8. Nuclear fluid density using scattering around the logging tool.

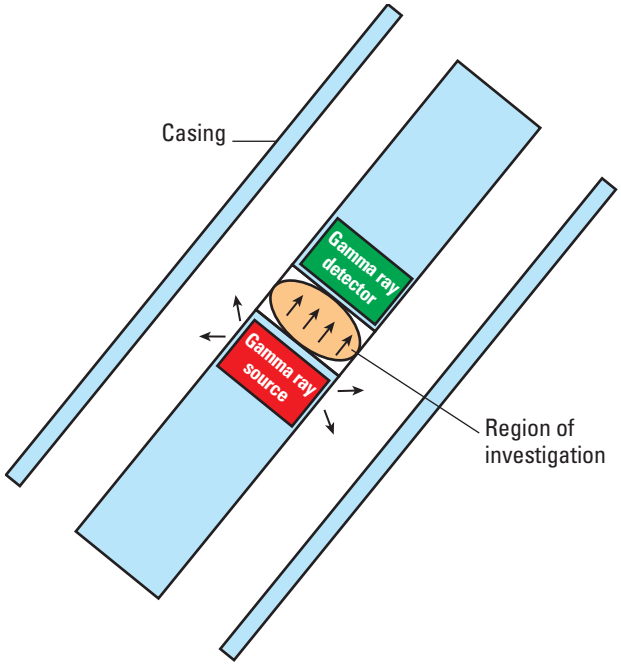

Figure 6-9. Nuclear fluid density using attenuation across a window inside the logging tool.

The main application for this technique is in very high-velocity wells where the Gradiomanometer friction corrections are unmanageably high and ρ_{shutin} is provided by a shut-in Gradiomanometer pass.

Surface calibrations of the scattering-type tool are rarely representative of downhole conditions; therefore, the tool normally is calibrated to known downhole densities when the well is shut in.

The tool in Fig. 6-9 uses an attenuation technique with a weak gamma ray source shining across a window in the tool to a gamma ray detector a few inches away. This technique relies upon uniform mixing of the light and heavy phases across the casing cross section because the density measurement is made only on the tool axis. High-velocity wells satisfy this requirement whereas deviated, medium- to low-velocity wells do not. Because this tool has a much smaller radial depth of investigation, it can be successfully calibrated at surface using air and water as references.

Density viscosity sensors

In recent years the vibrating density sensor has been rediscovered (Stansfeld, 1980). This small, mechanically vibrating sensor has its resonant frequency changed by the density of the surrounding fluid (Fig. 6-10). Additionally, the degree of resonant damping is a function of the surrounding fluid viscosity.

Microelectromechanical systems (MEMS) sensor technology means that a density-viscosity (DV) sensor can be miniaturized and installed inside a formation testing tool to measure some basic properties of pure oil and pure gas in situ.

Because the sensor needs no deviation correction and does not require friction or acceleration corrections, it appears to be a promising replacement for the Gradiomanometer measurement. Unfortunately when applied to production logging, some serious limitations of the DV sensor have been observed.

- The region of investigation of the sensor is limited to the immediate proximity of the sensor. Unless the flow is very well mixed, a point measurement of density is not representative of the whole pipe.

- At high fluid velocities, vortex shedding off the logging tool body can interfere with the vibrations and introduce a pseudo-pipe-friction offset.
- The preferential wettability of the sensor material, water wet or oil wet, attracts one phase and then biases the measurement toward that phase (Fig. 6-11).
- The technique does not work in gas-liquid mixtures.

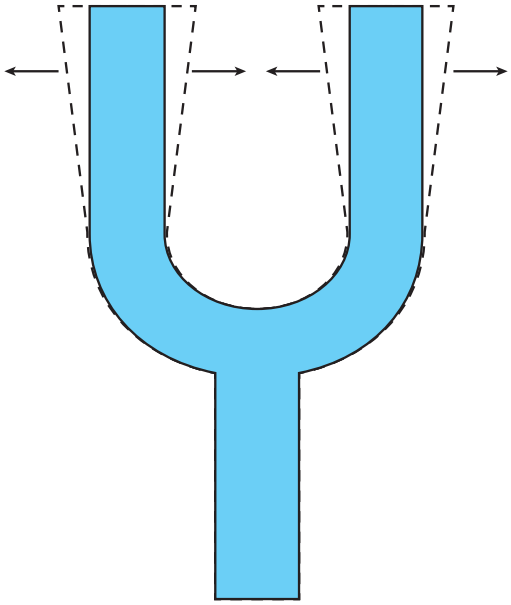

Figure 6-10. Density-viscosity sensor schematic.

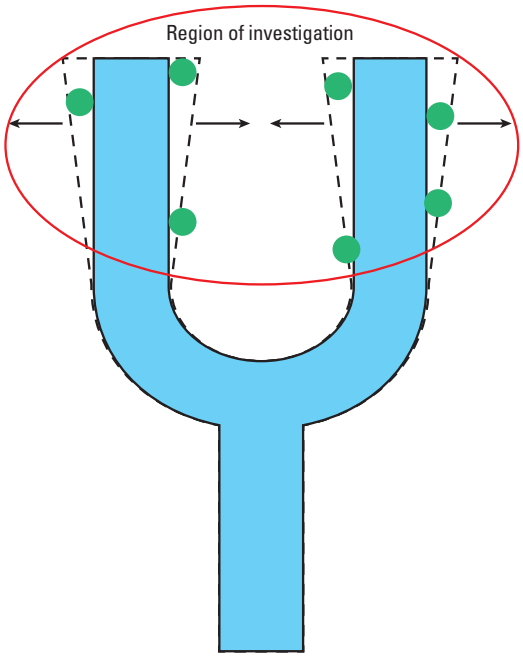

Figure 6-11. Density-viscosity sensor with preferential wetting and depth of investigation.

Reference

Stansfeld, J.W. "Fluid Density Transducer," US Patent No. 4,354,377 (November 4, 1980).

7 Probe Holdup Measurements

Probe measurements have been successfully used for velocity, temperature, and holdup measurement under a variety of conditions. However, in downhole oil and gas wells only probe holdup (and occasionally discontinuous flow rate) has been successfully measured.

Water holdup probes

FloView* water holdup probes use the electrical conductivity of water to distinguish between the presence of water and hydrocarbons (Fig. 7-1).

In a water-continuous phase, current is emitted from the probe tip and returns to the tool body. A droplet of oil or gas only has to land on the probe tip to break the circuit and be registered. In an oil-continuous phase, a droplet of water touching the probe tip does not provide an electrical circuit. Instead the water droplet must connect the electrical probe to the ground wire. This requires a larger droplet than is needed for gas or oil detection in a water-continuous phase.

In both cases the best measurement is made with the bubbles approaching the probe from below. Fast up passes in low-velocity wells drag the probe backward through the bubbles and deliver an inferior water holdup measurement. It is not unusual to disregard all water holdup probe measurements acquired during up passes.

To discourage the droplet from loitering permanently on the probe, care must be taken to use materials with the appropriate preferential wettability and of as small a diameter as possible. If the measurement is made with a DC signal, there are accelerated electrical corrosion of the anode and the effects of parasitic electrochemical cells to correct for. The use of too high of an electrical frequency makes the probe sensitive to dielectric effects as well as conductivity changes.

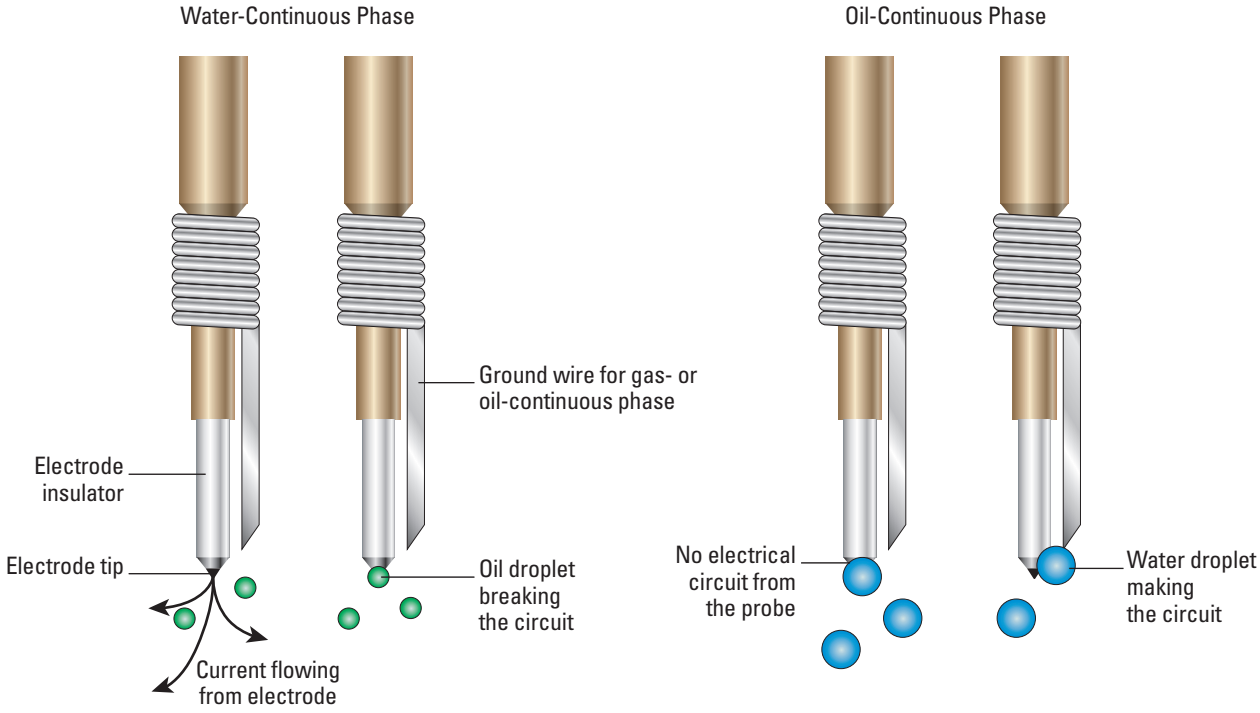

Figure 7-1. Operation of the FloView water holdup probe.

The downhole droplets of oil and water can become too small (as a result of bubble shear) for the probes to detect and the discontinuous phase is then undercounted. As there is a first-order inverse correlation between mixture velocity and bubble size, empirical velocity limits have been determined for the purposes of job planning and data validation:

- for an oil- or gas-continuous phase, the mixture velocity must be less than 1 m/s [3.3 ft/s]
- for a water-continuous phase, the mixture velocity must be less than 2 m/s [6.6 ft/s]
- for horizontal wells with gravity segregation, the velocity must be less than 3 m/s [9.8 ft/s].

High-velocity entries into the wellbore, often associated with high-permeability streaks in the reservoir, can shear the bubbles and make them too small to be detected. The resulting microbubbles eventually coalesce but not on a timescale that is of use to a production log analyst.

Very fresh water does not have sufficient conductivity for the electrical measurement. Figure 7-2 shows the required water salinity as a function of temperature. At higher temperatures, electrical noise in the downhole electronics limits the measurement to >1,000-ppm NaCl.

The signal from the FloView probe lies between two baselines of the continuous-water-phase response and the continuous-hydrocarbon-phase response (Fig. 7-3). To capture small transient bubble readings, a dynamic

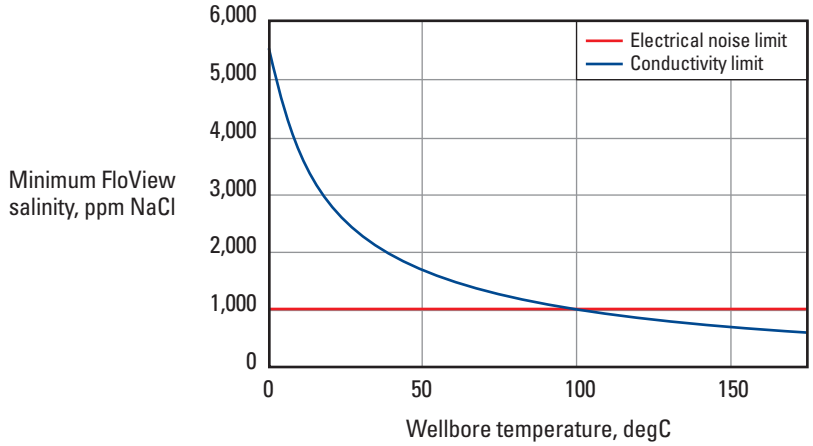

Figure 7-2. Lower limit for salinity for the FloView probe in the Flow-Caliper Imaging Sonde (PFCS).

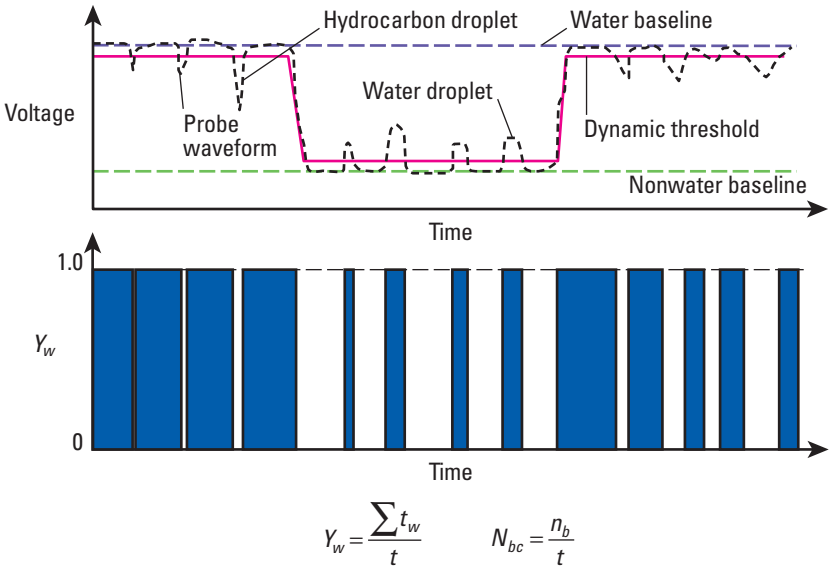

Figure 7-3. FloView probe waveform processing. Y_w = water holdup, Σt_w = total time that the probe is in water during time t, t = arbitrary time to travel 6 in, N_{bc} = bubble count frequency, and n_b = number of bubbles.

threshold is adjusted close to the continuous phase and then compared with the probe waveform. A binary water holdup signal results, which, when averaged over time, becomes the probe holdup. The entire probe waveform during a 6-in depth frame is processed in this way.

The number of times the waveform crosses the threshold is counted and divided by 2 to deliver a probe bubble count. Attempts have been made to process the bubble counts and cable velocity by using a spinner-like crossplot into a bubble velocity. The example in Fig. 7-4 is quite typical and delivers a bubble velocity in Fig. 7-6 that is much slower than the apparent spinner velocity in Fig. 7-5, whereas the bubbles would be expected to be travelling as fast, if not faster, than the mixture velocity. The author suspects that the bubble crossplot needs not a straight line, but instead, a poorly defined curve fitted to the data points to deliver the appropriate bubble velocity.

Sidebar 7A. Salinity effects

A salinity level of 480- to 1,500-ppm NaCl is regarded as a healthy level for most aquatic invertebrates and plants. People can drink water in this range, but it would start to taste very salty. Some plants, such as peas, apricots, and grapes, cannot be grown with water that is over 1,000-ppm NaCl.

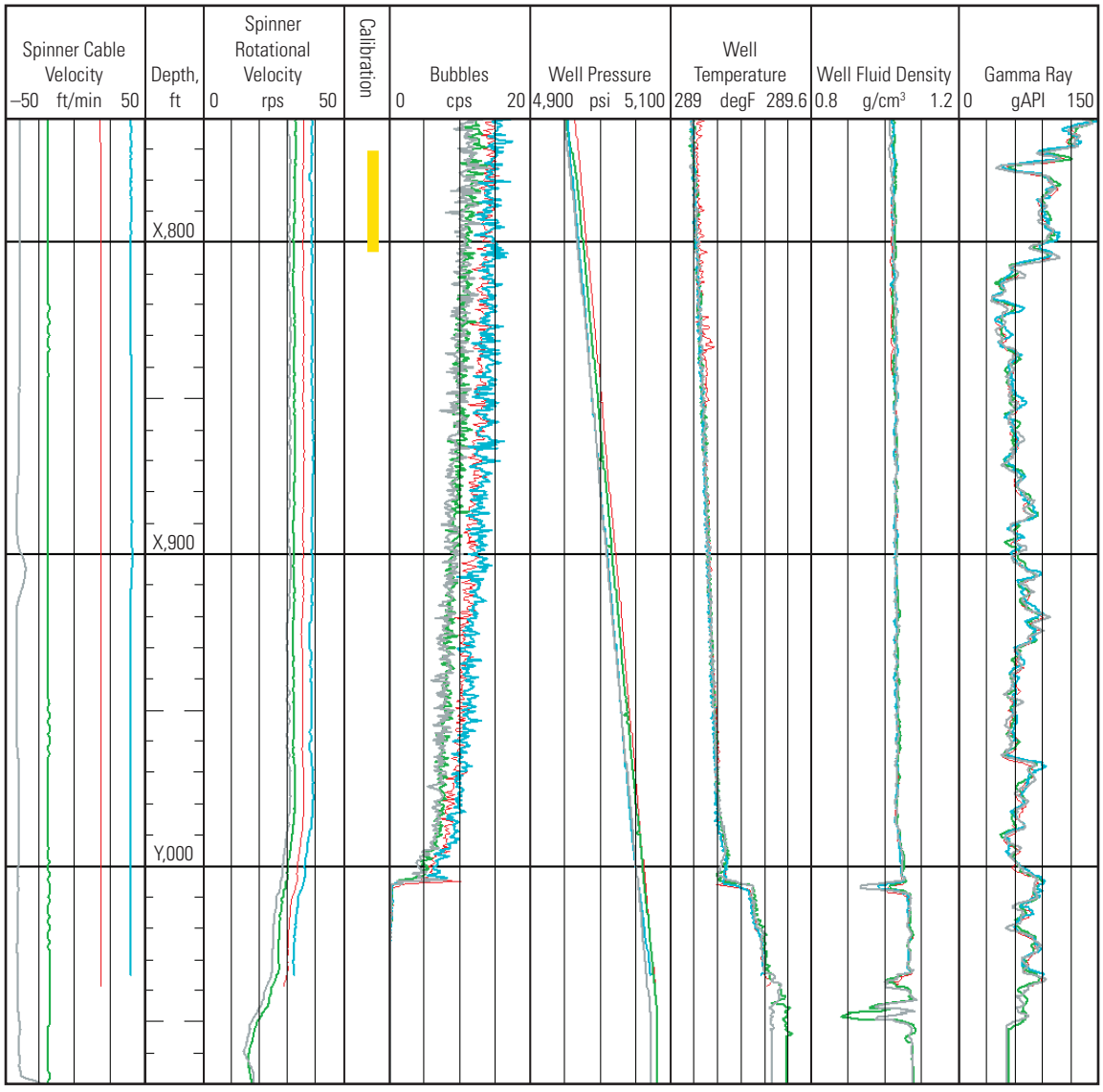

Figure 7-4. High-quality spinner and bubble count dataset.

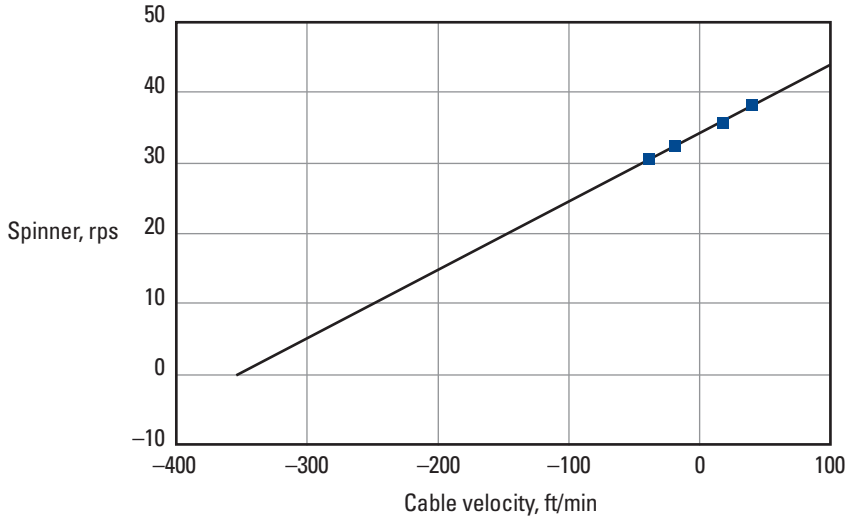

Figure 7-5. Flowmeter calibration.

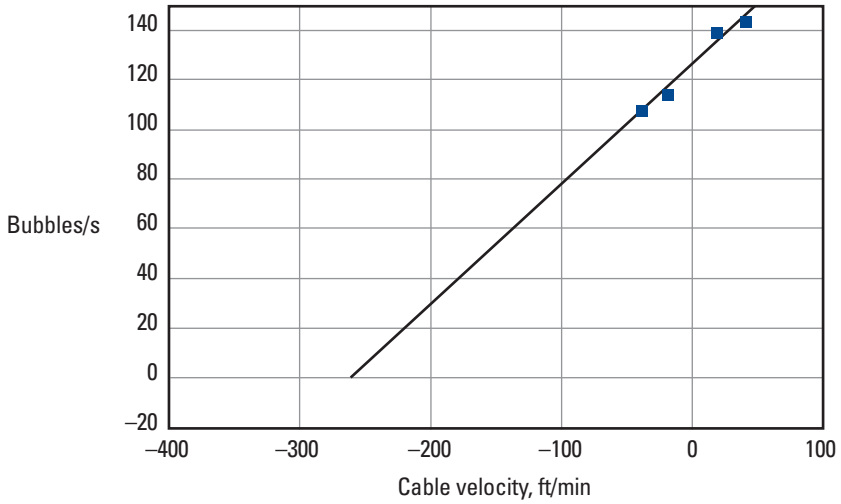

Figure 7-6. Bubble count calibration.

Log quality control of FloView data

Bandwidth limitations on the wireline telemetry used to communicate with any logging toolstring equipped for FloView measurement mean that only a fragment of the probe waveform can be sent to surface. Therefore, to use all the data acquired by the probe, it is necessary to process the waveforms downhole using automatic thresholding algorithms. To ensure that these algorithms are working properly, curves corresponding to the waveform minimum, maximum, and threshold are transmitted to surface and displayed in a log quality control (LQC) presentation (Fig. 7-7).

The hydrocarbon baseline (waveform minimum) should be well separated from the water baseline (waveform maximum), with the dynamic threshold close to the continuous-phase baseline. Except in regions of monophasic flow, the threshold should be above the minimum and below the maximum.

The FloView probes are used in the Flow-Caliper Imaging Sonde (PFCS), Digital Entry and Fluid Imaging Tool (DEFT), and Flow Scanner production logging tools. The PFCS and DEFT each have four FloView probes mounted on the arms of a four-blade centralizer. The probe positions can be configured at surface to move them closer or farther away from the pipe wall. Typically a probe measurement closer to the casing wall delivers a more usable measurement but at the penalty of exposing the probe to more danger of damage occurring. Although the PFCS geometry changes are quite subtle, the DEFT options are more significant (Fig. 7-8).

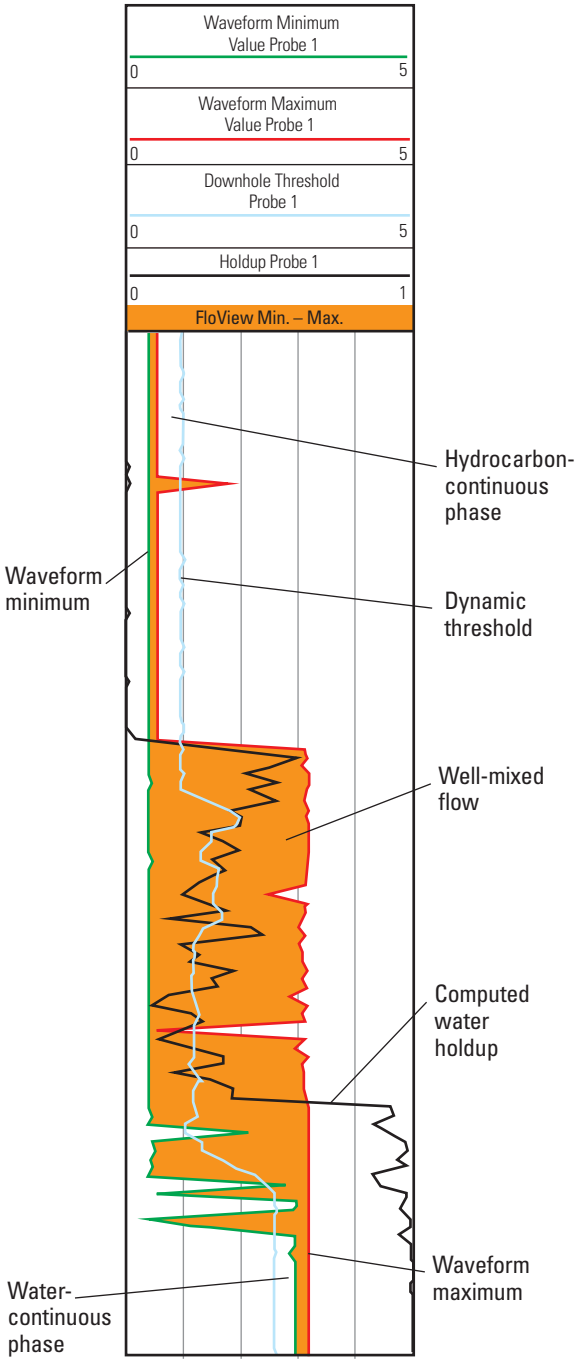

Figure 7-7. Water holdup probe LQC display.

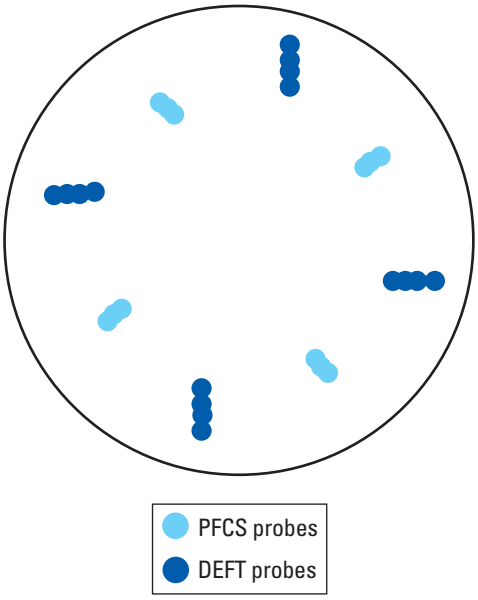

Figure 7-8. Possible PFCS and DEFT probe positions in 6-in-ID pipe.

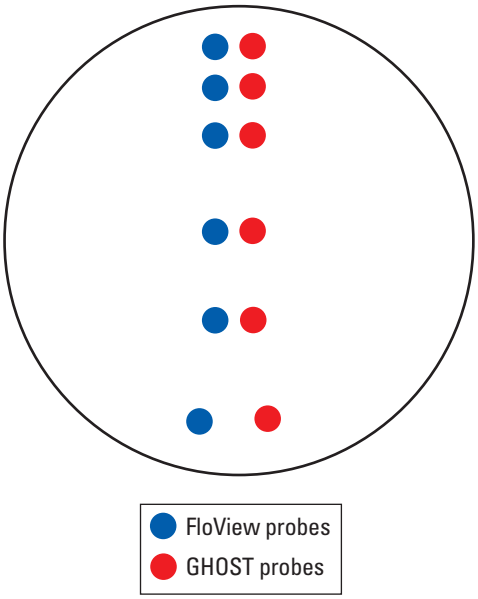

Figure 7-9. Flow Scanner probe positions in 6-in-ID pipe.

Both the PFCS and DEFT are free to rotate around the pipe axis; however, measurement of the tool's relative bearing and the caliper diameter enable determining the probes' locations. If desired, both a PFCS and a DEFT can be run in combination to deliver eight holdup measurements, as configured in Fig. 7-8. For comparison, the Flow Scanner probe positions are shown in Fig. 7-9 (see the "Flow Scanner Interpretation" chapter).

In well-mixed flow a single FloView probe delivers a representative pipe water holdup. However, as the deviation increases gravity begins to segregate the phases, and more probe measurements are required to accurately capture the average pipe holdup (Fig. 7-10).

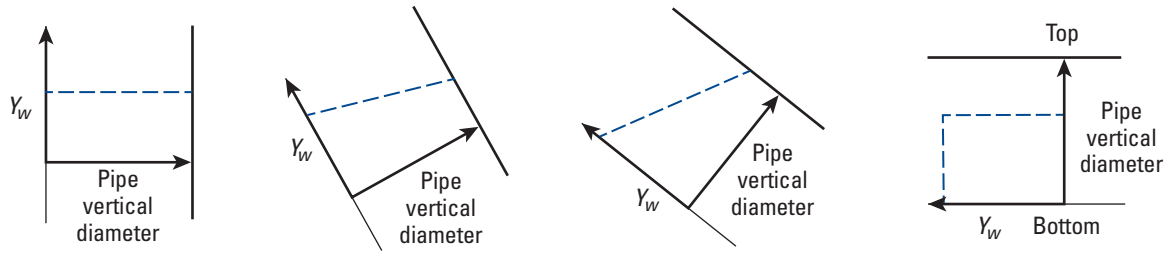

Figure 7-10. Variations of water holdup (Y_w) across the pipe as deviation is varied.

For deviations below 30°, an arithmetic mean of four evenly distributed PFCS or DEFT probes delivers an acceptably accurate water holdup:

$$Y_w = \frac{1}{4}\sum_{n=1}^{n=4} Y_{w_n}. \quad (7\text{-}1)$$

In the case of a bad probe, the average of the remaining three probes usually delivers an inferior holdup compared with the average of the two probes adjacent to the bad probe.

Therefore, for a bad probe 1 or 3:

$$Y_w = \frac{1}{2}\left(Y_{w_2} + Y_{w_4}\right), \quad (7\text{-}2)$$

whereas for a bad probe 2 or 4:

$$Y_w = \frac{1}{2}\left(Y_{w_1} + Y_{w_3}\right). \quad (7\text{-}3)$$

For deviations above 50° with low-velocity, poorly mixed flow and more extreme phase segregation, a combination of the PFCS and DEFT is required to accurately measure the average pipe holdup. In addition the tendency toward stratification means that high-side and low-side probe holdups should be weighted less than measurements made closer to the middle of the pipe, which represent more of the cross-sectional area. In Fig. 7-11 the least weight should be given to the holdup readings from probes DFH1 and DFH3. The most weighting should be applied to probes DFH2 and DFH4. A stratified average imposes horizontal stratification and applies the appropriate areal weighting to each probe based on its position in the pipe. Although a stratified holdup model is correct for a near-horizontal well of 80° to 100° deviation, it is not correct for a deviated well of 50° to 70° deviation. However, it is probably less wrong than using an arithmetic mean of the holdup probes at 50° to 70°.

If the measured holdup values are projected the vertical pipe diameter of Fig. 7-12, then a curve-fitting algorithm can be used to make a best fit through the holdup values and minimize the effect of rogue probe readings. This is accomplished with MapFlo* multiphase flow mapping and is discussed in more detail in the "Flow Scanner Interpretation" chapter.

The log fragment in Fig. 7-13 shows a PFCS and DEFT log from a horizontal oil-water well with the logging tool slowly rotating approximately every 100 m.

The "Y_w holdup" track shows the distribution of water and oil around the circumference described by the probes. The high side is in the middle of the track and the track edges correspond to the low side.

The "Y_w bubbles" track shows the number of bubbles per second, with darker colors indicating more bubbles.

The final track, "Y_w computed," shows the average water and oil holdups calculated from a stratified average processed with MapFlo software of the eight probes, DFH1 through 8.

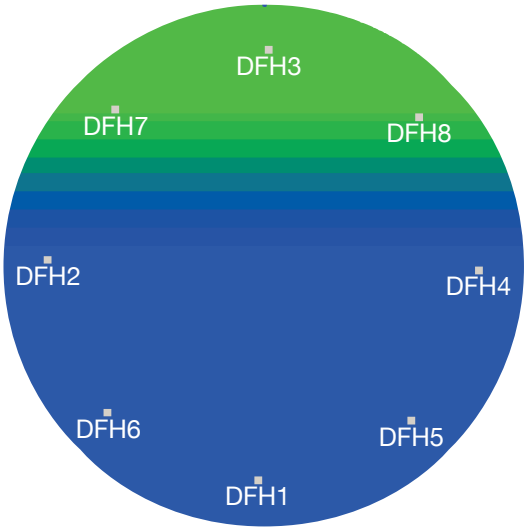

Figure 7-11. Stratified holdup in horizontal well.

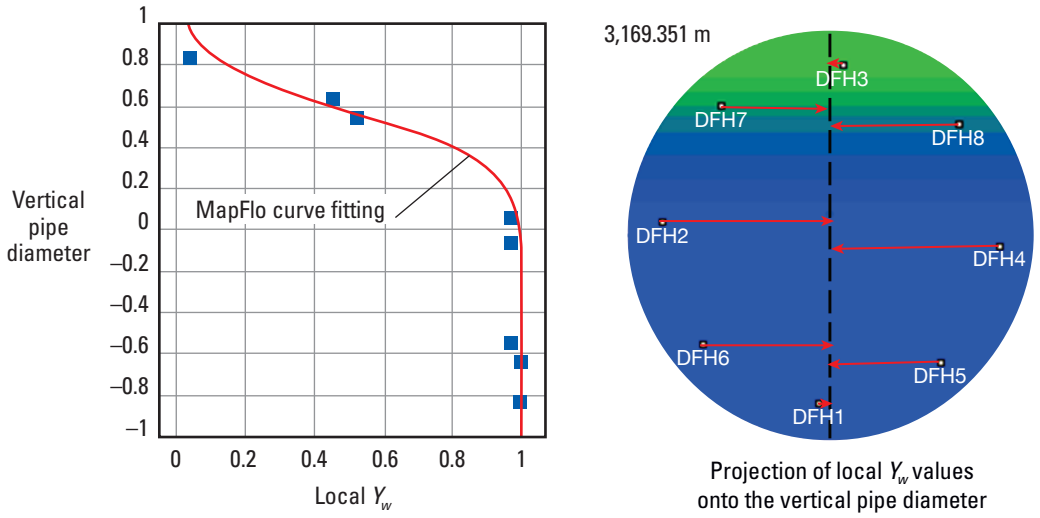

Figure 7-12. MapFlo curve fitting applied to local holdup readings.

Sidebar 7B. A virtual tool from multiple passes

Since 2010 it has been possible to use multiple passes of production logging tool data when converting the discrete probe holdups into an average pipe holdup; previously, each logging pass would create its own value of Y_w and then these Y_w values were used to make the average pipe holdup. If the logging tool follows a random relative-bearing orientation from pass to pass, then a single tool containing four probes can, by combining multiple passes, deliver a virtual tool containing 8, 12, 16, or more probes. Unfortunately, the requirement for random tool relative-bearing orientations is rarely satisfied because the toolstring tends to follow the same orientation from one pass to the next. Shown in Fig. 7B-1 is a rare example where two passes did not follow the same orientation, so the PFCS and DEFT combination yields a combination 16-probe pass.

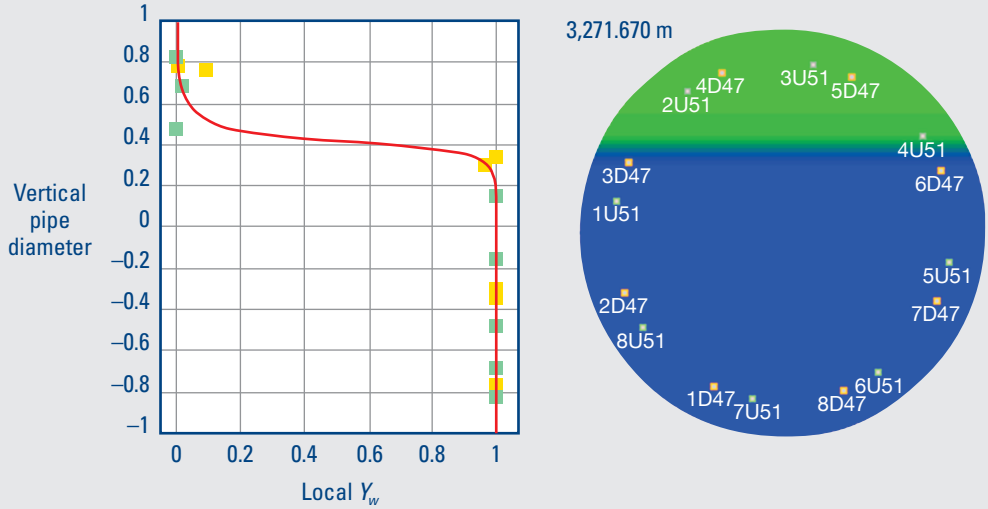

Figure 7B-1. Two passes of PFCS and DEFT data processed simultaneously.

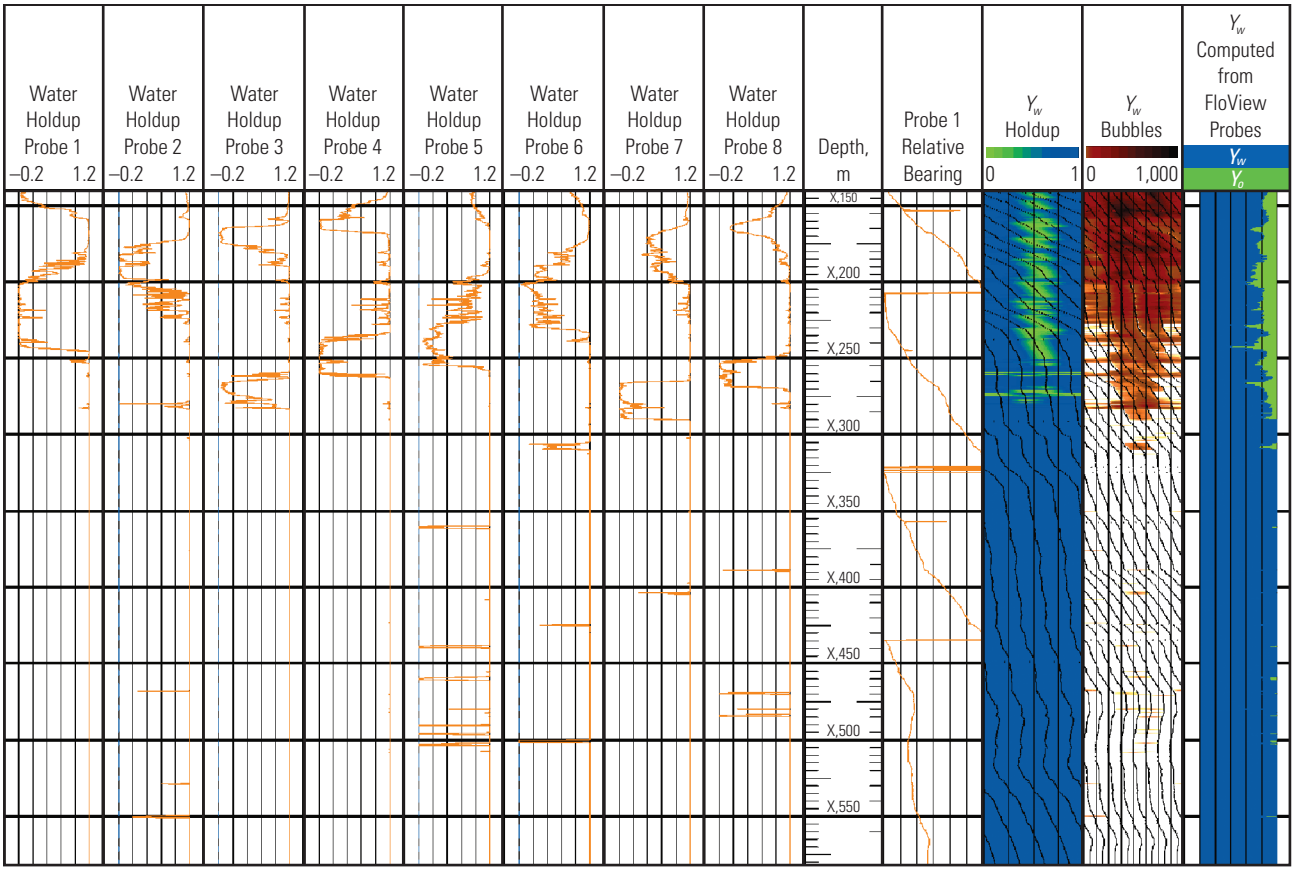

Figure 7-13. PFCS and DEFT combination in a horizontal well.

PFCS and DEFT Curve Mnemonics

Mnemonic	Spelled-Out Name
DFH*n*	Probe *n* water holdup
DFB*n*	Probe *n* bubbles per second
DFN*n*	Minimum waveform voltage of probe *n*
DFX*n*	Maximum waveform voltage of probe *n*
PFTH*n*	Threshold voltage of probe *n*
D1RB	Relative bearing of probe 1
D1RB2	Relative bearing of probe 5
PFC1	Caliper measured with PFCS probe arms 1 and 3
PFC2	Caliper measured with PFCS probe arms 2 and 4
PFC12	Caliper measured with DEFT probe arms 1, 2, 3, and 4

Bubble flow rate

Based on a number of assumptions it is possible to compute a bubble or light-phase flow rate using just the measurements from a probe holdup tool. The model is described first and the assumptions analyzed second.

A bubble flow rate is defined as the product of the velocity of the bubbles, bubble holdup, and pipe cross-sectional area:

$$q_b = v_b Y_b A, \tag{7-4}$$

where

q_b = bubble flow rate, m^3/s
v_b = bubble velocity, m/s
Y_b = bubble holdup
A = pipe internal area, m^2.

The velocity of the bubble is given by the bubble diameter and the time taken for the bubble to pass a FloView probe. Because some bubbles only glance off the probe, the true diameter is reduced by one-third:

$$v_b = \frac{2}{3}\frac{d_b}{t_b}. \tag{7-5}$$

The time for a bubble and the accompanying "non-bubble" continuous phase to pass a probe is given by the reciprocal of the bubble counts per second. The fraction of that time belonging to the bubble is given by the bubble holdup:

$$t_b = \frac{1}{N_{bc}} Y_b. \tag{7-6}$$

Solving for q_b delivers

$$q_b = \frac{2}{3}\left(d_b N_{bc} A\right), \tag{7-7}$$

where

A = pipe cross-sectional area, m^2
d_b = average diameter of the bubbles, m
t_b = presence time of the bubble on the probe tip, s
⅔ = geometrical factor to correct for uncentered bubbles
N_{bc} = bubble count frequency.

Equation 7-7 is true for a stationary measurement, but to process a logging pass a correction must be made for the additional bubble flow rate created by the tool velocity:

$$q_b = \frac{2}{3} d_b N_{bc} - v_{\text{tool}} Y_b \quad A, \tag{7-8}$$

where

v_{tool} = logging speed, m/s.

All the inputs to Eq. 7-8 are provided by the FloView measurement with the exception of the bubble diameter, for which a model is needed. Based on some field measurements and laboratory experiments a simple model has been developed. This model uses a stand-alone bubble size from values of bubble holdup less than 1% and then increases the bubble diameter with increasing bubble holdup as bubbles coalesce and grow. This model does not correct for the change from a continuous heavy phase to a continuous light phase (Fig. 7-14), nor does it correct for bubble shear at high mixture velocities.

Values of stand-alone bubble size are tried until the computed bubble flow rate matches either the other downhole measurements or the surface-measured flow rates and the computed bubble rates from passes recorded at different logging speeds match each other. A good starting point in a low-flow-rate well would be 0.2 in [5 mm]. In a given field the stand-alone bubble diameter chosen for one well should be applicable to the next well.

The bubble model is

$$d_b = d_{\text{pipe}} \left(\frac{d_{sa}}{d_{\text{pipe}}}\right)^{(1-Y_b)^{0.25}}, \tag{7-9}$$

where

d_{sa} = stand-alone bubble size
d_{pipe} = pipe ID.

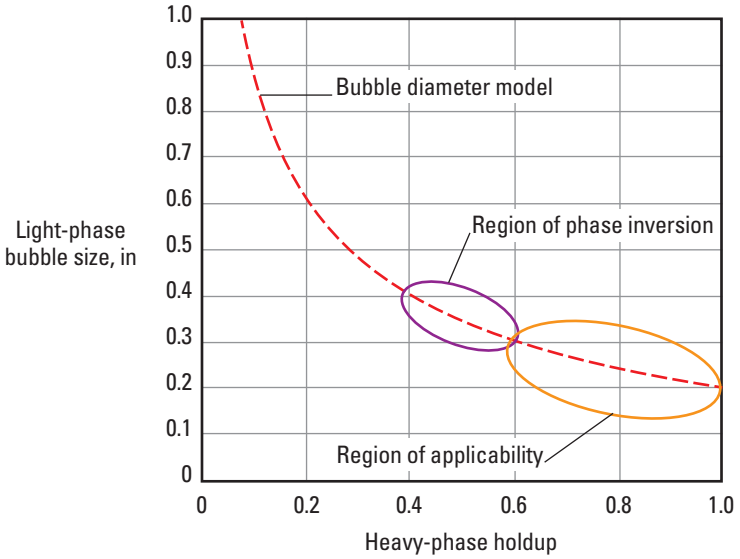

Figure 7-14. Bubble diameter model for 0.2-in stand-alone bubbles in a 6-in-ID pipe.

The complete bubble flow rate equation becomes

$$q_b = \left(\frac{2}{3} N_{bc} d_{\text{pipe}} \times \left(\frac{d_{sa}}{d_{\text{pipe}}} \right)^{(1-Y_b)^{0.25}} - v_{\text{tool}} Y_b \right) A. \quad (7\text{-}10)$$

In oilfield units (using the pipe ID instead of an area) the equation becomes

$$q_b = 1.4 \left(3.33 N_{bc} d_{\text{pipe}} \times \left(\frac{d_{sa}}{d_{\text{pipe}}} \right)^{(1-Y_b)^{0.25}} - v_{\text{tool}} Y_b \right) d_{\text{pipe}}^{\,2}, \quad (7\text{-}11)$$

where

q_b = bubble flow rate, bbl/d
d_{sa} = stand-alone bubble diameter, in
N_{bc} = bubble count, cps
v_{tool} = cable velocity, ft/min
d_{pipe} = pipe ID, in.

In SI units (still using a pipe ID and stand-alone bubble diameter in inches):

$$q_b = 0.73 \left(39.2 N_{bc} d_{\text{pipe}} \times \left(\frac{d_{sa}}{d_{\text{pipe}}} \right)^{(1-Y_b)^{0.25}} - v_{\text{tool}} Y_b \right) d_{\text{pipe}}^{\,2}, \quad (7\text{-}12)$$

where

q_b = bubble flow rate, m^3/d
d_{sa} = stand-alone bubble diameter, in
N_{bc} = bubble count, cps
v_{tool} = cable velocity, m/min
d_{pipe} = pipe ID, in.

For the FloView probe:

$$Y_b = 1 - Y_w, \quad (7\text{-}13)$$

whereas for the GHOST* gas holdup optical sensor tool:

$$Y_b = Y_g, \quad (7\text{-}14)$$

where

Y_g = gas holdup.

Regions of applicability

The bubble flow rate requires a standard bubble size that varies only slightly with increasing oil holdup and has no dependency on the mixture velocity. This criterion is satisfied if the equilibrium bubble size is created by balance between the bubble shearing turbulence of the oil droplets rising through the column of water with the coalescent forces trying to form ever larger bubbles. Therefore, for wells where the slip velocity remains much larger than the mixture velocity, an unchanging stand-alone bubble size should exist over the interval of interest.

All bubbles are assumed to be moving parallel to the pipe axis and toward the surface. Recirculation with down flow and flow perpendicular to the pipe axis causes an overcomputation of the bubble flow rate. Adjustments to the stand-alone bubble diameter may, in part, correct for this effect.

No bubble droplet size correction exists for the change from a heavy continuous phase to a light continuous phase. Therefore the algorithm should not be trusted in the region of $0.4 < Y_b < 0.6$.

Large values of Y_b correspond to the "bubbles" being the continuous phase and also to high mixture velocities (needed to lift the heavy phase to surface). Both of these conditions fall outside of the region of applicability of this technique.

It therefore follows that the bubble flow rate model works best in low-deviation wells with low flow rates and high heavy-phase holdups.

Examples of bubble flow rates

The example in Fig. 7-15 shows an oil rate of 65 bbl/d. The bubble count and water holdup were smoothed with a 10-ft filter before computing the oil bubble rate.

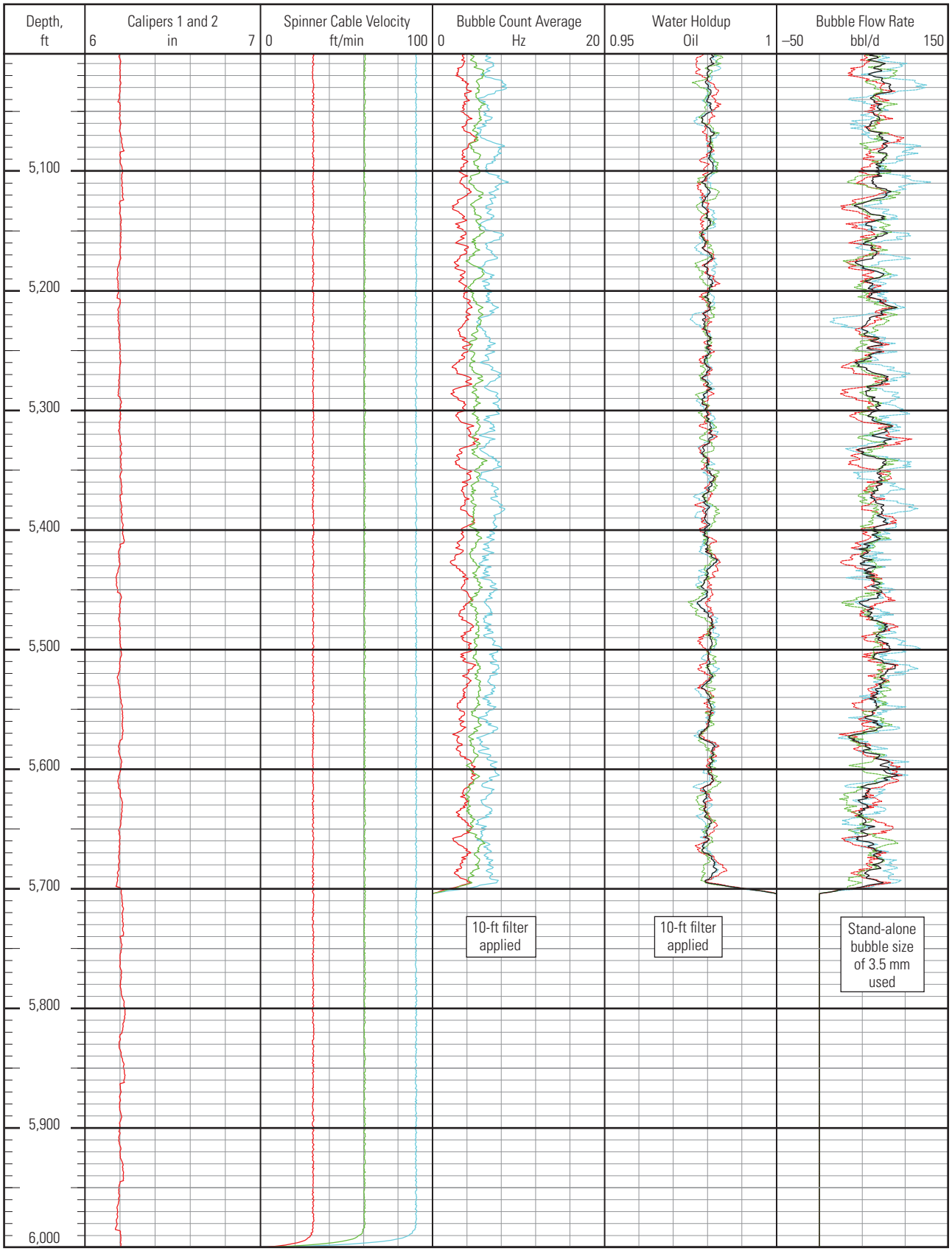

Figure 7-15. Bubble flow rate example with an oil rate of 65 bbl/d.

In the second example in Fig. 7-16, a low-flow-rate large-diameter completion resulted in no usable velocities from either a fullbore spinner or a tubing spinner. The only velocity information came from the oil bubble flow rate. Therefore the water flow rate was computed using the holdup information, bubble flow rate, and Choquette slip correlation.

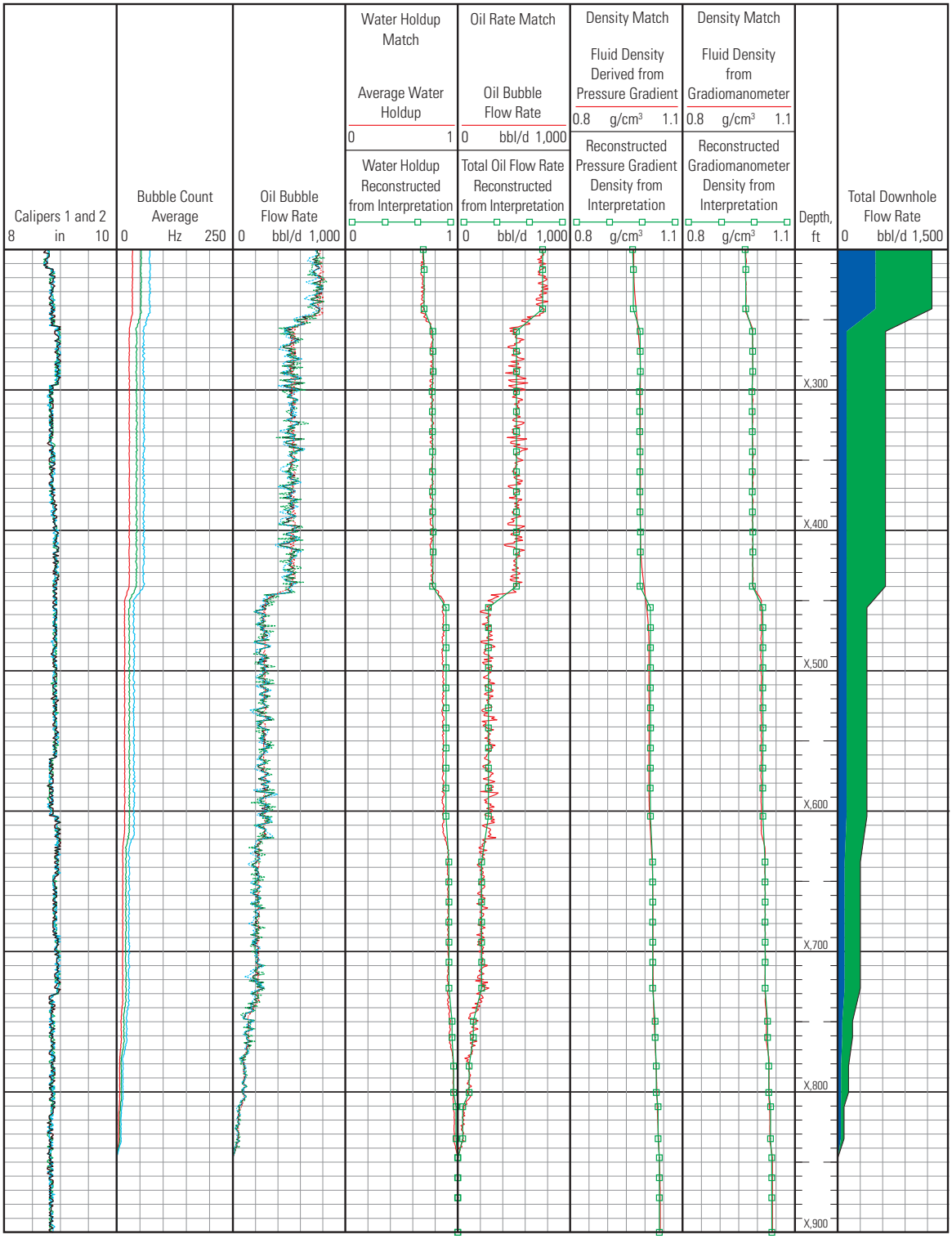

Figure 7-16. Bubble flow rate replacing spinner velocity information.

Droplet persistence

In a minority of wells worldwide, the Schlumberger FloView and GHOST probes have been observed to overread the water holdup. The physics of this error is not completely understood, but it appears to be triggered by water droplets clinging to the probe tips when low-density gas has insufficient energy or momentum to clean the probe tip. The phenomenon is called "droplet persistence." Following some laboratory flow loop experiments, a proprietary correction algorithm has been developed and implemented inside SPRINT* single-pass production log interpretation, BorFlow production logging tool analytical software package, Schlumberger proprietary multipass interpretation software for Flow Scanner data, and Emeraude and PLATO interpretation software.

A typical FloView correction coefficient is between 0 and –0.3 and is applied identically to all FloView probes (Fig. 7-17). A typical GHOST correction coefficient is between 0 and 0.1 (Fig. 7-18).

It must be emphasized that the majority of wells worldwide do not need these corrections. These corrections should not be routinely applied.

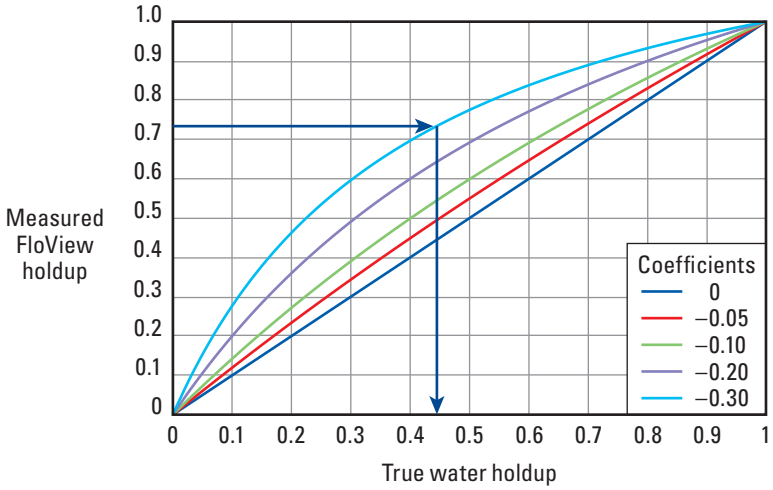

Figure 7-17. FloView droplet persistence correction.

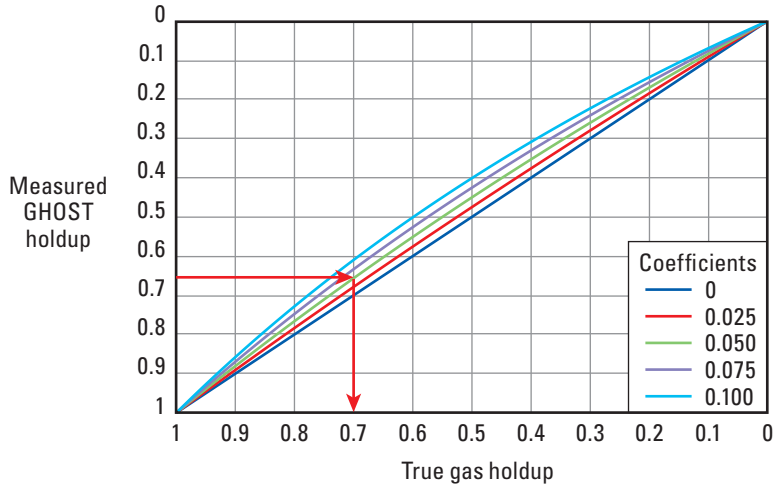

Figure 7-18. GHOST droplet persistence correction.

Gas holdup probes

The GHOST gas holdup optical sensor tool uses the refractive indices of gas, oil, and water to distinguish between the presence of gas and liquid (Fig. 7-19). (In the absence of gas, the GHOST tool can sometimes be used to make a water holdup measurement, but this is not discussed further here. See Jackson et al., 2001)

Light produced by a light-emitting diode (LED) at a suitable frequency is fed down an optical fiber through a Y coupler and finally to an optical probe made from a synthetic sapphire crystal (Fig. 7-20).

The optical probe has a carefully engineered profile that through total internal reflection concentrates the optical fiber-wide light beam down to the probe tip. At the probe tip a change in the curvature of the sapphire allows light to escape from the probe if the refractive index of the well fluid is high enough (Fig. 7-21).

Light that does not escape is returned via the Y coupler to a photodiode and is converted to a voltage (Fig. 7-22). The sensitive area of the tip is much smaller than the FloView probe, enabling the accurate measurement of much smaller bubbles at higher velocities.

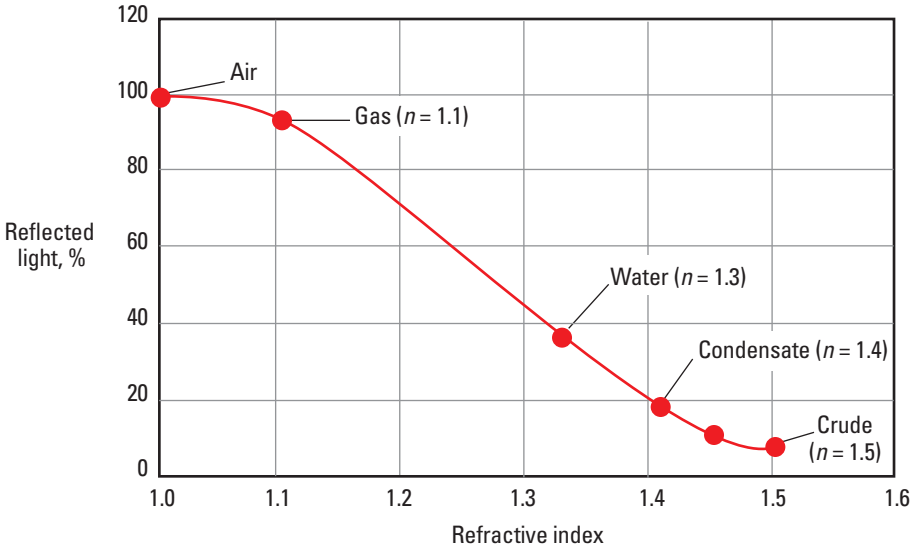

Figure 7-19. GHOST probe response with refractive index.

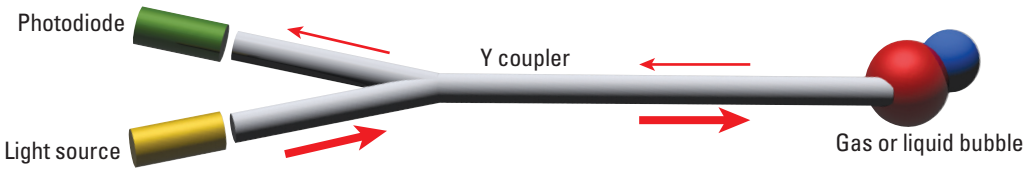

Figure 7-20. Optical path of GHOST light beam.

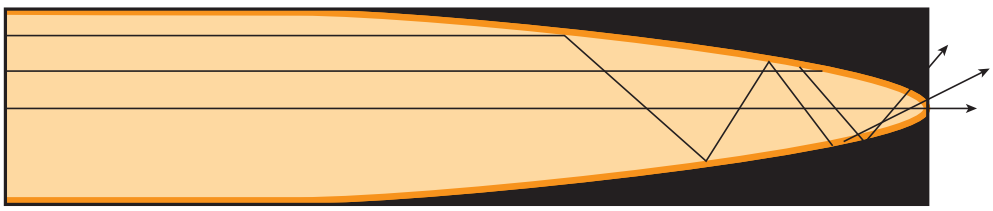

Figure 7-21. Light focusing at the GHOST probe tip.

The signal from the optical probe is at or below the gas baseline and at or above the oil baseline (Fig. 7-23). To capture small transient bubble readings, a dynamic threshold is adjusted close to the continuous gas phase and close to the continuous liquid phase. The threshold is then compared with the probe waveform to deliver a binary gas holdup signal, which is averaged over time. The entire probe waveform during a 6-in depth frame is processed in this way.

Bandwidth limitations on the wireline telemetry mean that only a fragment of the probe waveform can be sent to surface. It is therefore necessary to process the waveforms downhole using automatic thresholding algorithms. To ensure that these algorithms are working properly, the waveform minimum, maximum, and threshold are displayed in an LQC presentation (Fig. 7-24).

The liquid baseline (waveform minimum) should be well separated from the gas baseline (waveform maximum), with the dynamic threshold close to the continuous-phase baseline. Except in regions of monophasic flow, the threshold should be above the minimum and below the maximum.

Optical probes are used in both the GHOST and Flow Scanner production logging tools. The GHOST tool has four optical probes mounted on the arms of a four-blade centralizer. A special optical extender can be used to move the optical probes closer to the pipe wall, but the extender has limited availability.

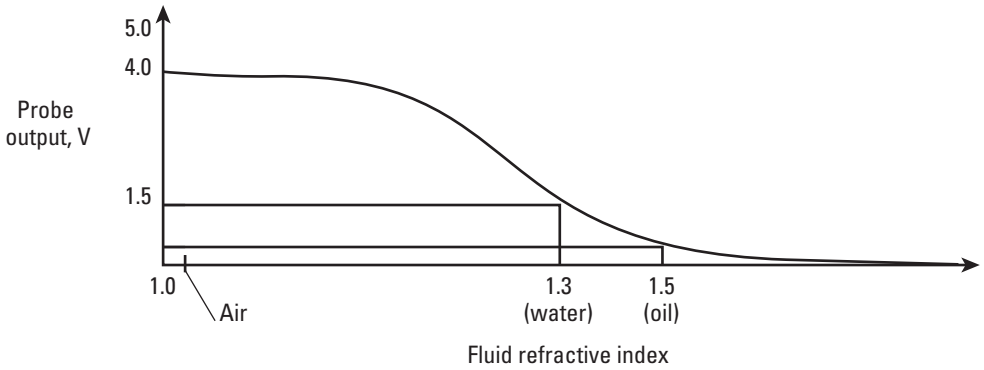

Figure 7-22. Photodiode voltage as a function of refractive index.

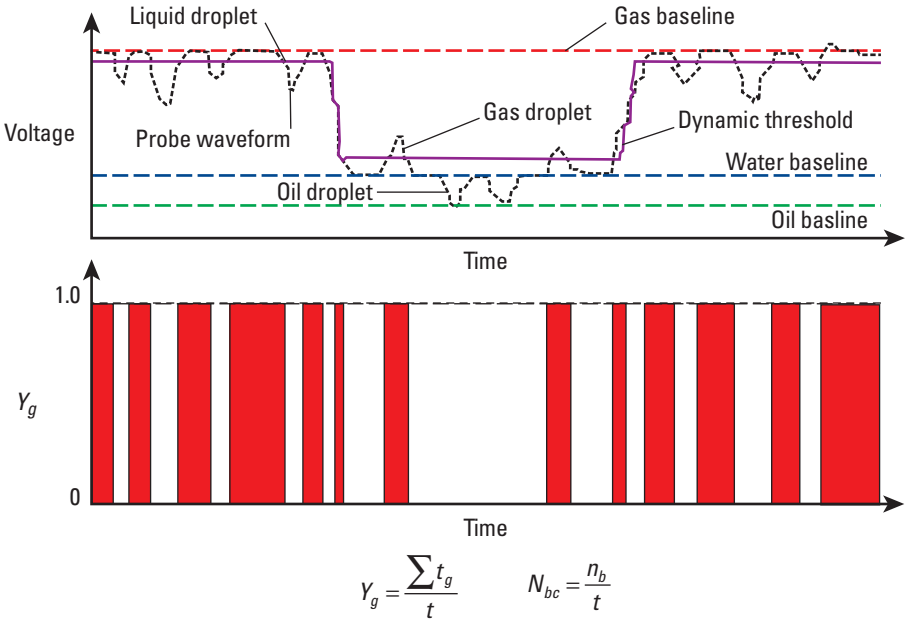

Figure 7-23. GHOST waveform processing. Σt_g = total time that the probe is in gas during time t.

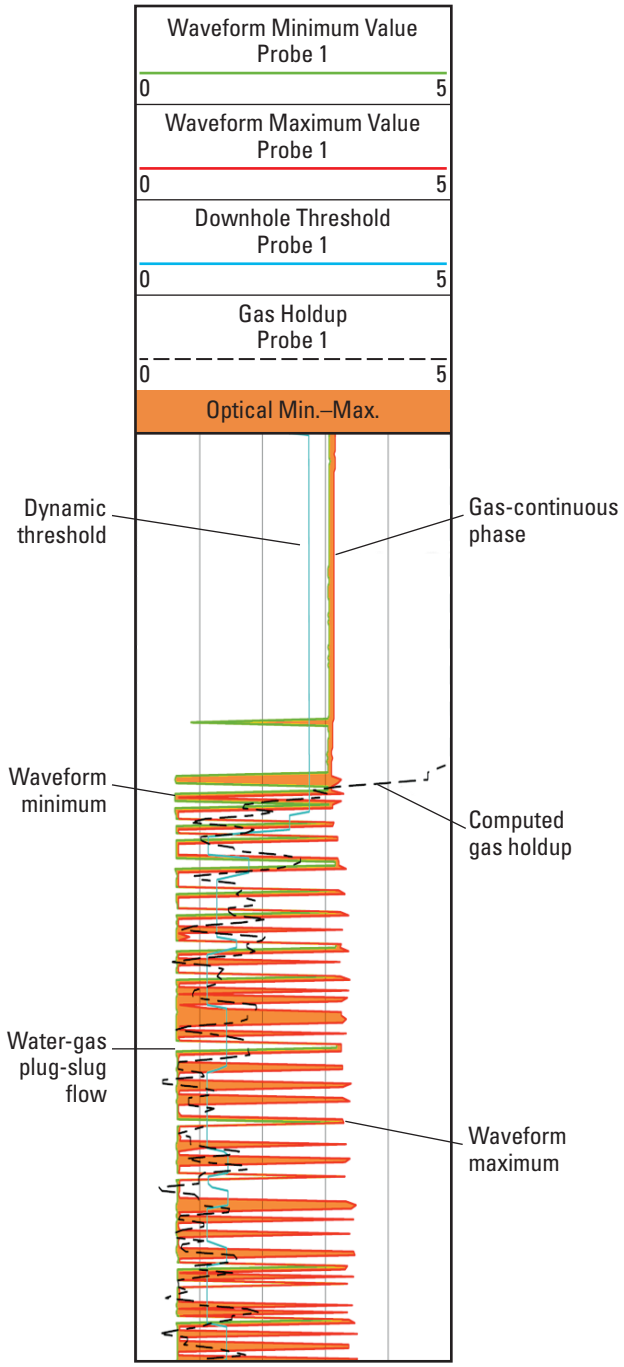

Figure 7-24. Gas holdup probe LQC display.

The GHOST tool is free to rotate around the pipe axis, so measurement of the tool's relative bearing and the caliper diameter are used to determine the probe locations. Improved pipe coverage in high-angle and deviated wells can be achieved using two GHOST tools connected with a 45° rotated sub (Fig. 7-25). For comparison, the Flow Scanner probe positions are shown in Fig. 7-26 (see the "Flow Scanner Interpretation" chapter for more information on Flow Scanner service).

In well-mixed flow a single optical probe delivers a representative pipe water holdup. However, as the deviation increases, gravity begins to segregate the phases and more probe measurements are required to accurately capture the average pipe holdup.

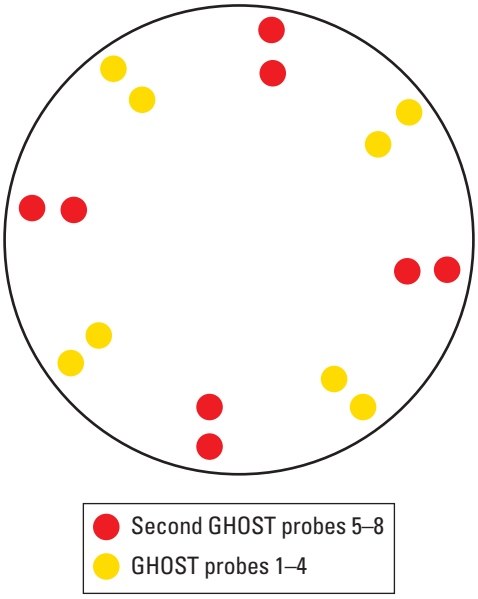

Figure 7-25. Possible GHOST and dual-tool GHOST probe positions in 6-in-ID pipe.

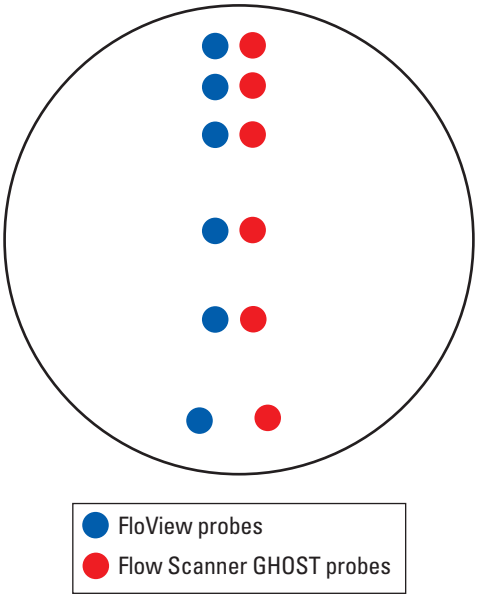

Figure 7-26. Flow Scanner probe positions in 6-in-ID pipe.

For deviations below 30°, an arithmetic mean of four evenly distributed optical probes delivers an acceptably accurate gas holdup:

$$Y_g = \frac{1}{4}\sum_{n=1}^{n=4} Y_{g_n}. \qquad (7\text{-}15)$$

In the case of a bad probe, the average of the remaining three probes usually delivers an inferior holdup compared with the average of the two probes adjacent to the bad probe. For a bad probe 1 or 3 it is better to use

$$Y_g = \frac{1}{2}\left(Y_{g_2} + Y_{g_4}\right), \qquad (7\text{-}16)$$

whereas for a bad probe 2 or 4 it is better to use

$$Y_g = \frac{1}{2}\left(Y_{g_1} + Y_{g_3}\right). \qquad (7\text{-}17)$$

For deviations above 50° with low-velocity, poorly mixed flow and more extreme phase segregation, a dual GHOST combination is required to accurately measure the average pipe holdup.

At high deviations the tendency toward stratification means that high-side and low-side probe holdups should be weighted less than measurements made closer to the middle of the pipe, which represents a larger portion of the cross-sectional area. In Fig. 7-27 the least weight should be given to the holdup readings from probes GHH2 and GHH4. The most weighting should be applied to probes GHH1 and GHH3. A stratified average applies the appropriate weighting to each probe based on its position in the pipe. Although a stratified holdup model is correct for a near-horizontal well of 80° to 100° deviation, it is not correct for a deviated well of 50° to 70° deviation because the equal holdup contours are no longer flat and become significantly curved. However, the stratified average is less wrong than using an arithmetic mean of the holdup probes.

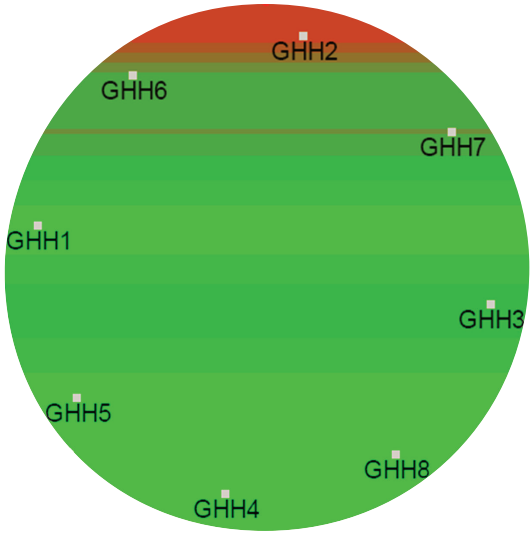

Figure 7-27. Dual GHOST tool stratified-flow probe configuration.

If the measured holdup values are projected onto the vertical pipe diameter of Fig. 7-28, then the MapFlo curve-fitting algorithm can be used to make a best fit through the holdup values and minimize the effect of rogue probe readings. MapFlo software is discussed in more detail in the "Flow Scanner Interpretation" chapter.

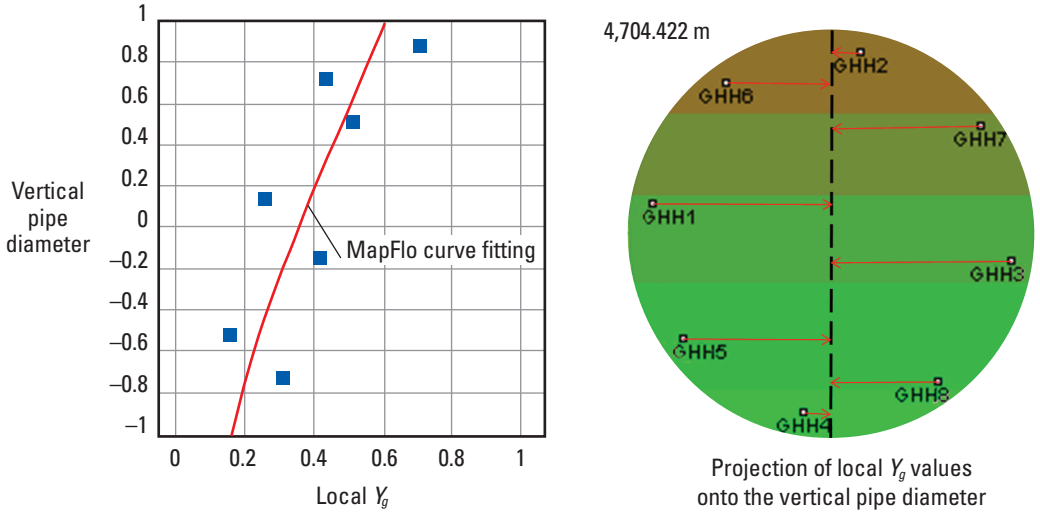

Figure 7-28. MapFlo curve fitting applied to local holdup readings.

The log fragment in Fig. 7-29 shows a log from dual GHOST tools in a horizontal gas-oil well. The left-hand image track displays the holdup around the circumference described by the holdup probes, with the high side positioned in the middle of the track. Probe GHH4 was intermittently spiking and was removed from the image processing.

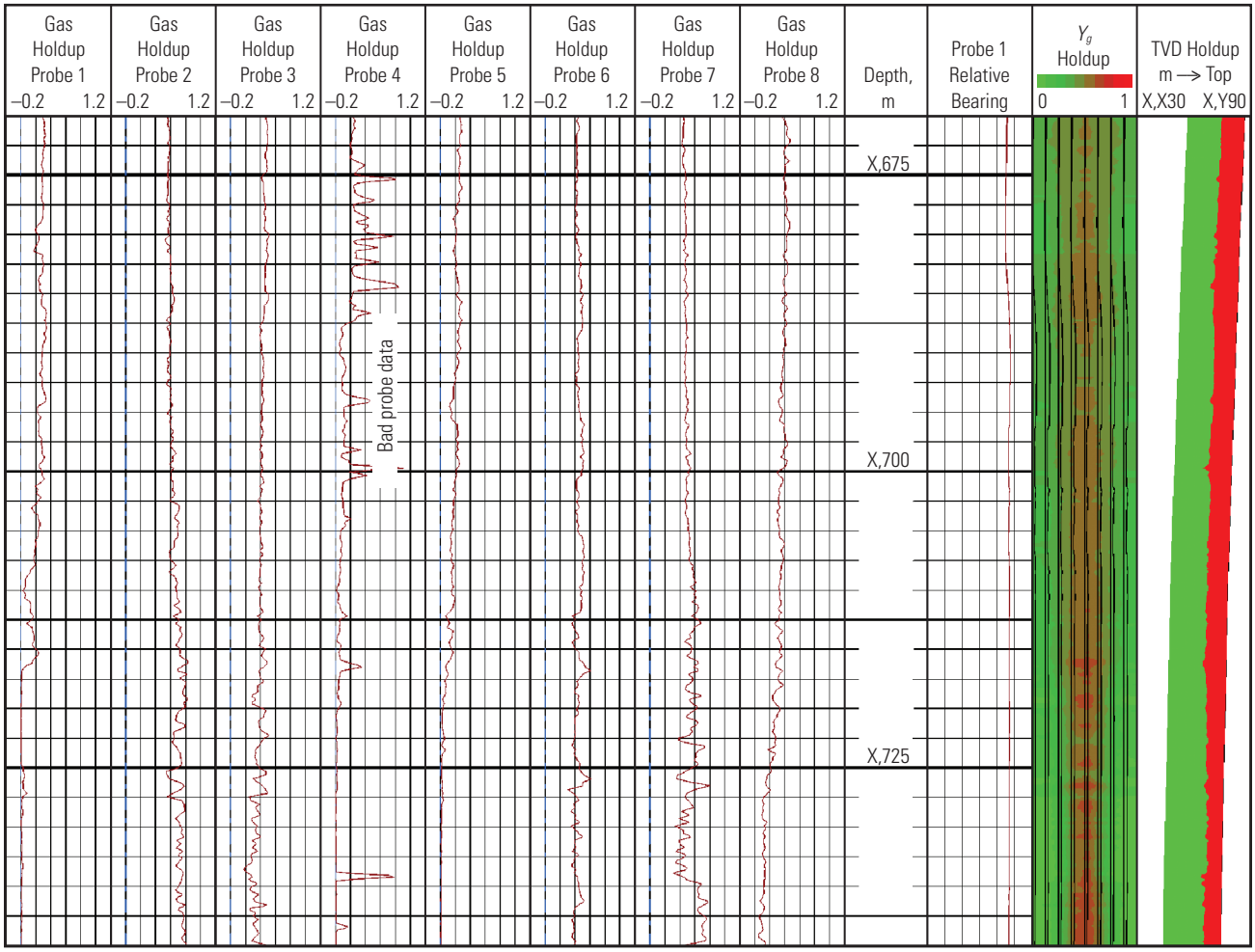

Figure 7-29. Log data from dual GHOST tools. (Oseberg field, Norway, courtesy of Statoil ASA)

GHOST Curve Mnemonics

Mnemonic	Spelled-Out Name
GHH*n*	Probe *n* gas holdup
GHB*n*	Probe *n* bubbles per second
DFN*n*	Minimum waveform of probe *n*
DFX*n*	Maximum waveform of probe *n*
PFTH*n*	Threshold voltage of probe *n*
D1RB	Relative bearing of probe 1
D1RB2	Relative bearing of probe 5
PFC1	Caliper measured on probe arms 1 to 4
PFC12	Caliper measured with probe arms 5 to 8

Reference

Jackson, R.R., Ayan, C., and Wakefield, J.: "Flow Diagnosis and Production Evaluation in High Flowrate Oil-Water Producers Using Optical-Fibre Holdup Sensors," paper SPE 71727 presented at the SPE Annual Technical Conference and Exhibition, New Orleans, Louisiana, USA (September 30–October 3, 2001).

8 Dielectric Holdup

Capacitance-Based Holdup Sensors

Although no longer used by Schlumberger, the capacitance-based dielectric sensor (also called a holdup meter [HUM]) is still in common use and is included in this book for completeness. Figure 8-1 shows a flow-through implementation. Some more modern tools use single or multiple probes.

Inside the tool is an oscillator with a frequency that varies with the capacitance of a sensor, which in turn is driven by the holdups and dielectric constants of the phases present:

$$f \propto \frac{1}{R_t\left(C_t + C_{\text{sensor}}\right)}, \tag{8-1}$$

where

f = frequency sent to surface
R_t = resistance within the oscillator
C_t = inherent tool capacitance
C_{sensor} = capacitance coming from the wellbore fluids within the sensor.

The theoretical response curves for different dielectric tools are shown in Fig. 8-2. Each tool, with its different geometry and electronics, is normalized to the oil point at a dielectric constant of 5 and water at 80. The response line between the two points is a gentle curve, the severity of which depends on the manufacturer. (Some dielectric tools are even specially engineered to have a linear response to the changing dielectric constant.) Many dielectric holdup tools are supplied with a calibration chart to enable a log analyst to remove the curve and linearize the response between 100% water and 100% hydrocarbon. Obviously, the tool type must be known to select the correct chart.

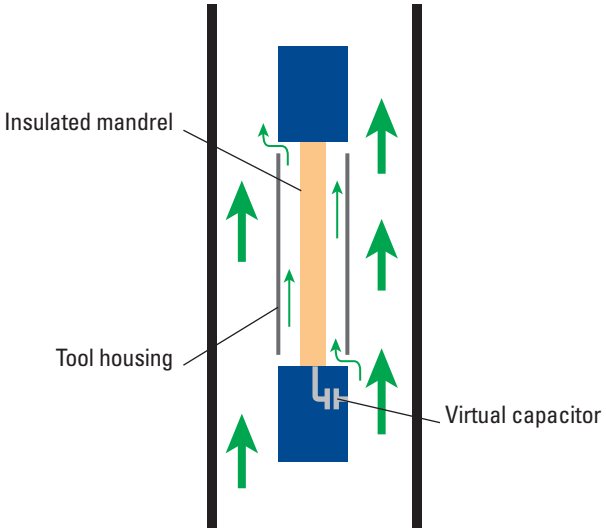

Figure 8-1. Schematic of a flow-through dielectric holdup meter.

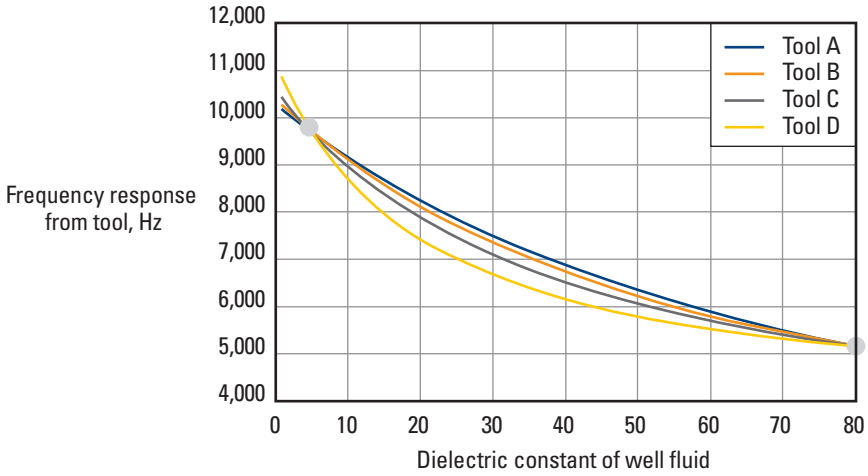

Figure 8-2. Theoretical response curves for dielectric holdup meters to a changing dielectric fluid mixture.

Curiously, the dielectric constant of water is not a constant but varies with pressure and temperature (Floriano and Nascimento, 2004). However, downhole calibration to a column of water provides an accurate end point.

Changing the scales produces the normal dielectric holdup response chart in Fig. 8-3 (an arbitrary frequency range is used in the figure). The tool frequency reading is traced up to a response line that joins the 100% oil and 100% water points and then followed across to indicate the water holdup.

This approach works well for an oil-continuous phase, but as water becomes the continuous phase the response changes owing to the conductivity of the water. A much weaker response to oil bubbles within water is exhibited, with a response slope that can be determined only empirically (Fig. 8-4). The changeover from an oil-continuous phase to a water-continuous phase occurs in the vicinity of a 50% water holdup and further complicates the analysis of dielectric holdup data. It is not uncommon for the dielectric calibration charts provided by the manufacturers to incorporate a correction for the continuous-phase changes from oil to water. A second chart may be supplied for gas-water wells.

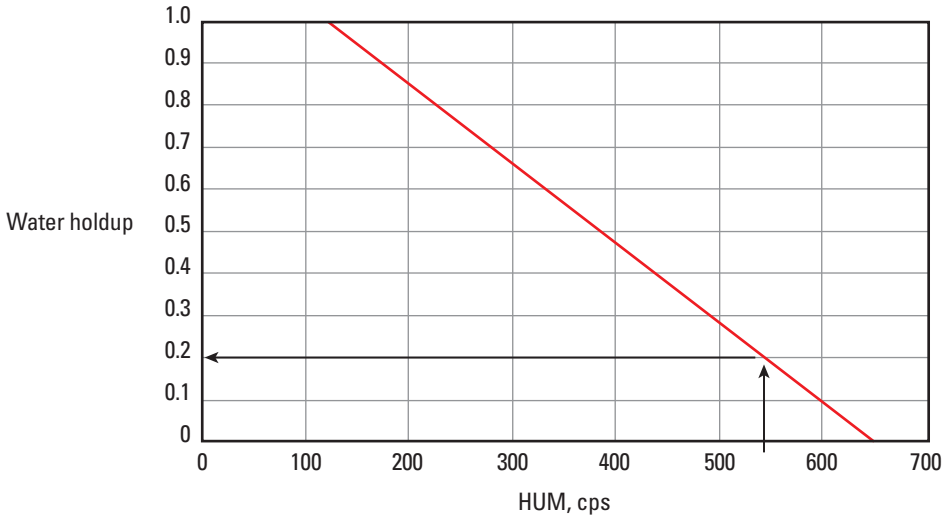

Figure 8-3. Theoretical dielectric holdup response.

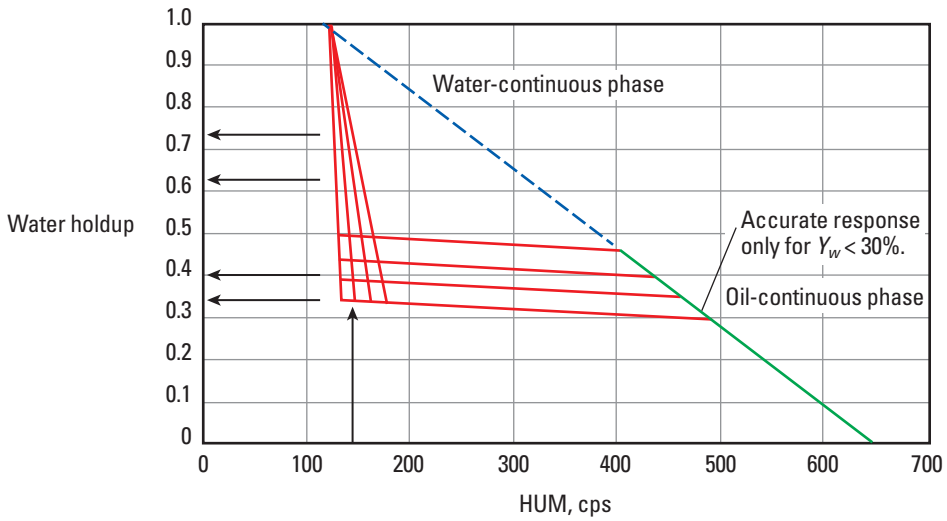

Figure 8-4. Practical dielectric holdup response.

Modern interpretation software allows a skilled log analyst to create the desired nonlinear response curve based either on a predefined calibration or, more usually, an empirical ad hoc "calibration."

Because the flow-through or single-probe dielectric holdup meter makes a pipe-axis reading, the tool reading rarely sees an average pipe holdup when run in deviated or horizontal wells (Fig. 8-5).

Multiple capacitance probes succeed in sampling a representative cross section of the pipe but must struggle with preferential wettability effects that skew the holdup readings toward one of the liquid phases. Accurate use of the HUM is generally restricted to near-vertical, low-water-cut wells with higher fluid velocities.

Reference

Floriano, W.B., and Nascimento, M.A.C.: "Dielectric Constant and Density of Water as a Function of Pressure at Constant Temperature," *Brazilian Journal of Physics* (March 2004) 34, No. 1, 38–41.

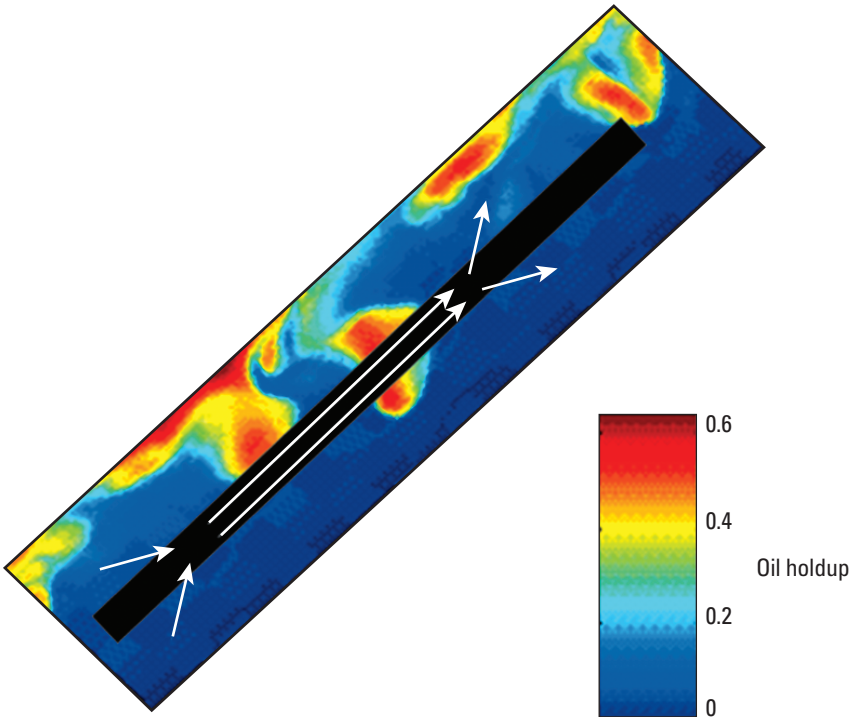

Figure 8-5. Flow-through tool in a deviated well.

9 Pulsed Neutron Interactions

At the heart of all pulsed neutron tools is a thermionic valve or tube. The Schlumberger version is the Minitron* device. The Minitron generator collides deuterium and tritium together to produce helium and high-energy neutrons:

$$ {}^{2}_{1}\mathrm{H} + {}^{3}_{1}\mathrm{H} \rightarrow {}^{4}_{2}\mathrm{He} + n. \qquad (9\text{-}1) $$

The neutrons are emitted with an energy of 14.1 MeV, and in the advanced Minitron device they can be turned on and off in less than a microsecond (Fig. 9-1).

These high-energy neutrons can interact with the wellbore fluids, casing, cement, matrix, and fluid-filled porosity in a number of ways. For the purposes of wellbore logging these interactions are simplified into three types:

- Inelastic scattering—defined in terms of what it does not do. The collisions are not elastic; therefore, the very light high-energy neutrons are able to interact with much heavier nuclei. Interaction means that the neutron loses a lot of energy while electrons in the heavier nuclei are pushed into higher, unstable shells from which they rapidly decay while spitting out gamma rays with a characteristic energy spectrum (Fig. 9-2). This is an early time effect that reaches its maximum strength within microseconds of the neutron burst starting.
- Neutron capture—the capture of low-energy thermal neutrons by certain nuclei. The nuclei in question gain a neutron to become a heavier isotope of the original element (Fig. 9-3). To balance the energy books, some energy must be lost and is again seen as a gamma ray with an energy spectrum specific to the isotope. Although the capture gamma rays peak a few milliseconds after the neutron burst, there are enough capture gamma rays present within a few microseconds of the neutron burst to contaminate the inelastic spectra.

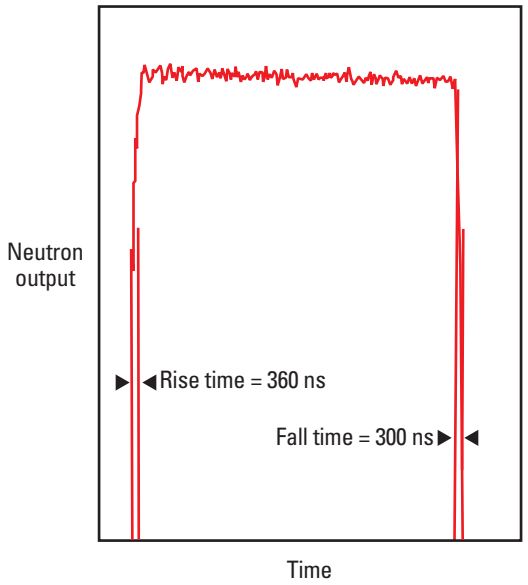

Figure 9-1. Typical neutron pulse shape from a Minitron generator.

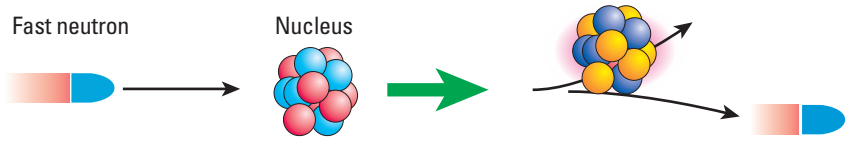

Figure 9-2. Inelastic scattering.

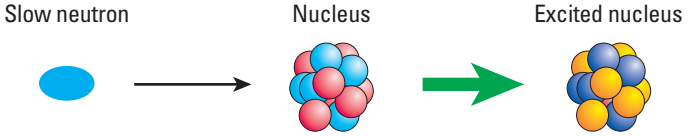

Figure 9-3. Thermal neutron capture.

- Neutron activation—a form of capture of oxygen, aluminium, silicon, sodium, copper, iron, and many more elements that liberates a proton to create a new element that decays through a number of steps until energy equilibrium is restored (Fig. 9-4). The activation of oxygen is used for the WFL* water flow log and the activation of silicon and aluminium is used for a gravel-pack quality log.

The RSTPro* reservoir saturation tool is used to measure the gamma rays that result from inelastic scattering, thermal neutron capture, and activation (Fig. 9-5).

O activation	$t_{½} = 7.1$ s	$(n + {}_{8}O^{16} \rightarrow {}_{7}N^{16} + \ldots \rightarrow {}_{8}O^{16} + \gamma + \ldots)$
Al activation	$t_{½} = 2.3$ min	$(n + {}_{13}Al^{27} \rightarrow {}_{13}Al^{28} \rightarrow {}_{14}Si^{28} + \gamma + \ldots)$
Si activation	$t_{½} = 2.3$ min	$(n + {}_{14}Si^{28} \rightarrow {}_{13}Al^{28} + \ldots \rightarrow {}_{14}Si^{28} + \gamma + \ldots)$

Figure 9-4. Example activation reactions. $t_{½}$ = half-life for the slowest nuclear decay in the series.

Specifications

	RST-C	RST-D
Temperature rating, degF [deg C]	302 [150]	302 [150]
Pressure rating, psi [MPa]	15,000 [103]	15,000 [103]
Diameter, in [cm]	1.71 [4.34]	2.51 [6.37]
Min. tubing, in	2⅜	3½
Min. restriction, in [cm]	1.813 [4.61]	2.625 [6.67]
Length, ft [m]	23 [7]	22.2 [6.8]
Weight, lbm [kg]	101 [46]	208 [94]

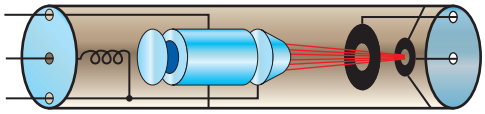

Minitron Neutron Generator
- High neutron yield
- Gain regulation
- Precise neutron burst control

Answers
- WFL water flow log
- PVL* phase velocity log
- TPHL* three-phase fluid holdup log from pulsed neutron measurements

Gadolinium Oxyorthosilicate (GSO) Detectors
- Shielded detectors for flowing wells
- Efficient gamma ray detection
- High count rate with little spectrum distortion

Figure 9-5. Key components and specifications of RSTPro reservoir saturation tools.

10 TPHL Three-Phase Holdup Log from the RSTPro Reservoir Saturation Tool

The TPHL* three-phase holdup log is run with the RSTPro reservoir saturation tool and uses the early-time gamma ray spectra that occur during the neutron burst. Unfortunately, a clean inelastic signal is not seen because the capture spectra begin almost as soon as the first inelastic spectra are seen. Therefore, a fraction of the late-time capture signal is subtracted from the inelastic signal to deliver a reasonable approximation to a clean inelastic spectrum (Fig. 10-2).

The resulting inelastic spectra are compared with the reference spectra of iron, carbon, sulfur, magnesium, calcium, silicon, oxygen, and a tool background signal made up of the different elements used in the neutron generator, crystal detectors, shielding, and tool pressure vessel (Fig. 10-1). There are more signals present than just these eight, but looking for more degrades the accuracy with which these eight are measured and in particular degrades the carbon and oxygen signals, which form a major part of the TPHL algorithm.

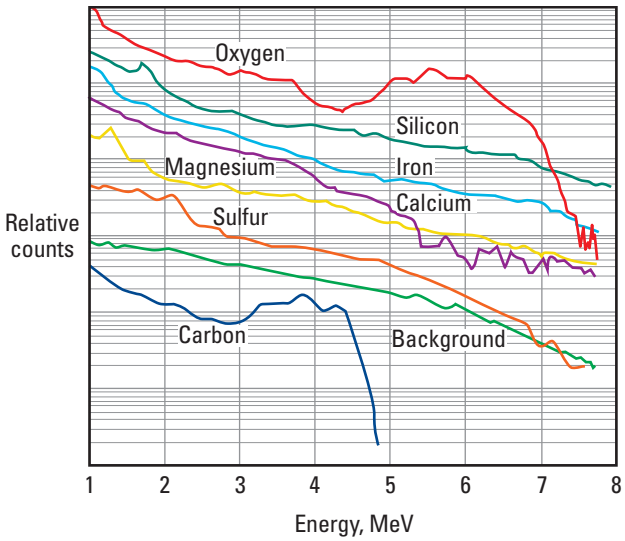

Figure 10-1. Inelastic scattering gamma ray spectra with an arbitrary count rate offset.

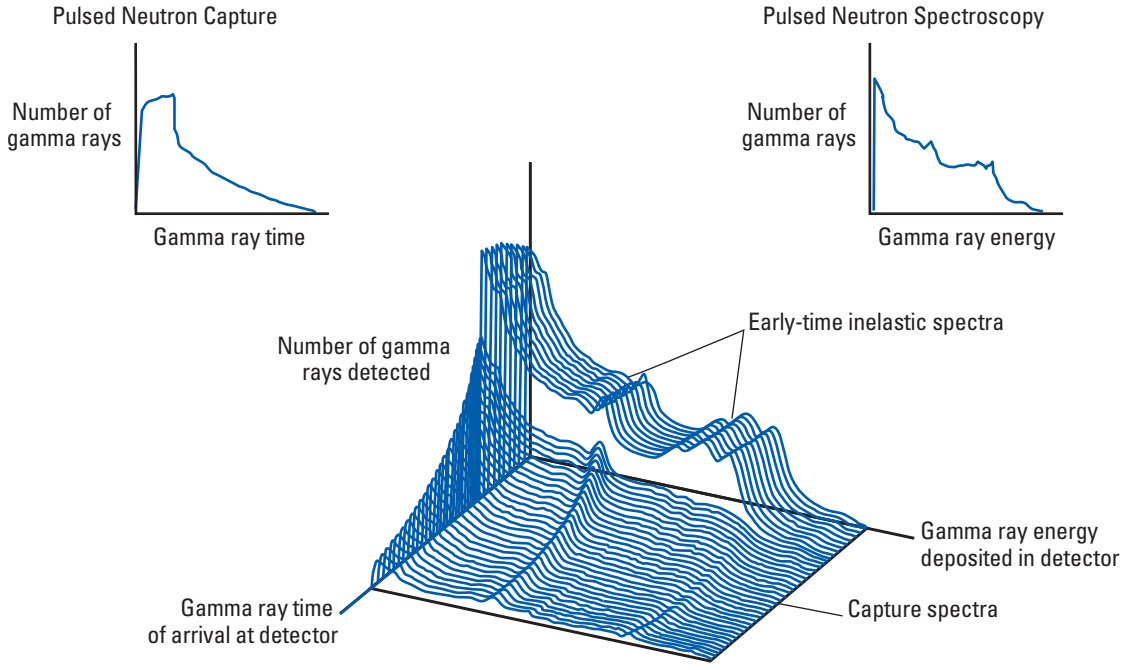

Figure 10-2. RSTPro spectra during inelastic capture in TPHL three-phase holdup logging.

In hydrocarbons and water, the only measured elements that are found are carbon and oxygen, whereas all the measured elements can be found in steel casing, cement, and formation matrix (Fig. 10-3).

The carbon yield extracted from the composite inelastic spectra could be coming from

- wellbore hydrocarbons (oil and gas)
- formation hydrocarbon-filled porosity
- formation matrix (carbonates).

Normally the original openhole interpretation supplies the formation lithology and formation porosity and therefore provides the amount of formation matrix carbon. Thus the problem becomes one of deciding how much of the carbon comes from the wellbore and how much from the fluid-filled porosity. With a single spectral gamma ray detector it is not be possible to perform this discrimination, but with a second detector spaced farther from the neutron source there is a significant difference between the formation carbon response and the wellbore carbon response, which enables determining the relative proportions of wellbore and formation carbon. A similar argument follows for the oxygen measurement. Put simply, the near detector is more affected by the wellbore fluids and the far detector is more affected by the formation.

The four response equations are

$$C_n = X_1(1-\phi) + X_2\phi S_o + X_3 Y_o, \quad (10\text{-}1)$$

$$O_n = Y_1(1-\phi) + Y_2\phi(1-S_o) + Y_3(1-Y_o), \quad (10\text{-}2)$$

$$C_f = X_4(1-\phi) + X_5\phi S_o + X_6 Y_o, \quad (10\text{-}3)$$

$$O_f = Y_4(1-\phi) + Y_5\phi(1-S_o) + Y_6(1-Y_o), \quad (10\text{-}4)$$

where

C_n = carbon yield from the near detector
C_f = carbon yield from the far detector
O_n = oxygen yield from the near detector
O_f = oxygen yield from the far detector
ϕ = formation porosity
S_o = formation oil saturation
Y_o = wellbore oil holdup
X_n = carbon characterization coefficient
Y_n = oxygen characterization coefficient.

If the characterization coefficients are known from artificial formation measurements or Monte Carlo modeling and the porosity is known from previous openhole logging, then the wellbore holdup and formation saturation are the two unknowns. Only two equations are needed for two unknowns, but the extra two equations

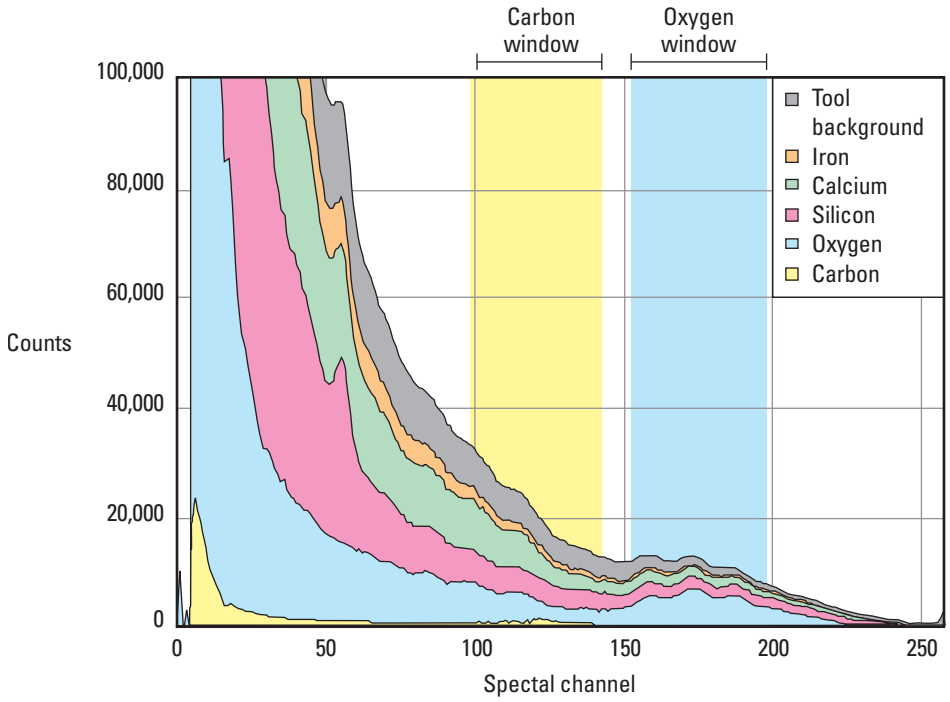

Figure 10-3. Composite spectra measured by the RSTPro tool.

(of Eqs. 10-1 through 10-4) are used to compensate for variations in both the neutron generator strength and crystal detector sensitivities by the use of the carbon to oxygen ratio from each detector. The resulting new equations are

$$\frac{C}{O_n} = \frac{X_1(1-\phi) + X_2\phi S_o + X_3 Y_o}{Y_1(1-\phi) + Y_2\phi(1-S_o) + Y_3(1-Y_o)}, \quad (10\text{-}5)$$

$$\frac{C}{O_f} = \frac{X_4(1-\phi) + X_5\phi S_o + X_6 Y_o}{Y_4(1-\phi) + Y_5\phi(1-S_o) + Y_6(1-Y_o)}. \quad (10\text{-}6)$$

The volume of gas that the tool sees is proportional to the ratio of the number of inelastic gamma rays seen on the near crystal detector to the number of inelastic gamma rays seen on the far detector. Unfortunately this provides just one equation and does not permit a solution for formation gas saturation and wellbore gas holdup. Therefore, the modeling requires a gas-free formation and uses the following equation:

$$Y_g = Z_1 \frac{N_{\text{near\_inelastic}}}{N_{\text{far\_inelastic}}}, \quad (10\text{-}7)$$

where

Y_g = wellbore gas holdup
Z_n = gas characterization coefficient
$N_{\text{near\_inelastic}}$ = number of inelastic gamma rays at the near detector
$N_{\text{far\_inelastic}}$ = number of inelastic gamma rays at the far detector.

Figure 10-4. Calibration blocks for nuclear logging tools.

Figure 10-5. Schlumberger Environmental Effects Calibration Facility in Houston, Texas, USA.

RSTPro TPHL three-phase holdup characterization

The TPHL characterization coefficients take into account the bit size, casing size, casing weight, formation lithology, and carbon concentration of the oil and gas. For normal RSTPro interpretations of formation saturation using carbon to oxygen ratios, the characterization coefficients are determined from a database of physical measurements made in artificial formations with different porosities, casing sizes, bit sizes, and casing weights and varying formation liquid saturations and wellbore liquid holdups (Figs. 10-4 and 10-5). However, the need to characterize gas under conditions equivalent to thousands of psi of downhole pressure requires a change to the methodology because experiments cannot be performed with large volumes of compressed and explosive natural gas.

The approach devised to characterize the RSTPro TPHL measurement is to build a Monte Carlo numerical simulator of high-energy pulsed neutron inelastic collisions and tune this simulator to match physical measurements of various water and oil formation saturations and various wellbore holdups of water, oil, and air (with the air at atmospheric pressure) (Roscoe, 1996). Once the Monte Carlo model is able to predict the physical measurements, the gas density in the model is increased and a set of virtual characterization coefficients computed. The resulting experimental space is in Table 10-1 (Hemingway et al., 1999).

At each point on the characterization database the characterization coefficients are calculated. If a log is made under characterized conditions it is a straightforward exercise to extract the coefficients that deliver saturations and holdups. However, in the more common situation where the log is made between points in the characterization database, a complicated multidimensional interpolation is made to derive the appropriate coefficients.

Errors in the computed TPHL saturations and holdups are difficult to assess in the absence of reference conditions. Processing of the synthetic RSTPro measurements

Table 10-1. TPHL Characterization Space (after Hemingway et al., 1999)

Hole Size, in	Casing Size, in	Casing Weight, lbm/ft	Limestone Formation Porosity†	Sandstone Formation Porosity†	Formation Fluid‡	Borehole Fluid‡
6	Open hole	na	Z, M, H	Z, M, H	W, O	W, O, A
	4.5	10.5	Z, M, H	Z, M, H	W, O	W, O, A
	5	11.5	Z, M, H	Z, M, H	W, O	W, O, A
8.5	Open hole	na	Z, M, H	M, H	W, O	W, O, A
	6.625	20	Z, M, H	M, H	W, O	W, O, A
	7	23	Z, M, H	M, H	W, O	W, O, A
10	Open hole	na	Z, M, H	Z, M, H	W, O	W, O, A
	7	23	Z, M, H	Z, M, H	W, O	W, O, A
	7.625	26.4	Z, M, H	Z, M, H	W, O	W, O, A
12	Open hole	na	Z, M, H	M, H	W, O	W, O, A
	7.625	26.4	Z, M, H	M, H	W, O	W, O, A
	9.265	32.3	Z, M, H	M, H	W, O	W, O, A

na = not applicable

†Porosity: Z = zero, 0 pu; M = medium, 15 to 19 pu; H = high, 33 to 35 pu

‡Fluid: W = freshwater, O = No. 2 diesel fuel, A = air

corresponding to the characterization database revealed an average error in the computed holdups of 5% to 6%, a number roughly the same as the errors delivered by the differential pressure Gradiomanometer tool and the water and gas holdup probes. Log measurements that require the use of interpolated coefficients probably have slightly worse errors; however, a skilled log analyst tries to tune the computed holdups using reference points such as water-filled sumps (Fig. 10-6) or gas- or oil-filled attics in shut-in horizontal wells (Fig. 10-7).

The data flow in the TPHL technique is shown in Fig. 10-8. It starts with an RSTPro recording of the inelastic spectrum, which is then broken down into an inelastic count rate ratio and a carbon to oxygen ratio on the near and far detectors. The inelastic count ratio goes into a simple gas holdup response model and the gas holdup is found. A special carbon-oxygen crossplot for the centered tool and correcting for the presence of wellbore gas are used to transform the carbon to oxygen ratio into water and oil holdups. Under favorable circumstances, a formation saturation can also be computed.

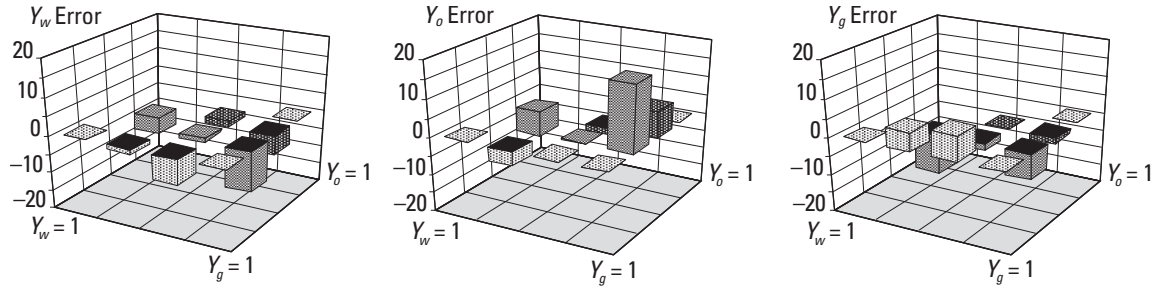

Figure 10-6. Self-consistency error checking for water-filled matrix (Roscoe, 1996).

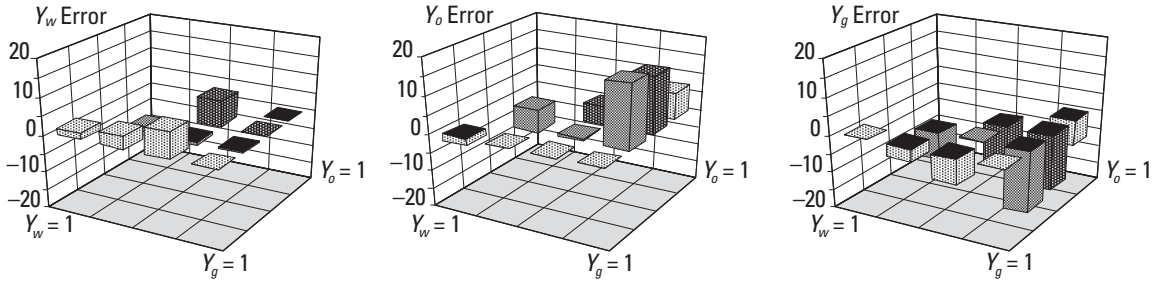

Figure 10-7. Self-consistency error checking for oil-filled matrix (Roscoe, 1996).

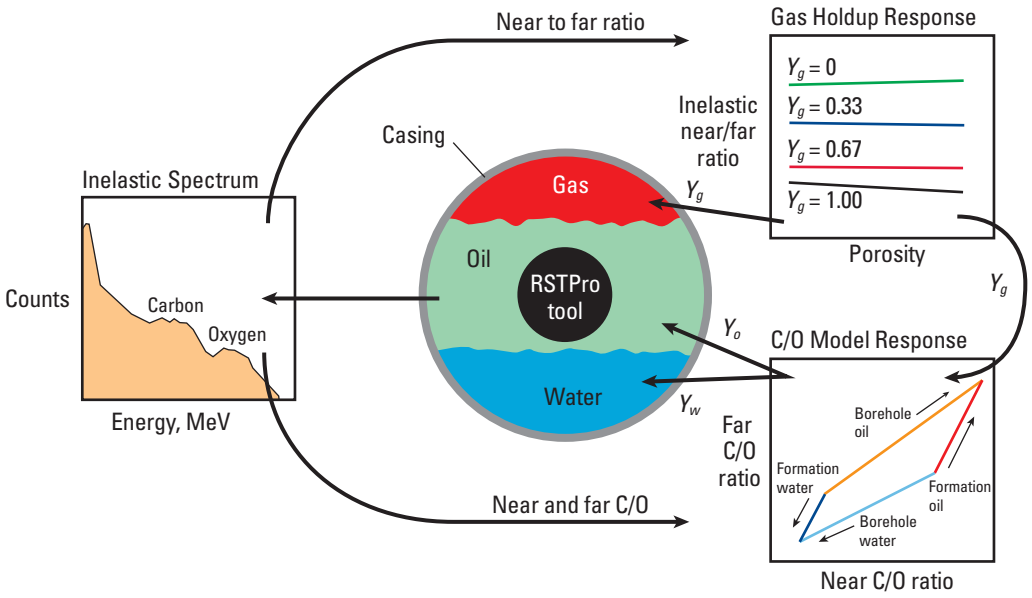

Figure 10-8. RSTPro TPHL data flow.

In 7-in completions and larger, most of the RSTPro signal comes from the wellbore with only a weak formation signal. Under these conditions, uncertainties in the formation parameters introduce only small errors in the computed holdups. Conversely, in 4½-in completions and smaller the formation response is much larger than that of the wellbore. In these conditions an accurate formation saturation answer is a prerequisite for getting a usable wellbore holdup.

Not included in the characterization database are slotted liners, wire-wrapped screens, heavy-wall casing, multiple tubulars, and many more common completions. The case of heavy-wall casings requires extrapolation outside of the database. Experience has shown that answers from a 7-in 30-lbm/ft liner (just outside the characterization space) look quite acceptable whereas answers from a 6⅝-in 66-lbm/ft liner are obviously wrong and can be corrected only by the empirical use of arbitrary gains and offsets to the input measurements. In a similar way, wire-wrapped screens also require the use of tuning factors that are adjusted until the computed holdups (and hence the computed surface rates) match the surface-measured flow rates. Caution should always be taken when proceeding outside of the characterization database and advice sought from an experienced RSTPro analyst.

RSTPro TPHL three-phase holdup logging speed

Although very slow logging speeds are needed for conventional RSTPro formation saturation analysis, the wellbore holdup signals are much stronger and in addition can be averaged over 10 to 20 ft [3 to 6 m] of borehole because conditions change very slowly in a typical horizontal well. The following equation can be used to compute the logging speed required to obtain a 10% uncertainty or precision in the computed water and oil holdup (owing to statistical noise). The gas holdup is much smoother.

$$v_{\text{logging}} = \left(0.25A_{\text{annular}}^{2} + 2.05A_{\text{annular}}\right)L_a, \qquad (10\text{-}8)$$

where

$$A_{\text{annular}} = \frac{\left(d_{\text{pipe}}^2 - d_{\text{tool}}^2\right)\pi}{4}, \qquad (10\text{-}9)$$

and

v_{logging} = logging speed, ft/h
A_{annular} = pipe-tool annular area, in^2
L_a = depth-smoothing interval, ft
d_{pipe} = completion ID, in
d_{tool} = tool OD, 1.6875 in.

For example, for a 6-in-ID liner with a 20-ft average interval along the measured depth, the suggested logging speed is 700 ft/h.

RSTPro TPHL three-phase holdup QC

Processing of the RSTPro TPHL data is today possible with GeoFrame*, Emeraude, or a standalone PC application. For quality control of the TPHL answers, the answer product contains the reconstructed curves corresponding to the holdup answer. In regions of 0% or 100% holdup of a given phase, these reconstructions should be checked to ensure that they match the measured curves. A poor match generally indicates that the interpretation should be rerun with revised settings. Particularly in horizontal wells, the TPHL answer should also be plotted versus TVD to verify that the answer is physically possible.

The example in Fig. 10-9 from a shut-in well shows a good reconstruction of the near carbon/oxygen ratio (NCOR), far carbon/oxygen ratio (FCOR), and near/far net inelastic count rate ratio (NICR) curves (after an offset was applied to the NICR and a small gain factor applied to the FCOR and NCOR) in which, somewhat surprisingly, a layer of oil appears to be sitting above a

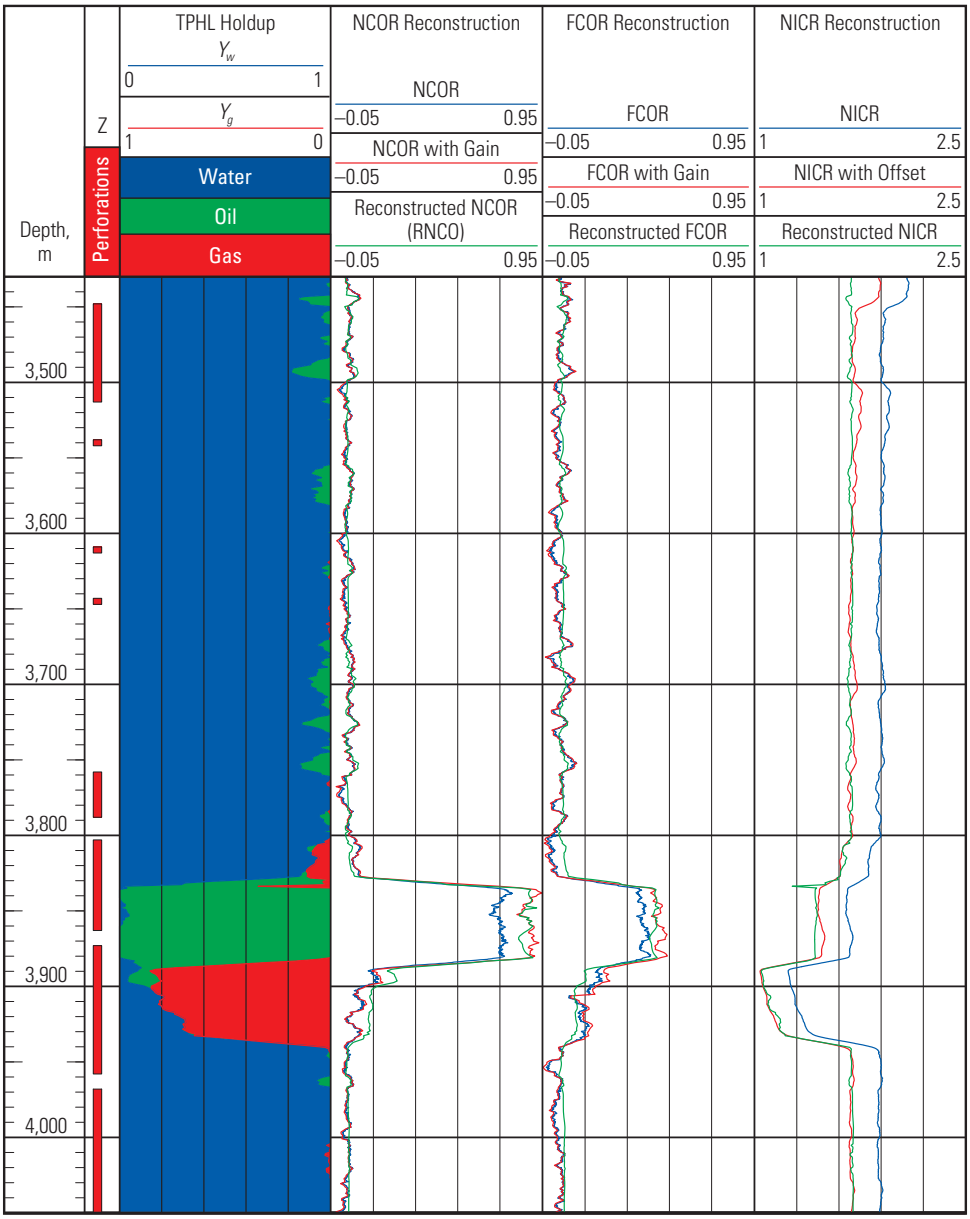

Figure 10-9. Processed TPHL log. Blue coding shows the raw filtered log curves, red shows the same data after applying a gain and offset, and green shows the reconstructed measurements based on the computed holdups. (Oseberg field, Norway, courtesy of Statoil ASA)

layer of gas. However, when the data is plotted versus TVD in Fig. 10-10, it becomes apparent that the oil and gas are present on a local downslope in a horizontal well. The fact that the gas is not centered on the local high point in the well path indicates that there is a small flow of water from right to left, which is pushing the gas and oil away from the local high point. The well logging also included Flow-Caliper Imaging Sonde (PFCS) and Digital Entry and Fluid Imaging Tool (DEFT) logs. The water holdup image is displayed alongside the TPHL track in Fig. 10-10 and shows the same results—oil and gas look the same to a water holdup probe.

Whenever possible, shut-in data with phase segregation should be used to tune the interpretation model to give the correct reconstruction in 100% and 0% of all phases present. The shut-in interpretation settings are then used to process the flowing TPHL data.

Running the RSTPro TPHL log

Although it is preferable and easier to eccenter a logging tool in a horizontal well, the 1.71-in RSTPro tool (RST-C) must always be centered to record usable data. A low-sided RSTPro tool in a 7-in liner is not only unable to see the high-side oil or gas but is also uncharacterized. The exception is for the uncharacterized data space of completions smaller than 4.5-in OD, where there is little to be gained from centering the tool.

Sidebar 10A. Centering and characterization

The RSTPro tool with asymmetric detectors and a tool diameter of 2½ in (RST-D) is unsuitable for TPHL logging not because the tool cannot be centered but because the tool is uncharacterized, which makes the data uninterpretable. The RST-D tool can be run in a horizontal oil-water well and processed to deliver a wellbore oil holdup; however, the accuracy is inferior to that of the RST-C TPHL log because the RST-D tool is not characterized for stratified oil-water holdup above the back-shielded near detector or for the presence of any wellbore gas.

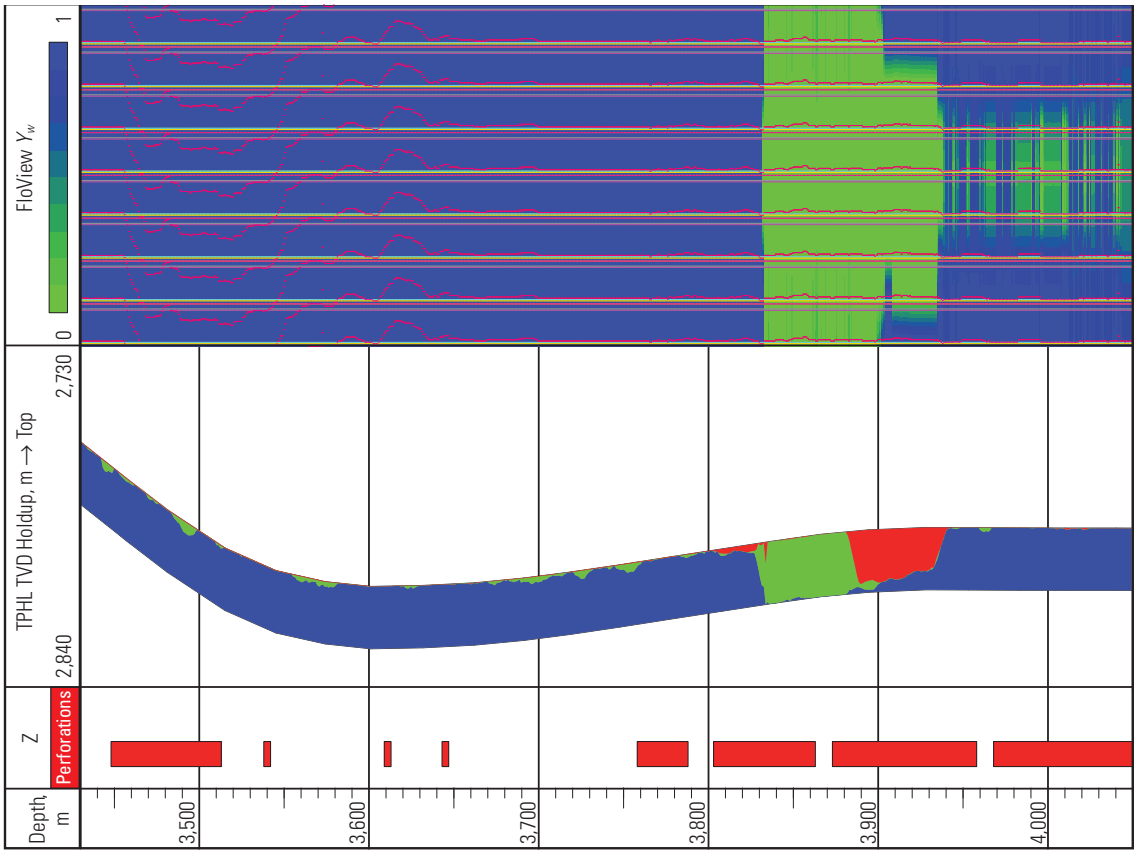

Figure 10-10. The same data set in Fig. 10-9 displayed against TVD. (Oseberg field, Norway, courtesy of Statoil ASA)

Applications (and misapplications) of the RSTPro TPHL log

Because the RSTPro TPHL measurement tends to be a long, slow, and relatively expensive tool to run, it is usually reserved for wells in which the Gradiomanometer measurement, FloView water holdup, and GHOST optical probes are unsuitable. For the Gradiomanometer tool this means wells that are horizontal or where the friction corrections are unmanageably large in high-velocity wells. For the FloView probes this means wells where bubble shear has left the bubbles too small to be seen, where the water is too fresh to be detected, or where excessive probe blinding occurs. For the FloView and GHOST probes this means wells with powerful jetting entries that can damage a probe or wells with asphaltene deposition where the probes are asphaltene coated and hence blinded. However, because asphaltene contains carbon, the presence of asphaltene on the RSTPro tool housing and the internal circumference of the completion introduces an offset to the measured carbon that requires careful correction.

Large uncemented annuli have the potential to confuse the TPHL interpretation. If the annulus is filled with water, then the oil is slightly undercomputed, whereas an oil-filled annulus can result in a significantly overcomputed oil holdup.

Perforate-stimulate-isolate (PSI) completions, with multiple packers and sliding side doors, have huge unrepresentative annulus holdups and are not suitable for TPHL logging.

Coal seams cannot be modeled, and computed holdups opposite coalbeds must be ignored.

References

Hemingway, J., Plasek, R., Grau, J., Das Gupta, R., and Morris, F.: "Introduction of Enhanced Carbon-Oxygen Logging for Multi-Well Reservoir Evaluation," *Transactions of the SPWLA 40th Annual Logging Symposium*, Oslo, Norway (May 30–June 3, 1999), paper O.

Roscoe, B.A.: "Three-Phase Holdup Determination in Horizontal Wells Using a Pulsed-Neutron Source," paper SPE 37147 presented at the SPE International Conference on Horizontal Well Technology, Calgary, Alberta, Canada (November 18–20, 1996).

11 Marker and Tracer Measurements of Velocity

Markers and tracers work by placing them in a phase of interest at time zero and measuring the time taken to reach a distant detector. By knowing the separation between the source and the detector, a velocity can be computed.

Radioactive tracers

The oldest marker or tracer technology used in the oil field is based on water-soluble radioactive iodine. With a half-life of just 8 days, radioactive iodine was available only in countries with a significant nuclear industry. Increasing concerns about safety mean that very few countries outside of North America still use this technique.

Figure 11-1 shows a typical radioactive tracer log run to verify the integrity of a well for water injection or disposal. The log is used to verify that the injected fluids do not contaminate shallower aquifers used for drinking water.

Sidebar 11A. Oilfield definitions

In oilfield terminology a marker is passive whereas a tracer is radioactive. Curiously, in medical terminology the opposite use is understood.

After the tracer is injected at the tubing shoe, a series of gamma ray logging passes are made up and down the well to track the passage of the "hot" slug. Opposite perforations that take injection, the gamma ray counts are seen to diminish. Gamma ray signals that diminish opposite unperforated pipe show an unintended injection path, whereas gamma ray signals that travel upward, against the flow, indicate channel flow behind the casing.

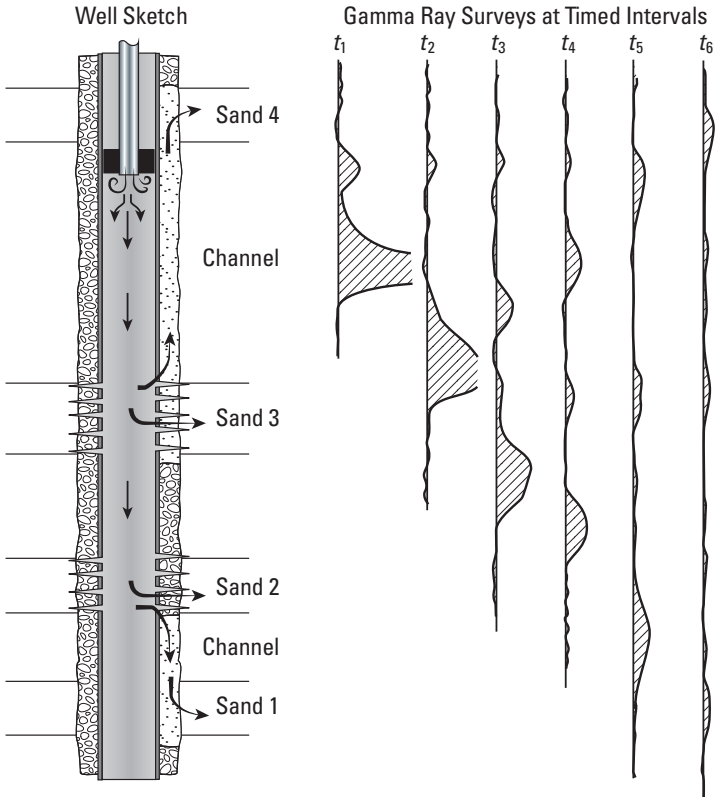

Figure 11-1. Radioactive tracer survey identifying injection zones and flow behind casing.

The requirement to make multiple passes means that the injection velocity must be much less than the logging tool velocity. A typical well logged in this way is injected at a few hundred barrels per day.

Attempts have been made to extend this technique with an oil-soluble tracer based on an emulsion of radioactive iodine. Although this approach can be made to work in the laboratory, the downhole temperature stability of the emulsion is doubtful and the tracer may only be water soluble at reservoir temperatures.

Dual-detector systems can also be used with radioactive tracers to determine tracer velocities and injection profiles. Because of tracer diffusion these systems usually require a downhole injection system.

Radioactive krypton gas is used in some steam injection wells to determine the velocity of the injected steam. Because of the shallow depths and high velocities associated with steam injection wells, tracer diffusion is not an issue and the krypton gas can be injected from the surface.

WFL water flow log physics

The WFL water flow log is another tracer technology that is still widely used. A pulse of neutrons is used to mark the oxygen in the vicinity of the neutron generator. The activated oxygen immediately starts to give off gamma rays. A static signal is created from all the fixed oxygen in the formation and cement while the moving oxygen in the water creates a gamma ray source that tracks the water velocity. Gamma ray detectors mounted downstream of the neutron source see a signal that rises and then falls as the marked oxygen approaches and then passes the detector (Fig. 11-2). Knowing the physical separation of the neutron source from the gamma ray detectors, it only remains to measure the transit time from the middle of the neutron burst to the peak of the detector signal to compute an oxygen, and hence a water, velocity. To improve the signal-to-noise ratio, multiple neutron bursts and their signals are recorded and stacked. Obviously this technique is applied as a station measurement.

The three-stage nuclear reaction initiated by the neutron burst is shown in the following three equations. Because it has a half-life of 7.1 s, this decay must be corrected for in order to locate the center of the activated oxygen slug.

$$^{16}O + n \rightarrow {}^{16}N + p, \qquad (11\text{-}1)$$

$$^{16}N \rightarrow {}^{16}O^{*} + \beta, \qquad (11\text{-}2)$$

$$^{16}O^{*} \rightarrow {}^{16}O + \gamma, \qquad (11\text{-}3)$$

where

^{16}O = normal oxygen present in water
n = high-energy neutron
^{16}N = unstable isotope of nitrogen with a half-life of 7.1 s
p = proton
$^{16}O^{*}$ = oxygen in an unstable excited state
β = beta particle (an electron)
γ = gamma ray.

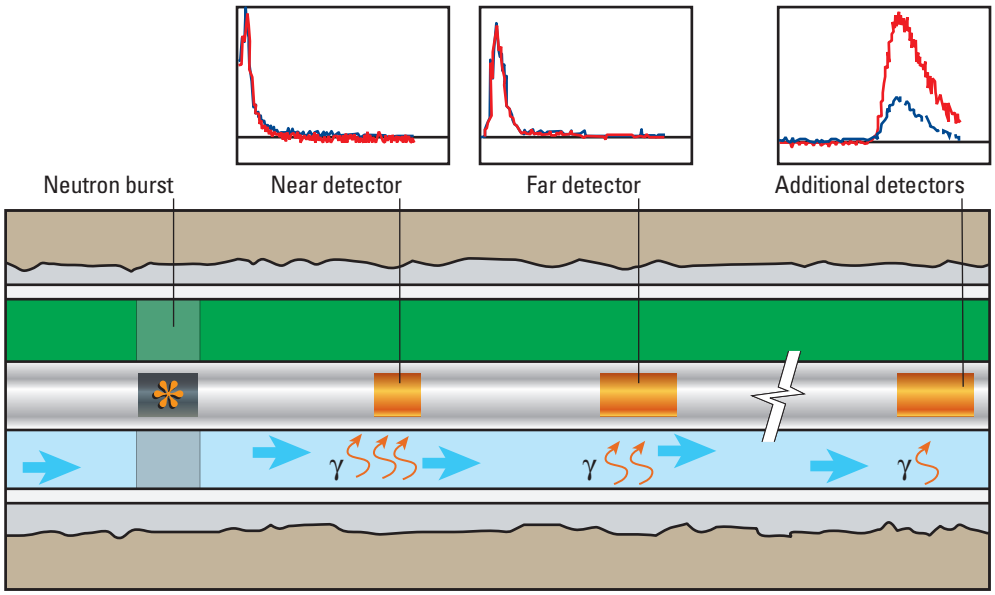

Figure 11-2. Principle of the stationary water flow log.

Activation of parts of the logging tool, casing, and formation by the neutron burst adds another decaying signal, called the "background CR" that has to be subtracted from the "measured CR," where CR is an abbreviation for count rate. The resulting signal is called the "net CR" (these labels are explained in the next section, "Understanding the RSTPro WFL water flow log stations"). When the gamma ray detector of the Platform Basic Measurement Sonde (PBMS) of the PS Platform production services platform is used to make measurements, there is no significant activation and the background count rates become a flat curve created by gamma rays from the formation and any radioactive scale.

For source-to-detector transit times of less than a second or two, the 7.1-s half-life decay does not have much effect. But for a transit time of >10 s, the half-life decay could be confused with the falling signal of the departing oxygen activation slug. Therefore a decay correction is added that has the effect of boosting the background subtracted signal by a factor of 2 every 7.1 s. This is the "decay-corrected net CR" signal.

RST WFL Station Summary

Log File Number	WFL Detector	Start Depth, m	Stop Depth, m	Flow Detected	Velocity, m/min	Velocity Error, m/min
NNN	RST-Far	XXXX	YYYY	Yes	20.2	1.4

Data acquired on: dd-mm-yyyy hh:mm
Detector is above Minitron (sensitive to Up Flow)
WFT Subcycle Time: 0.80 sec On - 52.27 sec Off
Number of WFL Cycles: 15

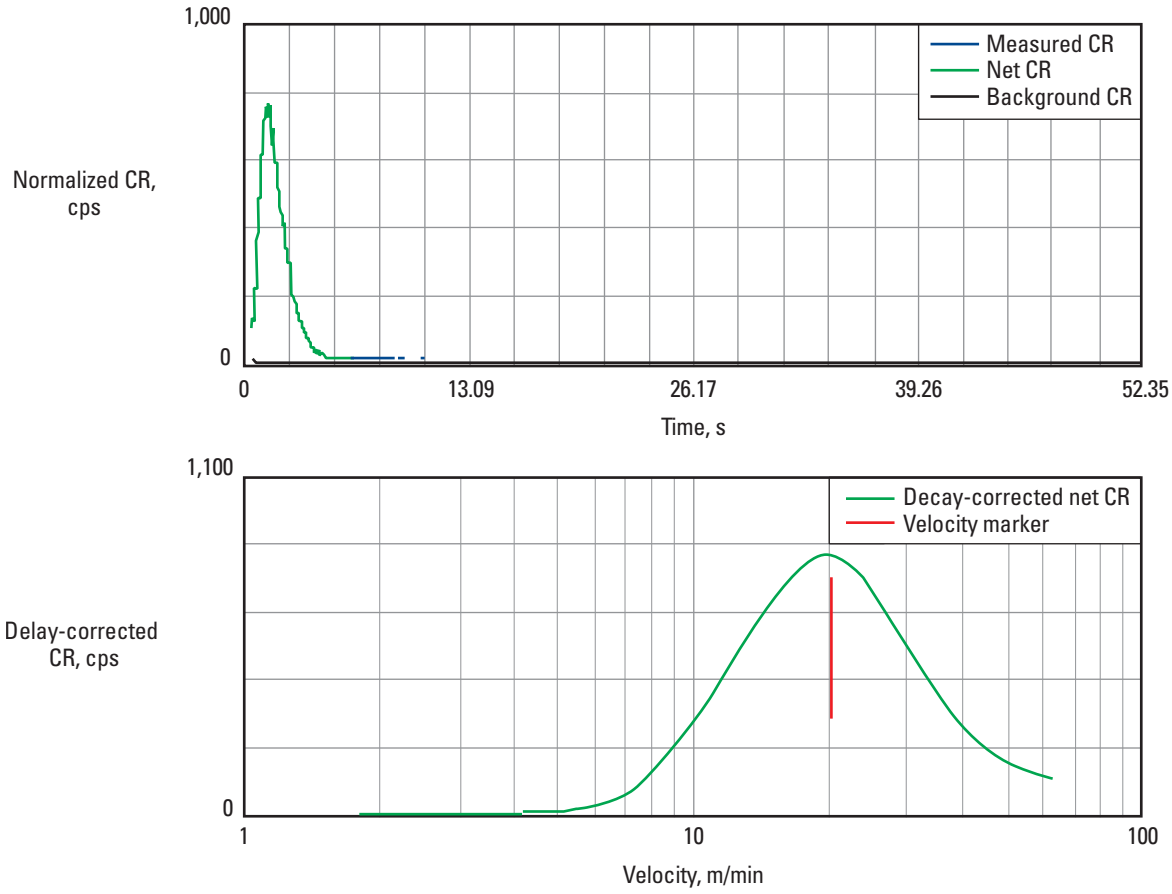

Figure 11-3. Standard WFL station display.

Understanding the RSTPro WFL water flow log stations

For some years Schlumberger has used the layout in Fig. 11-3 to display WFL stations. The explanation that follows explains some of the slightly obscure labels.

- WFL detector—gamma ray detector used for computing the velocity, with typical values of RST-Far, RST-Near, and PBMS-GR and occasionally other more obscure detectors
- Start depth—depth of the neutron generator
- Stop depth—depth of the gamma ray detector
- Flow detected—attempt by a very basic (and often mistaken) algorithm to distinguish between the presence of moving water and no-flow conditions
- Velocity—value to be used in the interpretation. The bottom plot shows the activation peak with all the corrections applied using a velocity for the x-axis. If the peak search algorithm pick looks wrong, a better peak can be chosen and the appropriate velocity read off. It must be remembered that this is an annulus velocity accelerated by the presence of the flow-diverting $1^{11}/_{16}$-in-diameter tool.
- Velocity error—the difference resulting from statistical noise between the current reported velocity and the velocity that would be computed after an infinite number of cycles. The true velocity error is typically much larger and indeterminate.
- WFL subcycle time—time that the neutrons were turned on followed by the neutron "off-time." Doubling the neutron "on-time" doubles the number of received gamma rays and improves the nuclear statistics. However, too long of an on-time results in the neutron burst running into the WFL velocity peak and the measurement being lost. Too long of an off-time after the WFL peak has occurred makes the WFL station unnecessarily long. The station in Fig. 11-3 could have the off-time reduced by 90% and still record a good WFL station.
- Number of WFL cycles—number of neutron bursts averaged to compute the answer displayed.

The time for the WFL station measurement is

$$t_{\text{station}} = N_{\text{WFL\_cycles}} \times \left(t_{\text{neutron\_on-time}} + t_{\text{neutron\_off-time}}\right), \quad (11\text{-}4)$$

where

t_{station} = WFL station time
$N_{\text{WFL\_cycles}}$ = number of WFL cycles
$t_{\text{neutron\_on-time}}$ = neutron on-time
$t_{\text{neutron\_off-time}}$ = neutron off-time.

Log quality control of WFL stations

The following is a nonexhaustive list of defects that can be encountered in WFL results.

- Wrong pick—Figure 11-4 shows a decay-corrected net count rate with the discrete sample times visible. The velocity marker at 75.2 m/min is too fast. A log analyst would be advised to use a velocity of 70 m/min.

RST WFL Station Summary

Log File Number	WFL Detector	Start Depth, m	Stop Depth, m	Flow Detected	Velocity, m/min	Velocity Error, m/min
NNN	RST-Far	XXXX	YYYY	Yes	75.2	2.7

Data acquired on: dd-mm-yyyy hh:mm
Detector is above Minitron (sensitive to Up Flow)
WFT Subcycle Time: 0.13 sec On - 1.07 sec Off
Number of WFL Cycles: 225

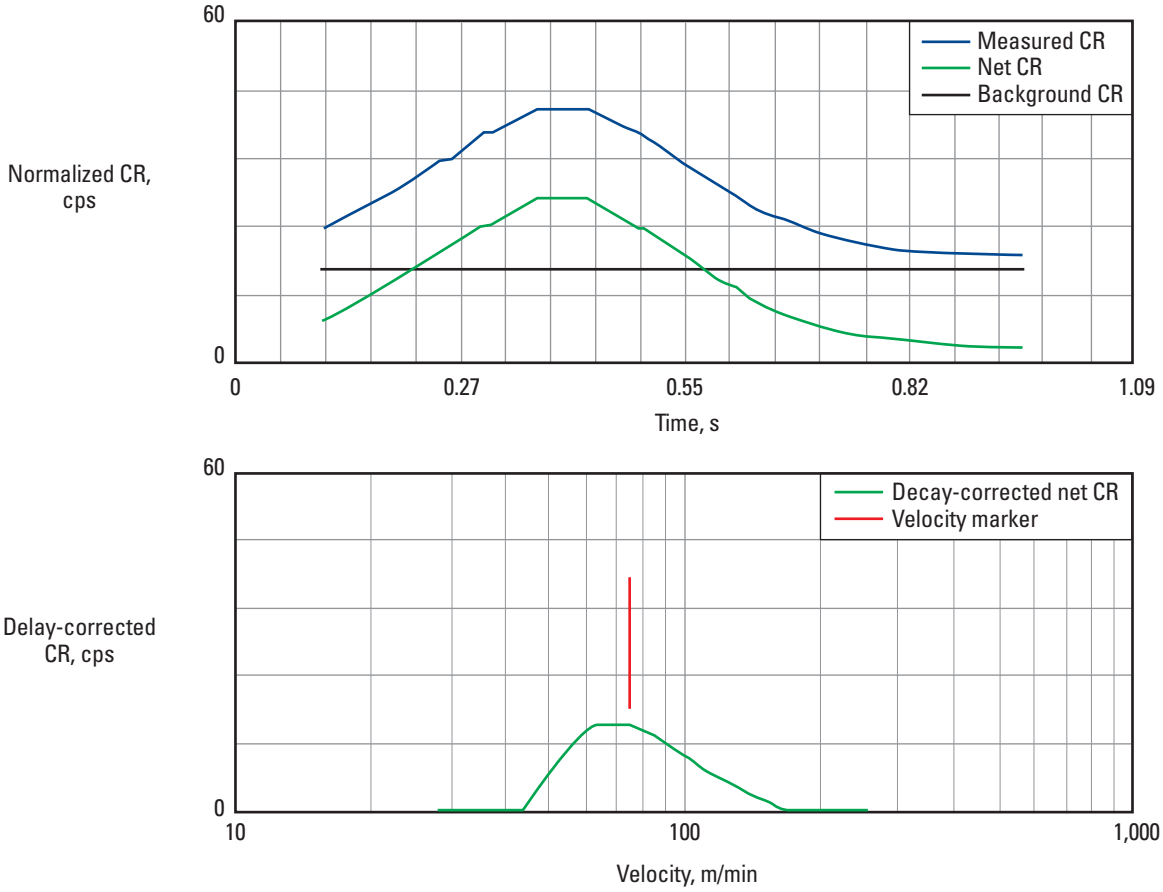

Figure 11-4. Wrong pick of WFL velocity.

- Zero flow—This condition is not strictly a defect but a plot characteristic of zero water flow. Because the measured count rate exactly matches the modeled background count rate, the net count rate comes to zero (Fig. 11-5). Whenever possible, zero-flow measurements should be confirmed with temperature log evaluation.

RST WFL Station Summary

Log File Number	WFL Detector	Start Depth, m	Stop Depth, m	Flow Detected	Velocity, m/min	Velocity Error, m/min
NNN	RST-Near	XXXX	YYYY	No	–	–

Data acquired on: dd-mm-yyyy hh:mm
Detector is above Minitron (sensitive to Up Flow)
WFT Subcycle Time: 0.80 sec On - 52.27 sec Off
Number of WFL Cycles: 11

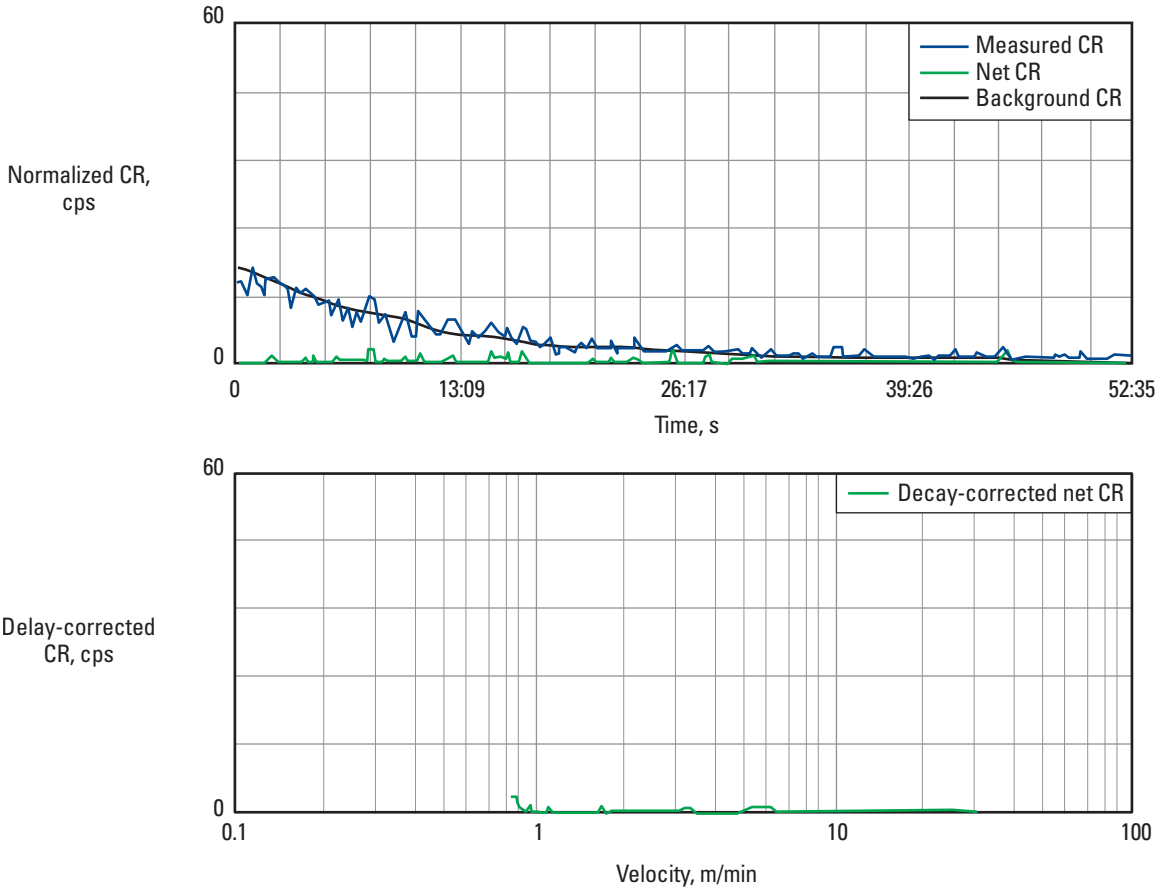

Figure 11-5. Zero-flow station.

- Neutron burst too long—In the example shown in Fig. 11-6, the neutron burst lasted for 10 s, which is 5 s before time zero and 5 s after time zero. The activation peak is somewhere in the vicinity of 10 to 12 s after time zero.

  A real velocity peak was detected, but the safety margin between the neutron burst and activation peak is smaller than what is comfortable. A neutron burst length of 5 s would be better. As in the wrong pick example in Fig. 11-4, the peak detection algorithm is off and a smaller velocity would be better (or would using the longer spaced far detector).

RST WFL Station Summary

Log File Number	WFL Detector	Start Depth, m	Stop Depth, m	Flow Detected	Velocity, m/min	Velocity Error, m/min
NNN	RST-Near	XXXX	YYYY	Yes	1.2	0.0

Data acquired on: dd-mm-yyyy hh:mm
Detector is above Minitron (sensitive to Up Flow)
WFT Subcycle Time: 10.00 sec On - 90.67 sec Off
Number of WFL Cycles: 5

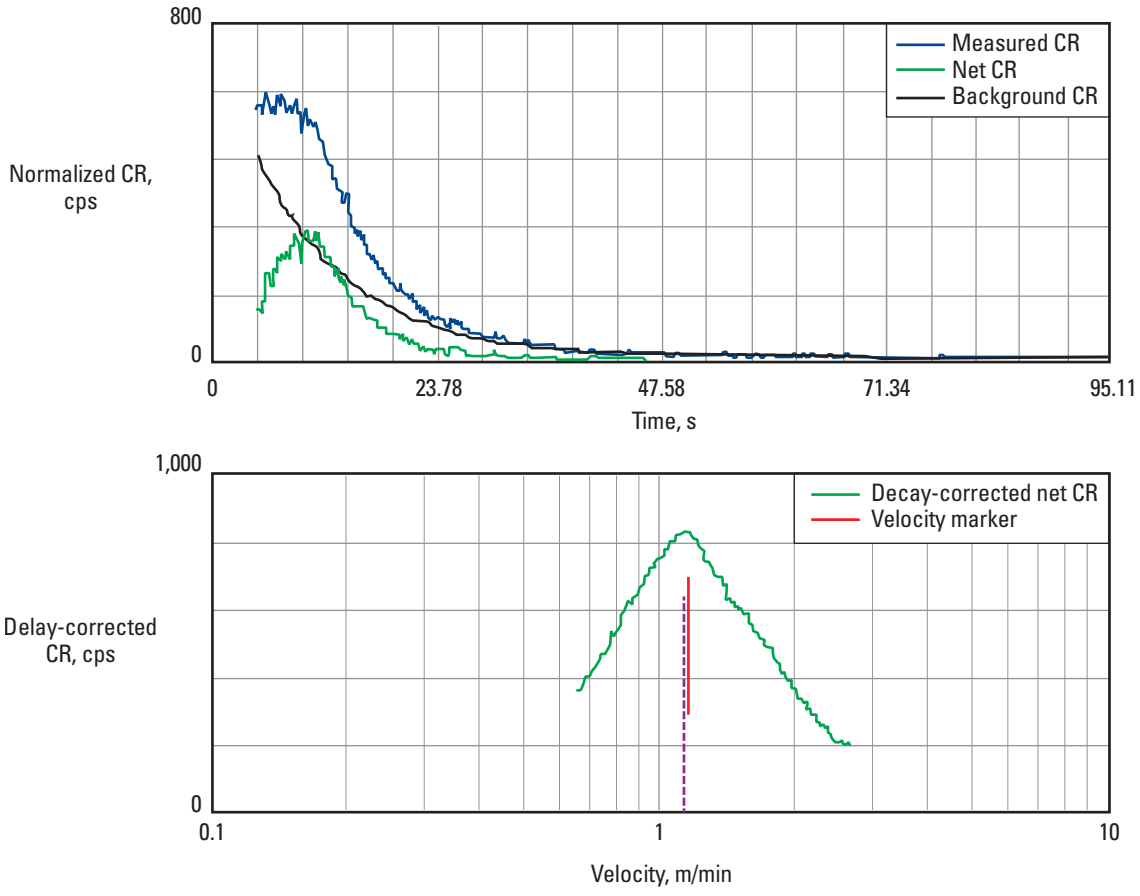

Figure 11-6. Neutron burst too long.

- Low signal-to-noise ratio—In the example in Fig. 11-7 the neutron burst was too short and the neutron off-time was too long. A peak was detected at 83.6 m/min but a velocity of 90 m/min looks like a better match to the center of the total activation slug. It is possible that the velocity came from random noise and therefore should be checked against another velocity measurement such as the spinner. A spinner velocity in the range of 80 to 100 m/min would be reassuring:

$$v_{spinner} = v_{WFL} \pm v_{difference}, \quad (11\text{-}5)$$

where

$v_{spinner}$ = spinner velocity
v_{WFL} = reported WFL velocity
$v_{difference}$ = velocity difference of 10 m/min.

The arbitrary 10-m/min velocity difference takes into account the slip velocity between the water and hydrocarbons and the velocity averaging of the spinner. When comparing spinner and WFL measurements, it is important to remember the spinner measures the total flow area velocity and the average of the oil and water velocities whereas the WFL tool measures the annular water velocity between the tool and the tubular.

RST WFL Station Summary

Log File Number	WFL Detector	Start Depth, m	Stop Depth, m	Flow Detected	Velocity, m/min	Velocity Error, m/min
NNN	PBMS-GR	XXXX	YYYY	Unknown	83.6	8.4

Data acquired on: dd-mm-yyyy hh:mm
Detector is above Minitron (sensitive to Up Flow)
WFT Subcycle Time: 0.07 sec On - 29.87 sec Off
Number of WFL Cycles: 31

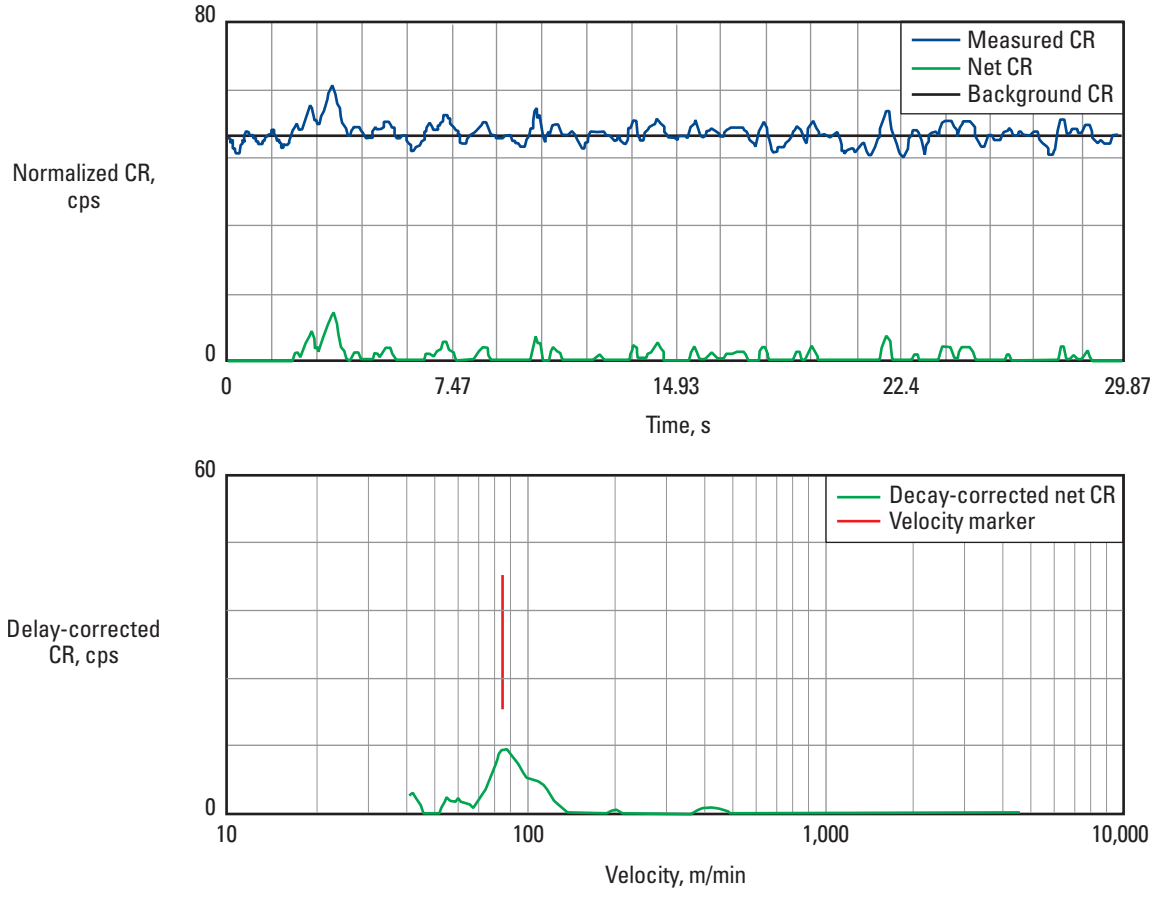

Figure 11-7. Low signal-to-noise ratio.

- Poor timing settings—Figure 11-8 does not contain any usable data. The neutron on-time was too long and overlapped the activation peak. In addition, the neutron off-time was too long, thus wasting time, and just two cycles of the neutron burst was insufficient to deliver the required signal-to-noise ratio.

In this example, the logging engineer realized that the settings were inappropriate and cancelled the station early.

RST WFL Station Summary

Log File Number	WFL Detector	Start Depth, m	Stop Depth, m	Flow Detected	Velocity, m/min	Velocity Error, m/min
NNN	PBMS-GR	XXXX	YYYY	Unknown	76.0	10.9

Data acquired on: dd-mm-yyyy hh:mm
Detector is above Minitron (sensitive to Up Flow)
WFT Subcycle Time: 10.00 sec On - 90.67 sec Off
Number of WFL Cycles: 2

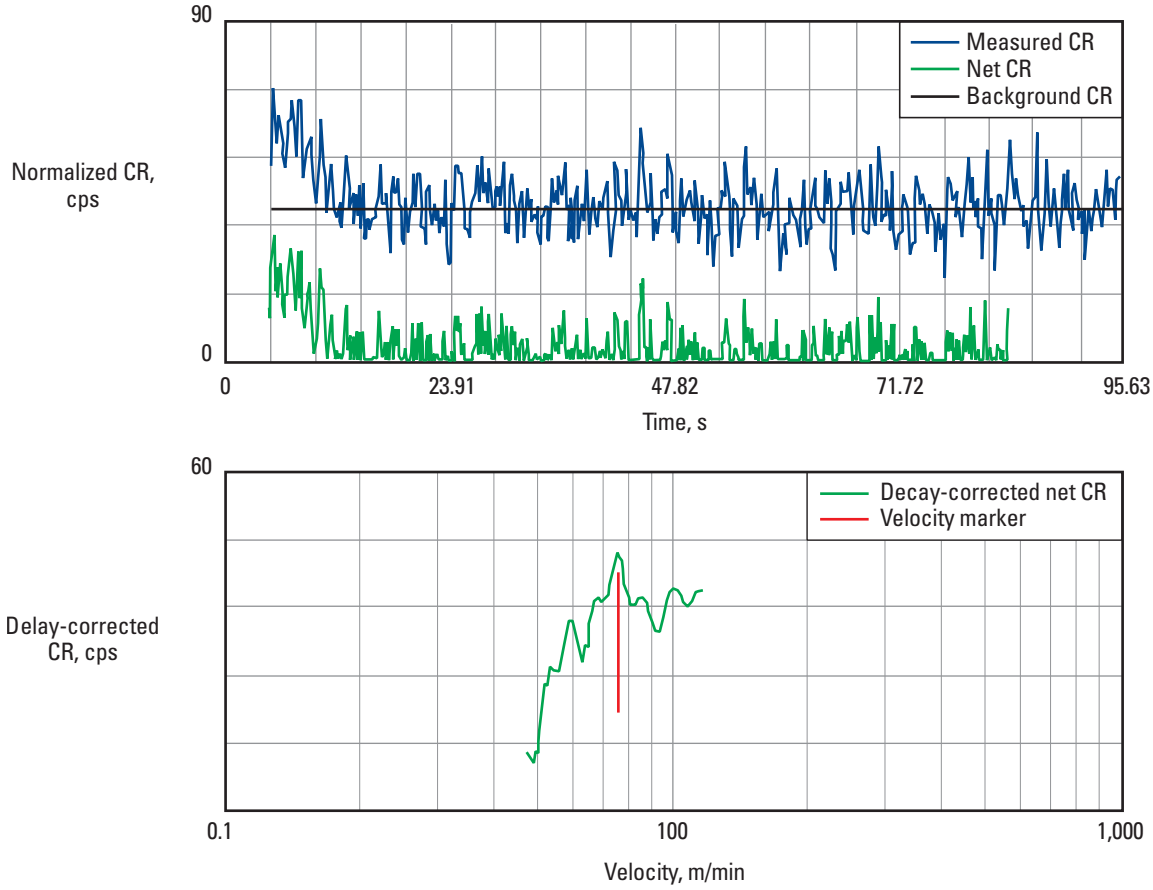

Figure 11-8. Poor timing settings, first example.

In the second example of poor timing setting in Fig. 11-9, the neutron burst should have been longer, say 2 s, with a shorter off-time of 20 s. In addition, more WFL cycles are needed to improve the poor statistics. The poor statistics seen may also be an indication of either a small borehole or a small water holdup.

RST WFL Station Summary

Log File Number	WFL Detector	Start Depth, m	Stop Depth, m	Flow Detected	Velocity, m/min	Velocity Error, m/min
NNN	RST-Far	XXXX	YYYY	Yes	4.4	3.6

Data acquired on: dd-mm-yyyy hh:mm
Detector is above Minitron (sensitive to Up Flow)
WFT Subcycle Time: 0.80 sec On - 52.27 sec Off
Number of WFL Cycles: 16

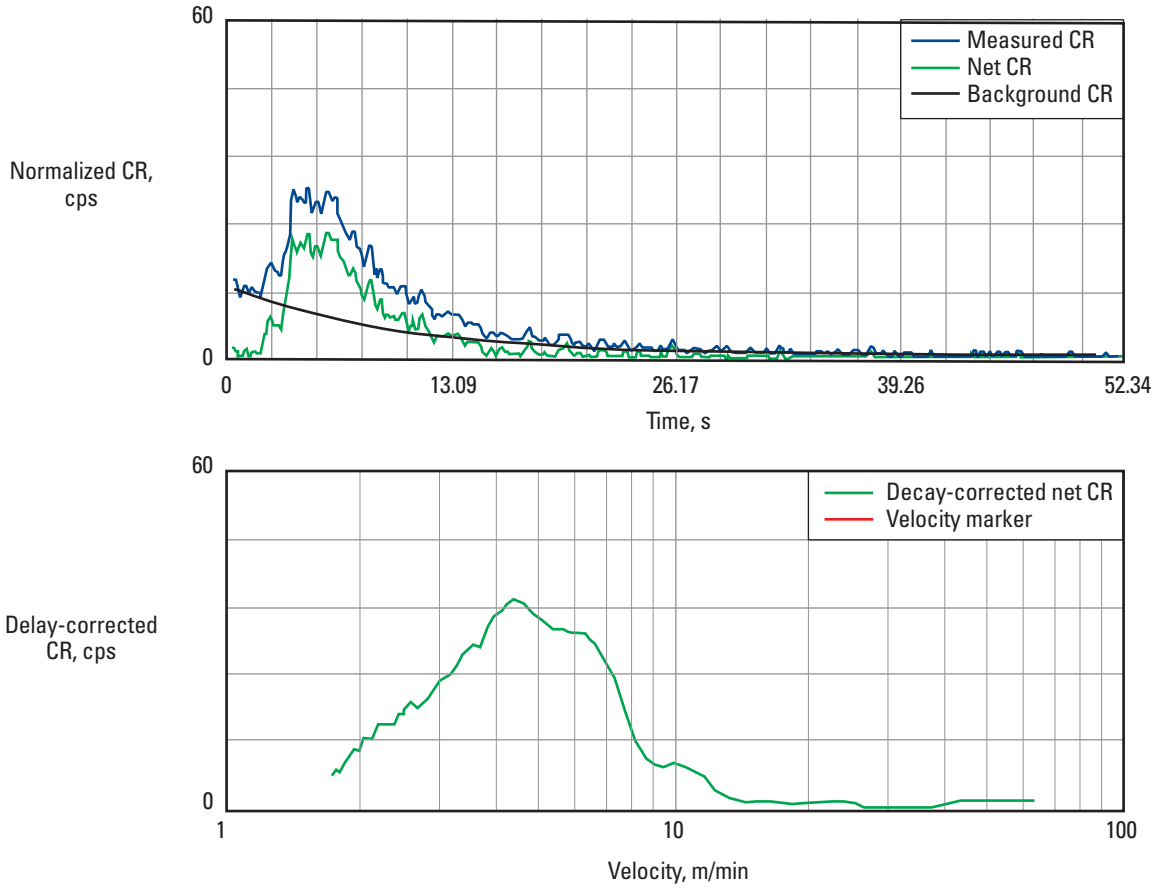

Figure 11-9. Poor timing settings, second example.

- Recirculation—The large range of velocities in Fig. 11-10 usually points to recirculation where water is being lifted with only partial success by fast-moving oil or gas before falling back down the wellbore. Because the water flow measurement with a single detector can only detect water moving in one direction, the missing downflow of recirculation leads to unfeasibly large upward velocities with a larger number of velocities present.

RST WFL Station Summary

Log File Number	WFL Detector	Start Depth, m	Stop Depth, m	Flow Detected	Velocity, m/min	Velocity Error, m/min
NNN	RST-Near	XXXX	YYYY	Yes	8.3	0.9

Data acquired on: dd-mm-yyyy hh:mm
Detector is above Minitron (sensitive to Up Flow)
WFT Subcycle Time: 0.47 sec On - 29.87 sec Off
Number of WFL Cycles: 21

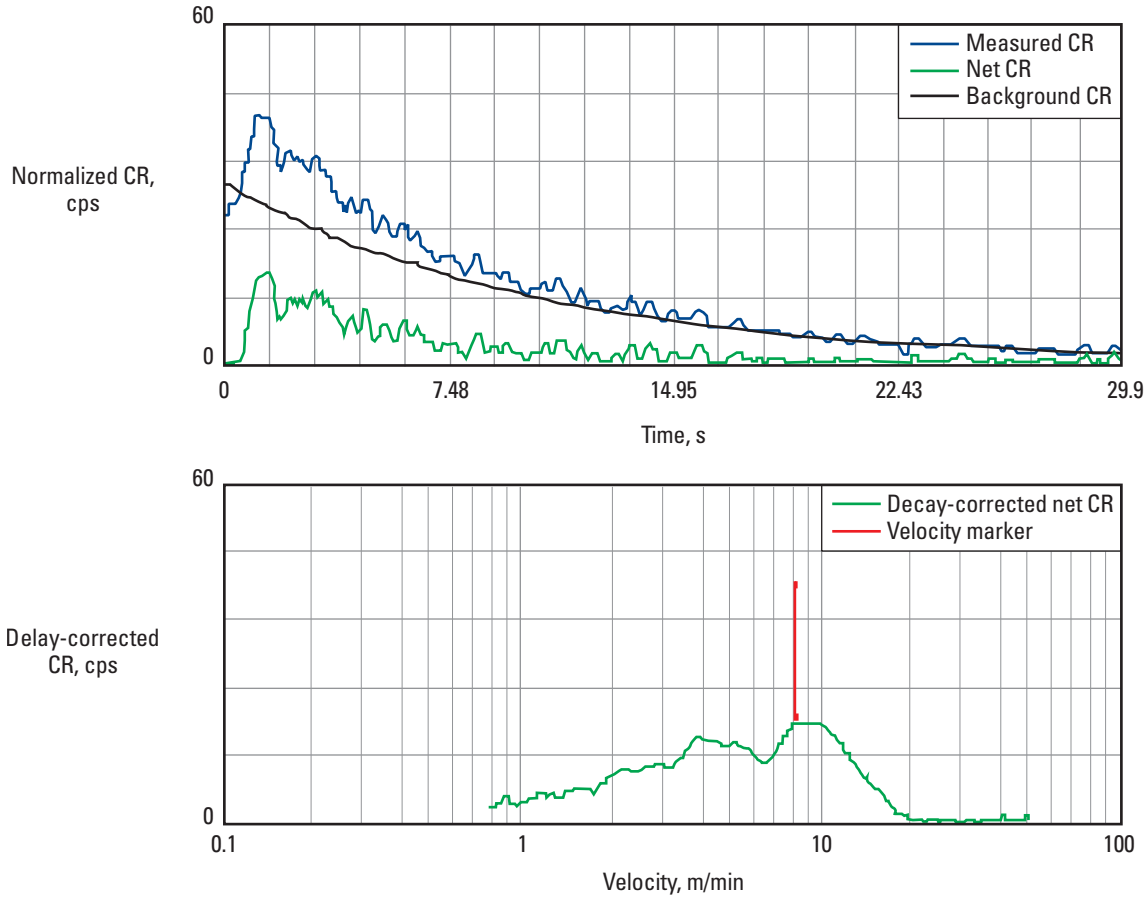

Figure 11-10. Semistagnant water with local uplift of water by rapidly flowing oil.

- Phantom water velocity—Figure 11-11 shows a very slow water velocity with perhaps a wider band of velocities than normally occurs. Other measurements have confirmed that there is no water flowing at this depth. The signal observed is actually a localized convection current triggered by heat-dissipating electronics inside the RSTPro tool. Velocities in the order of 1 to 2 ft/min are found inside 4- to 5½-in tubulars whereas in 12-in holes convection currents are larger, at about 3 to 4 ft/min. Identifying convection currents is very much a judgment call.

Regions of applicability

The far detector on the RSTPro reservoir saturation tool is used in preference to the near detector for all but the slowest (less than 10 ft/min [3 m/min]) WFL measurements. In high-speed wells the sampling rate on the far detector loses precision above approximately 300 to 350 ft/min [91 to 107 m/min]. Although flow can be detected up to 500 ft/min [152 m/min] with the far detector, accurate WFL measurements require the use of a longer spacing gamma ray detector such as that in the PBMS of the PS Platform production services platform.

RST WFL Station Summary

Log File Number	WFL Detector	Start Depth, ft	Stop Depth, ft	Flow Detected	Velocity, m/min	Velocity Error, m/min
NNN	RST-Near	XXXX	YYYY	Yes	1.4	0.6

Data acquired on: dd-mm-yyyy hh:mm
Detector is above Minitron (sensitive to Up Flow)
WFT Subcycle Time: 10.00 sec On - 59.73 sec Off
Number of WFL Cycles: 8

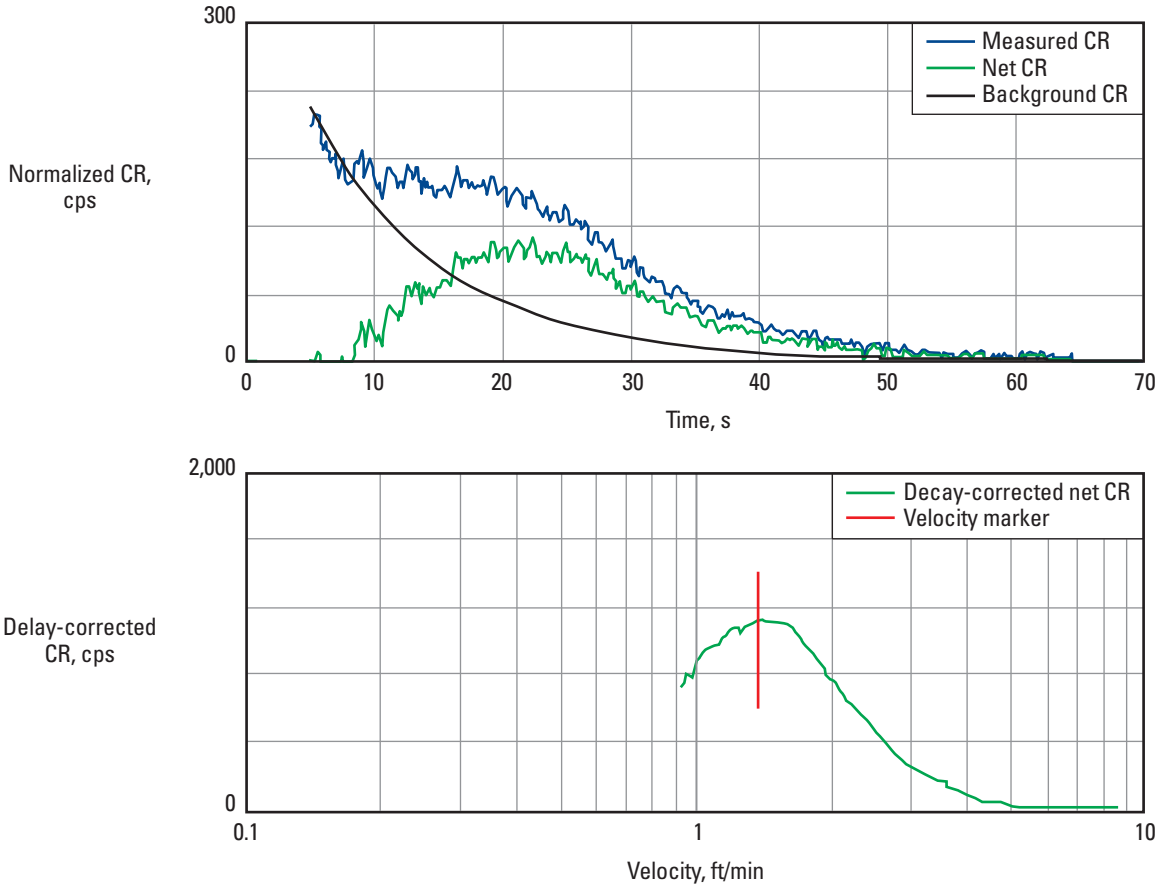

Figure 11-11. Phantom water velocity.

The WFL water flow log can be used to measure flow behind casing or tubing as long as there is no masking flow inside the casing or tubing. However, the neutron flux found in a channel is much smaller than the neutron flux inside the borehole. In addition, as the gamma ray detector-to-channel spacing increases, the probability of a randomly emitted gamma ray finding the detector decreases with the square of the spacing. In the case of a low-side RSTPro tool positioned above a water-filled low-side 7-in casing-channel leak, a usable water flow signal is still expected, but if the RSTPro tool is centered inside the same casing, then the WFL signal is at least an order of magnitude smaller.

Flow behind multiple tubulars is theoretically possible, but the signal is so small that a WFL station may take an hour or more before a statistically valid signal can be seen.

Recirculation confuses the WFL measurement because half of the bidirectional water flow is ignored by the RSTPro measurements (Fig. 11-12). Flow loop experiments show that errors become unmanageable below about 80 ft/min [24 m/min] in 5½- to 7-in casings. A rule of thumb from multiphase fluid mechanics says that for a marker or tracer technique to record the average phase velocity, the source-to-detector spacing should cover >15 pipe diameters. In a 7-in casing the far detector on the RSTPro tool is of the order of 3 pipe diameters away from the neutron source and is therefore subject to recirculation effects. If measurement of a 10-ft/min water velocity is attempted with a detector at 15 pipe diameters, then the signal peak is calculated to occur after

$$t_{peak} = 15 \times \frac{l}{v} = 15 \times \frac{\frac{6.264 \text{ in}}{12 \text{ in}}}{10 \text{ ft/min}} = 0.783 \text{ min} = 47 \text{ s}, \quad (11\text{-}6)$$

where

t_{peak} = time of signal peak
l = pipe internal diameter
v = water velocity.

This is equal to 47/7.1 or approximately 6 half-lifes, meaning that only 1.5% of the original signal remains by the time the activation peak has reached the detector. Determining the location of the activation peak thus requires a very long station.

In summary, in regions of recirculation, where the conventional spinner is struggling to return a usable velocity, there is no benefit in switching to the RSTPro WFL water flow log.

The main application for the WFL water flow log is in horizontal wells with stratified flow. Where the centered spinner is confused by the high stratified slip velocities, the WFL measurement provides a reliable velocity input to the production log interpretation.

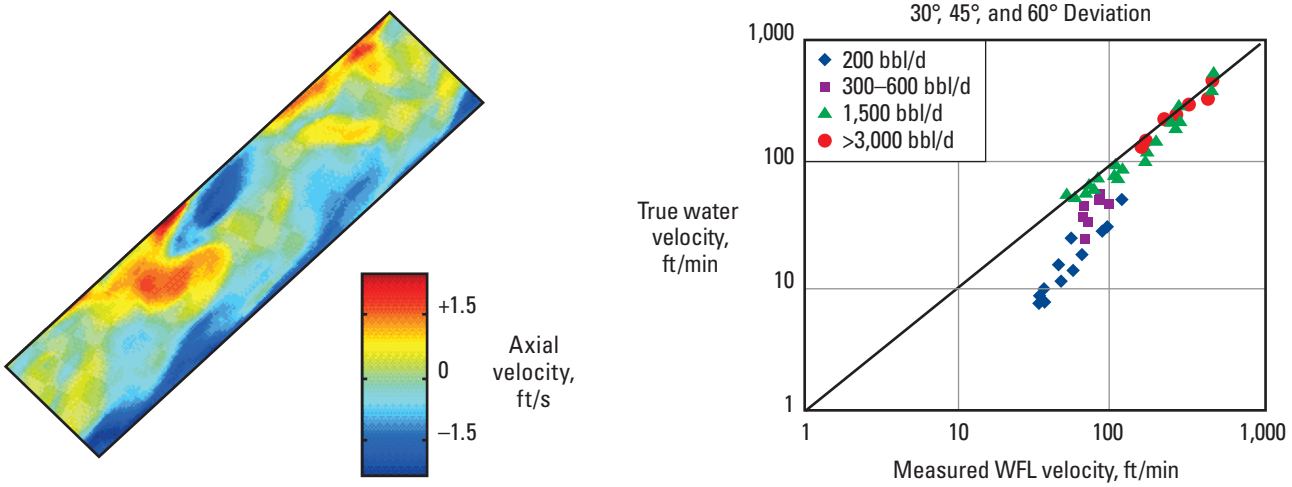

Figure 11-12. Recirculation effect on WFL velocity measurement.

Planning WFL station timing sequences

Table 11-1 can be used at the wellsite for choosing appropriate settings for acquiring a WFL station. Slow, normal, and fast are fixed timing sequences used by the logging computer; a custom sequence allows user-defined pulse timings.

Assuming a Flow-Caliper Imaging Sonde (PFCS) 2½-in spinner is a part of the toolstring and that the spinner velocity is dominated by the water velocity, the table enables converting a spinner rps value back to a timing sequence and a detector. For example, a stationary spinner speed of 2.5 rps is probably too fast for the normal timing sequence. Both the fast and custom timing sequences would work, but the custom sequence would deliver the answer faster because the range of the minimum to maximum rps more closely brackets the spinner reading.

Logging times using a given detector are inversely proportional to the neutron on-time percentage value. More neutrons are better!

PVL phase velocity log

The PVL* phase velocity log was created for PL Flagship* advanced well flow diagnosis service, which was a horizontal production logging service of the mid-1990s. It has been replaced worldwide by the minispinners of the Flow Scanner production logging tool and is included here only for historical completeness (see the "Flow Scanner Interpretation" chapter).

The PVL phase velocity log makes use of a marker technique to track the velocity of the fluids. The marker used is nonradioactive (gadolinium) and can be mixed in oil or water. The method requires a marker ejection tool

Table 11-1. RSTPro Wellsite Timing Sequences

WFL Timing Sequence	Pulse Timing, s		Neutron On-Time, %	Velocity Range						PFCS 2½-in Spinner	
				RSTPro Near Detector		RSTPro Far Detector		PBMS Detector†			
	On	Off		Min., ft/min [m/min]	Max., ft/min [m/min]	Min., ft/min [m/min]	Max., ft/min [m/min]	Min., ft/min [m/min]	Max., ft/min [m/min]	Min., rps	Max., rps
Slow	10	90.67	9.9	1 [0.3]	2 [0.5]	1 [0.4]	3 [0.9]	14 [4]	30 [9]	–‡	–‡
Normal	0.8	52.27	1.5	1 [0.4]	23 [7]	2 [0.7]	35 [11]	24 [7]	373 [114]	–‡	2
Fast	0.07	29.87	0.2	3 [0.8]	257 [78]	4 [1.2]	400 [122]	43 [13]	4,257 [1,298]	–‡	23
Custom§	0.2	10	2.0	8 [2]	90 [27]	12 [3.7]	140 [43]	128 [39]	1,490 [454]	–‡	8

† Assumed that the PBMS is mounted directly above an RSTPro tool containing no inline centralizers

‡ Below the spinner threshold velocity

§ Suggested custom timing settings for high-water-velocity detection with the PBMS gamma ray detector

(originally a modified Tracer Ejector Tool [TET], then the Phase Velocity Sonde [PVS], and finally the General-Purpose Marker Ejector Tool [GMET]) and a pulsed neutron sigma tool, the RSTPro reservoir saturation tool. The schematic in Fig. 11-13 shows the arrangement of the complete toolstring in the well. The tool can be either centered or eccentered.

With the tool stationary in the well, an amount of the marker is released from the ejection port. The marker is transported by the moving fluid up to the sensing volume around the RSTPro pulsed neutron source and near detector. The gadolinium marker has a very high neutron capture cross-section and causes a perturbation in the wellbore sigma, as shown in the top part of Fig. 11-13. The phase velocity is computed from the transit time (t) and the separation (l) of the ejection port to the sensing volume of the RSTPro tool. Depending on the choice of marker ejected, either a water or an oil velocity is recorded.

Other marker techniques

In the water industry use is made of fluorescent dyes that are detected with an ultraviolet light source. Underground cave systems and distances of kilometers can be connected using this technique.

Soluble ferromagnetic dyes for detection by a sensitive casing collar locator have been considered and dismissed.

Labeling the flow with a temporary burst of heat and looking for a temperature anomaly downstream has also been considered and dropped.

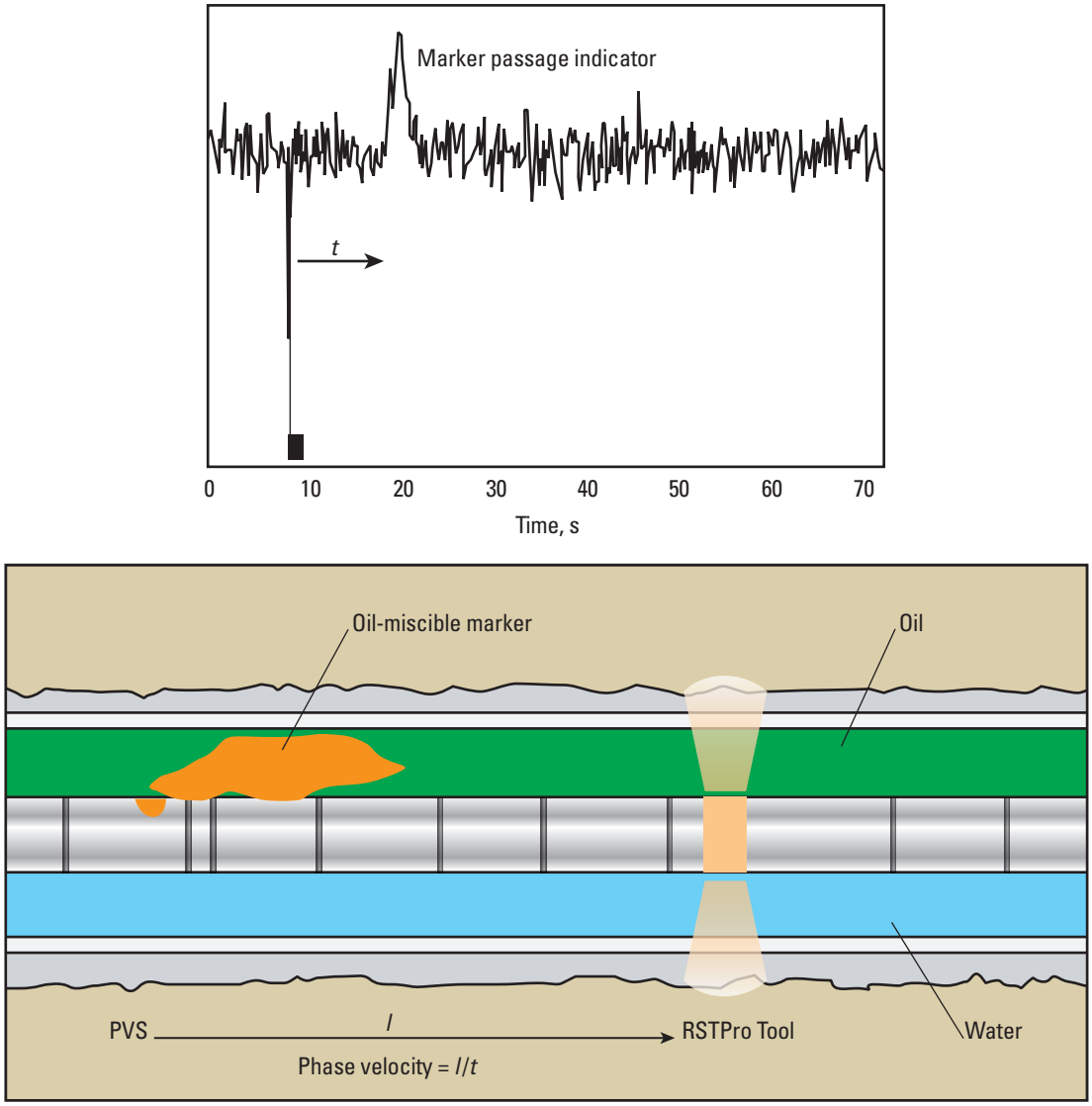

Figure 11-13. Log (top) and schematic (bottom) of the PVL method.

12 Flow Scanner Interpretation

Traditional production logging sensors have sought to measure a global pipe quantity such as mixture density, mixture velocity, water holdup, water velocity, or gas holdup. Even measurements with local holdup probes were designed to deliver an average pipe measurement.

The Flow Scanner horizontal and deviated well production logging system marks a departure from this approach and instead makes local measurements of holdup and velocity that are in turn converted into local measurements of flow rate. It is these local flow rates that are finally combined into average pipe flow rates.

Tool hardware

The Flow Scanner tool is designed to run on the low side of the pipe (Figs. 12-1 and 12-2). Two spring-loaded arms are used to mount the sensors and orient the tool to the vertical pipe axis (diameter). On the leading arm (when running in hole) are mounted four minispinners; on the trailing arm are five water holdup probes and five gas holdup probes. A fifth minispinner and a sixth water holdup probe and gas holdup probe are mounted on the tool body. Measurements of the spring-loaded arm caliper and tool relative bearing are used to determine the physical location of each sensor within the circular cross section of the pipe.

Figure 12-1. Flow Scanner side-view schematic.

For details on the physics of the holdup probes and minispinner calibration, refer to the "Spinner Velocity Tools" and "Probe Holdup Measurements" chapters.

When the tool is correctly oriented, a vertical diameter through the pipe is sampled and discrete values of holdup and velocity are recorded (Fig. 12-3).

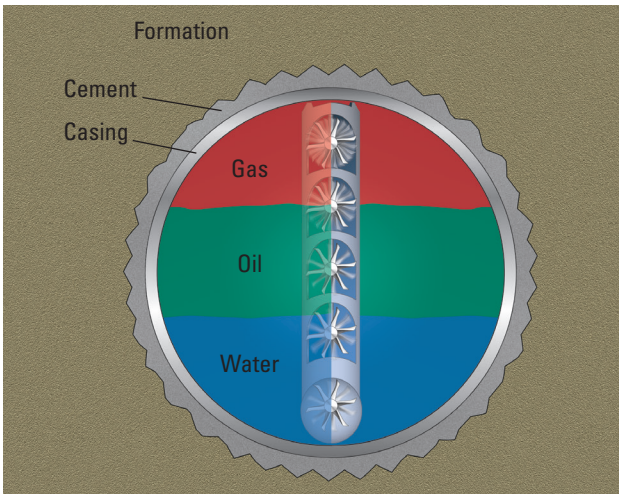

Figure 12-2. Flow Scanner end-view schematic.

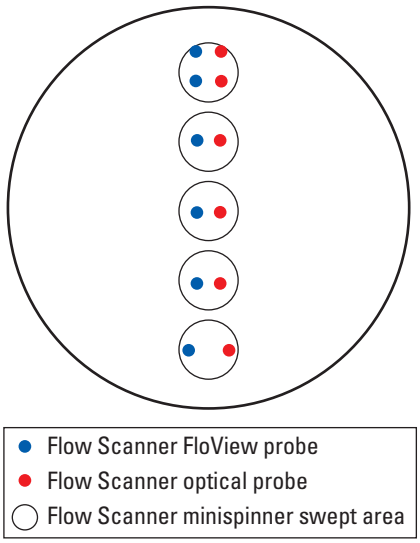

Figure 12-3. Holdup probe and minispinner locations in 6-in-ID pipe.

Flow Scanner interpretation techniques

As of 2012 there are three distinct ways in which Flow Scanner data is interpreted. The first technique is a stand-alone single-pass interpretation and is performed by proprietary Schlumberger inflow profiler software and by Emeraude software. The second and newer technique used by proprietary Schlumberger multipass interpretation software involves merging multiple Flow Scanner passes into one synthetic pass, which is then interpreted in the same way as the single-pass technique. The third and most recent technique is significantly different and involves interpreting the local measurements of holdup and velocity inside a 2D solver. This is the way the PLATO and Emeraude software work. Extensions to this third technique allow external measurements to constrain the Flow Scanner interpretation.

Single-pass processing

Single-pass processing occurs when there is only one pass or when multiple passes cannot be stacked because of a nonrepeating tool orientation (Figs. 12-4 and 12-5) or changing downhole flow rates.

Data from the two orientations in Figs. 12-4 and 12-5 cannot be stacked and averaged because although the probes and minispinners are identical, with their different orientations they are measuring different velocities and holdups. Likewise, the minispinners cannot be calibrated because the velocity from a spinner on a logging pass at one orientation does not match the velocity from an identical spinner on a different pass and orientation.

The holdup probes from a single pass can easily be converted into a holdup profile, but changing the spinner rps from a single pass into a velocity profile is less straightforward. A spinner pitch (or slope) and threshold need to be found for each minispinner.

Although the Flow Scanner minispinner calibration values are known from laboratory tests of the turbine used, early experiments with the Flow Scanner sonde in the Schlumberger Gould Research Center's flow loop showed that the presence of the Flow Scanner tool body was significantly influencing the minispinners' responses, thus making a single spinner calibration for all five minispinners inappropriate. Most affected by the tool body was minispinner 0 (mounted on the tool body), with more subtle effects on minispinners 1 through 4. To simplify and improve the analysis of single-pass Flow Scanner data, Table 1 of correction coefficients was created for a 7-in casing size flowing monophasic water. Application of these correction coefficients returns a minispinner to the theoretical calibration. For positive minispinner rps values, the flow-up coefficients should be used, whereas for negative minispinner rps values, the flow-down coefficients should be used.

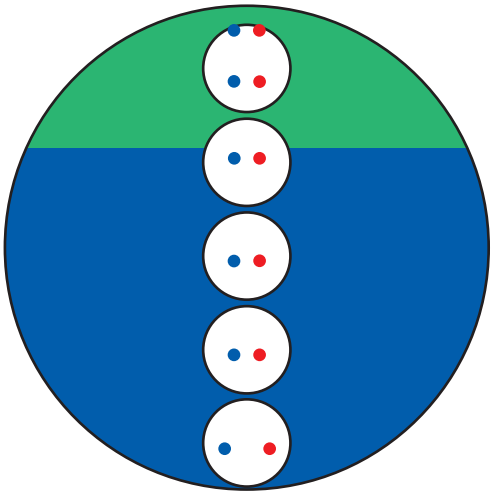

Figure 12-4. Correctly oriented Flow Scanner tool.

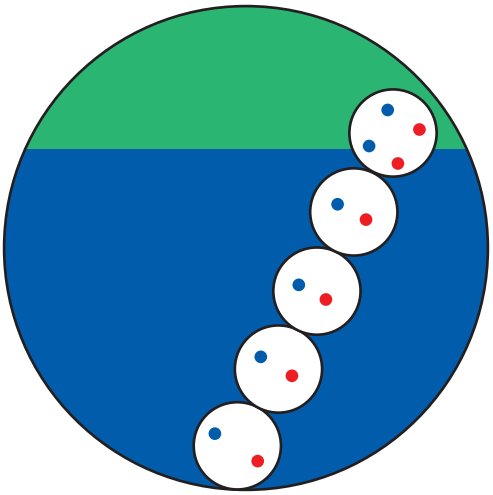

Figure 12-5. Poorly oriented Flow Scanner tool.

Sidebar 12A. Flow Scanner minispinner laboratory calibration

Pitch	= 3.54 in [9.0 cm]
Slope	= 0.056 rps/ft/min [0.185 rps/m/min]
Threshold in water	= 4 ft/min [1.2 m/min]
Threshold in oil	= 7 ft/min [2.1 m/min]
Threshold in gas	= 30 ft/min [10 m/min]

Table 12-1. Flow Scanner Minispinner Reading Correction Coefficients

Coefficient	Minispinner 0	Minispinner 1	Minispinner 2	Minispinner 3	Minispinner 4
Flow up	1.4	0.82	0.86	0.85	0.86
Flow down	2	0.84	0.88	1	1.12

In the MAXIS* wellsite logging unit, only the flow-up coefficients are used and applied in the following manner:

- SPI*n*_FSI = raw minispinner reading, no correction or depth filtering
- SPIC*n*_FSI = SPI*n*_FSI × flow-up coefficient
- SPIF*n*_FSI = SPIC*n*_FSI with a 6-ft depth filter.

Of these three channels, the customer Digital Log Information Standard (DLIS) file contains SPIF*n*_FSI. When performing a Flow Scanner single-pass interpretation it is important to know which channel is being used and what corrections have already been applied.

Because the Flow Scanner spinner calibration can be expected to change as the minispinner moves from gas to oil and from oil to water, single-pass interpretation software, such as the proprietary Schlumberger inflow profiler software, attempt to correct for phase-induced changes in the spinner response pitch (or slope) and threshold by using phase-dependent values of pitch and threshold (Fig. 12-6). Although this technique may work for a transition from 100% of phase A to 100% of phase B, the idea that 30% holdup of phase A and 70% holdup of phase B has a holdup-weighted pitch and threshold is a little optimistic. Multipass spinner interpretation techniques to perform an in situ spinner calibration remove this dependency on correction coefficients and arbitrary holdup mixing laws; because of that, they are much preferred.

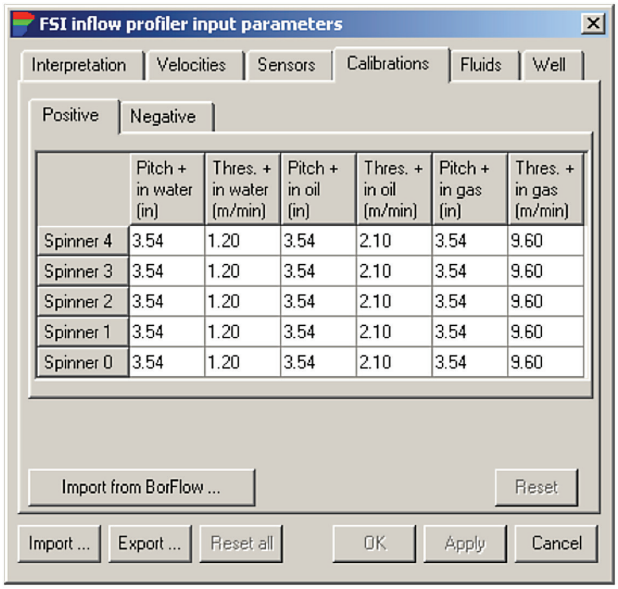

Figure 12-6. Multiphase Flow Scanner spinner calibration table from Schlumberger inflow profiler software.

Stacked data approach to Flow Scanner interpretation

With multiple passes of the Flow Scanner tool recorded under stable well conditions and with a repeatable tool orientation, the probe and minispinner measurements can be stacked (or averaged). Stacking the data allows removing intermittent data glitches to present a complete glitch-free pass to a single-pass interpretation engine. Although the holdup data from any one probe should be identical from pass to pass (at least for the down passes) and therefore easily averaged, the same is not true for the minispinner speeds. Because the minispinner fluid velocity is a function not only of the fluid velocity but also the tool velocity (cable speed), it is necessary to convert the minispinner speeds and tool velocity into a fluid velocity before the averaging can take place.

As with conventional spinner interpretation, a series of spinner calibration zones are required to accommodate changes in the spinner slope and threshold as different phases are encountered at different places along the well trajectory. Figures 12-7 and 12-8 show the raw minispinner speeds and the conversion to spinner velocities. Intervals where the spinner velocities fail to overlay from pass to pass indicate that the spinner calibration is wrong (and needs correction), the well is unstable, or sticky spinner data are present (which need editing).

Although the five Flow Scanner minispinners have the same diameter and profile they do not show the same spinner response slope and threshold even in a homogenous monophasic fluid. This is due to turbulence, vortex shedding, interference, and other effects from the tool housing and the effects of magnetic well debris collected by the sensor magnet on the spinner body. Whenever possible, an in situ calibration of each spinner at multiple places along the wellbore should be performed.

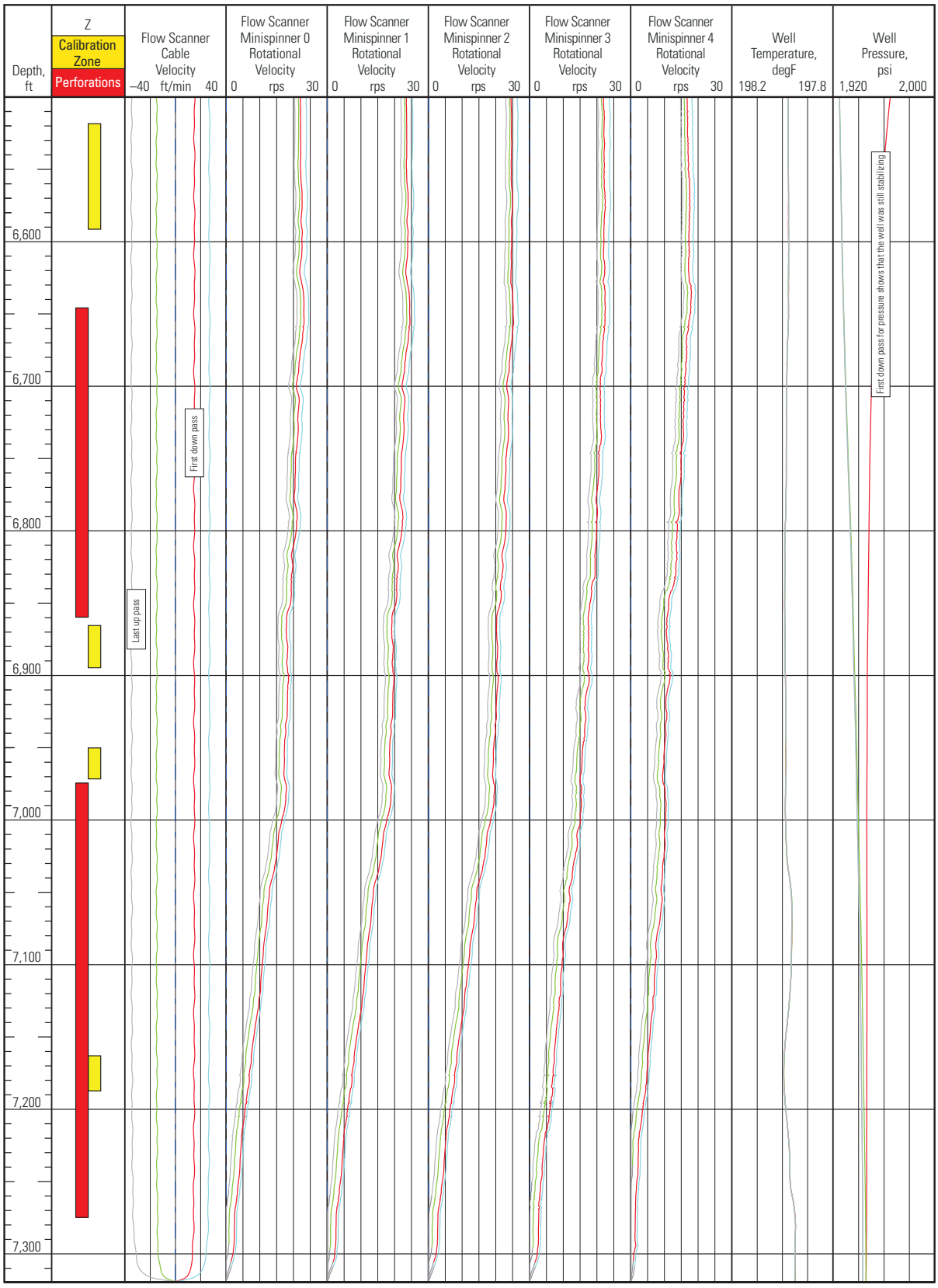

Figure 12-7. High-quality Flow Scanner minispinner data.

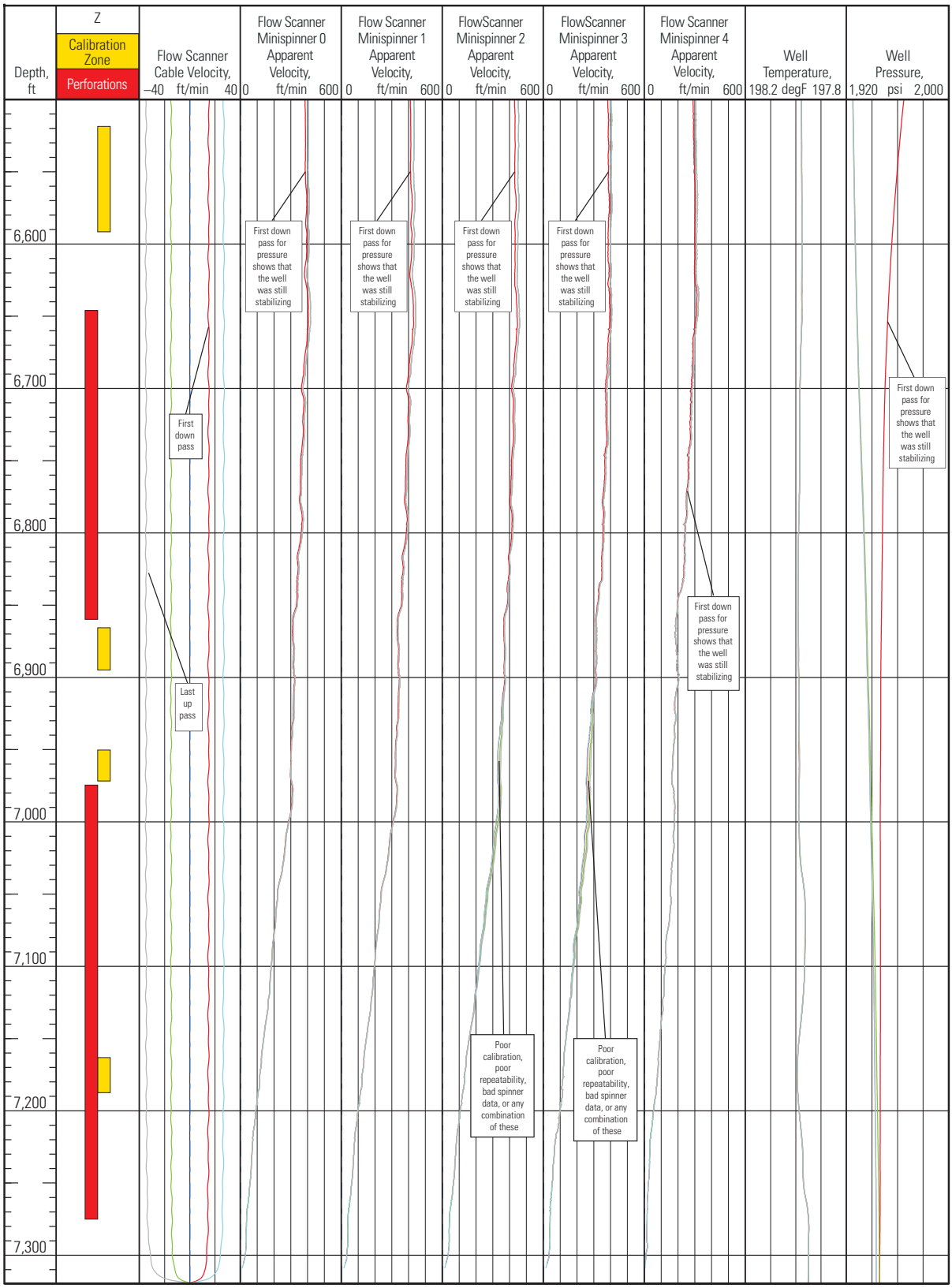

Figure 12-8. Quality control of spinner data by inspecting velocities.

The plot in Fig. 12-9 shows a simulation of a low-velocity horizontal gas-water well. On the down slopes the flow regime is stratified and the water holdup is very small. On the up slopes the flow regime is plug or slug flow with a high water holdup. Different spinner calibrations can be expected in these two different flow regimes, and therefore each change of slope requires a new spinner calibration zone (shown in yellow). Because a fluid entry (perforations shown in red) may change the holdup, velocity, and hence the spinner calibration slope and threshold, additional spinner calibration zones are added to ensure that all entries are bracketed by a calibration.

Working with 10 spinner calibration zones is not easy; for an actual dataset the raw curves are inspected to identify nonproducing perforations (no temperature kick, no holdup change, and no spinner rps change) for the purpose of removing as many spinner calibration zones as possible.

Interpretation of holdup and velocity array data

Irrespective of whether the source of the velocity and holdup data is stacked passes or a stand-alone pass, the resulting six water holdup probes, six gas holdup probes, and five minispinner velocities need to be transformed into a downhole flow rate. The first step is to project the readings back onto the vertical pipe axis assuming horizontal stratification of holdup and velocity inside the pipe (Figs. 12-10 and 12-11). For holdup data in horizontal wells this is a good assumption. But velocity data must fall to zero at the pipe wall, so horizontal stratification is not strictly true. However, for small displacement angles of the tool from the vertical, the measured velocities can be safely projected back to the vertical pipe axis.

Taking the case of a typical horizontal water-oil well, it can be seen that there are six water holdup points across the vertical pipe diameter and five spinner velocity points (Figs. 12-12 and 12-13, respectively). These discrete measurements need to be expanded into a holdup and velocity map across the entire pipe area.

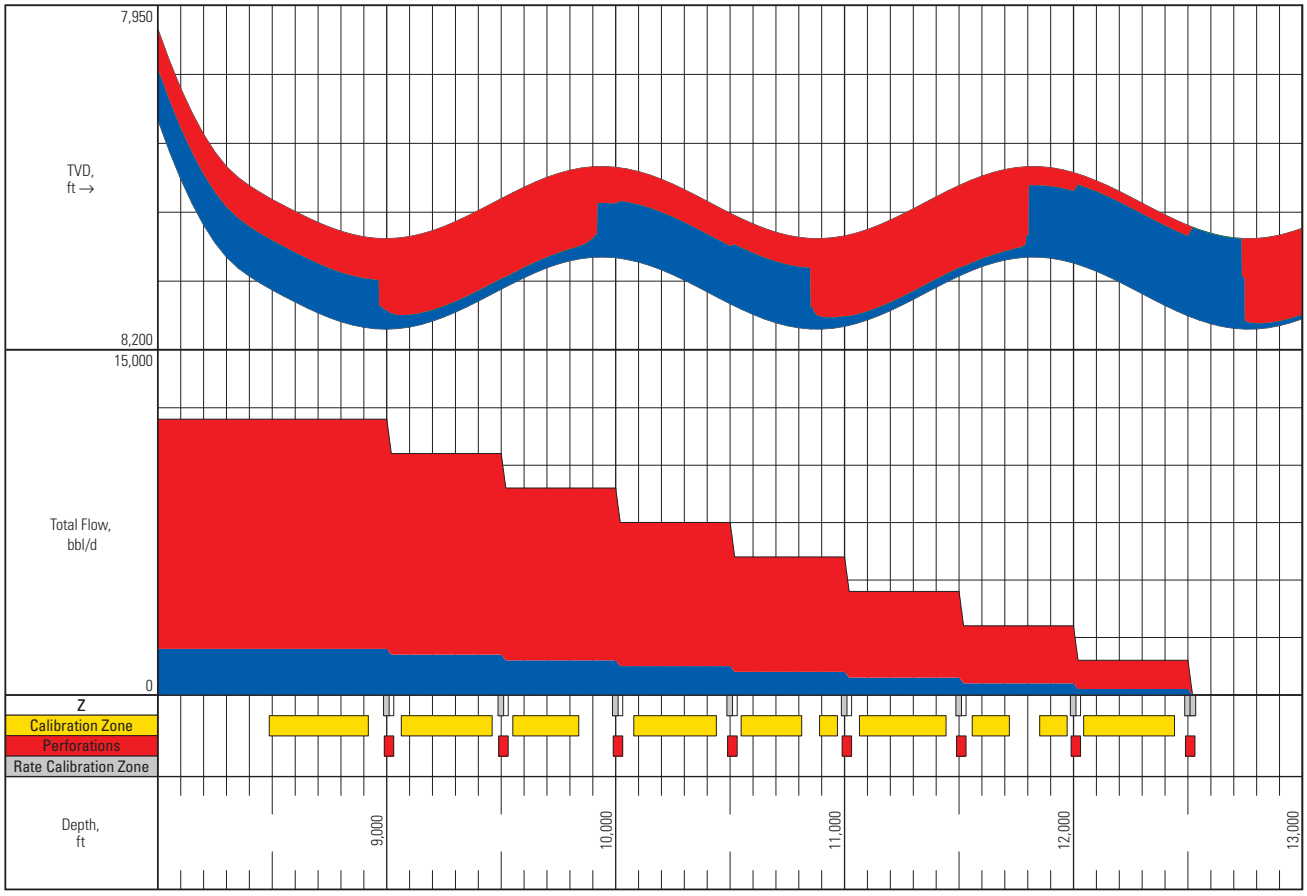

Figure 12-9. Simulated conditions for horizontal gas-water (red and blue, respectively) well.

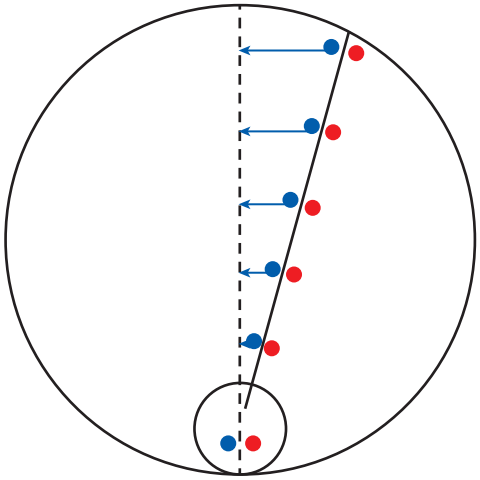

Figure 12-10. Projection of holdup data back to the vertical pipe diameter.

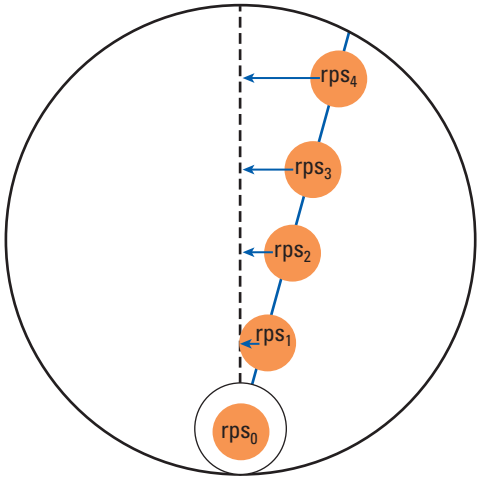

Figure 12-11. Projection of spinner readings back to the vertical pipe diameter.

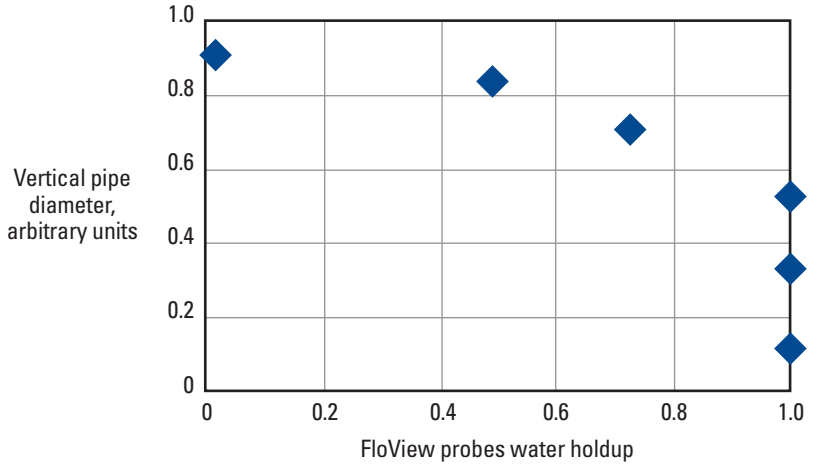

Figure 12-12. Flow Scanner holdup data projected onto the vertical pipe axis.

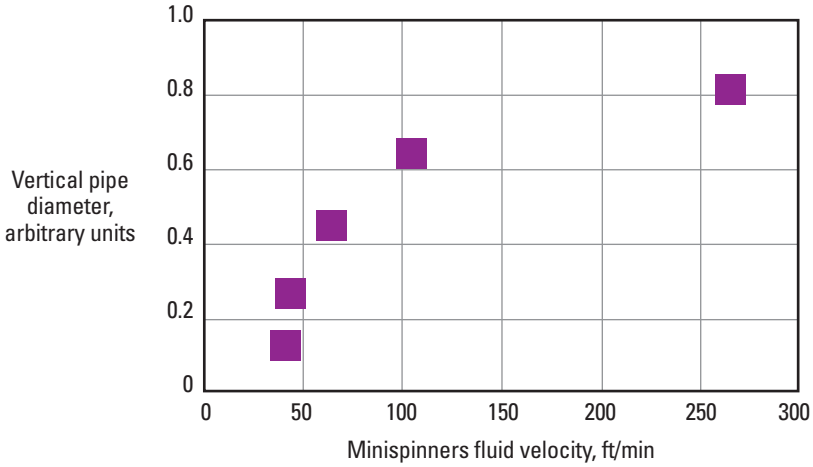

Figure 12-13. Flow Scanner velocity data projected onto the vertical pipe axis.

The first step is to create a continuous curve through the holdup points. The simplest approach is to join up the datapoints, otherwise known as a linear fit. This method works reasonably well for good-quality holdup data (Fig. 12-14).

More advanced methods use a spline fit or a smoothed spline fit, which results in a more aesthetically pleasing curve through the datapoints but does not introduce any physical constraints to the water holdup profile; water on the top and bottom of the pipe with oil in the middle would be quite acceptable to a spline-fitting algorithm. A simple geometrical curve that takes its shape from the balance of buoyancy and turbulent diffusion forces was created by Schlumberger as MapFlo multiphase flow mapping in deviated wells (Fig. 12-15). This curve forces a maximum heavy-phase holdup on the low side of the pipe with a matching maximum light-phase holdup on the high side of the pipe and a monotonic change from one to the other. A refinement to MapFlo software applies a greater weighting to holdup points that are not reading 0 or 1 because readings of 0 and 1 are often associated with a failed probe.

Although MapFlo processing is a proprietary Schlumberger function it has been made available to third-party production logging interpretation software developers for use only with Schlumberger production logging tools. The example in Fig. 12-16 shows how MapFlo processing working inside the proprietary Schlumberger single-pass inflow profiler software ignores a bad datapoint because of its physical improbability.

Before too much time is spent trying to fit a curve through the velocity data, it is important to inspect the velocity trends displayed. Most interpretation packages can display the velocity profile across the pipe diameter interactively, following movement of the cursor up and down the log. Erroneous velocity points, either too high

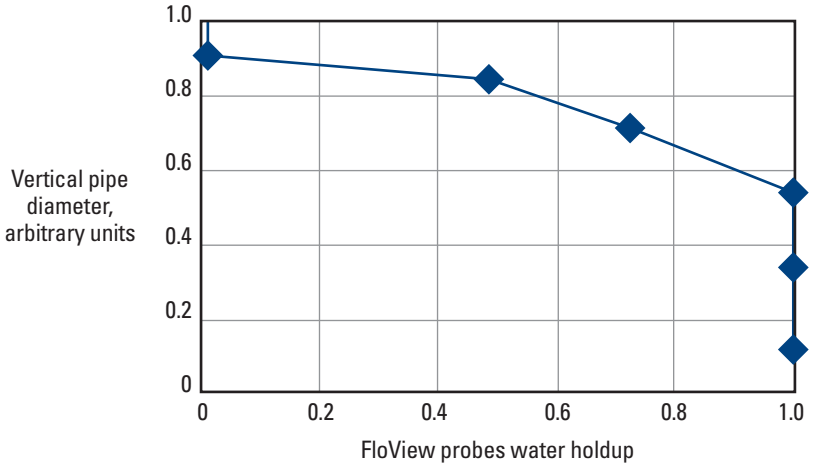

Figure 12-14. Linear curve fitting.

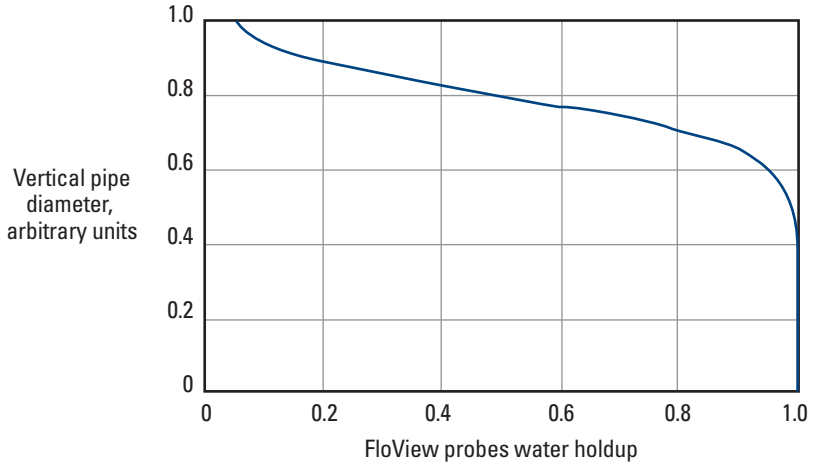

Figure 12-15. MapFlo curve fitting to probe holdup data.

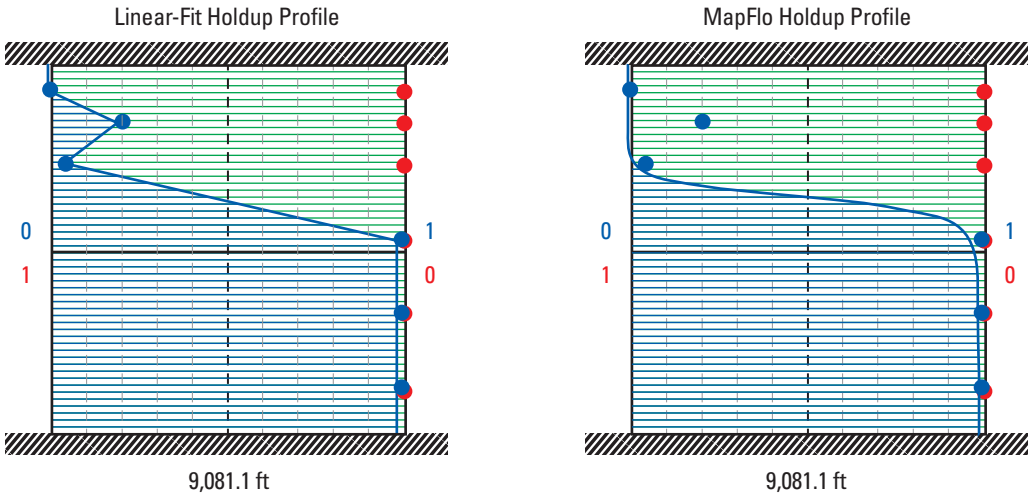

Figure 12-16. Linear fit (left) and MapFlo fit (right) to water holdup probe data.

or too low, indicate a bad spinner slope or pitch and threshold, a stalled (0-rps) spinner, or a sticky spinner. The presence of erroneous velocity points calls for either a revised spinner calibration or the elimination of sticky spinner data.

However, since 2010, it is possible to use a combination of the MapFlo holdup curve shape combined with a Prandtl power law velocity profile. Applying the Prandtl power law to the horizontal pipe axis results in a 3D model (Fig. 12-17) in addition to a more physical velocity profile (Fig. 12-18).

Although originally designed for oil-water holdup, MapFlo processing can also be applied to gas-liquid holdup and even three-phase gas, oil, and water holdup, for which two separate MapFlo curves are used.

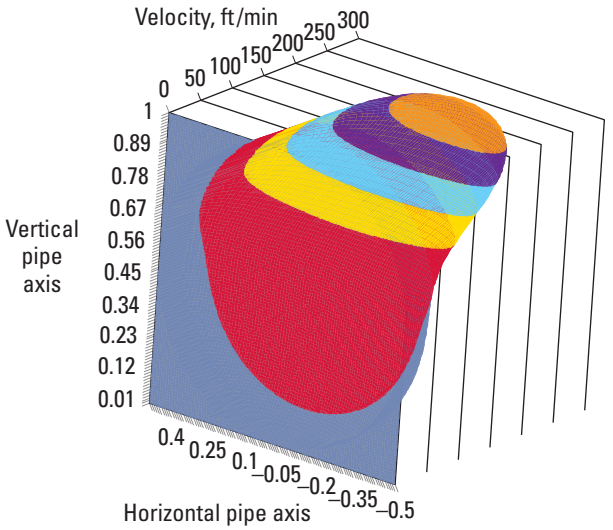

Figure 12-17. 3D velocity profile created from a MapFlo holdup profile and Prandtl profile. Pipe axes in arbitrary units.

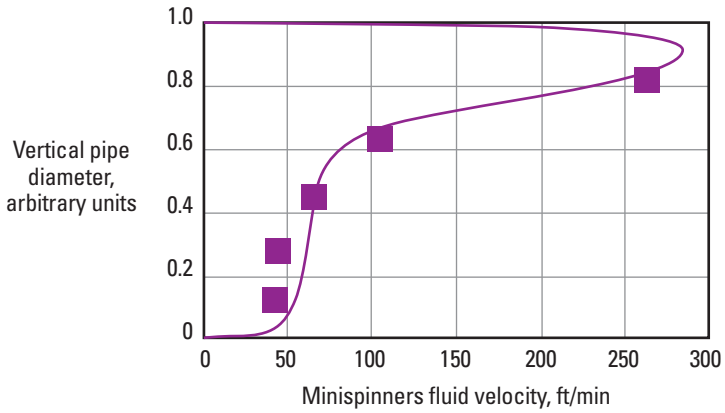

Figure 12-18. MapFlo and Prandtl curve fitting to minispinner velocities.

Velocity curve fitting to three-phase flow using the holdup MapFlo profile and Prandtl power law is theoretically possible, but in practice is usually too difficult.

Ignoring the application of the Prandtl velocity curve in the horizontal axis, there are two main ways of computing phase flow rates from the velocity and holdup profiles across the vertical axis of the pipe (Fig. 12-19).

The first approach assumes that no local slip velocity is present between the phases and merely sums the local product of holdup velocity and pipe area. Taking the water rate as an example:

$$q_w = \int_{-r}^{+r} Y_w(x) \times v(x) \times 2\sqrt{\left(r^2 - x^2\right)}dx. \qquad (12\text{-}1)$$

The second approach applies a slip model to the local measurements, changing the water rate as follows:

$$q_w = \int_{-r}^{+r} Y_w(x) \times \left[v(x) - v_s(x) \times \left(1 - Y_w(x)\right)\right] \times 2\sqrt{\left(r^2 - x^2\right)}dx, \qquad (12\text{-}2)$$

where

$Y_w(x)$ = local water holdup along the vertical pipe axis
$v(x)$ = local mixture velocity along the vertical pipe axis
r = internal radius of the pipe
$v_s(x)$ = local slip velocity up the vertical pipe axis.

Sidebar 12B. Global slip velocity

To create a global (whole-pipe) slip velocity does not require the presence of a local slip velocity. As long as there is a velocity and holdup profile, a slip velocity is created. Therefore, a Flow Scanner interpretation with no local slip still shows a global slip. A basic study of multiphase fluid mechanics rapidly reveals that local slip velocities are much smaller than the global (whole-pipe) slip velocity; therefore, ignoring the local slip introduces much smaller errors than ignoring the global slip whereas imposing a global slip model on a local measurement of velocity and holdup probably introduces too much slip.

Although Eq. 12-2 is more complete, it does require a local slip model—of which there are none. Therefore, a standard whole-pipe slip model is used instead, which probably introduces too much slip. There is also the problem of finding a slip model that works close to the horizontal. It can be said with some confidence that the true water flow rate lies between the answers from Eqs. 12-1 and 12-2 and, with less confidence, that Eq. 12-1 is probably closer to the truth.

In both Eqs. 12-1 and 12-2 the whole pipe area is assumed to be available for the well fluids. In practice, a small area is occupied by the body of the logging tool (Fig. 12-20). To correct for this "dead" volume, the effective tool width at each point along the vertical pipe diameter must be subtracted from the local chord length.

This modifies Eq. 12-1:

$$q_w = \int_{-r}^{+r} Y_w(x) \times v(x) \times \left[2\sqrt{\left(r^2 - x^2\right)} - t(x)\right]dx, \qquad (12\text{-}3)$$

where

$t(x)$ = effective tool width across the vertical pipe diameter:

- $r + x < 0.009$

$$t(x) = 2\sqrt{(0.043/2)^2 - \left((r - 0.043/2) + x\right)^2}$$

- $r + x \geq 0.009$ and $r + x < 0.016$

$$t(x) = 0.035$$

- $r + x \geq 0.016$ and $r + x < d_{\text{Flow\_Scanner\_max}}$

$$t(x) = 0.00027/(2 \times r - 0.016)$$

- $r + x \geq d_{\text{Flow\_Scanner\_max}}$

$$t(x) = 0,$$

where

$d_{\text{Flow\_Scanner\_max}}$ = maximum caliper opening diameter of the Flow Scanner tool (0.229 m)

with all dimensions in meters.

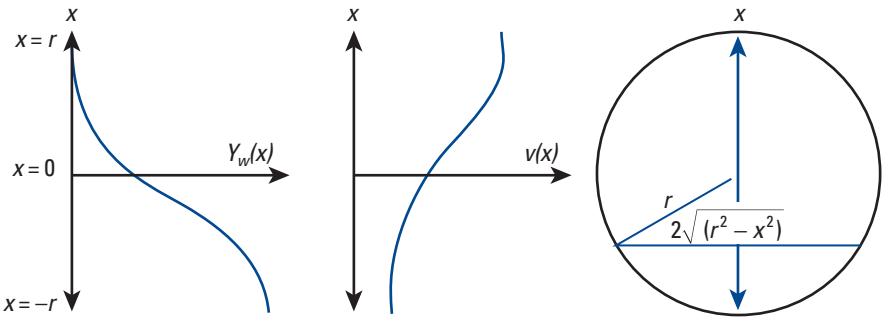

Figure 12-19. Computation of flow rates from Flow Scanner measurements.

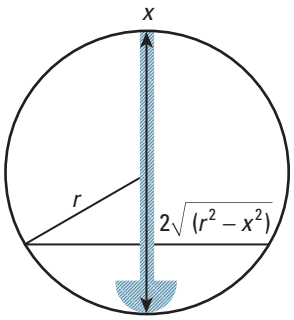

Figure 12-20. Pipe cross section occupied by the Flow Scanner tool.

Inside a 6-in pipe the dead volume occupied by the Flow Scanner tool has the width shown in Fig. 12-21.

While the objective of a Flow Scanner interpretation should be to compute the phase flow rates, it is also possible to extract the phase holdups and phase velocities. The average holdup of phase n is simply computed from the product of the local holdup multiplied by the local pipe width and normalized by the total available pipe area:

$$Y_n = \int_{-r}^{+r} \frac{Y_n(x) \times 2\sqrt{(r^2 - x^2)}}{\pi r^2} dx. \qquad (12\text{-}4)$$

The phase velocities cannot be so directly computed and are instead derived from the phase flow rates and phase holdups previously computed:

$$v_n = \frac{q_n}{AY_n}, \qquad (12\text{-}5)$$

where

v_n = phase velocity of phase n
q_n = flow rate of phase n computed from Eq. 12-3
A = pipe area
Y_n = holdup of phase n calculated from Eq. 12-4.

Because v_n is derived from the phase n flow rate, it should be obvious that it makes no sense to use v_n to compute a new and different phase n flow rate using a conventional pipe-averaged interpretation model.

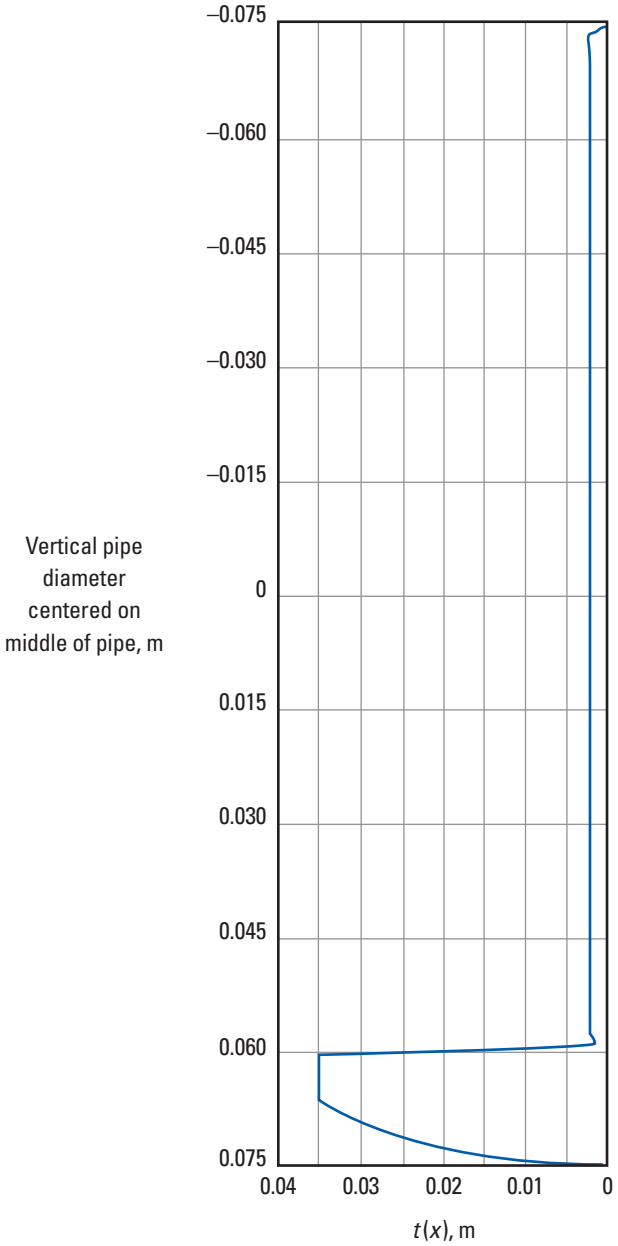

Figure 12-21. Effective Flow Scanner tool width in 6-in [0.15-m] pipe.

2D solver approach to Flow Scanner interpretation

In mathematical terms the 2D solver tries to minimize the following error function at each depth:

$$E = \sum \left[M(x_i, y_i) - m_i \right]^2, \qquad (12\text{-}6)$$

where

$M(x_i, y_i)$ = modeled value of holdup or velocity or an average pipe property with x_i and y_i corresponding to the coordinates of the local measurement

m_i = measurement that corresponds to an individual probe holdup, individual spinner velocity, or traditional average pipe measurement of holdup or phase velocity (Fig. 12-22). A single logging pass or multiple logging passes (without stacking or averaging) can supply m_i. A standard Flow Scanner tool provides 17 measurements per logging pass.

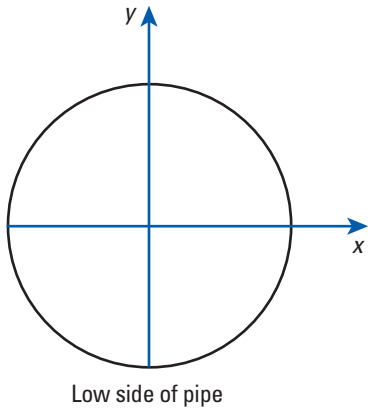

Figure 12-22. Coordinate system for the 2D model.

Although there are no full 2D models, there are some basic 2D features of the flow that can be used.

- The model can be reduced by one dimension and a horizontally stratified holdup and velocity can be imposed. This is not true for vertical and deviated wells, but it is quite close to the truth for horizontal wells, where local measurements are needed and used.
- The water holdup can be required to monotonically increase from the top to the bottom of the pipe, with the gas holdup doing the reverse. Again, this is not true for vertical or deviated wells but close to the truth for horizontal wells.
- A more powerful technique is to impose the shape of the MapFlo curve to the holdup profile and to use the shape of the holdup curve to describe a velocity profile (after applying a gain and offset to the MapFlo curve and taking the wall velocity to zero using the Prandtl profile).
- A global pipe slip correlation can be imposed on the assumption that an appropriate slip correlation can be found for the given pipe deviation.
- A global pipe holdup can be imposed from another logging measurement such as the TPHL three-phase fluid holdup log obtained from RSTPro measurements.

Initially all 2D Flow Scanner solvers treated the holdup and velocity data as point readings. Although this is realistic for the FloView and GHOST holdup probes, the minispinners are sampling all the fluid velocities within the swept area of each minispinner. This means that instead of using the model in Eq. 12-7, the model can be refined as shown in Eq. 12-8 to correct for the average velocity within the swept area of the minispinner. Figure 12-23 shows the difference in the velocity profile that results from using Eq. 12-8 as compared with Eq. 12-7. However, the minispinner is not a perfectly circular averaging device because there is a dead space in the center for the minispinner hub. This dead space is incorporated in Eq. 12-9, with further refinements for a mass-fraction average implemented in Eq. 12-10.

$$M(x,y) = v(x,y), \tag{12-7}$$

$$M(x,y) = \frac{1}{A_s}\int_{A_s} v(x,y)dS, \tag{12-8}$$

$$M(x,y) = \frac{1}{A_s - A_h}\int_{A_s - A_h} v(x,y)dS, \tag{12-9}$$

$$M(x,y) = \frac{1}{A_s}\frac{\int_{A_s} \rho(x,y)\times v(x,y)dS}{\int_{A_s} \rho(x,y)dS}, \tag{12-10}$$

where

A_s = swept area of the minispinner disc
S = surface over which the integration must be performed
A_h = area of the center hub of the spinner that does not contribute to the velocity measurement
ρ = density.

Figures 12-24 and 12-25 show the effect of the switch from a point to a swept-area velocity model. Not only are the computed flow rates changed but the computed holdups are also slightly altered as the error-minimizing routine seeks a new optimal solution.

A patent application (Whittaker, 2011) has been published for the improved minispinner interpretation techniques of Eqs. 12-8 through 12-10.

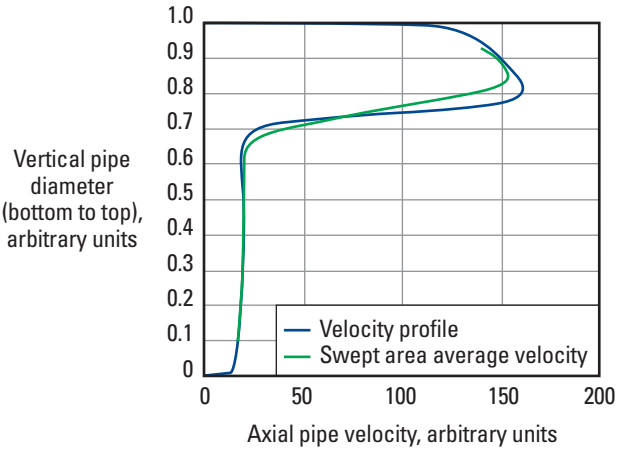

Figure 12-23. Response of Eq. 12-7 in blue and Eq. 12-8 in green showing significant differences.

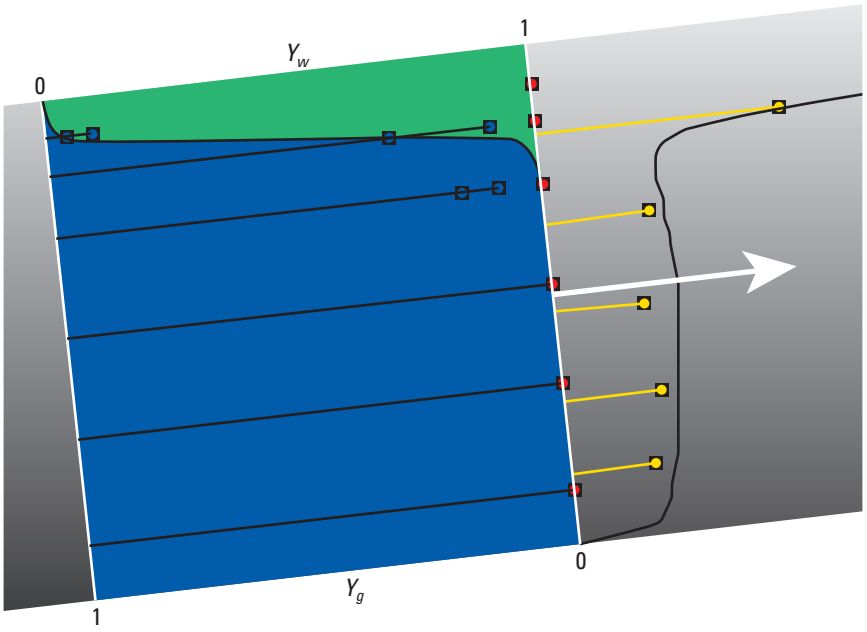

ID: 6.57 in	Y_w: 0.907	Q_w: 5,819.56 bbl/d
Deviation: 83.65°	Y_o: 0.093	Q_o: 6,000.69 bbl/d
Relative tool bearing: 0°	Y_g: 0	Q_g: 0 bbl/d

Figure 12-24. Flow Scanner processing with a point spinner reading. Blue symbols = water holdup probe values on the vertical pipe diameter, red symbols = gas holdup probe values on vertical pipe diameter, yellow symbols = minispinner velocities, white arrow = flow indication, here from left to right.

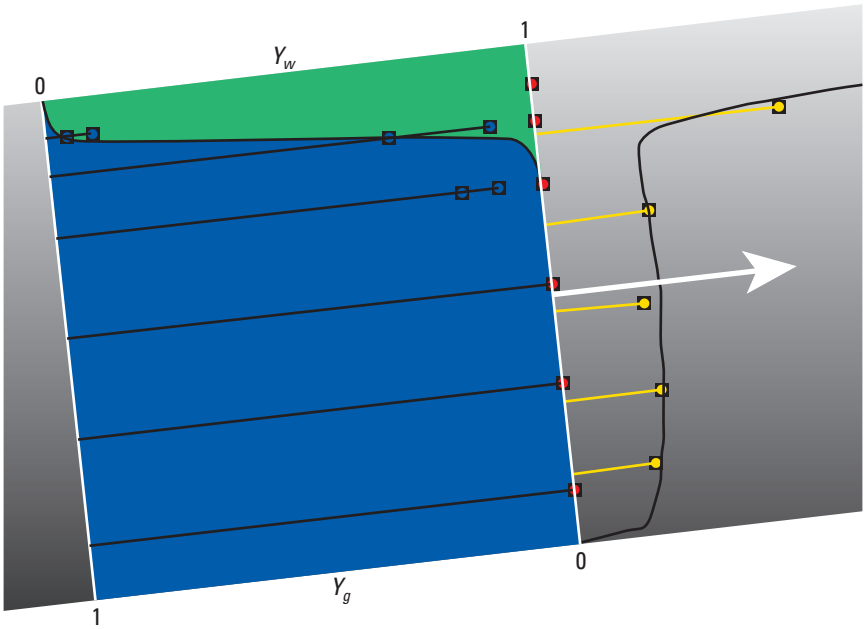

ID: 6.57 in	Y_w: 0.921	Q_w: 5,169.35 bbl/d
Deviation: 83.65°	Y_o: 0.079	Q_o: 4,857.13 bbl/d
Relative tool bearing: 0°	Y_g: 0	Q_g: 0 bbl/d

Figure 12-25. Flow Scanner processing with a swept-area average velocity from the minispinner readings.

A Flow Scanner dataset

Let's look at a Flow Scanner dataset from an openhole oil-water horizontal well logged with wireline tractor conveyance.

The first log (Fig. 12-26) shows the raw spinners. The red down pass has a very noisy cable velocity because the openhole tractor fought to travel 4,000 ft down the barefoot completion. The relative-bearing curve on the down pass (red) in Track 1 shows that the tool is rocking from side to side while the caliper in Track 2 sees some restrictions and washouts. The washouts correspond to reduced spinner speeds. Sticky spinner readings have been edited out.

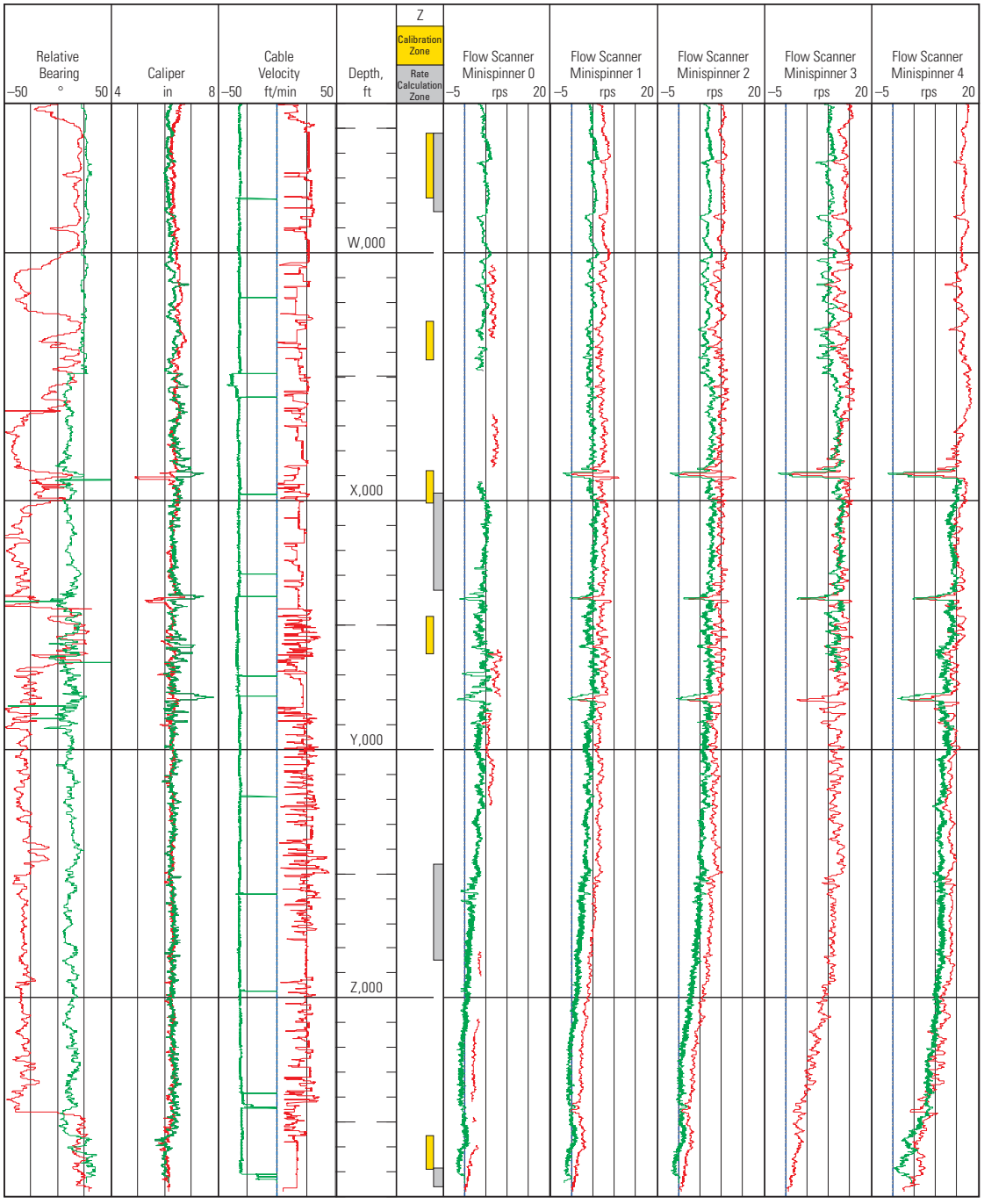

Figure 12-26. Flow Scanner minispinner readings from an openhole horizontal well. Red = down pass, green = up pass.

After the conversion to velocity profiles in Fig. 12-27, the minispinner velocities from the two passes match very closely except for the computed apparent fluid velocity from minispinner 3, where the changes in the relative bearing from pass to pass may be moving the minispinner between the oil layer and the water layer.

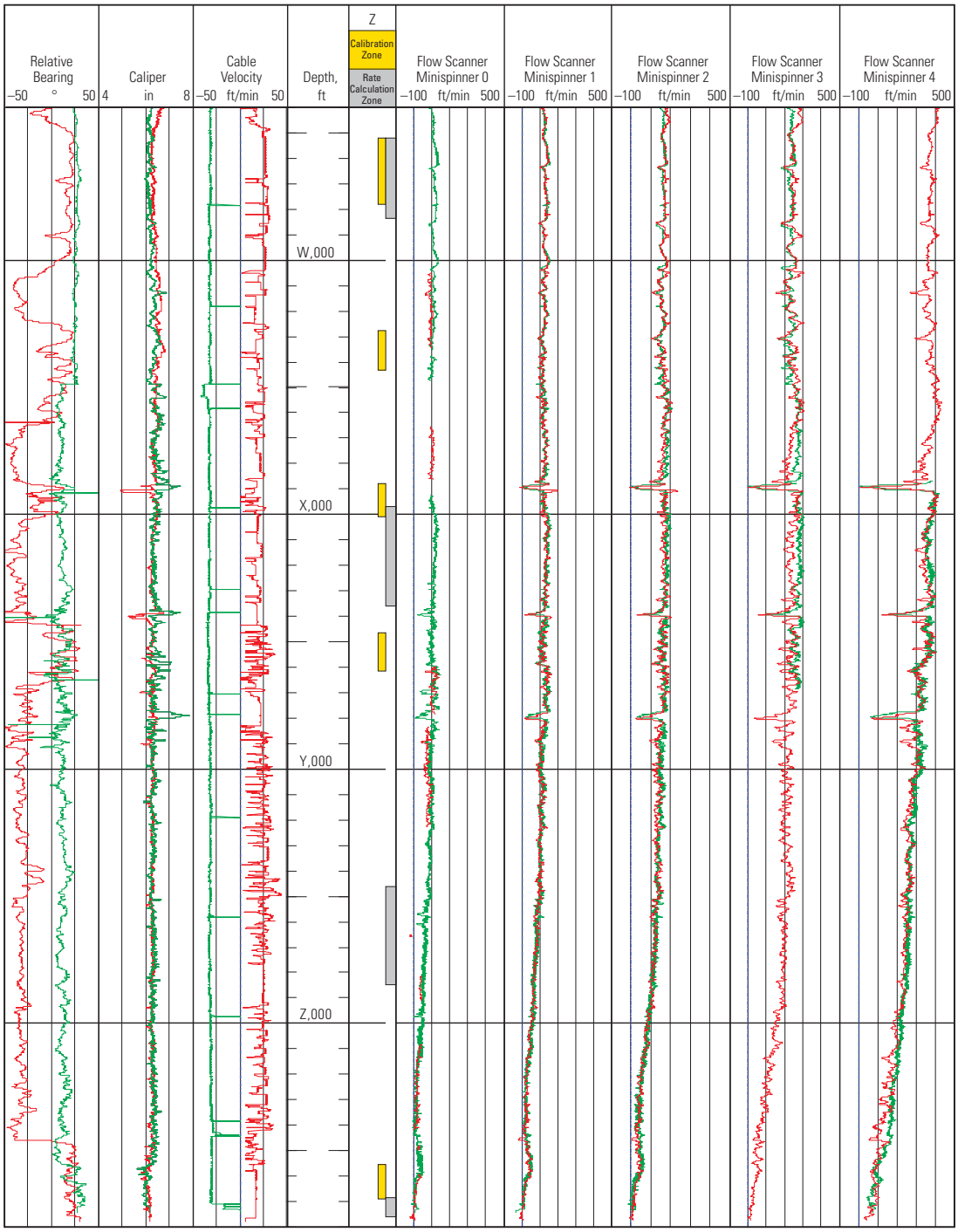

Figure 12-27. Flow Scanner minispinner velocities from an openhole horizontal well.

Inspection of the water holdup data (Fig. 12-28) shows that the fluid velocities are high enough to provide good holdup responses on the up passes (as well as on the down passes). The water holdup for probe 0 is suspiciously flat, but this may reflect the total absence of oil bubbles on the low side of the pipe.

In a perfect world the resulting flow profiles would look good and the interpretation would be finished, but in this case the oil flow profile increases and then falls as the heel of the well is approached (Fig. 12-29).

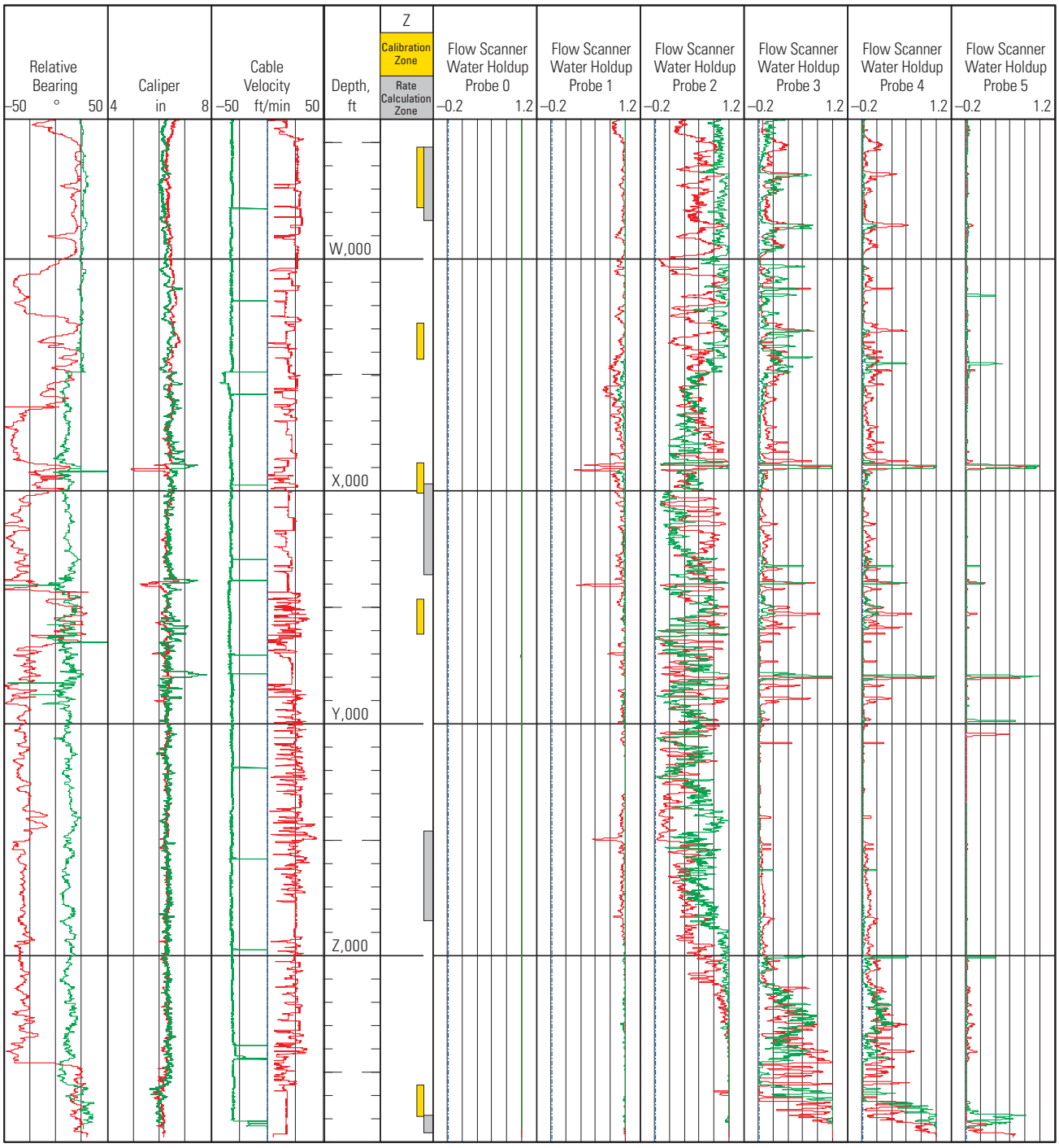

Figure 12-28. Water holdup probe data from an openhole horizontal well.

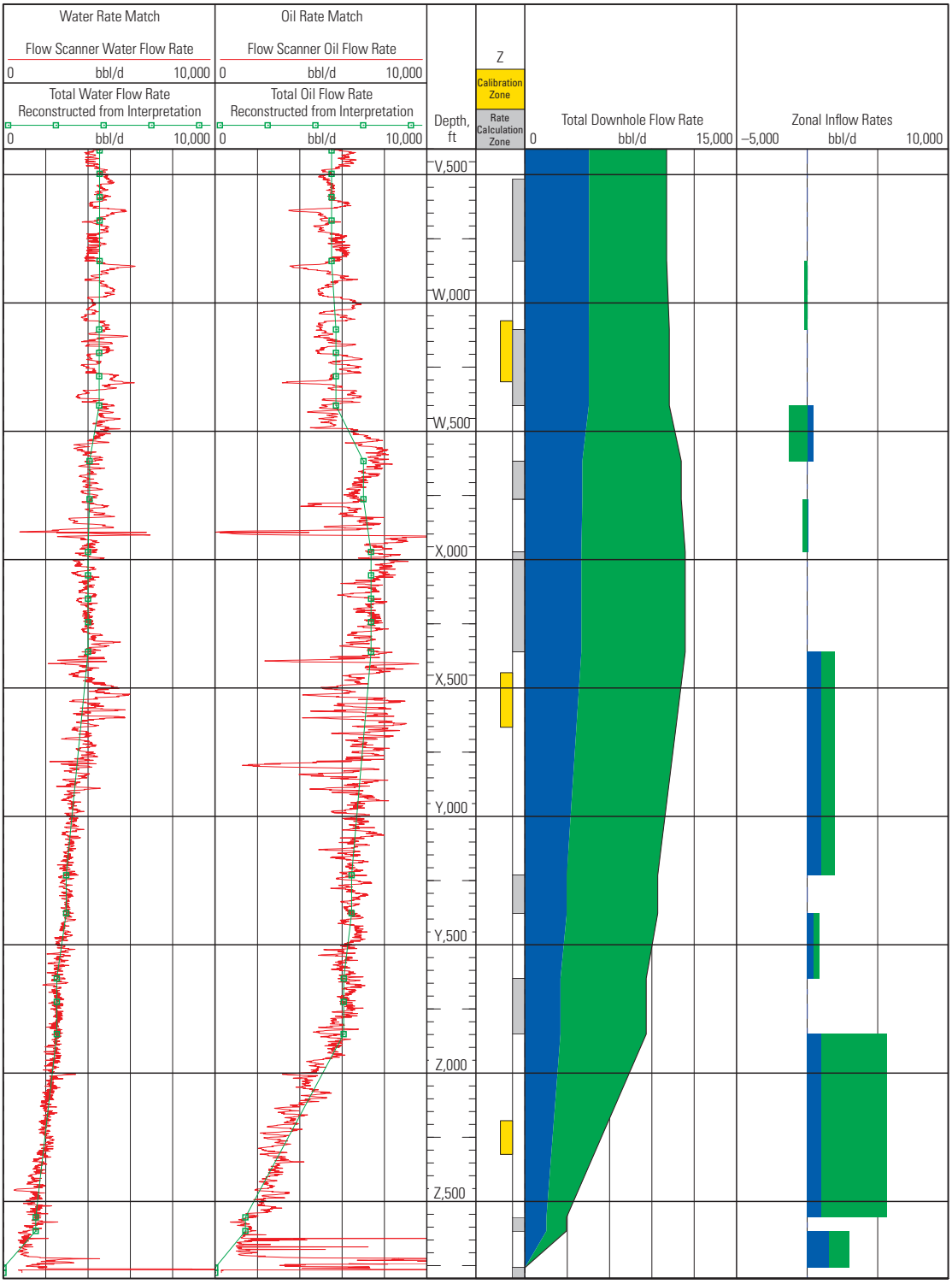

Figure 12-29. First interpretation of Flow Scanner data from an openhole horizontal well.

Inspection of the holdup and velocity profile from the middle of the well in Fig. 12-30 shows that minispinner 4 is reading suspiciously high or that minispinner 3 is suspiciously low. The comparison of measured to reconstructed velocities can also be performed on the log display of spinner velocities (Fig. 12-31).

Sidebar 12C. The essence of interpretation

An old log analyst once wrote, "If you torture data enough, it will tell you anything."

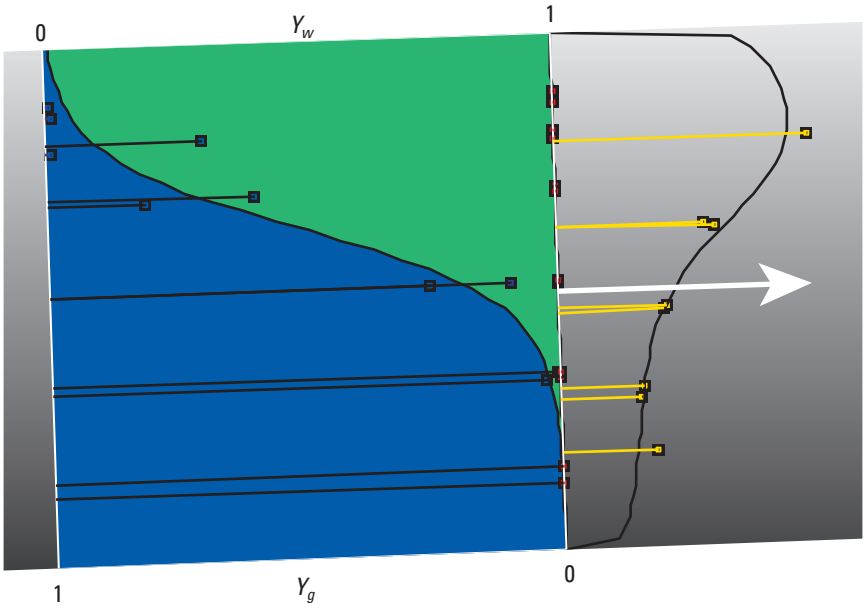

ID: 6.32 in	Y_w: 0.655	Q_w: 4,928.94 bbl/d
Deviation: 88.1°	Y_o: 0.345	Q_o: 4,958.89 bbl/d
Relative tool bearing: 0°	Y_g: 0	Q_g: 0 bbl/d

Figure 12-30. Inspection of holdup and velocity profile.

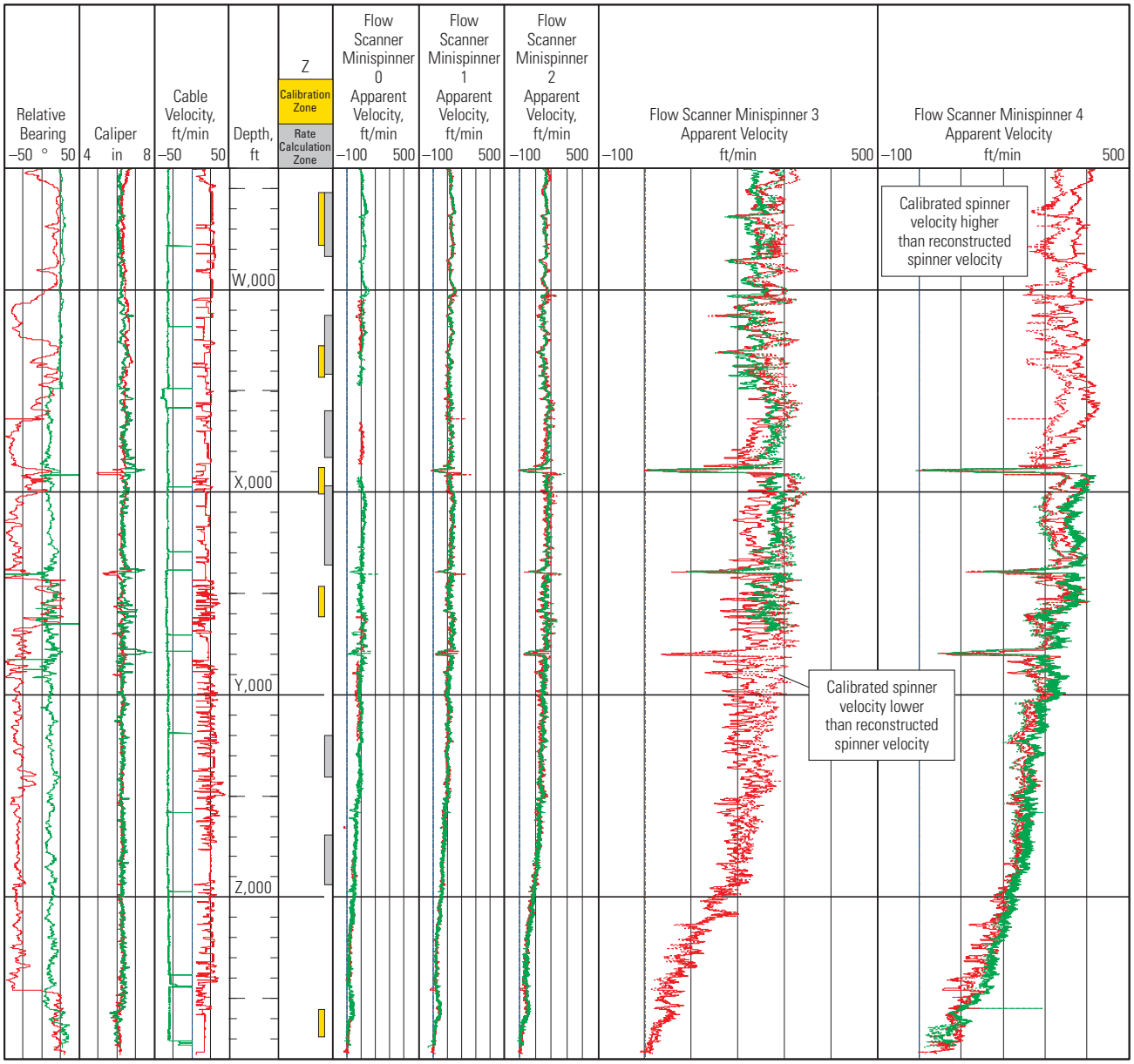

Figure 12-31. Comparison of calibrated minispinner velocities (solid curves) and reconstructed minispinner velocities (dotted curves).

Once it is known in which way the interpretation needs to be adjusted, the spinner calibration can be pushed, but not forced, and unhelpful water holdup data eliminated until an acceptable flow profile is computed (Figs. 12-32 and 12-33).

The reconstructed velocity profile is generated by the model chosen by the log analyst. If a linear fit is chosen for the shape of the velocity profile, then the reconstruction should exactly match the calibrated velocities. However, as soon as a curve is fitted, some reconstruction errors are introduced.

Figure 12-32 can be summarized as follows:

- Track 1 shows the water holdup data from the six electrical probes that correspond to the curve-fitting model.
- Track 2 shows the velocity profile from the five mini-spinners that correspond to the curve-fitting model.
- Tracks 3 and 4 show the computed water and oil flow rates, respectively. The red curves show the raw response with no global regression imposed to avoid thief zones and pseudoseparators, which are zones

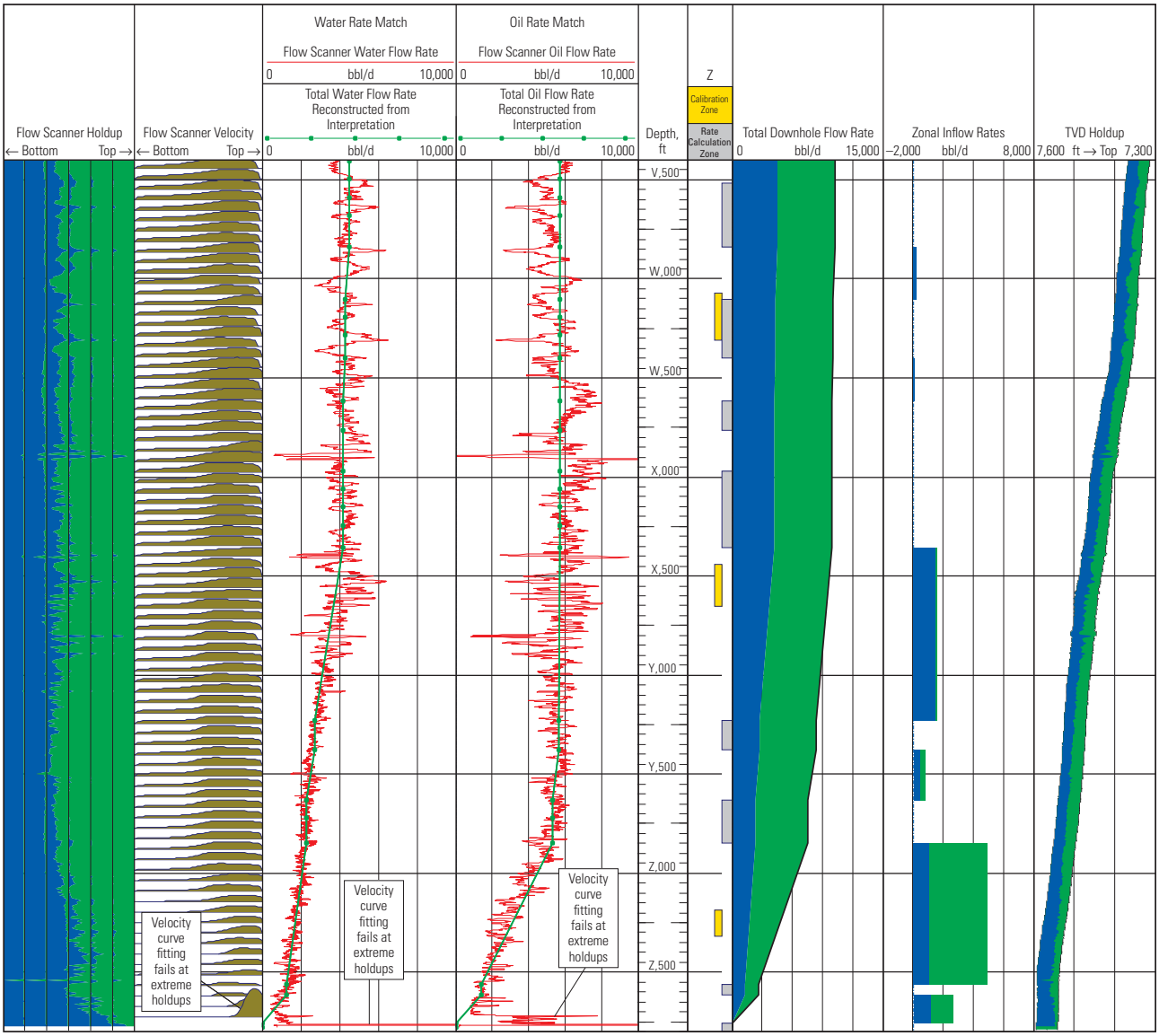

Figure 12-32. Final flow profile after application of log interpretation skills.

that appear to take one phase while producing a different phase (against all the laws of physics). The green lines show the reconstructed water and oil flow rates after the application of the global regression. A close match between the red and green curves shows that the global regression has done no more than tidy up the flow profile.

- Track 5, to the right of the depth track, is the zones track and shows the location of the spinner calibration zones in yellow and stable flow rate zones in gray.
- Track 6 is the cumulative downhole flow rate.
- Track 7 shows the zonal inflows and is the major deliverable from a production log interpretation.
- Track 8 shows the water holdup plotted inside a borehole of diameter determined by the tool caliper and deviation provided by an accelerometer mounted on the long axis of the tool body.

Global solver approach to Flow Scanner data

In the "Production Logging Interpretation Equations and Techniques" chapter, the global solver and global regression sections include the use of a 2D model of wellbore holdup and wellbore velocity. The reader is advised to turn to this next chapter to see where Flow Scanner interpretation techniques may be heading.

Flow Scanner interpretation limits

The stand-alone and the merged or stacked approaches to Flow Scanner interpretation as implemented in proprietary Schlumberger single-pass and multipass processing software are designed to work with a complete set of Flow Scanner sensor measurements but no other measurements. An RSTPro TPHL measurement or a WFL water flow log velocity cannot be used inside the Flow Scanner interpretation. Therefore, an absence

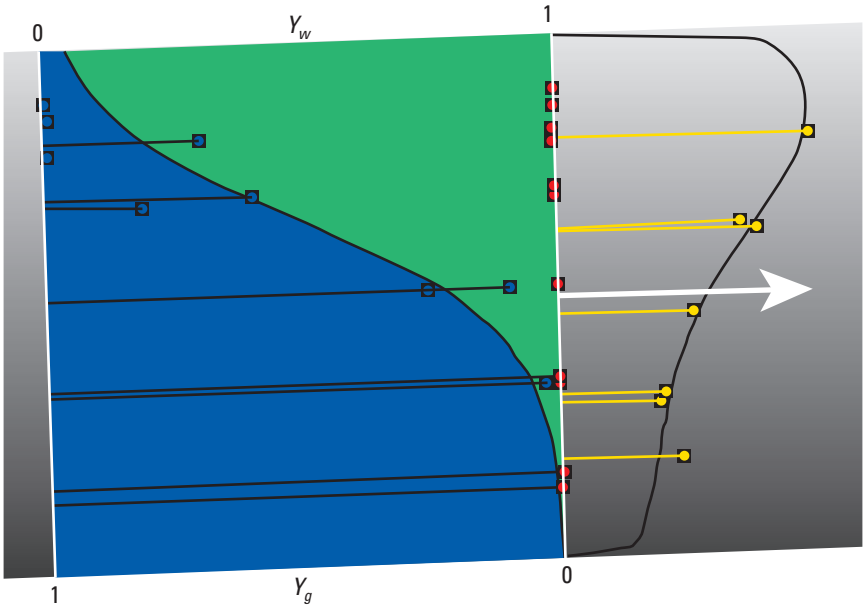

ID: 6.32 in	Y_w: 0.672	Q_w: 5,188.03 bbl/d
Deviation: 88.1°	Y_o: 0.328	Q_o: 4,011.52 bbl/d
Relative tool bearing: 0°	Y_g: 0	Q_g: 0 bbl/d

Figure 12-33. Improved interpretation of the holdup and velocity profile in Fig. 12-30.

of holdup data (resulting from bubble shear, probe damage, asphaltenes, or other causes) means that the spinner array data cannot be processed and used. The situation is slightly better for good holdup data in the absence of spinner data because holdup array measurements can be converted to an average pipe holdup and interpreted with other average pipe measurements.

Taking the Flow Scanner measurements into the latest 2D solver allows other averaged pipe measurements to be included in the global solver. This means that the absence of one of the Flow Scanner measurements does not stop an interpretation from using what Flow Scanner measurements remain (although the results are not as good).

The Flow Scanner production logging can identify recirculation but the Flow Scanner interpretation cannot quantify recirculation. In part this is due to the horizontally stratified holdup and velocity model used to interpret the data and may also be caused by the minispinner responses to nonaxial flow.

Applications of Flow Scanner production logging

The primary application of the Flow Scanner measurements is for production logging in nearly horizontal wells (80° to 100° deviation). However, niche applications also exist for high-velocity gas-liquid wells, where the eccentered Flow Scanner tool can tolerate higher flow velocities (and the consequent weight loss) than a conventional centered production logging tool, and for deviated wells with very high water holdup, where the remaining high-side oil is more easily visible to the Flow Scanner probes than to other FloView tools. In the latter case, the Flow-Caliper Imaging Sonde (PFCS) and Digital Entry and Fluid Imaging Tool (DEFT) probes normally do not have the desired tool (and probe) orientation and, additionally, the PFCS probes cannot be mounted very close to the casing wall (Fig. 12-34).

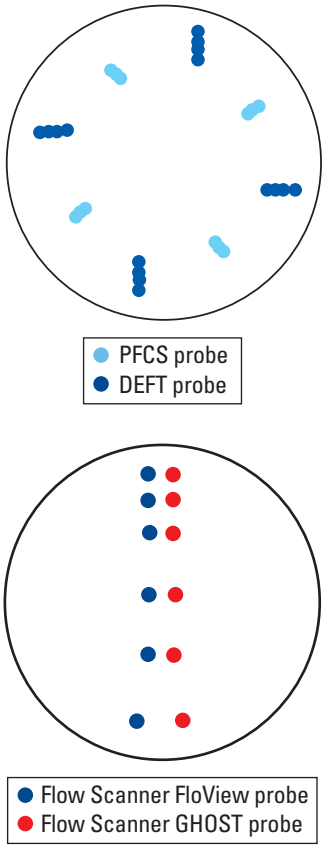

Figure 12-34. Relative proximity of water holdup probes to the high side of 6-in-ID pipe.

Reference

Whittaker, A.C.: "Methods and Systems for Interpreting Multiphase Fluid Flow in a Conduit," US Patent Application Publication No. 20120166157 (December 4, 2011).

13 Production Logging Interpretation Equations and Techniques

Single-phase flow

Single-phase flow is typically found in gas or water injection wells. Less commonly, dry gas and water-free oil are encountered in producing wells.

To calculate the flow rate of a single phase flowing inside a pipe, the pipe area and the average velocity are needed. Typically a spinner or turbine measurement in revolutions per second (rps) is used and then converted into a tool velocity and subsequently a mixture velocity (for details, see the "Spinner Velocity Tools" chapter).

The equation for the downhole flow rate is

$$q_{dh} = v_m A, \tag{13-1}$$

which can be rewritten as

$$q_{dh} = \frac{v_m \pi d^2}{4}. \tag{13-2}$$

In a world of SI units, Eq. 13-2 would suffice, but in oilfield units

$$q_{dh} = 1.4 v_m d^2, \tag{13-3}$$

where

q_{dh} = downhole flow rate, bbl/d
v_m = average velocity, ft/min
d = pipe internal diameter, in.

The SI equivalent is

$$q_{dh} = 0.73 v_m d^2, \tag{13-4}$$

where q_{dh} is in m³/d and v_m in m/min, but d remains in inches.

Shrinkage from downhole to surface means that for an oil well

$$q_{o_{sc}} = \frac{q_{o_{dh}}}{B_o}, \tag{13-5}$$

$$q_{sg_{sc}} = q_{o_{sc}} R_{so}, \tag{13-6}$$

whereas for a gas well

$$q_{g_{sc}} = \frac{q_{g_{dh}}}{B_g}. \tag{13-7}$$

For a water producer

$$q_{w_{sc}} = \frac{q_{w_{dh}}}{B_w}, \tag{13-8}$$

$$q_{sg_{sc}} = q_{w_{sc}} R_{sw}, \tag{13-9}$$

whereas for a water injector Eq. 13-8 is still used but Eq. 13-9 can be dropped.

For a well flowing oil and water and gas

$$q_{g_{sc}} = q_{o_{sc}} R_{so} + q_{w_{sc}} R_{sw} + \frac{q_{g_{dh}}}{B_g}, \tag{13-10}$$

where

B = shrinkage factor (dimensionless)
R = solution gas ratio, standard ft³/stock-tank bbl [standard m³/m³]

with the subscripts

o = oil
g = gas
w = water
sg = solution gas
sc = standard conditions
dh = downhole
sw = solution in water
so = solution in oil.

The origin of shrinkage factors and solution gas ratios is in the "PVT for Production Logging" chapter.

Two-phase flow

To calculate the flow rate of a two-phase mixture inside a pipe, one holdup measurement and two velocities are needed. However, the spinner provides only one mixture velocity. Therefore, the missing measurement has to be supplied by a slip correlation (see "The Downhole Environment" chapter for more information on how slip correlations work).

In two-phase flow the slip velocity is the difference in velocity between the light and heavy phases:

$$v_s = v_{lp} - v_{hp}. \tag{13-11}$$

The phase holdups sum to 1:

$$Y_{lp} + Y_{hp} = 1, \tag{13-12}$$

and the mixture velocity is equal to the sum of the holdup-weighted phase velocities:

$$v_m = Y_{lp} v_{lp} + Y_{hp} v_{hp}. \tag{13-13}$$

By substitution, the light-phase holdup is eliminated:

$$v_m = \left(1 - Y_{hp}\right) v_{lp} + Y_{hp} v_{hp}, \tag{13-14}$$

and then the light-phase velocity is substituted for by $(v_s + v_{hp})$:

$$v_m = \left(1 - Y_{hp}\right)\left(v_s + v_{hp}\right) + Y_{hp} v_{hp}. \tag{13-15}$$

Multiplying everything out and solving for v_{hp} gives

$$v_{hp} = v_m - \left(1 - Y_{hp}\right) v_s. \tag{13-16}$$

Given that

$$q_{hp} = Y_{hp} v_{hp} A, \tag{13-17}$$

substituting Eq. 13-16 into Eq. 13-17 gives

$$q_{hp} = Y_{hp}\left[v_m - \left(1 - Y_{hp}\right) v_s\right] A. \tag{13-18}$$

Similarly,

$$q_{lp} = \left(1 - Y_{hp}\right)\left(v_m + Y_{hp} v_s\right) A, \tag{13-19}$$

where
v_s = slip velocity
v_{lp} = light-phase velocity
v_{hp} = heavy-phase velocity
Y_{lp} = light-phase holdup
Y_{hp} = heavy-phase holdup
v_m = mixture velocity
q_{hp} = heavy-phase flow rate
A = internal pipe area
q_{lp} = light-phase flow rate.

Equations 13-18 and 13-19 enable converting a spinner mixture velocity, holdup measurement, slip correlation velocity, and the internal pipe area into a heavy-phase flow rate and a light-phase flow rate.

Rearranging for oilfield units and using the pipe diameter delivers the following equations:

$$q_{hp} = 1.4 Y_{hp}\left(v_m - \left(1 - Y_{hp}\right) v_s\right) d_{\text{pipe}}^{\,2}, \tag{13-20}$$

$$q_{lp} = 1.4\left(1 - Y_{hp}\right)\left(v_m + Y_{hp} v_s\right) d_{\text{pipe}}^{\,2}, \tag{13-21}$$

Sidebar 13A. Adjustment for tool size

In the case of a holdup tool that occupies a significant fraction of the pipe cross-sectional area (e.g., a 1 11/16-in Gradiomanometer tool inside a 4-in-ID pipe), a further complication arises. The mixture velocity is typically measured by a fullbore flowmeter that occupies a negligible fraction of the pipe cross section at the point where the measurement is made. However, the slip velocity comes primarily from the holdup reading, which is made in an annulus of significantly reduced cross-sectional area. Therefore, some Schlumberger interpretation programs reduce the size of the slip flow rate in proportion to the reduction in area:

$$q_{hp} = Y_{hp}\left(v_m - \left(1 - Y_{hp}\right) v_s \frac{A'}{A}\right) A, \tag{13A-1}$$

where
A' = flowing cross-sectional area around the density or holdup measurement.

However, this model assumes that a slip correlation velocity developed for an empty pipe can be accurately applied to a small annulus around a logging tool. This is probably not the case, and it is not obvious that this refinement improves the accuracy of the flow rate computation.

and for SI units:

$$q_{hp} = 0.73 Y_{hp}\left(v_m - \left(1 - Y_{hp}\right) v_s\right) d_{\text{pipe}}^{\,2}, \tag{13-22}$$

$$q_{lp} = 0.73\left(1 - Y_{hp}\right)\left(v_m + Y_{hp} v_s\right) d_{\text{pipe}}^{\,2}, \tag{13-23}$$

where
q = flow rate, bbl/d [m³/d]
v = velocity, ft/min [m/min]
d_{pipe} = pipe internal diameter, in.

The shrinkage factors from single-phase flow still apply to convert the downhole answers to surface flow rates.

Three-phase flow

To calculate the flow rate of a three-phase mixture inside a pipe, two holdup measurements and three velocities are needed. Holdup measurements are easily obtained with a Gradiomanometer density and holdup probes for water, gas, or both; however, there is normally just one spinner-derived mixture velocity. Therefore, similar to the approach for two-phase flow, the two missing velocity measurements have to be supplied by two slip correlations.

The three-phase flow calculations start with the gas-liquid slip, gas and liquid holdups, and flow rate of the gas and liquid mixture:

$$v_{s_{gl}} = v_g - v_l, \tag{13-24}$$

$$Y_g + Y_l = 1, \tag{13-25}$$

$$v_m = Y_g v_g + Y_l v_l. \tag{13-26}$$

Proceeding in a similar fashion to Eqs. 13-14 through 13-18 gives

$$q_l = \left(1 - Y_g\right)\left(v_m - Y_g v_{s_{gl}}\right)A, \tag{13-27}$$

$$q_g = Y_g\left(v_m - \left(1 - Y_g\right)v_{s_{gl}}\right)A, \tag{13-28}$$

and the liquid velocity

$$v_l = \frac{q_l\left(1 - Y_g\right)}{A}. \tag{13-29}$$

In exactly the same way, the liquid flow rate is divided into oil and water:

$$q_w = Y_w\left(v_l - \left(1 - Y_w\right)v_{s_{ow}}\right)A, \tag{13-30}$$

$$q_o = \left(1 - Y_w\right)\left(v_l + Y_w v_{s_{ow}}\right)A, \tag{13-31}$$

where

$v_{s_{gl}}$ = gas-liquid slip velocity
$v_{s_{ow}}$ = oil-water slip velocity
v_g = gas velocity
v_l = liquid velocity
Y_g = gas holdup
Y_l = liquid holdup
Y_w = water holdup
q_l = liquid flow rate
q_g = gas flow rate
q_w = water flow rate
q_o = oil flow rate.

The use of a gas-liquid slip correlation followed by an oil-water slip correlation is not strictly correct because neither correlation was developed to work in conjunction with the other, but in the absence of a true three-phase slip correlation no alternative is possible.

Because three-phase flow is really too complicated to be processed using a forward model and the preceding equations, the conversions to oilfield and SI units are not provided. The proper approach to a three-phase flow interpretation is to use a global solver.

Global solver

The global solver, as used in PLGLOB, BorFlow, Emeraude, and PLATO production interpretation software, starts by making a guess of the downhole oil and water and gas flow rates. Using the necessary number of slip correlations as defined by the log analyst, the flow rates are converted into phase holdups and phase velocities (Fig. 13-1).

With the wellbore now described in terms of phase velocity and phase holdup, a tool response model is used to predict what the different logging tools would measure under these conditions.

The spinner model is very simple and assumes a symmetrical velocity profile around the pipe axis with a curve described by Prandtl or a similar empirical model. The size of the spinner and the pipe diameter are used to determine the appropriate spinner correction factor. A switch can be toggled to use either a volumetric or a mass-fraction mixing model for multiphase flow. The resulting apparent spinner velocity is not corrected for recirculation, horizontal stratified flow, high-speed gas-liquid annular flow, or other conditions.

The Gradiomanometer model for the deviation-corrected well fluid density (WFDE) from a Gradiomanometer PGMS sonde works out the mixture density, frictional pressure drop on an eccentred tool with inverted pressure ports, acceleration effects, and deviation corrections and predicts what the Gradiomanometer measurement should be. This is a good, rugged tool response model albeit highly sensitive to the unknown parameter of pipe roughness in high-velocity wells. If the Gradiomanometer measurement was recorded with the wrong deviation correction, then the filtered density uncorrected for deviation (UWFD) channel can be used instead with the revised model omitting the wellsite deviation correction.

Because standard global solvers work with average pipe values, the water and gas probe holdup values from the Flow-Caliper Imaging Sonde (PFCS), Digital Entry and Fluid Imaging Tool (DEFT), and GHOST gas holdup optical sensor tool are first converted to average pipe holdup readings by using whichever averaging technique and droplet persistence correction factor the log analyst feels are appropriate. The holdup tool response model makes no corrections for bubble shear and emulsion blinding.

The WFL water flow log velocity recorded at the wellsite is an annulus velocity boosted by the factor $d_{\text{pipe}}^2/(d_{\text{pipe}}^2 - d_{\text{tool}}^2)$, where d_{pipe} is the pipe ID and d_{tool} is the tool OD. The WFL model in the solver must incorporate the same factor although the effect is significant only in smaller completions.

The TPHL three-phase holdup log modeled holdups can be taken directly from the flow rate inversion to velocities and holdups.

From the Flow Scanner production logging system, the only channels that should be loaded into the solver are the computed phase flow rates q_w, q_o, and q_g because the solver is not being used to calculate the flow rates. The objective of running the interpretation engine is to run the global regression (see the "Global regression" section in this chapter).

Unless the flow rate was correctly guessed, there is a discrepancy between the tool response model outputs and the actual tool measurements. The discrepancies are used to compute an error:

$$E = \Sigma\left(M_i - m_i\right)^2, \tag{13-32}$$

where

E = error
M_i = modeled response of a tool in the interpretation
m_i = physical measurement from a tool in the interpretation.

Incrementing or decrementing the individual phase flow rates causes the error to shrink and reach a minimum. The minimum is the solution and gives the phase flow rates that correspond to the measured tool readings.

Weighting of residuals

A simple two-phase flow situation with one holdup measurement and one spinner velocity normally finds a solution in which the holdup and spinner can be matched exactly and the error function goes to zero. But in the case of a Gradiomanometer measurement, water holdup probes, and spinner velocity measuring two-phase flow, it is not normally possible to match both the Gradiomanometer measurement and the water holdup probes. The error or uncertainty with which the Gradiomanometer density holdup and a probe-derived holdup are measured is about 5%–10%.

One of the key jobs of a log analyst is to determine which measurements are more trustworthy. The favored measurements are then given more weight with a modification of Eq. 13-32:

$$E = \Sigma\left(M_i - m_i\right)^2 \times w_i, \tag{13-33}$$

where

w_i = weighting factor determined by the log analyst.

A simple weighting function such as this automatically applies more weight to measurements with larger numbers. For example, a spinner reading 10 rps and modeled at 9 rps generates a squared error signal of 1, whereas a holdup reading of 1 that is modeled as 0.9 generates a squared error signal of 0.01. Density readings give still smaller error signals.

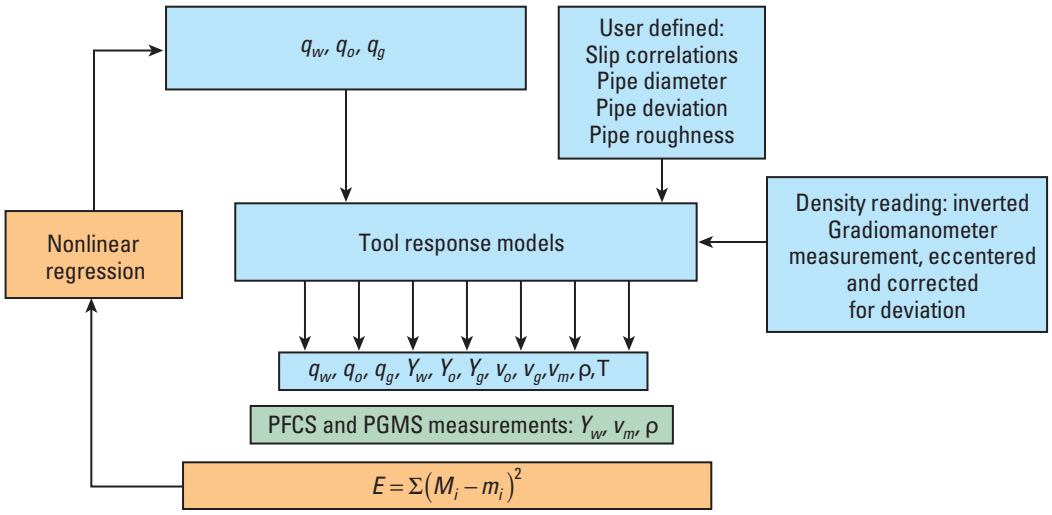

Figure 13-1. Global solver data flow.

Some software packages such as BorFlow analysis try to automatically adjust the initial value of w_i to make all things equal. Other software packages such as Emeraude use a revised error function of the form

$$E = \sum \left(1 - \frac{M_i}{m_i}\right)^2 \times w_i. \qquad (13\text{-}34)$$

The weighting functions normally vary from the top to the bottom of a log. Toward the bottom of a well in regimes of recirculation, the spinner velocity is unreliable and a weighting function of 0.1 or 0.01 may be used. At the top of the well where the mixture velocity approaches or exceeds the FloView probe limits, the water holdup weighting should similarly be reduced.

Residual weighting of slip velocities

A global solver starts with a flow rate and via the application of a slip model creates downhole holdups and downhole phase velocities. Whereas a spinner velocity and a holdup measurement can be given a residual weighting in the global solver, the slip model velocity is generally treated as an absolute that must be honored. However, the accuracy of a slip velocity correlation does not deserve this degree of confidence. State-of-the-art global solvers now allow some wriggle space for the slip velocity to move, thus giving some matching wriggle space to the modeled holdup. PLATO and Emeraude software operate in this way. PLATO, besides finding the flow regime and slip velocity through optimization, also allows flow regimes (and the concomitant slip velocity) to be enforced or forbidden with a controllable transition between flow regimes.

Local minima

Because of the presence of many nonlinear equations inside the slip correlations, the route to the best error, the global minimum, can pass through a local minimum. The global solver stops at the local minimum and delivers the wrong answer (Fig. 13-2). The log analyst normally detects this as a poor match or reconstruction over a zone. Restarting the global solver from a different initial set of conditions may help to find the global minimum.

Use of a drift-flux slip correlation should improve the ability of the global solver to find the global minimum because the discontinuities in slip velocity associated with changing flow regimes have been smeared away. However, nothing is free in life, and the drift-flux correlations probably deliver less accurate slip velocity values.

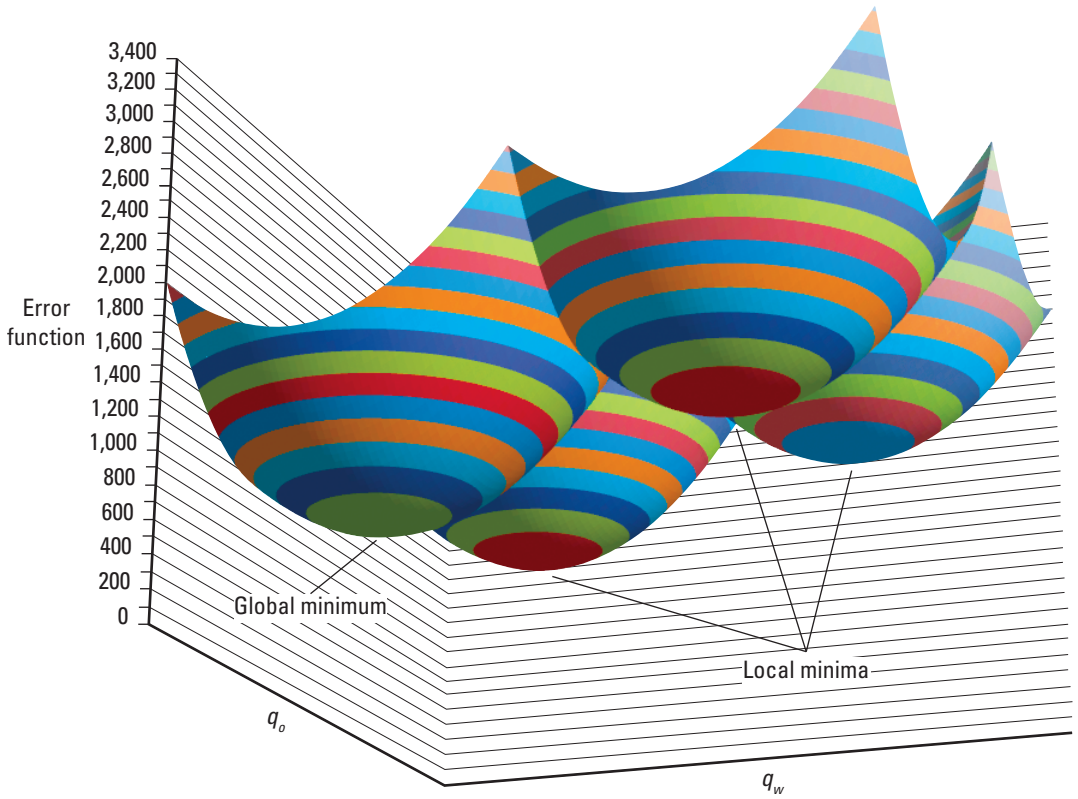

Figure 13-2. Local minimum errors.

Hybrid genetic algorithm

An automated approach to the problem of local minima uses genetic algorithms (Goldberg, 1989). Before starting the normal global solver, an extended series of random flow rate guesses are tried and an associated error computed. After several thousand guesses have been tried, the guess that corresponds to the smallest error is probably in the vicinity of the global minimum. The global solver is therefore started from this best guess and should quickly converge to the correct answer.

Global solver log quality control display

The log analyst spends a lot of time adjusting parameters inside the global solver in order to match the modeled tool response to the measured tool response. Figure 13-3 shows a simple case of a density curve and a spinner velocity in a gas-water well.

When the measured and the modeled are in agreement over the entire log interval, the interpretation is consistent with the measurements. Consistency is considered much better than inconsistency, but even with a good consistency if the tool response model is wrong or the slip velocities are in error then the flow profile can still be wrong.

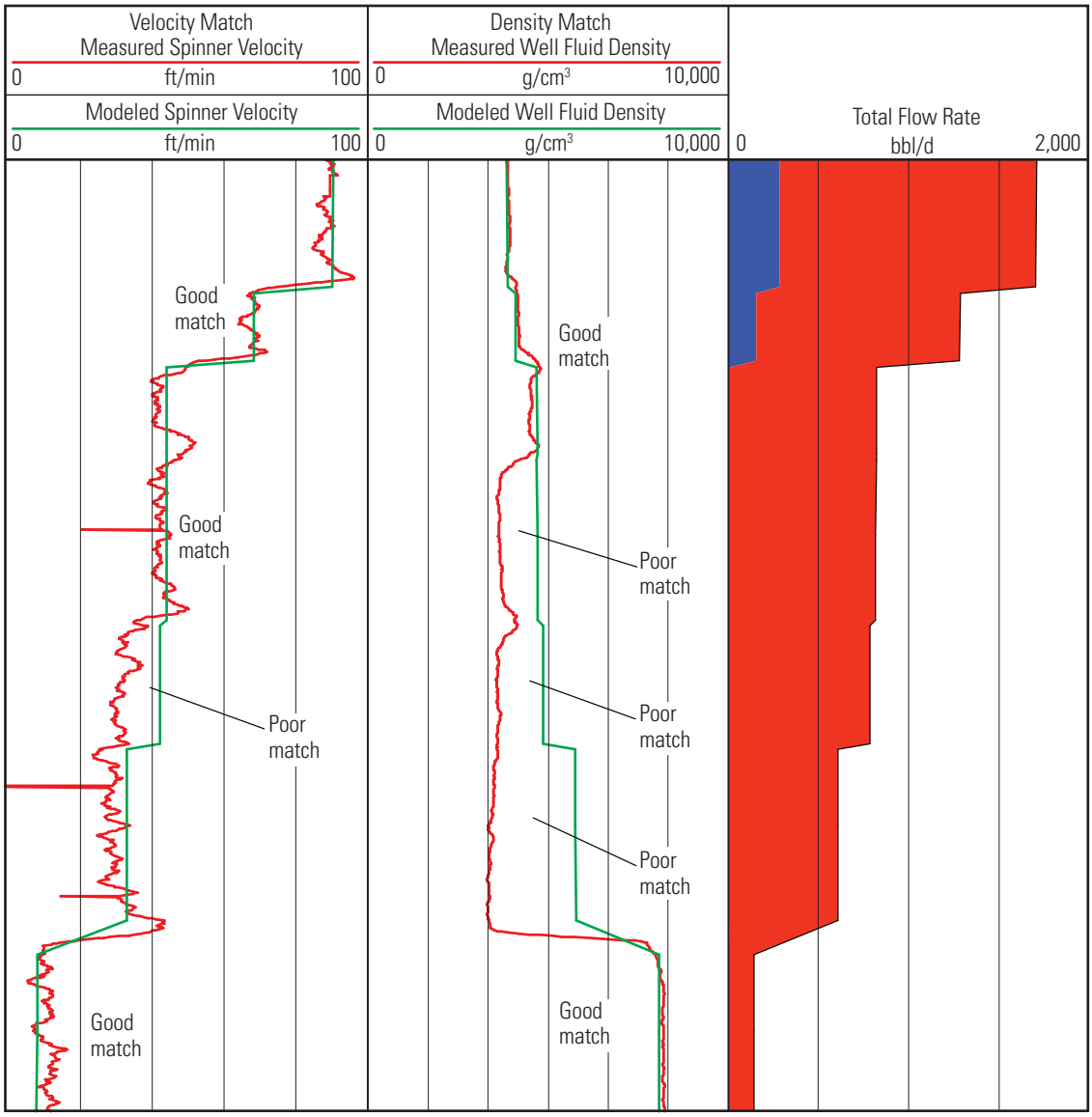

Figure 13-3. Poor match of spinner velocity and density. (Brachfield S.E. [Cotton Valley] field, Rusk County, Texas, USA, courtesy of Fidelity Exploration & Production Company)

In the log in Fig. 13-3, there is a large region where the density model and density measurement refuse to converge. It is in these conditions that production log analysts start to earn their salary. Something is wrong and it could easily be one of the following:

- Is the correct well diameter being used?
- Is the well deviation correctly set up?
- Has the density reading been corrected for deviation?
- Has the density been corrected for the correct deviation?
- Has the density reading been twice corrected for deviation?
- Is the density reading drifting? Does it repeat from pass to pass?
- Is the well stable? Do the pressure readings repeat from pass to pass?
- Have the PVT parameters been correctly entered? Are the downhole density values of water and gas correct?
- Does the density reading need a small shift to the left or right? (The Gradiomanometer density error can be significant.)
- Is this gas-water well also flowing oil?
- Is the gas-liquid slip correlation giving an erroneous velocity?
- Or something else altogether?

Having checked the ID, deviation, and PVT numbers (Fig. 13-4), no mistake was found. The density reading had been correctly modeled as a PGMS WFDE channel. The density curves and pressure curves were repeating well. The density curve in the bottom of the log interval was matching the expected density of water with a little bit of gas holdup; therefore, no shift of the density could be justified.

Where the density match is the worst, the Dukler model's slip velocity was ~69 ft/min (Fig. 13-5) (see "The Downhole Environment" chapter for information on modeling). The density identifies the borehole as mainly gas-filled, but with the spinner velocity reading just 28 ft/min, the only way the equations would balance was if there were a negative flow rate of water (down flow of water). Quite correctly, the interpretation software refused to allow countercurrent flow and the poor interpretation match resulted.

Alternative slip models to the Dukler model can be tried, and those that deliver a smaller slip velocity would allow matching the curves but now there would be too much water computed at surface because a reduced slip velocity means more water being lifted to surface. This well did not have huge amounts of water measured at surface.

What was needed was a model that said that the spinner was affected more by the dense slow-moving water and relatively lightly by the fast low-density gas. This describes the mass-fraction spinner response (Whittaker, Lenn, and Hammond, 2005), called the *m*-weighted spinner response (Fig. 13-6). Turning on this model brought the measured and modeled (called calculated in Fig. 13-6) results into agreement.

Most commercial log analysts would stop at this point; however, the mass-fraction spinner model is only supposed to work for bubble flow and the Dukler model predicted slug flow downhole. In slug flow the

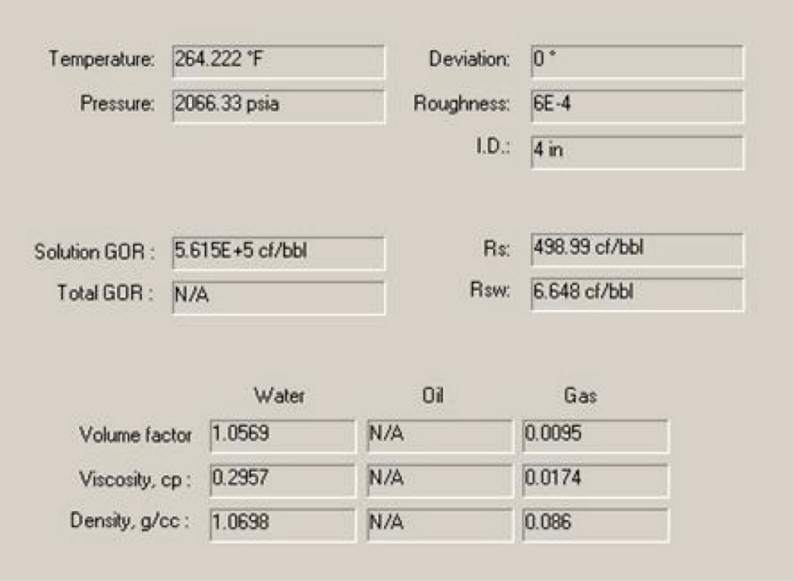

Figure 13-4. Review of PVT, ID, and deviation.

spinner responds first to a gas slug velocity and then to a liquid velocity, so the average spinner velocity is the normal holdup-weighted average of the gas- and water-phase velocities. Possibly the Dukler model is mistaken about the flow regime. For these flow rates, deviation, and casing size, there may actually have been bubble flow, but in this case the slip velocity would be computed differently. A trawl through alternative slip models may reveal a model that predicts bubble flow and a similar slip velocity. If such a slip model is found, then the entire interpretation would be tried with the new model.

For the production log analyst to correctly weight and match the modeled and measured curves, the analyst must have an understanding of the tool physics and errors, the derivation and accuracy of the slip correlations, and the multiphase flow interpretation models. Without this understanding, the situation can easily resemble a well-known exercise involving a lot of monkeys with typewriters.

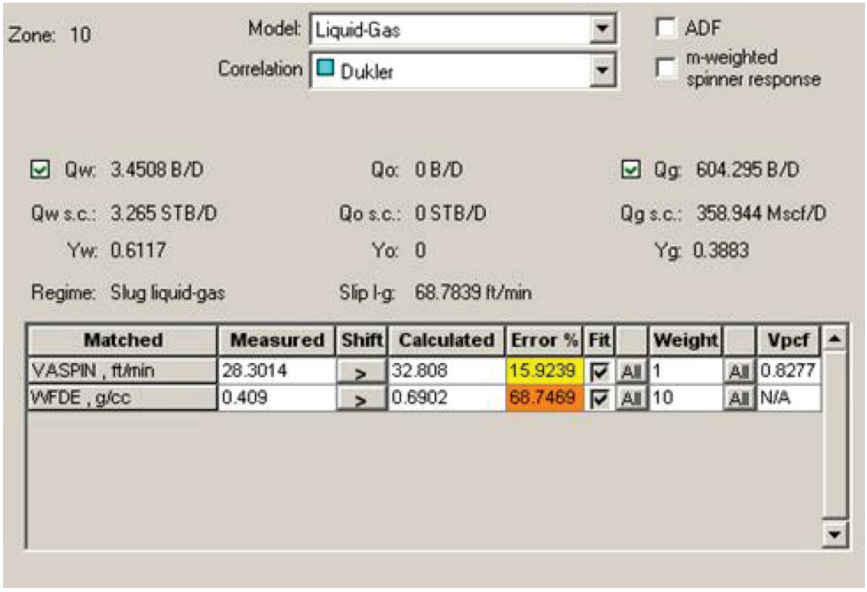

Figure 13-5. Global solver display.

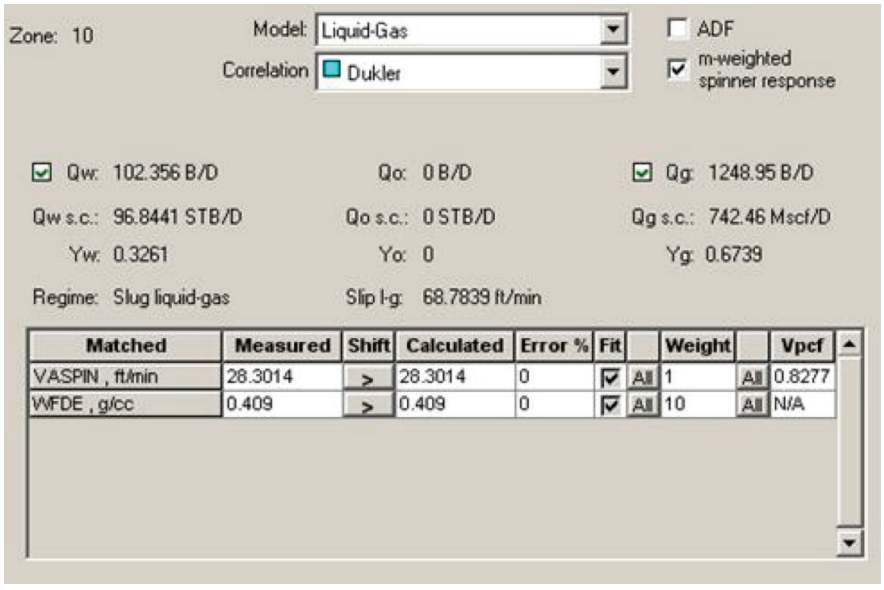

Figure 13-6. Global solver with mass-fraction spinner response enabled.

Downhole separators and density shifts

Because a global solver tries to find the smallest match error at each depth (or stable interval) in the well, the answer computed in zone n may be incompatible with zone $n + 1$. One example of this is the downhole separator. This is a producing interval that appears to take one phase while producing another phase. The global solver is quite happy with the match above and below the producing interval but does not take the analysis far enough. An example of this effect is shown in Fig. 13-7.

A look at the density above 5,400 ft shows that the interpretation is ignoring the density and using only the water holdup. Perhaps the top perforation is creating bubble shear inside the formation and although the

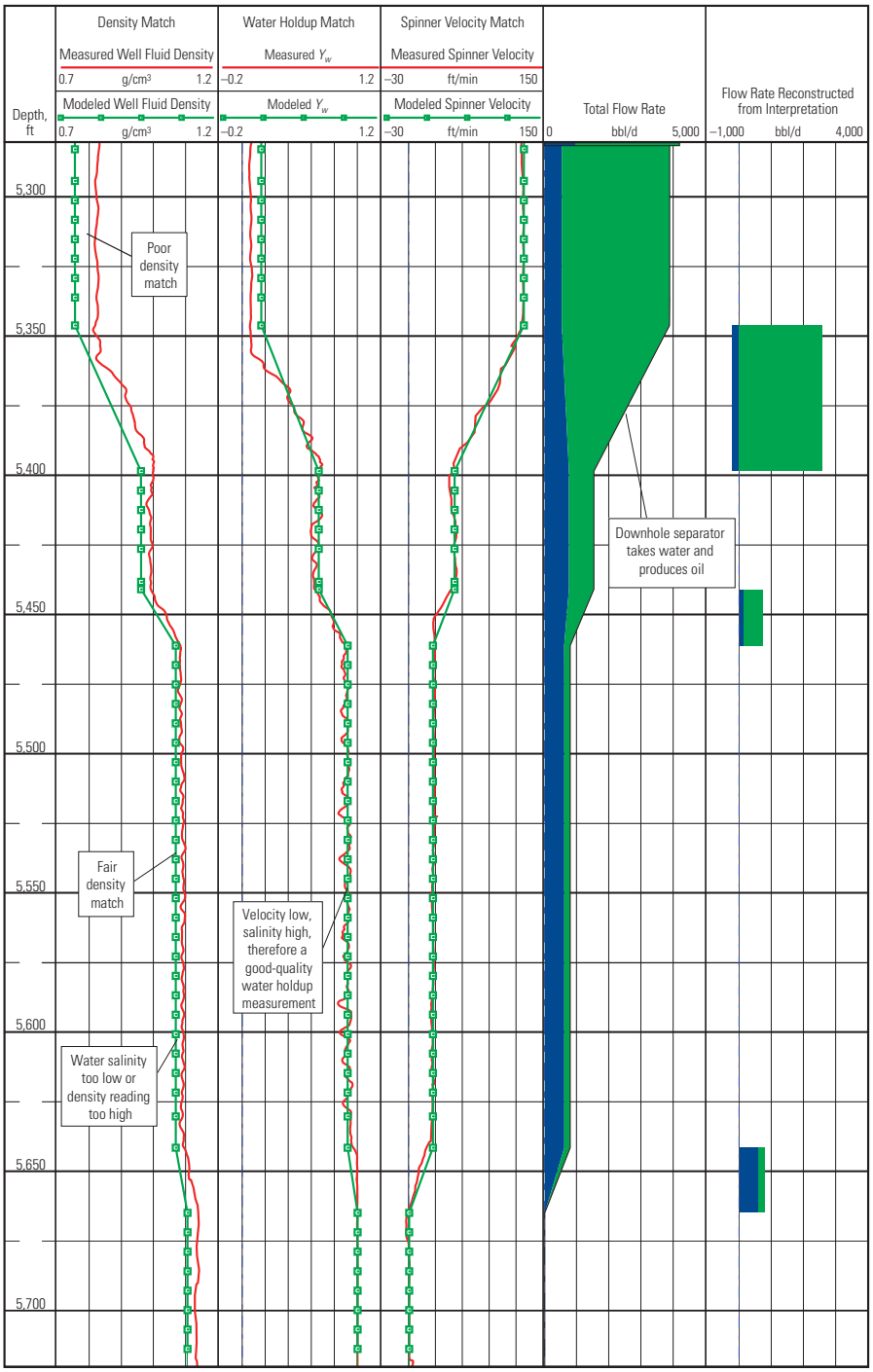

Figure 13-7. Pseudo separator effect at the start of interpretation.

bubble velocity is below 1 m/s, could the water holdup probes still be missing a lot of the water bubbles? Turning off the water holdup in the global solver for the top zone is a good first step.

The next step is to look at the bottom of the log and observe that the water density does not match at 5,680 ft. Because this is at the bottom of the log, stagnant high-density completion fluid could be present, or there is an error in the water salinity, or a density shift is needed, or any combination of these three. An experienced log analyst knows to resist the urge to calibrate spinner and density responses in the sump.

Another density measurement is available. In a stable well, the pressure can be differentiated with respect to depth to deliver a pressure gradient density (*dp/dZ*, for which the curve mnemonic is DPDZ; Fig. 13-8). Because errors from a pressure gauge tend to be constant for small changes in pressure and temperature, the derived density has a very good accuracy albeit with a relatively poor vertical depth resolution. Loading the DPDZ density into the interpretation shows that the modeled water density needs to be higher. Increasing the water salinity from 195,000 to 220,000 ppm provides a good match between the DPDZ density and the FloView water holdup.

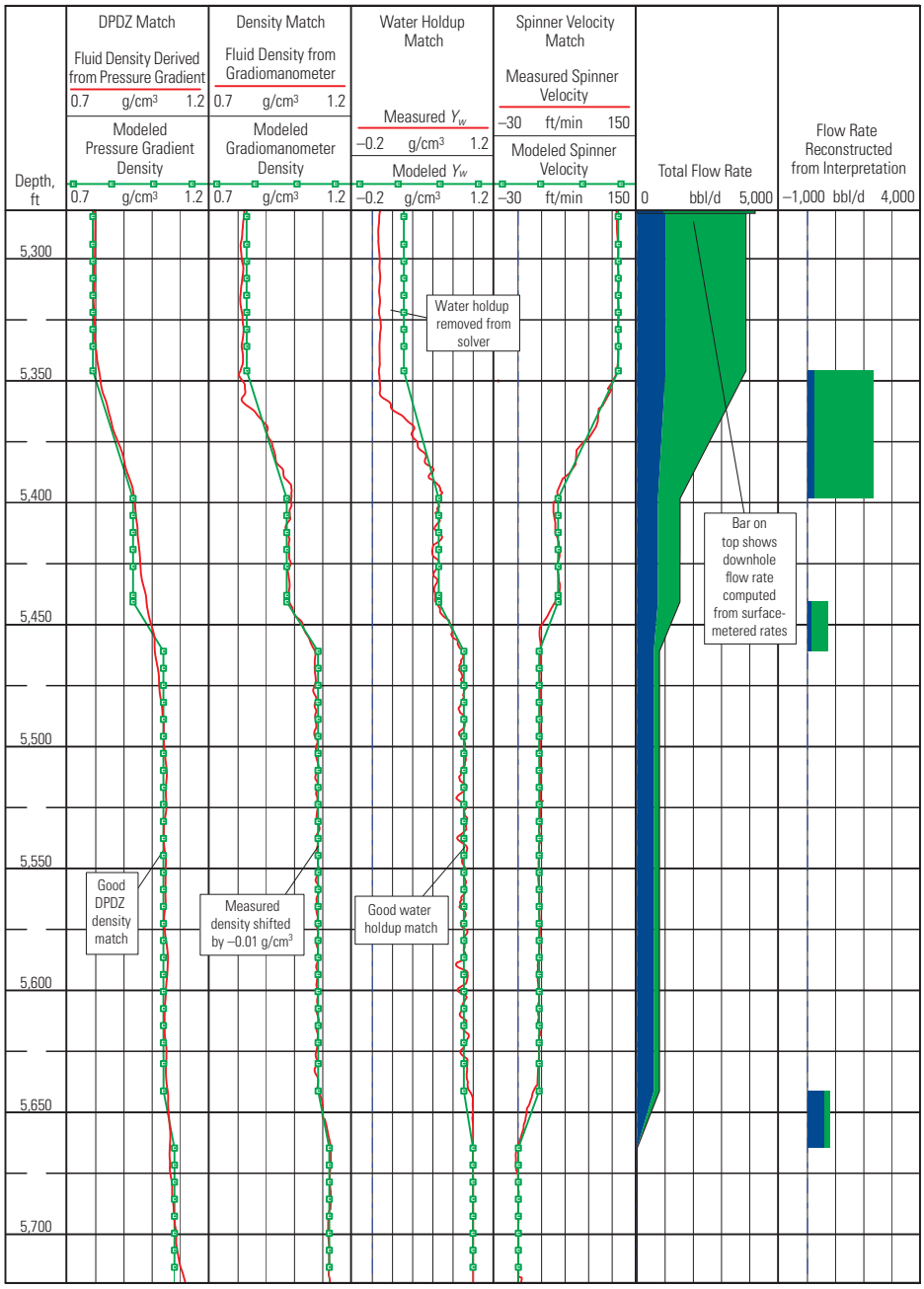

Figure 13-8. Pseudo separator effect at the end of interpretation.

However, the Gradiomanometer density is still reading high by 0.01 g/cm³. The quoted accuracy of the Gradiomanometer measurement under these conditions is 0.02 g/cm³; therefore, the Gradiomanometer measurement is shifted by –0.01 g/cm³. The small difference in readings results because the "measured well fluid density" curve is deviation corrected whereas the DPDZ curve is not.

The downhole oil density was computed from the basic PVT correlation of Standing (see the "PVT for Production Logging" chapter for information on PVT correlations). This should give errors of >10% in the computed oil density; however, in this well the computed oil density must be close to the truth because the holdup and density measurements are in good agreement.

A plug was set to isolate the lowest set of perforations and the flow profile in Fig. 13-9 was recorded a year later. Although one source of water was banished, another has appeared to take its place. Managing water production is a defensive action in a war that can ultimately only be lost.

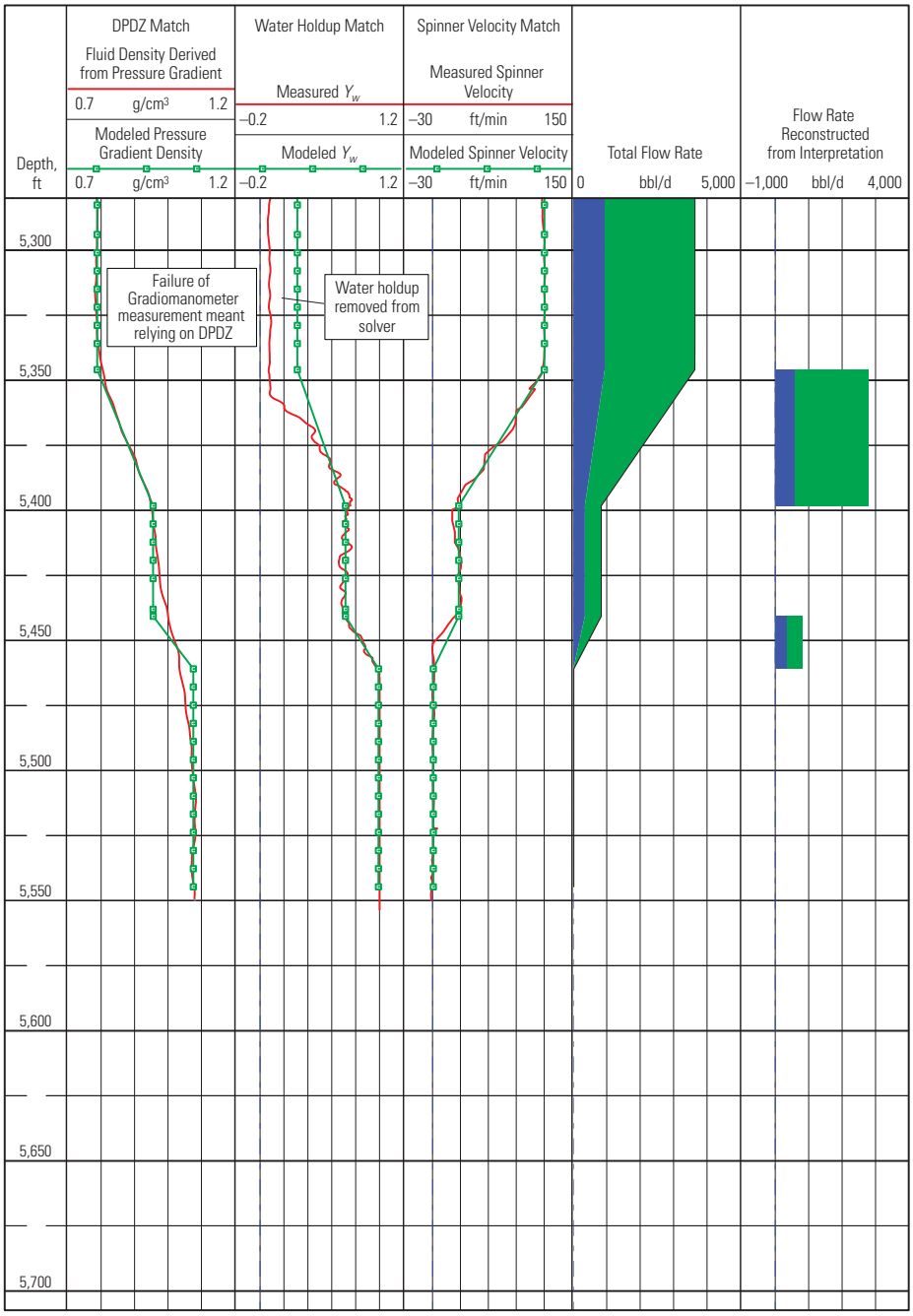

Figure 13-9. Well in Figs. 13-7 and 13-8 one year after workover.

Global regression

Although global solvers for petrophysical interpretations are free to choose the least-error solution at every depth, the situation is different for production logging; at each depth the flow rate measured is the sum of all contributions from deeper in the well. The computed flow rates at depth x must honor the computed flow rates at depth $x + 1$.

In the absence of crossflow or thief zones, a good condition to apply is that all flow rates should monotonically increase up the well. This changes Eq. 13-34 to the more complicated arrangement of Eq. 13-35 in Fig. 13-10, thus imposing constraints on the sign of the first differential of the flow rate with respect to depth and introducing a new term for the global error (E_{global}).

Stable interval 1	$E_1 = \sum\left(1-\frac{M_i}{m_i}\right)^2 \times w_i$
$dq_w > 0,\ dq_o > 0,\ dq_g > 0$	+
Stable interval 2	$E_2 = \sum\left(1-\frac{M_i}{m_i}\right)^2 \times w_i$
$dq_w > 0,\ dq_o > 0,\ dq_g > 0$	+
Stable interval …	$E_{\ldots} = \sum\left(1-\frac{M_i}{m_i}\right)^2 \times w_i$
$dq_w > 0,\ dq_o > 0,\ dq_g > 0$	+
Stable interval n	$E_n = \sum\left(1-\frac{M_i}{m_i}\right)^2 \times w_i$
	=
	$E_{\text{global}} = \sum_{i=1}^{i=n} E_i.$ (13-35)

Figure 13-10. Global regression to obtain Eq. 13-35.

Computing and optimizing a global regression error involves more CPU work than just optimizing a global solver once at each depth, but this is still well within the capabilities of quite basic desktop computers. However, if the length of the stable intervals is decreased until they match the sampling rate of the production logging tool measurements, then the computation task becomes nontrivial, with a need for fast computers and efficient code. Temperature interpretation with finely detailed global regression is driving code development in this direction.

Pseudo thief zones

The concept of a thief zone is so powerful that this is the first explanation many analysts reach for when confronted with a velocity that starts to decrease instead of steadily increasing.

For a thief zone to exist, the reservoir pressure must be lower than the wellbore pressure, thus causing flow from the wellbore into the reservoir. When the well is shut in, the wellbore pressure rises, increasing the pressure difference with the thief zone, and therefore increasing the flow rate into the thief zone. Therefore, any diagnosis of a thief zone in a flowing well should be confirmed by inspection of the shut-in data and observation of an even bigger thief zone. However, most thief zones disappear when shut in. Why is this?

The production logging toolstring does not measure a flow rate. The spinner measures revolutions per second that are converted into an apparent velocity that then becomes a mixture velocity and, finally, with the addition of a flowing cross-sectional area, a flow rate. For a given flow rate the mixture velocity decreases if the area increases. Apparent thief zones where the lost flow is exactly returned by a shallower producing interval are probably cases of increased flowing area through a poorly cemented annulus.

The first example in Fig. 13-11 is quite typical. The 7-in liner has a nominal internal diameter of 6.264 in. At X,800 ft the spinner velocity of 40 ft/min gives a flow rate of

$$\begin{aligned} q &= 1.4 v_{app} F_{vpc} d_{\text{pipe}_{\text{internal}}}{}^2 \\ &= 1.4 \times 40 \times F_{vpc} \times 6.264^2 \\ &= 1{,}980 \text{ bbl/d}, \end{aligned} \quad (13\text{-}36)$$

where

q = flow rate, bbl/d
v_{app} = apparent spinner velocity, ft/min
F_{vpc} = spinner correction factor (a typical value was used)
$d_{\text{pipe}_{\text{internal}}}$ = internal pipe diameter, in.

The same velocity is observed at X,640 ft, suggesting that the drop in velocity to 20 ft/min at X,670 ft is due to an increase in effective diameter. Assuming that the flow rate is conserved, the annulus is circular, and the same velocity occurs in both the casing and annulus, the following equation can be written:

$$q = 1.4 v_{app} F_{vpc} \left[{d_{\text{pipe}_{\text{internal}}}}^2 + \left({d_{\text{annulus}}}^2 - {d_{\text{pipe}_{\text{external}}}}^2 \right) \right], \quad (13\text{-}37)$$

where

d_{annulus} = unknown annulus diameter, in

$d_{\text{pipe}_{\text{external}}}$ = external pipe diameter, in.

Solving for d_{annulus} gives

$$\begin{aligned} d_{\text{annulus}} &= \sqrt{\frac{q}{1.4 v_{app} F_{vpc}} - {d_{\text{pipe}_{\text{internal}}}}^2 + {d_{\text{pipe}_{\text{external}}}}^2} \\ &= \sqrt{\frac{1{,}980}{1.4 \times 20 \times 0.9} - 6.264^2 + 7^2} \\ &= 9.40 \text{ in.} \end{aligned} \quad (13\text{-}38)$$

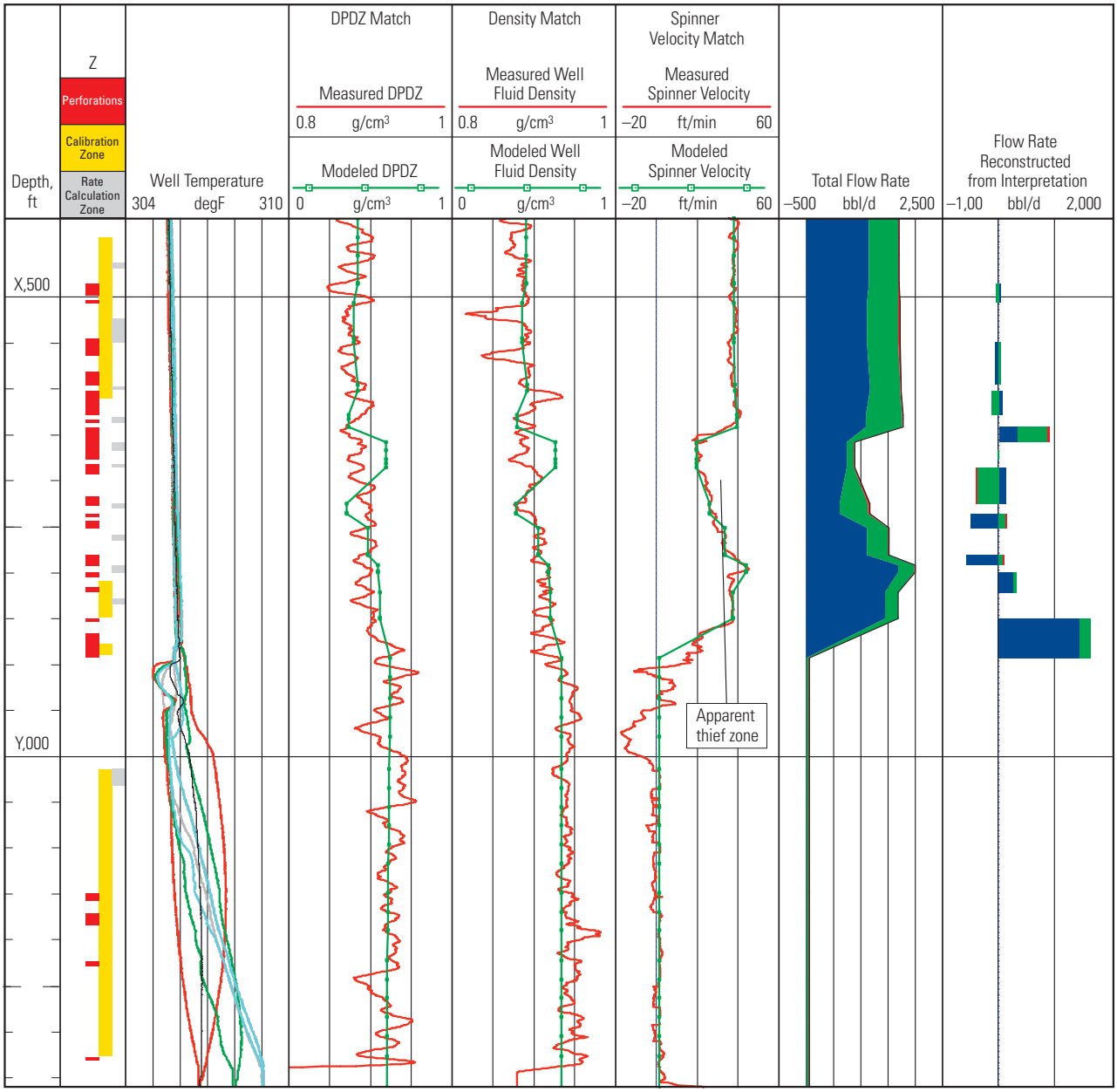

Figure 13-11. Pseudo thief zone.

Sidebar 13B. Background to the pseudo thief zone example in Figs. 13-11 and 13-12

In this very deep well tool movement is quite erratic because of the elasticity of the logging cable. This gives noisy spinner velocities, noisy pressure-gauge-derived densities, and noisy Gradiomanometer densities as a result of the yo-yo effect.

The temperature curves show poor repeatability below the fluid entry point because the thermal time constant of the temperature probe shows a logging direction and logging speed effect.

Therefore, the annulus appears to be approximately 1 in bigger than the bit size used to drill the original hole, which is a not-unrealistic situation. Eliminating the thief zone results in the flow profile of Fig. 13-12.

In the second example in Fig. 13-13, the reservoir engineer would be even more upset because there now appears to be a series of depleted layers in the gas well.

The log in Fig. 13-13 shows negligible flow from below 6,555 m, with the major gas entry at 6,550 m accompanied by a Joule-Thomson heating effect (due to the elevated reservoir pressure). From 6,430 m up to the top perforation, there appears to be a series of thief zones.

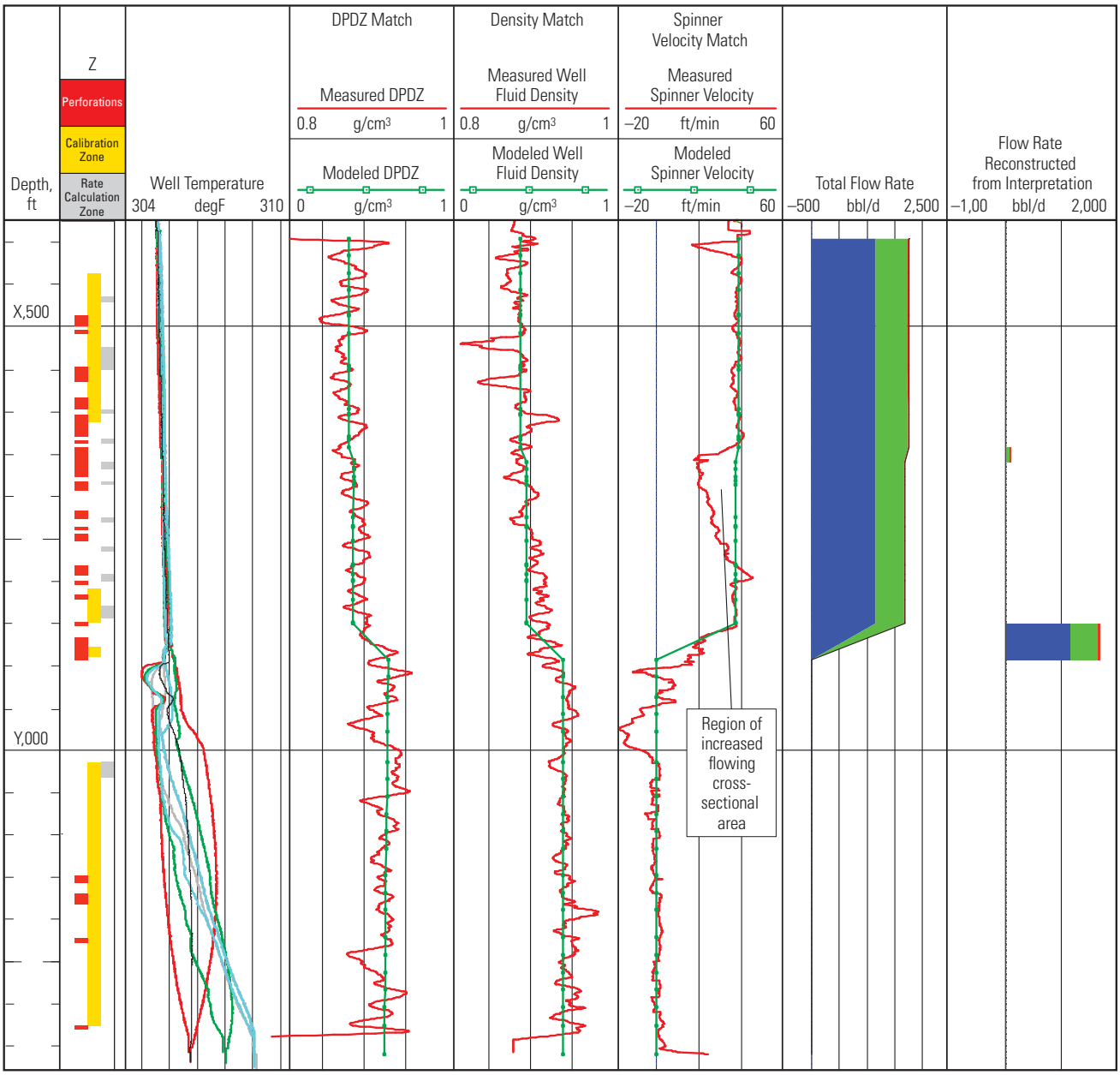

Figure 13-12. Example of pseudo thief zone after adjustment of the interpretation.

Close inspection of the log shows that most of the abrupt changes in spinner velocity occur at the very top or very bottom of a perforation set. This behavior is characteristic of flow into and out of a casing annulus.

Sidebar 13C. Joule-Thomson effects

Gas wells at reservoir pressure below about 5,000 psi show the commonly expected Joule-Thomson cooling effect. But taking the reservoir pressure above 7,000 psi normally results in a Joule-Thomson heating effect.

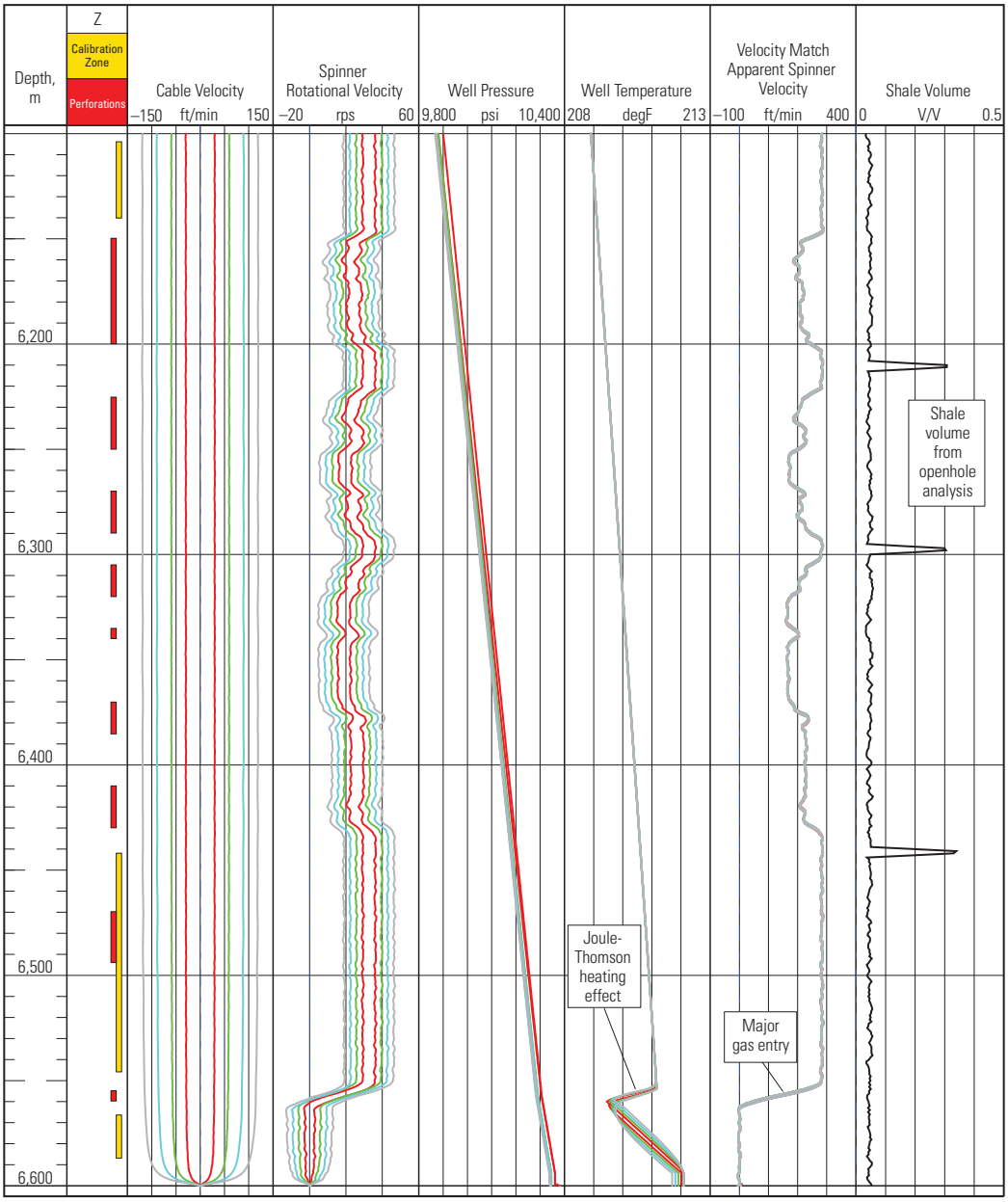

Figure 13-13. Series of pseudo thief zones in a gas well.

The shut-in data in Fig. 13-14 confirms that there are no underpressured zones; however, the spinner data exhibits an unusual anticorrelation, known to old timers as the “Mae West” effect, between the up spinners and down spinners. When the spinner is calibrated, the slopes can be seen to change from a minimum of 0.103 rps/ft/min to a maximum of 0.115 rps/ft/min (Fig. 13-15). The pressure gradient indicates that the wellbore contents are homogeneous. What is changing is the effective cross-sectional area, and this is producing a

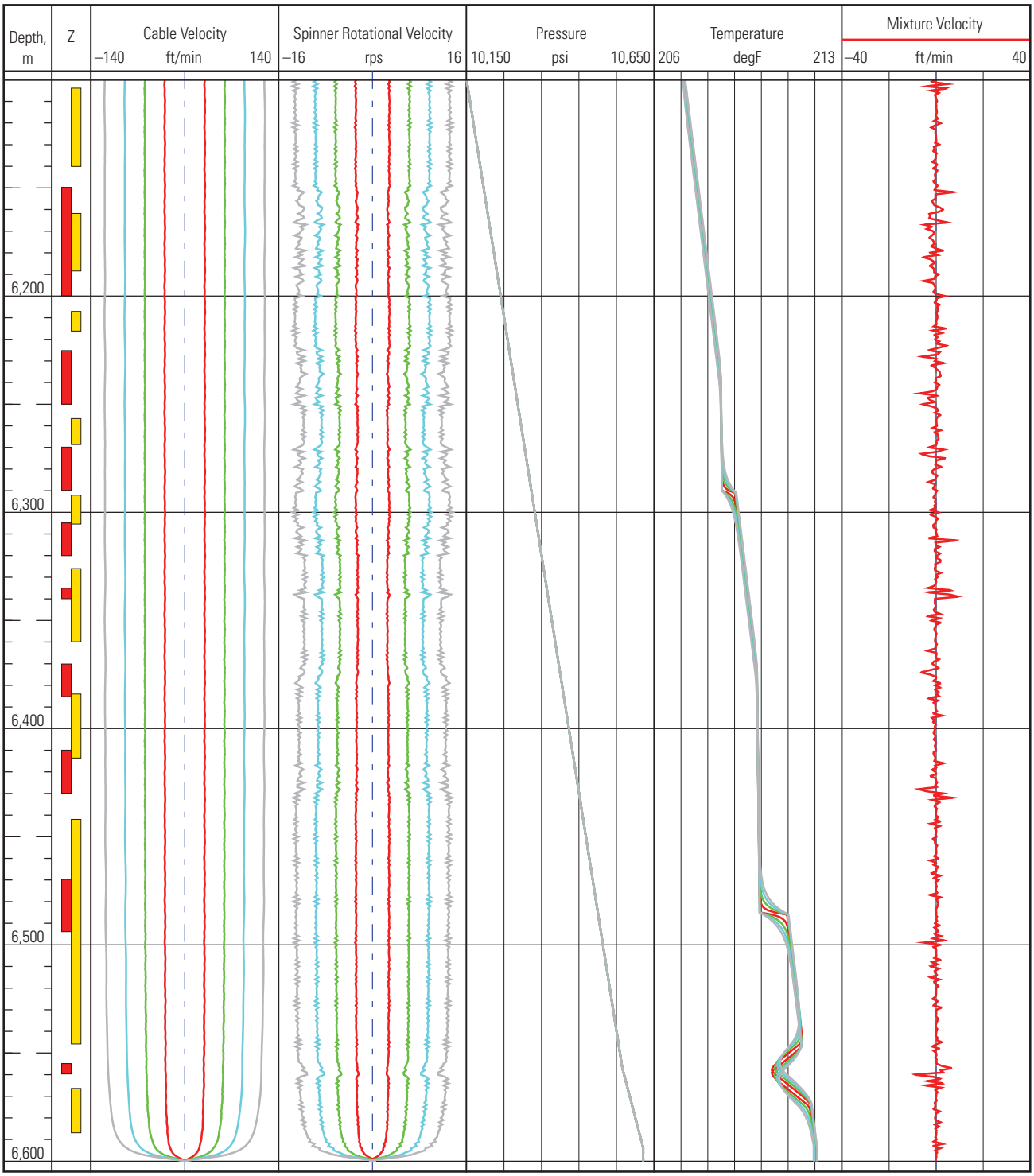

Figure 13-14. Shut-in log from the gas well in Fig. 13-13.

series of different spinner calibration slopes all with an apparent spinner velocity of near zero.

To complicate matters, a cement bond log showed good cement over the interval of the production log. However, an acid stimulation was performed after the bond log and appears to have removed the good cement. Interestingly, on the shale volume (V_{sh}) curve from open-hole logging plotted in Fig. 13-13, the small shale streaks appear to be sealing the annulus and forcing the gas back into the casing.

As a result of these conditions in this well, the vast majority of the production occurs at just one depth, 6,550 m.

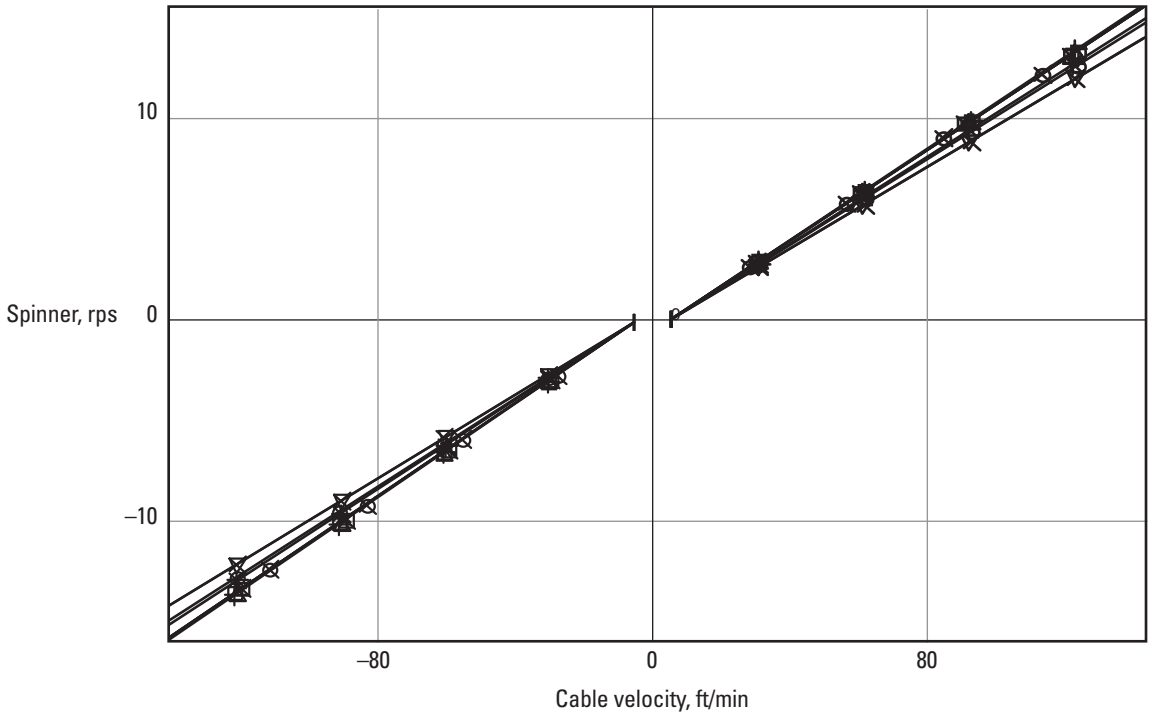

Threshold/Interval: 0.5

Calibration Zone, m	Slope (+)	Slope (–)	Interval (+), ft/min	Interval (–), ft/min	Interval Difference, ft/min
□ 6,103.9–6,140.1	0.115	0.115	5.00	–5.00	10.00
○ 6,161.8–6,188.4	0.108	0.108	5.00	–5.00	10.00
+ 6,207.1–6,216.2	0.115	0.115	5.00	–5.00	10.00
× 6,256.6–6,268.7	0.103	0.103	5.00	–5.00	10.00
△ 6,292.1–6,305.4	0.115	0.115	5.00	–5.00	10.00
▽ 6,326.0–6,359.9	0.103	0.103	5.00	–5.00	10.00
✳ 6,384.0–6,413.6	0.115	0.110	5.00	–5.00	10.00
⊠ 6,442.0–6,545.8	0.115	0.115	5.00	–5.00	10.00
⊗ 6,566.3–6,586.9	0.115	0.115	5.00	–5.00	10.00

Figure 13-15. Shut-in spinner calibration plots from the gas well in Fig. 13-14.

Global solvers and horizontal wells

Global solvers are applicable to horizontal wells as long as the slip correlations and tool models are appropriate to horizontal conditions. However, the default slip correlations and tool models are often inappropriate and the log analyst must take more control of the weightings in the residuals. For example, a differential density curve recorded at 80° deviation is processed, despite the absence of any usable information, unless the log analyst turns it off.

Segregated or stratified flow usually means that a centered spinner velocity is determined by just one phase. At 90% water holdup the spinner is returning a water velocity but the global solver believes that this is an oil-water mixture velocity. In some interpretation packages the spinner velocity can be exported and then reimported as a continuous water velocity measurement.

A number of slip correlations have been designed for vertical pipe use and extended to work in moderately deviated pipe. These models return arbitrary slip velocities if used in horizontal wells. The log analyst must check that the default slip correlation really is applicable. There are still very few horizontal slip correlations available, and the log analyst may decide to work with no slip velocity or just intelligent guesses about the slip velocity.

With the redundancy of measurements in a modern horizontal toolstring comes duplication of the channel names. Y_w could come from the RSTPro THPL three-phase holdup log or the FloView probes; v_w could come from the annulus measurement of an RSTPro WFL water flow log or a minispinner in stratified water. The log analyst is encouraged to use informative and distinctive channel names such as Vw_WFL, Vw_FSI, Vw_SPIN, Yw_TPHL, and Yw_PFCS.

Temperature interpretation

The heat flux from the Earth's core to the Earth's surface is about 60 to 100 mW/m^2. Because the sedimentary rocks that are logged have a finite thermal conductivity, there is a temperature gradient from deeper to shallower sections. Typical geothermal gradients range from about 1.5 to 3.0 degF/100 ft [0.8 to 1.7 degC/30 m]. Because different rocks can have different values of thermal conductivity, the slope of the geothermal temperature can correlate with lithology. Wells do not always have a constant deviation, and changes in the well trajectory also change the slope of the temperature gradient. Nevertheless, when making a temperature interpretation of production logging data it is normal practice to assume that the temperature gradient is a straight line (which is sometimes corrected for deviation changes).

Wellbore temperature departures from the geothermal temperature gradient contain information about fluid movement into, out of, and along the wellbore. These departures from geothermal conditions can be small and are commonly smaller than the accuracy (but not the resolution) with which the wellbore temperature is measured. It follows from the previous statements that

- accurate knowledge of the geothermal temperature is crucial for temperature interpretation
- the temperature log needs shifting to correct for measurement errors or, more commonly, the geothermal temperature needs shifting to match the logged temperature data.

Geothermal temperature

When a well is shut in, in the absence of any cross-flow the temperature eventually returns to geothermal equilibrium. The timescale needed for this depends on complex geometric and reservoir parameters. Typically the shut-in period before a production logging survey is insufficient for equilibrium to be established.

Fortunately, the temperature below the bottom perforation should be at equilibrium or at geothermal conditions. Unfortunately, most production logging surveys barely lower the spinner below the bottom perforation—to avoid sensor damage from unknowns lurking in the well sump—and it is rare to have a temperature sensor logged down into unambiguously geothermal conditions.

Above the top perforation, geothermal equilibrium is established more rapidly after shut-in than in the reservoir itself, but this may still not be fast enough for the timescales of production logging. Permanent temperature monitoring with a distributed temperature sensing (DTS) system has an advantage over production logging when determining geothermal temperature because of the ability to acquire data after extended shut-in periods that result from unplanned production shutdowns.

Heat loss coefficient

A difference between the wellbore and geothermal temperature causes a heat flux from one to the other. Theoretically the heat loss coefficient can be computed from first principles, and based on the Reynolds number, thermal heat capacity, and thermal conductivity of the wellbore fluids, the temperature gradient, if any, across the wellbore can be computed. The tubing or casing thermal conductivity can be predicted from elementary geometry and standard tables of thermal conductivity. The presence of an annulus complicates the calculations, with larger annuli subject to additional convective heat flows and gas-filled annuli exhibiting non-negligible radiative heat flows. The thermal conductivity of the cement sheath must be accounted for, and finally the reservoir matrix must be considered not as a fixed-

temperature thermal sink but as a heat reservoir that responds slowly to changes in the wellbore temperature. Even with all this information the previous thermal history of the well must also be known, in the same way that well testing requires knowing the previous flow rate history. Normally, insufficient information is available to the log analyst to accurately calculate the heat loss coefficient. A more elegant approach is to use the heat loss coefficient as a single-value variable (assuming that the completion does not change over the interval of interest) that is tuned to match the wellbore temperature relaxation back to geothermal conditions in the long blank pipe regions between perforations.

Enthalpy equations

The enthalpy, or heat (h), equations are

$$h_{ae} = h_{be} + h_{oe}, \tag{13-39}$$

$$h_{ae} = \left(q_{w_{ae}} C_{w_{ae}} \rho_{w_{ae}} + q_{o_{ae}} C_{o_{ae}} \rho_{o_{ae}} + q_{g_{ae}} C_{g_{ae}} \rho_{g_{ae}}\right) T_{ae}, \tag{13-40}$$

$$h_{be} = \left(q_{w_{be}} C_{w_{be}} \rho_{w_{be}} + q_{o_{be}} C_{o_{be}} \rho_{o_{be}} + q_{g_{be}} C_{g_{be}} \rho_{g_{be}}\right) T_{be}, \tag{13-41}$$

$$h_{oe} = \left(q_{w_{oe}} C_{w_{oe}} \rho_{w_{oe}} + q_{o_{oe}} C_{o_{oe}} \rho_{o_{oe}} + q_{g_{oe}} C_{g_{oe}} \rho_{g_{oe}}\right) T_{oe}, \tag{13-42}$$

where

C_w = thermal heat capacity of water
C_o = thermal heat capacity of oil
C_g = thermal heat capacity of gas
ρ_w = downhole density of water
ρ_o = downhole density of oil
ρ_g = downhole density of gas
T = absolute temperature

and subscripts denote the following:

ae = above the entry
be = below the entry
oe = of the entry.

The complete equation for h should include a term for pressure and volume; however, for all practical temperature interpretation purposes the mechanical work terms can be ignored for wellbore mixing.

Pressure-drop temperature effects

The temperature above and below any entry can easily be measured and the temperature of any entry can be assumed to be at the geothermal temperature of that depth as long as there is no significant change in pressure from reservoir to wellbore. As pressure differences increase, gas entries experience Joule-Thomson cooling (Eq. 13-43) and liquid entries are heated (Eq. 13-44).

Joule-Thomson cooling is typically observed on low-pressure gas (less than 5,000 psi) and heating is seen on high-pressure gas (greater than 7,000 psi) as the sign of dz/dT changes:

$$\Delta T = \frac{\frac{V_M T}{z}\left(\frac{dz}{dT}\right)_p}{C_p} \Delta p, \tag{13-43}$$

where

ΔT = change in temperature
V_M = volume of one unit of mass of the gas
T = geothermal gas temperature
z = gas z factor at pressure p and temperature T
dz/dT = rate of change of z factor with temperature (at constant pressure)
C_p = thermal heat capacity of one unit of mass of the gas
Δp = pressure drop.

Great care must be taken to use a compatible unit system for calculating Joule-Thomson cooling.

In addition, liquids flowed through a pressure gradient gain in temperature because of the work done:

$$\Delta T = \frac{\Delta p}{C\rho}, \tag{13-44}$$

where

ΔT = change in temperature, degC
Δp = change in pressure, Pa
C = thermal heat capacity of the fluid, J/(kg.degC)
ρ = density of the fluid, kg/m^3.

Fortunately these two different mechanisms of Joule-Thomson cooling and pressure-drop heating normally help to distinguish gas from liquids. More subtly, the difference between the thermal heat capacities of oil and water provides a weak way of discriminating oil from water.

Sidebar 13D. Pressure drop, temperature rise

A well flowing water through a 1,000-psi drawdown would see the water arrive at the wellbore at about 1.6 degC [2.9 degF] hotter than the geothermal temperature if no heat loss occurred to adjacent reservoir layers.

This heating effect is the reason why many wells show an elevated temperature response, above geothermal, opposite the lowest producing perforations.

Reservoir model

Serious wellbore temperature interpretation applications require using the thermal conductivity of fluid-filled reservoir rocks, pressure drop from reservoir pressure to wellbore pressure, and permeability, skin, and porosity of the reservoir rocks to determine where the heating effect occurs and how much heat is lost or gained en route to the wellbore (Fig. 13-16). Further complications can be introduced by the partial penetration of reservoir layers by inflow zones, dipping reservoir layers that intercept a range of geothermal temperatures, and the impact of relative permeability on the location of pressure drops.

The simple temperature models of 20 years ago were very basic, working from just a geothermal gradient and one pressure drawdown and often ignoring liquid heating.

For the interpretation of distributed temperature surveys recorded with a DTS system, additional information in the form of the tubing head pressure, nodal pressure drops from surface down to the perforations, and metered surface rates are used to drive and constrain the interpretation. In the case of production logging interpretations using temperature flow-rate information, measurements of holdup and slip velocity models provide alternative constraints; nevertheless, most production logging–driven interpretations also use the measured surface rates as a constraint.

Both DTS and production logging sensor interpretations struggle to tell the difference between a temperature event caused by inflow and a temperature event caused by heat loss between the wellbore and formation. Therefore, the log analyst must carefully identify inflow zones and noninflow zones before starting the interpretation regression.

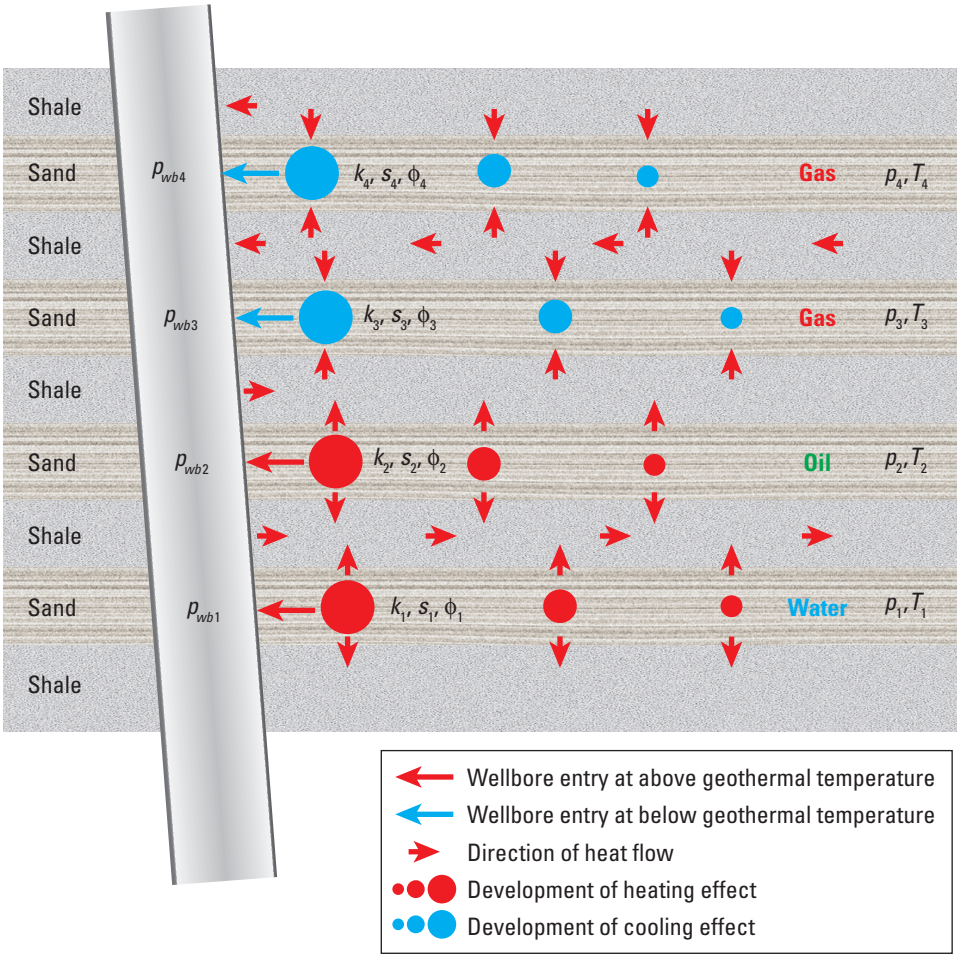

Figure 13-16. Temperature signals from water, oil, and gas. p_{wb} = wellbore pressure, k = permeability, s = skin, ϕ = porosity, p = reservoir layer pressure, T = geothermal temperature.

Sidebar 13E. Temperature interpretation in gas wells

A key application of temperature interpretation is detecting small water entries in gas wells. In annular flow, any water present is mainly a thin layer on the casing wall. Invisible to standard water holdup measurements, the water can sometimes be identified by the thermal anomalies it creates.

Although most of the wellbore is occupied by gas, the gas has a much lower density than water and a much lower heat capacity than water. Gas entries are typically associated with a cooling entry below geothermal temperature whereas water entries have a heating entry above geothermal temperature.

The spinner provides a good gas flow profile to drive the gas temperature model. Deviations from this temperature model are assigned to water production. Water entries of a few barrels per day can sometimes be identified in this manner.

Gas-condensate interpretation

Gas-condensate PVT models are designed to predict how much condensate drop-out there will be as the pressure falls toward surface pressure. These models do not accurately predict the condensate density and therefore cannot help in a multiphase interpretation.

The following holdup measurements do not work for gas-condensate wells:

- Density—The condensate density is not known and friction effects are large.
- GHOST optical probes—The condensate may be liquid or may be gaseous depending on the pressure and the GHOST tool cannot discriminate gaseous condensate from natural gas. In addition, at high velocities the liquid condensate travels as an annular film.
- RSTPro TPHL log—The condensate density and hence the carbon density volume factor are unknown. In addition, the condensate fraction is probably much smaller than the accuracy and resolving power of the measurement.
- Dielectric (HUM)—There is negligible contrast between the dielectric constant of condensate and gas and the HUM samples the center of the borehole whereas the liquid condensate is on the walls.

In a typical gas-condensate well with sensor technology at the time of writing, it is possible to compute a spinner flow profile and little else.

Global solvers and Flow Scanner interpretation

As of 2012, no global solvers can interpret Flow Scanner data. Flow Scanner data is always preprocessed into phase flow rates before being loaded into a global solver to gain access to global regression and to eliminate unphysical zonal contributions. To avoid global solver "improvement" of the flow rates, the global solver is normally loaded with only the Flow Scanner flow rates (no phase velocities or holdups are added to the global solver computation).

The future of global solvers and Flow Scanner interpretation

The future may allow interpretation of the individual Flow Scanner probe holdups and minispinners within the global solver and global regression. If this happens, then the following methodology can be expected.

If the standard error function looks like

$$E = \sum \left(M_i - m_i \right)^2 \times w_i, \tag{13-33}$$

then a 2D error function looks like

$$E = \sum \left(M_{x_i, y_i} - m_i \right)^2 \times w_i, \tag{13-45}$$

where

M = tool probe modeled response
m = tool probe measurement
i = index of the local measurement
x_i, y_i = coordinate of the local measurement within the borehole cross section (Fig. 13-17).

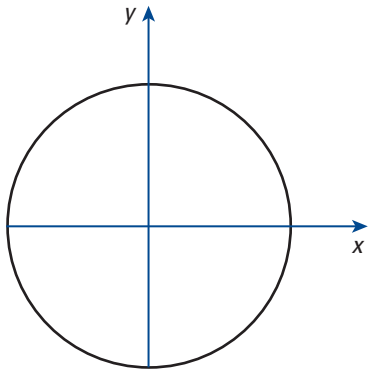

Figure 13-17. Coordinate system for 2D model.

Although there are no comprehensive 2D flow models, there are some basic 2D features of the flow that can be implemented:

- impose horizontally stratified holdup and velocity, which although they are not true for vertical and deviated wells, they are quite close to the truth for horizontal wells, where local measurements have the most application
- impose a water holdup gradient that monotonically decreases from the bottom to the top of the pipe and a similar constraint on the gas holdup; again, these are not true for nonhorizontal gas-water wells
- impose a MapFlo holdup shape
- use a Prandtl model to provide a velocity profile that goes to zero at the pipe wall
- use bubble count distributions to infer flow regimes and hence drive the appropriate global slip correlation
- use a Stratflo slip model weighted residual.

In this manner, even quite basic physical constraints can be used to build a useful 2D flow model. However, it remains to be seen whether the algorithms will be invented and the computer horsepower will be available to provide a usable system that quickly and reliably converges to a believable solution.

Matching surface rates

Modern production logging interpretation software allows the surface rates to be used for more than just the gas/oil ratio. If desired, the surface-measured rates can be matched exactly by the use of arbitrary coefficients in the interpretation (Fig. 13-18, for Emeraude) or used to create another error term in the global regression (Fig. 13-19, for Emeraude and PLATO).

The availability of these software features poses some interesting philosophical questions.

- Is there a true surface flow rate of impeccable accuracy?
- Are the PVT correlations accurate enough?
- Is the production logging tool's computed surface flow rate more or less accurate than separator turbine meter? What about a separator Daniel® orifice plate and Bourdon differential pressure gas rate?
- Should the diversity of flow rates be embraced as part of the holistic whole or does a single consistent (albeit inaccurate) surface flow rate deliver more successful management of the reservoir?

Log analysts within Schlumberger are taught to compare and comment on the differences between the surface-measured and surface-computed flow rates. As

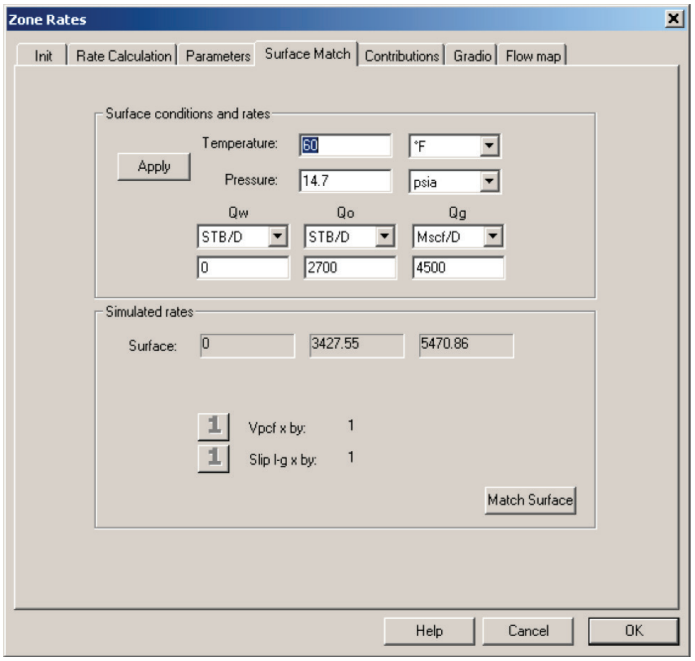

Figure 13-18. Forcing the interpretation to match the measured surface flow rates.

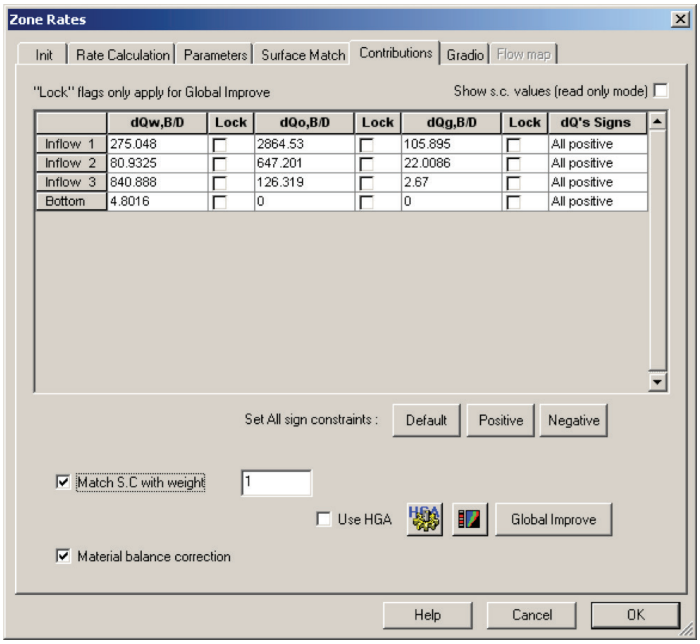

Figure 13-19. Using the measured surface flow rates as a residual in the global regression. S.C. = surface conditions.

a consequence, the "match surface" facility of Fig. 13-18 is not provided within Schlumberger interpretation software and is removed from Emeraude whenever a Schlumberger corporate license is detected.

For monophasic injector or producer wells it is normal to see a good match between the computed and measured surface rates with maybe a few percentage difference; in multiphase producers a match that is within 10% is a pleasant surprise. The example in Fig. 13-20 shows an oil difference of

$$(\text{oil measured} - \text{oil computed})/\text{oil measured} = 17\%,$$

and a water difference of

$$(\text{water measured} - \text{water computed})/\text{water measured} = 19\%,$$

and is considered an example of good-quality production logging tool measurements and a good-quality production logging interpretation.

What causes the differences between measured and computed flow rates? The list could start with

- poor-quality production logging measurements
- poor-quality data editing
- poor-quality interpretation software
- poor-quality interpretation technique
- poor-quality PVT conversions
- well instability while logging
- mechanical failure of the well between the logging interval and surface
- inaccurate surface metering equipment
- broken surface metering equipment but still being recorded
- surface measurements made at a different drawdown
- surface measurements made at a different time
- surface "measurements" made by back allocation.

Although a good match arrived at by an unconstrained interpretation is to be commended because it suggests that all the systems and measurements are working well, the alternative of a good match arrived at by force may just be offering a false sense of security.

Sometimes measured surface rates are needed to make the interpretation. Examples are if significant Gradiomanometer friction corrections are required then the pipe roughness has to be tuned until the surface water cut is matched or if the bubble flow rate algorithm is being used then the stand-alone bubble size needs tuning until the surface oil rate is matched. However, in these conditions the use of the surface flow rates to drive the interpretation should be explicitly documented in the report.

A log analyst who happily changes the computed rates by 100% to match a reported surface probably does not understand how the production log interpretation is being made.

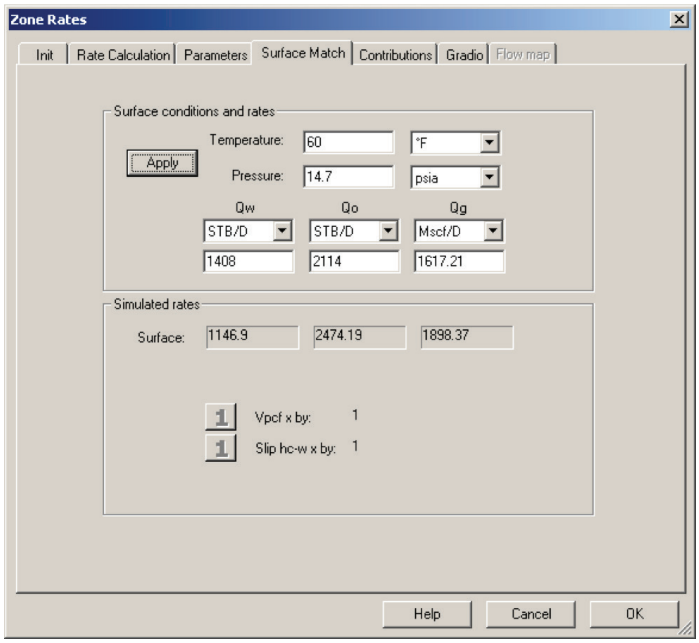

Figure 13-20. Comparison of measured and computed surface flow rates.

References

Goldberg, D.E.: *Genetic Algorithms in Search, Optimization, and Machine Learning*, Reading, Massachusetts, USA, Addison-Wesley (1989).

Whittaker, A.C., Lenn, C.P., and Hammond, P.: "Improving Multiphase Production Logging Answers: A New Multiphase Spinner Response Model for Gas-Liquid Flows," *Transactions of the SPWLA 46th Annual Logging Symposium*, New Orleans, Louisiana, USA (June 26–29, 2005), paper NN.

14 Leak Detection and Localization

Too many leak detection logs are poorly planned and poorly executed, resulting in ambiguous logs that fail to identify the leak. However, with a little planning most leaks are susceptible to detection and localization.

Typical well completion

A typical well has a surface conductor pipe, casing(s), liner(s), tubing, packer, tubing hanger, and a Christmas tree (Fig. 14-1). The pressure rating of the inner tubulars is generally higher than the pressure rating of the outer tubulars, which means that a leak from tubing to casing could result in overpressuring and rupturing of the casing, followed by an uncontrolled release of well fluids and potentially the inability to pump fluid into the well to kill it.

Wells that require artificial lift do not normally appear as wells with problem leaks. Water injection wells can normally tolerate quite large leaks because any annulus pressure can be safely bled away and the completion pressure is under surface control. Producing wells with leaking hydrocarbons and gas injection wells with leaking gas are the typical leak detection candidates.

The majority of the leaks are caused by a tubing leak and are detected by an increase in the tubing to casing annulus pressure measured at the tubing hanger. Thermal expansion joints in the tubing are particularly failure prone. Packers rarely fail once they have passed the commissioning tests. Sealbore assemblies (not shown in Fig. 14-1) can fail as downhole pressure is increased. The pressure seal at a liner hanger is normally backed up by a cement seal between the liner and base of the casing, and there is cement around the casing back to surface; it is very rare for the liner hanger and cement to fail.

A detailed well completion schematic is needed for planning a leak detection log.

Evaluating the problem

The log analyst planning a leak detection log needs to know where the unexpected pressure has been detected and at what rate the leak is flowing. An increase in the casing pressure in Fig. 14-1 would point to a tubing or packer failure whereas an elevated conductor pressure would point to a bad cement seal. Gas or liquid seeping from the ground or appearing in a local river or lake is not normally amenable to production log leak detection.

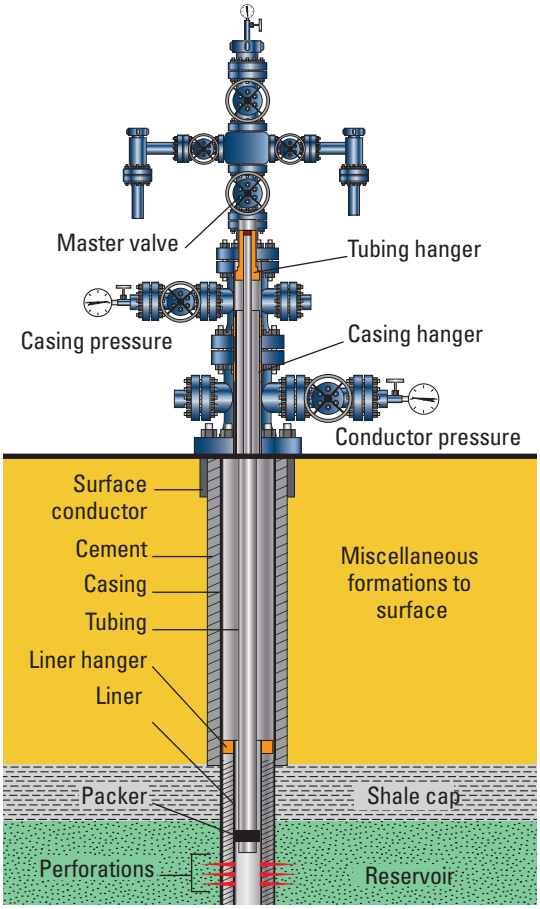

Figure 14-1. A typical well completion.

Leaks are rarely big enough to measure with a test separator, and leak rates are usually in nonstandard units, such as liters per minute, minutes per bucket, or, perhaps, seconds per gas-filled balloon.

The usual approach to leak detection in tubing is to set a plug in a tubing end nipple and then circulate fluid down the tubing through the leak and back to surface via the annulus. The leak should then be apparent as a discontinuity on the spinner log, temperature log, or both. Unfortunately, without a lot of experience it is difficult to know whether the leak signature will be big enough to see.

Sidebar 14A. Flow rates by the bucket

A standard bucket (yes, it does exist) has a volume of 4 imperial gallons (galUK) [18.2 L]. Therefore, if it takes 15 s to fill the bucket, the flow rate of the leak is

$$q_{leak} = \frac{4\ \text{galUK} \times 0.0286\ \text{bbl/galUK} \times 24\ \text{h/d} \times 60\ \text{min/h} \times 60\ \text{s/min}}{15\ \text{s}} = 659\ \text{bbl/d}, \quad (14A\text{-}1)$$

or

$$q_{leak} = \frac{18.2 \times 24 \times 60 \times 60}{1{,}000 \times 15} = 105\ \text{m}^3\text{/d}. \quad (14A\text{-}2)$$

This flow rate is big enough to be detected by a spinner if the leaking tubing is 7 in or smaller.

Unfortunately, the standard bucket is a somewhat archaic unit of measurement and a wellsite bucket could easily be half that size.

Sidebar 14B. A trial balloon for gas rates

A spherical balloon has a volume of

$$V_b = \frac{4}{3}\pi r^3. \quad (14B\text{-}1)$$

If the annulus valve is fully opened to the atmosphere until steady-state conditions are achieved and it then takes 3 s to inflate a balloon of diameter 40 cm, then the gas flow rate is

$$q_{leak} = \frac{\frac{4}{3}\pi\left(\frac{0.4\ \text{m}}{2}\right)^3 \times 24\ \text{h/d} \times 60\ \text{min/h} \times 60\ \text{s/min}}{3\ \text{s}} = 965\ \text{m}^3\text{/d}, \quad (14B\text{-}2)$$

or

$$q_{leak} = \frac{\frac{4}{3}\pi\left(\frac{0.4}{2}\right)^3 \times 24 \times 60 \times 60}{3} \times 35.3 = 34{,}000\ \text{ft}^3\text{/d}, \quad (14B\text{-}3)$$

If this flow rate is accompanied by a 1,000- to 2,000-psi pressure drop across a pinhole leak, then it might be detected by a temperature log. If the same flow rate had only a 50- to 100-psi pressure drop, then the leak would not have a detectable temperature signature.

The inflation pressure of a party balloon is only about one-tenth of an atmosphere; therefore, to a first-order approximation the gas in a balloon can be considered as being at atmospheric pressure.

Simulating the downhole leak

There is now a thermal model inside Emeraude production logging software that can be used to predict the temperature (and spinner) response at the depth of a tubing leak. Although the model calculates the heat transfer from tubing to annulus to casing and then to the formation, the key output is the change in temperature at the depth of the leak (Fig. 14-2).

Figure 14-3 shows the pressure drop and flow rate matrix for a tubing leak of water at 5,000 ft in 3½-in tubing inside a cemented 7-in liner after 1 h. The model displays the user-defined geothermal temperature in red, tubing temperature in blue, and annulus temperature in green.

At the higher leak rate of 100 bbl/d, the temperature and any spinner present would show an obvious leak signature as cool circulating water from the surface meets stagnant water below the leak. However, as the leak size decreases, the heating effect of the pressure drop becomes more important. When the exercise is repeated in Fig. 14-4, after 10 h the temperature signal of the

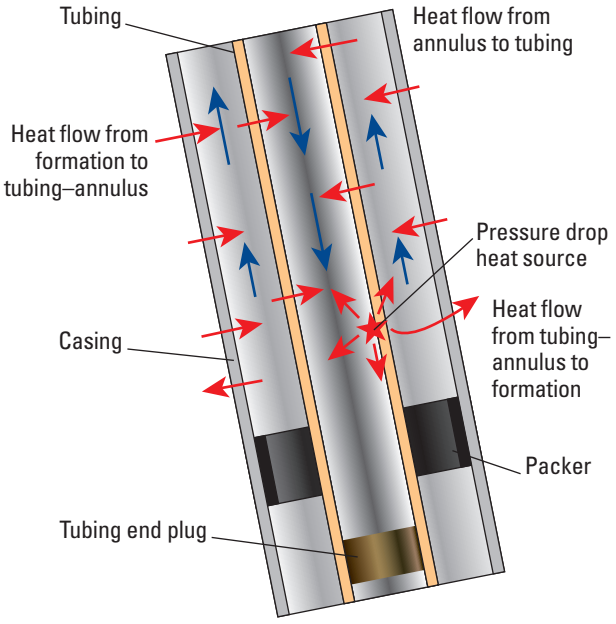

Figure 14-2. Flow paths and heating at a leak.

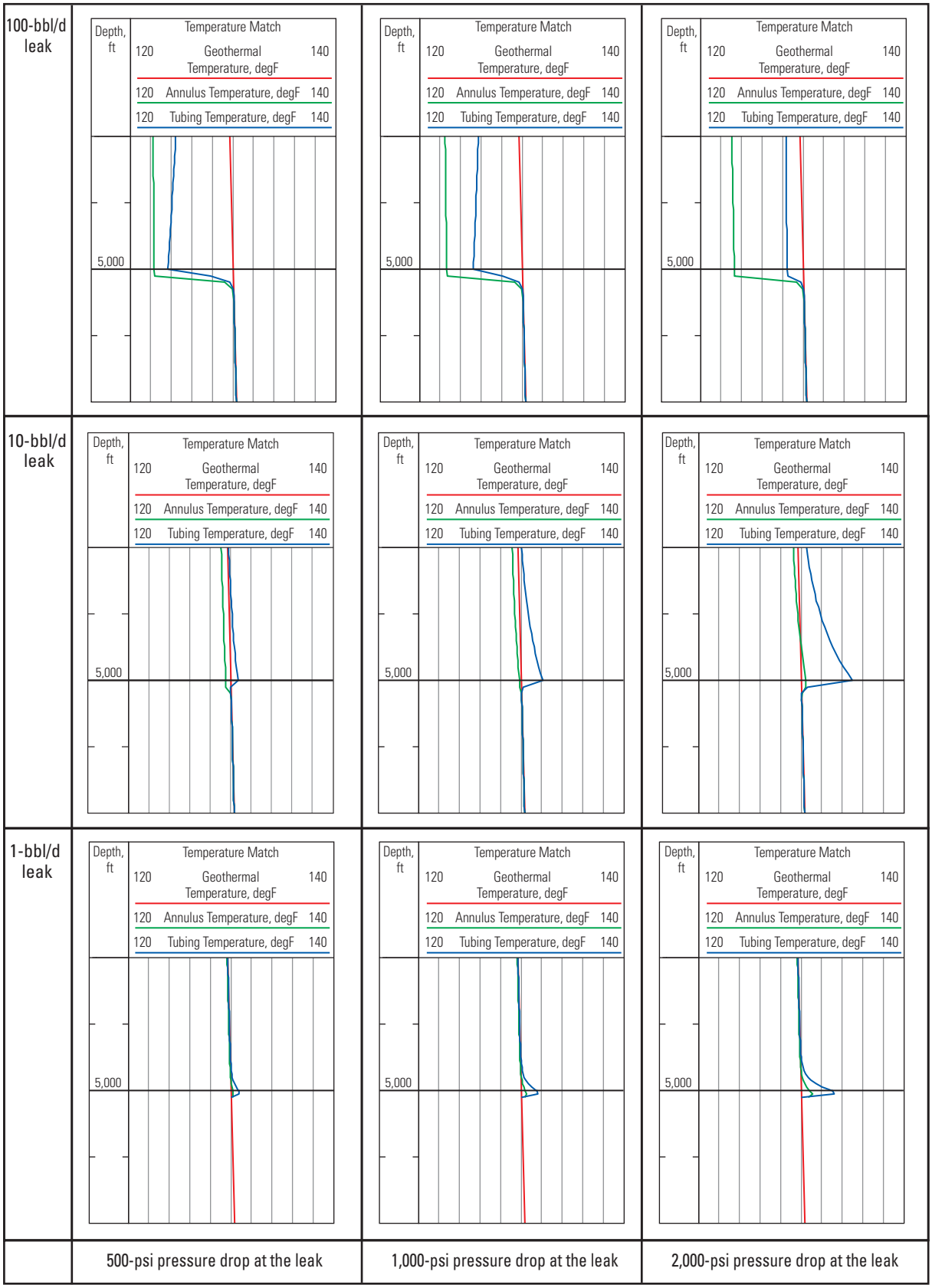

Figure 14-3. One-hour transient leak response.

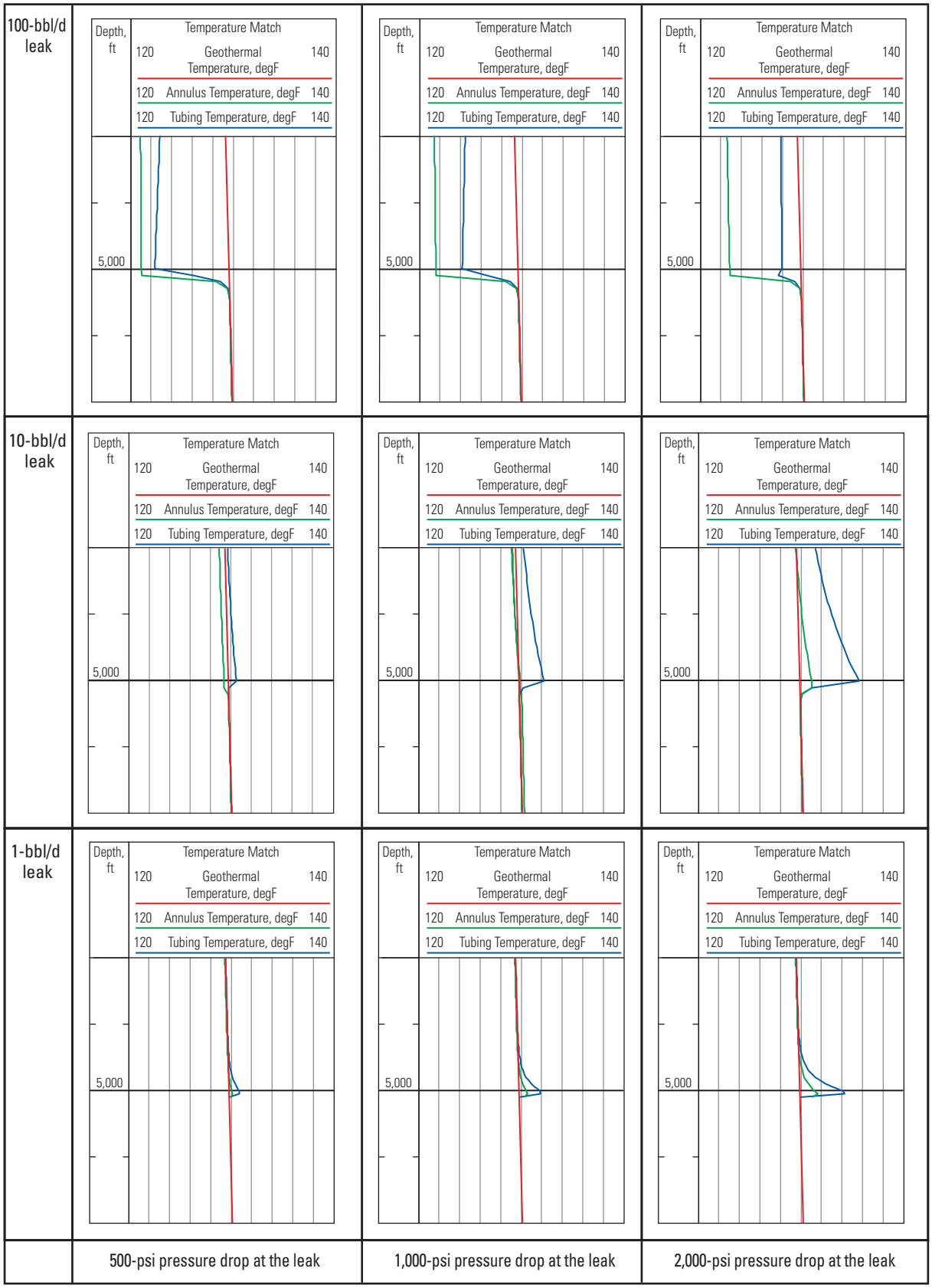

Figure 14-4. Ten-hour transient leak response.

smaller leak has changed again, making the leak location clearer as the temperature asymptotically trends toward steady-state.

In Figs. 14-3 and 14-4, for the 1-bbl/d leak rate with a 2,000-psi pressure drop, the heat source at the leak has a power of

$$P = p_{\text{leak}} \times q_{\text{leak}}, \tag{14-1}$$

where

P = power, W
p_{leak} = pressure drop across the leak, Pa
q_{leak} = flow rate through the leak, m^3/s.

In customary units of bbl/d and psi this equation becomes

$$P = 0.013 \times p_{\text{leak}} \times q_{\text{leak}}, \tag{14-2}$$

giving

$$P = 0.013 \times 2000 \times 1 = 26 \text{ W}. \tag{14-3}$$

A change in temperature gradient at the depth of the leak can easily be confused with other natural temperature gradient changes, but a step change or a localized heating event is an unambiguous leak signature. A 0.5-degF [0.3-degC] change in temperature should be detectable by any production logging tool if the thermal mass of the temperature probe is not too great and the well is logged slowly downward.

Successful temperature leak detection operations need thermal modeling to verify that there will be a signature that can be identified and to predict the timescale needed for the signature to develop.

Alternative temperature logging technique

If gas pressure is detected in the tubing to casing annulus, any leak detection exercise is normally conducted with water owing to the risks of venting an explosive gas. Where gas is detected in a casing-to-casing annulus, the surface flow rate may be quantifiable but the downhole pressure drop is an unknown. It is therefore impractical to model the expected temperature response. In these cases the following approach has had some success in locating gas leaks.

After the well and the leak have been shut in for several days, a geothermal temperature log is recorded. The gas is bled off in a safe and continuous manner for at least one day and a second temperature log is recorded (ideally with the same tool at the same speed with the same tubing contents) while the gas continues to be bled away. An overlay of the two temperature logs may show a separation caused by the presence of flowing gas behind the tubing and casing. This overlay approach is well suited to the use of distributed temperature sensing (DTS) fiber-optic monitoring.

Pulsed neutron leak detection

Another technique with a tubing end plug that can be applied for leak detection relies on contrast between the salinity of the injection water and the salinity of the annulus fluid. A pulsed neutron tool is run in sigma mode and the borehole sigma measurement is inspected to detect a change in the borehole sigma resulting from a change in the annulus salinity at the depth of the leak, where injection water displaces the completion fluid (Fig. 14-5). Because changes in the completion weight can be confused with an annulus salinity change, a time-lapse approach should be used, with one log recorded before injection starts and a second log after an hour or so. With the injection rate, injection time, and annular cross section known, the length of the time-lapse borehole sigma overlay separation can be predicted and verified.

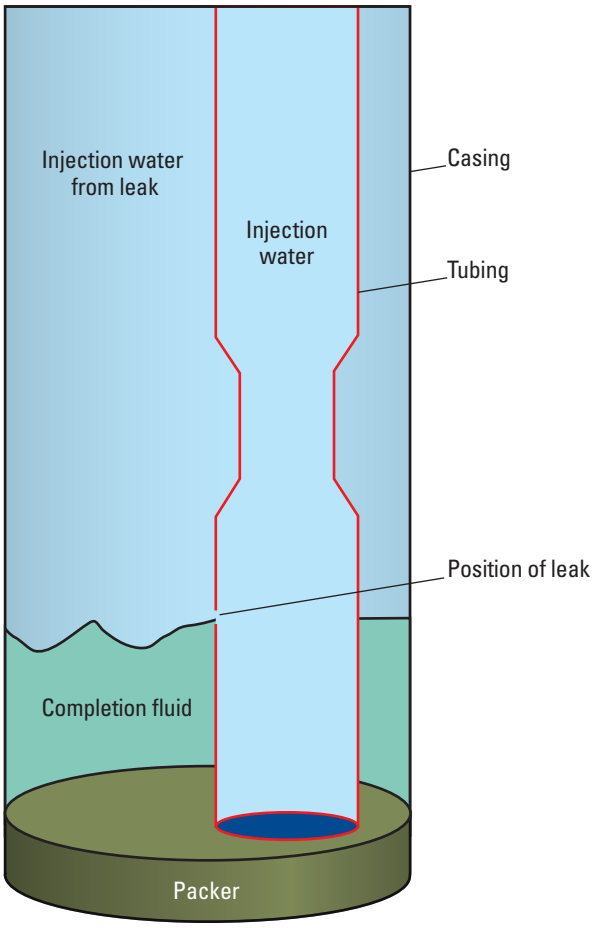

Figure 14-5. Detecting a leak through salinity changes.

Another pulsed neutron technique that can be used is the WFL oxygen-activation water flow log (for more details on the WFL water flow log, refer to the "Marker and Tracer Measurements of Velocity" chapter). The configuration of pulsed neutron source and detector is sensitive to the upward flow of water. This up flow can be in the tubing or the annulus. For leak detection, an upward water velocity indicates that the tool is above the depth of the leak whereas zero flow means that the tool is below the leak. Unfortunately the 1.71-in RSTPro tool shown in Fig. 14-6 makes its own water velocity from the convection currents created by a hot spot on the tool body, effectively masking any annulus signal. The solution for the RSTPro tool is to use the reversing adapters and run the tool upside down (Fig. 14-7). The convection currents are now moved away from the measurement zone and the RSTPro tool is used to look for down flow within the tubing. Detected velocities again mean the measurement is above the leak and no velocity detection means that the measurement is below the leak.

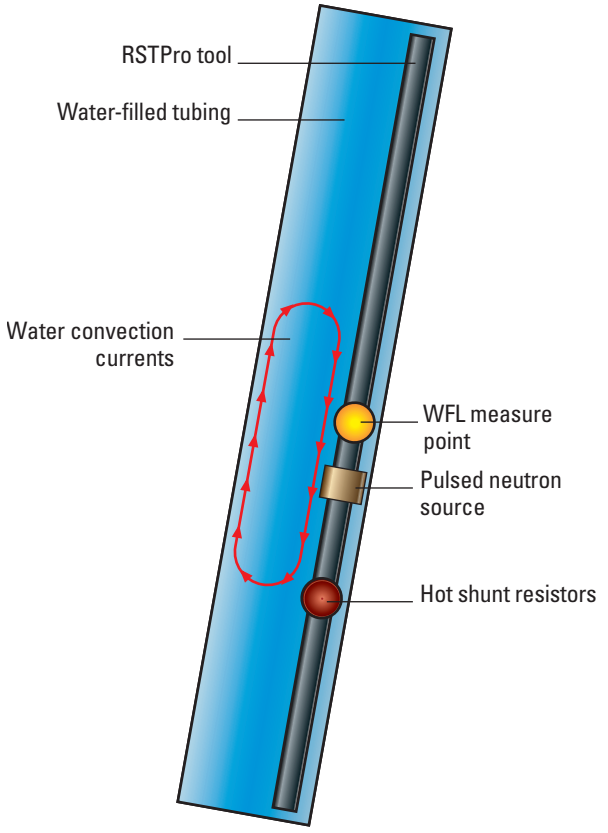

Figure 14-6. RSTPro WFL water flow log in normal configuration.

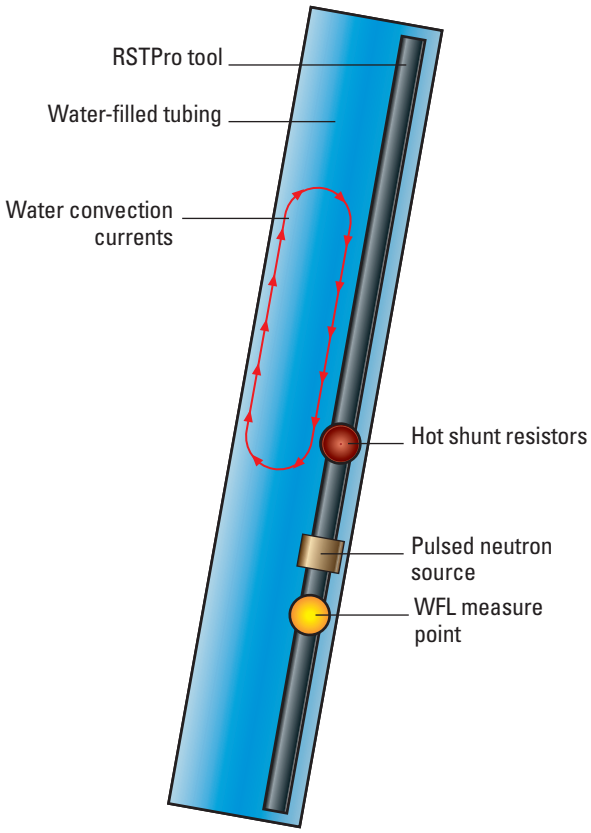

Figure 14-7. RSTPro WFL water flow log in inverted configuration.

Noise logs for leak detection

Although a downhole microphone can be used to detect the position of a leak, the problem comes from separating the noise of the leak from the surface platform noise (which is fed down the tubing and casings) and "road" noise created by the movement of the logging tool as a depth log is recorded.

While basic noise tools sample all the audio frequencies available downhole, more sophisticated tools employ bandpass filters and move into ultrasonic frequencies.

Job planning

Successful leak detection logs require the leak to be the biggest movement of fluid in the well. This automatically requires the well to be shut in, normally by a tubing end plug.

Big leaks are easier to find than small leaks; therefore, leaking annuli should be fully opened and any injection pressures safely maximized.

Logging programs should explicitly state the required well status for each stage of the data acquisition, and the wireline logs must indicate the well conditions during each logging pass.

15 Steam Injection

For water and gas injection wells the objective of logging is to determine the quantity of water or gas that is entering each reservoir zone. Steam injection is different.

Enthalpy of water and steam

Consider the energies involved for a simple case of steam at 200 degC [392 degF] being used to heat a reservoir at 100 degC [212 degF]. Turning 1 kg of steam vapor at 200 degC to water at 100 degC releases heat:

$$\begin{aligned} E &= m \times \left(h''_{200} - h'_{100}\right) \\ &= 1 \times \left(2{,}792 - 419\right) \\ &= 2{,}373 \text{ kJ}, \end{aligned} \tag{15-1}$$

whereas 1 kg of condensed liquid water at 200 degC cooling to 100 degC releases only this heat:

$$\begin{aligned} E &= m \times \left(h'_{200} - h'_{100}\right) \\ &= 1 \times (852 - 419) \\ &= 433 \text{ kJ}, \end{aligned} \tag{15-2}$$

where

E = energy, kJ
m = mass of steam or water, kg
h''_{200} = enthalpy of steam vapor at 200 degC, kJ/kg
h'_{100} = enthalpy of water at 100 degC, kJ/kg
h'_{200} = enthalpy of water at 200 degC, kJ/kg.

It follows that steam that arrives at the reservoir has a much greater heating effect than the same mass of water at the same temperature. Therefore, the objective of steam injection logging is not only to measure the quantity of steam but also the quality of the steam entering each reservoir zone.

Steam quality

Steam quality (Q) is defined as the ratio of the mass of vapor to the mass of vapor and liquid:

$$Q = \frac{m_{\text{vapor}}}{m_{\text{vapor}} + m_{\text{liquid}}}. \tag{15-3}$$

In terms more familiar to a production log analyst this becomes

$$Q = \frac{Y_{\text{vapor}}\rho_{\text{vapor}}}{\left(Y_{\text{vapor}}\rho_{\text{vapor}}\right) + \left(Y_{\text{liquid}}\rho_{\text{liquid}}\right)}. \tag{15-4}$$

where

m_{vapor} = mass of water vapor
m_{liquid} = mass of liquid water
Y_{vapor} = water vapor holdup
ρ_{vapor} = water vapor density
Y_{liquid} = liquid water holdup
ρ_{liquid} = liquid water density.

However, because the vapor and liquid are traveling at different speeds, Eq. 15-4 is incomplete and needs to be rewritten as

$$Q = \frac{Y_{\text{vapor}}\rho_{\text{vapor}}v_{\text{vapor}}}{\left(Y_{\text{vapor}}\rho_{\text{vapor}}v_{\text{vapor}}\right) + \left(Y_{\text{liquid}}\rho_{\text{liquid}}v_{\text{liquid}}\right)}, \tag{15-5}$$

where

v_{vapor} = velocity of water vapor
v_{liquid} = velocity of liquid water.

Steam flow rate

In practice, using commercial values of steam quality, the flow regime is invariably annular with a thin film of water on the casing wall (Barnea et al., 1982). In this case the centered production logging spinner records the core steam velocity. Again, with commercial values of steam quality, the water holdup is a few percent, meaning that essentially the entire pipe cross section is occupied by the flowing steam. Therefore, the steam flow rate is given by

$$q_{\text{vapor}} = v_{\text{app}}F_{vpc}\frac{\pi\left(d_{\text{pipe}}{}^2\right)}{4}, \tag{15-6}$$

where

q_{vapor} = flow rate of water vapor
v_{app} = apparent spinner velocity
F_{vpc} = spinner correction factor
d_{pipe} = pipe ID.

Phase behavior of water

Commercial steam injection uses saturated steam, which is water vapor in equilibrium with liquid water, with the pressure-temperature relationship defined by the line in Fig. 15-1 that extends from the triple point to the critical point. Therefore, a production logging toolstring for steam injection needs only a pressure or a temperature measurement to determine the operating point on the saturated steam line.

The density of liquid water and water vapor can be determined from either the pressure or the temperature by using polynomial expressions from the *International Steam Tables* (Wagner and Kretzschmar, 2008). Because the polynomial expression is tediously long with 34 terms, for simplicity it is asserted that

$$\rho_{vapor} = f\left(p_{vapor}\right), \tag{15-7}$$

where

p_{vapor} = steam pressure.

Mass flow rate of steam and steam quality

The mass flow rate of steam becomes

$$w_{vapor} = v_{app} F_{vpc} \frac{\pi \left(d_{pipe}^{\ 2}\right)}{4} \times f\left(p_{vapor}\right), \tag{15-8}$$

where

w_{vapor} = mass flow rate of water vapor.

If the mass flow rate of both steam and water going to the well (w_{total}) is measured at surface somewhere between the Christmas tree and the steam-generating plant, then the steam quality at any depth above the top perforation is given by

$$Q = \frac{w_{vapor}}{w_{total}}. \tag{15-9}$$

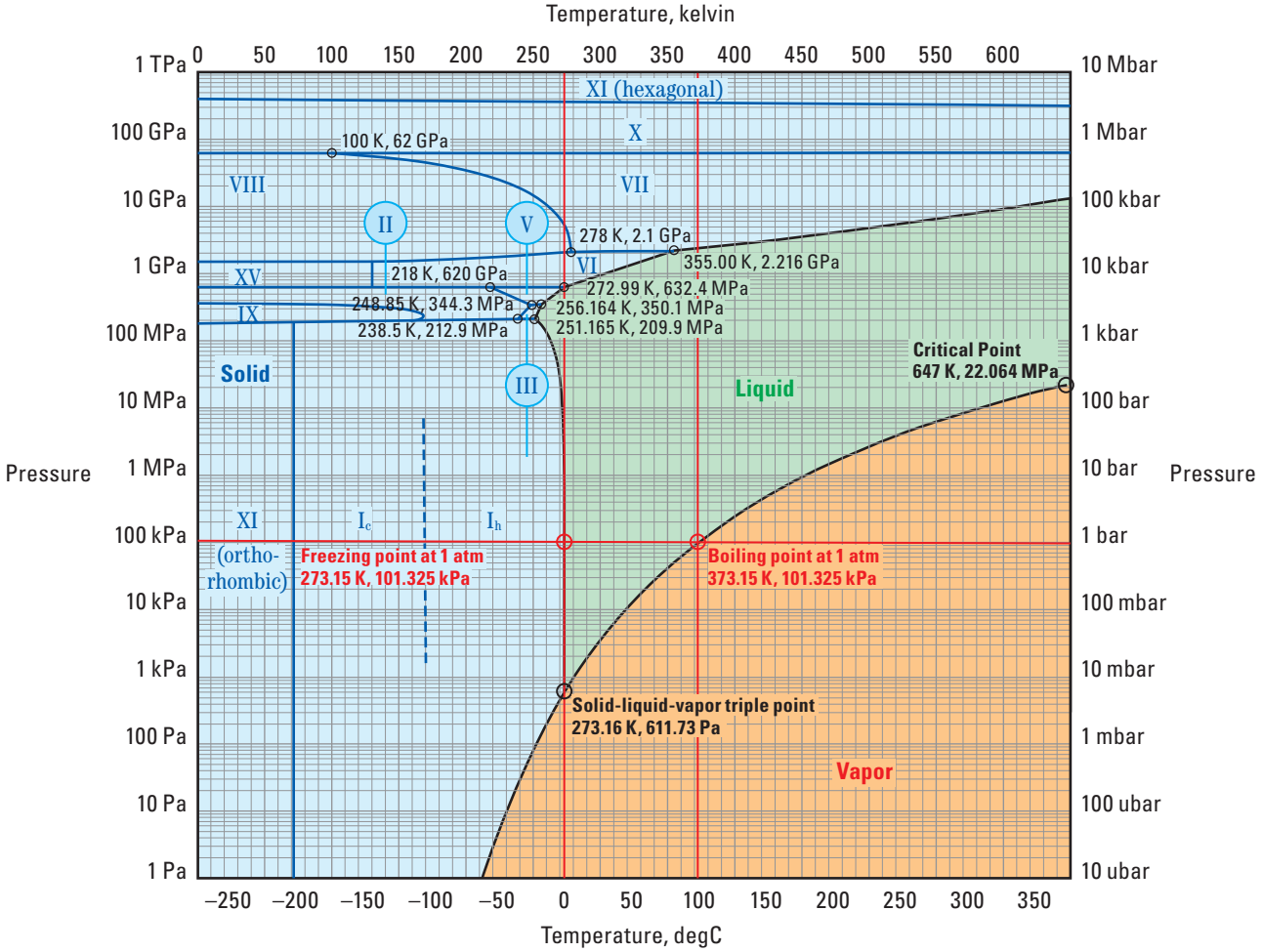

Figure 15-1. Semilog pressure-temperature phase diagram of water. The Roman numerals indicate various ice phases.

Validating the presence of annular flow

Because this method is valid only for annular flow, the superficial velocity of water should be checked against a suitable flow pattern map from Barnea et al. (1982) (Fig. 15-2). A simple rule of thumb is that it should be <0.6 m/s for annular flow:

$$v_{sup\_liquid} = q_{liquid} \frac{4}{\pi\,(d_{pipe}{}^2)}, \qquad (15\text{-}10)$$

$$q_{liquid} = \frac{w_{liquid}}{\rho_{liquid}}, \qquad (15\text{-}11)$$

$$w_{liquid} = (1-Q) \times w_{total}, \qquad (15\text{-}12)$$

and

v_{sup_liquid} = superficial velocity of liquid water
q_{liquid} = flow rate of liquid water
w_{liquid} = mass flow rate of liquid water.

Below the top perforation no further computations of water superficial velocity or steam quality are possible and all open intervals are assumed to be taking the same steam quality.

Example of a steam injection well

Figure 15-3 shows data from a vertical steam injection well. At first glance the up- and down-pass spinners appear to be off depth with each other. In fact, the low density of the steam and the high moment of inertia of the spinner means that there is an appreciable time constant for the spinner to respond to changes in the steam velocity.

Figure 15-4 shows the same data processed in a number of ways.

Track 1 shows the average measured pressure together with the saturated pressure curve obtained from the average measured temperature. The difference between these two curves comes from the accuracy with which the pressure and temperature are measured (assuming that there is a saturated mixture of steam and water).

Track 2 contains the matching temperature curves. Where the two curves begin to separate more widely, the borehole contents have become a column of monophasic water.

Track 3 shows the computed water and steam density based on the pressure reading and assuming a saturated steam and water mixture. The steam has an extremely low density compared with normal gas well densities.

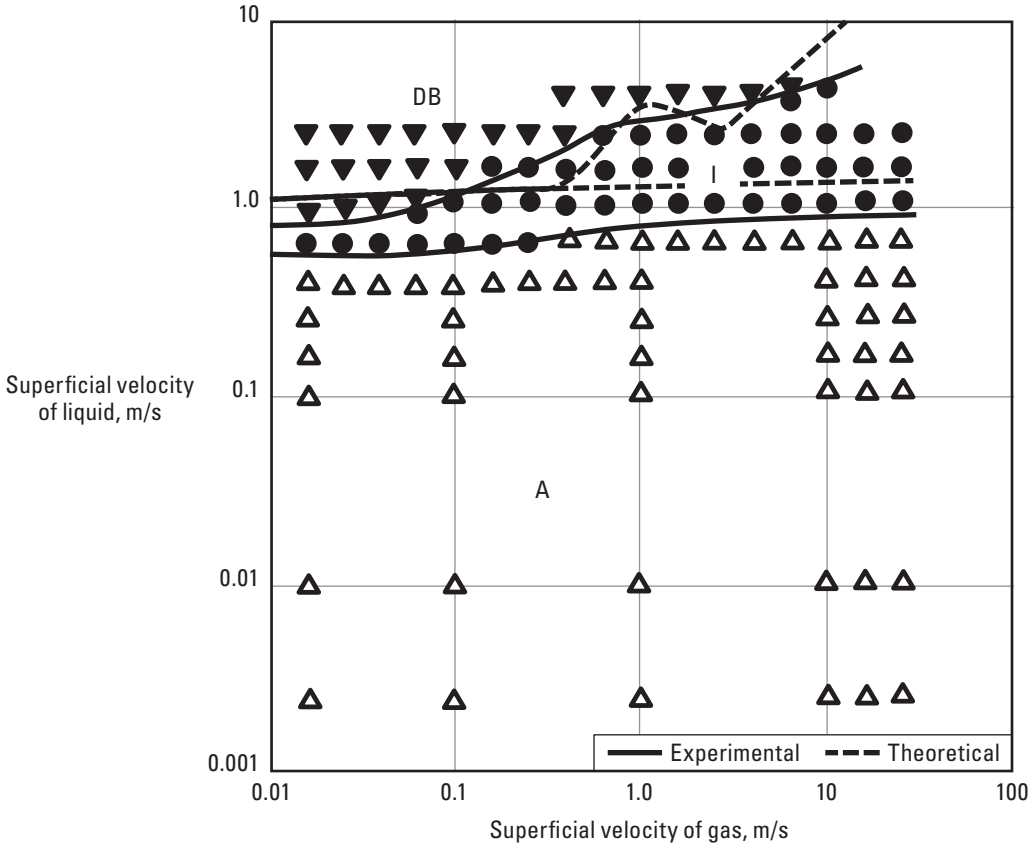

Figure 15-2. Flow pattern map of vertical downward flow in a 5.1-cm pipe (Barnea et al., 1982). A = annular, I = intermittent, and DB = dispersed bubble.

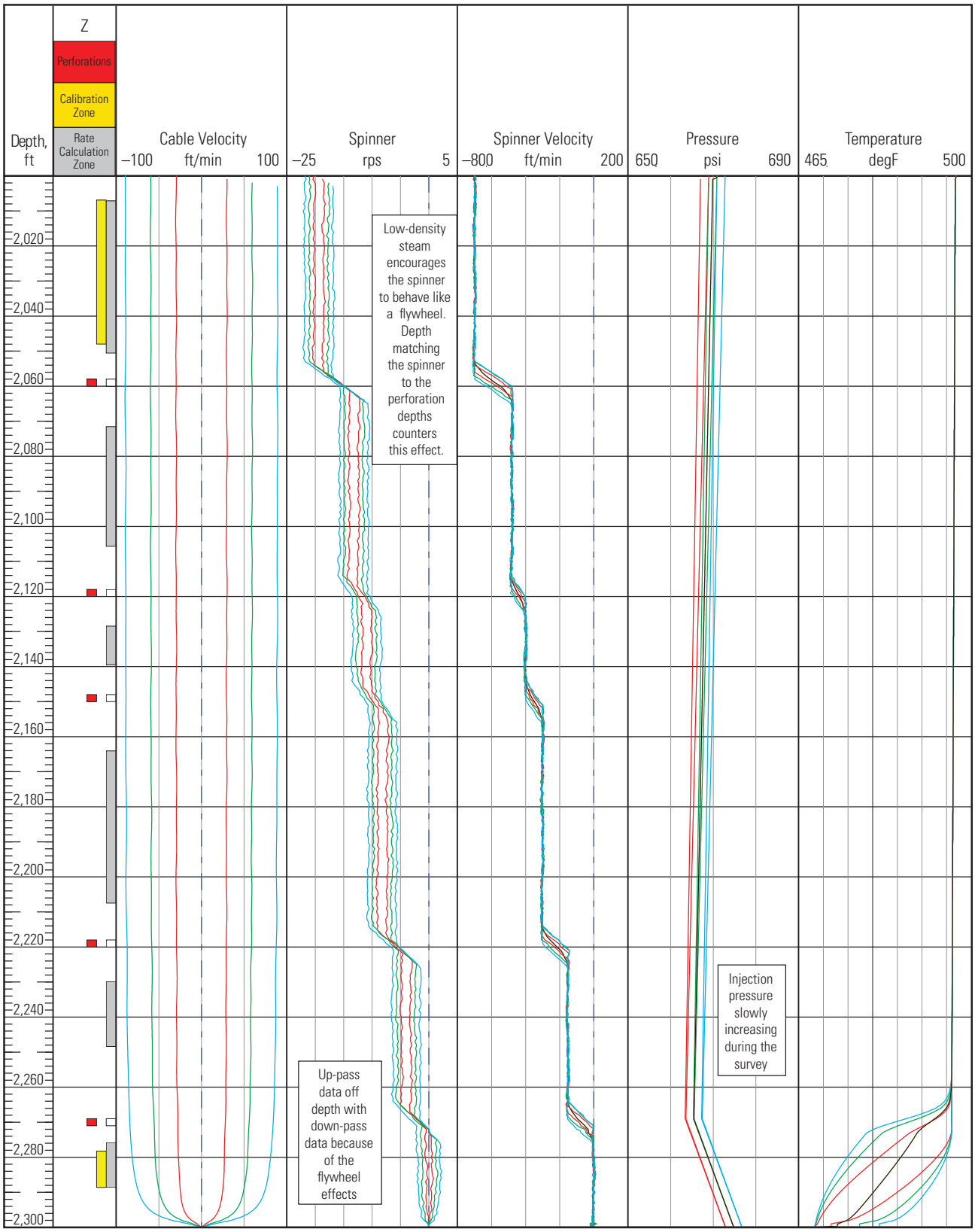

Figure 15-3. Steam injection log curves and computed spinner velocity in a vertical well at 495 degF.

Track 5 shows the velocity profile correction factor for the velocity profile across the pipe and the diameter of the spinner blade. This is computed using the Prandtl power law equation from "The Downhole Environment" chapter.

Track 6 shows the computed superficial water velocity based on the total surface mass flow rate minus the mass flow rate of steam. With the blue computed superficial water velocity well to the left of the limit curve in red there is a high confidence in the presence of annular flow.

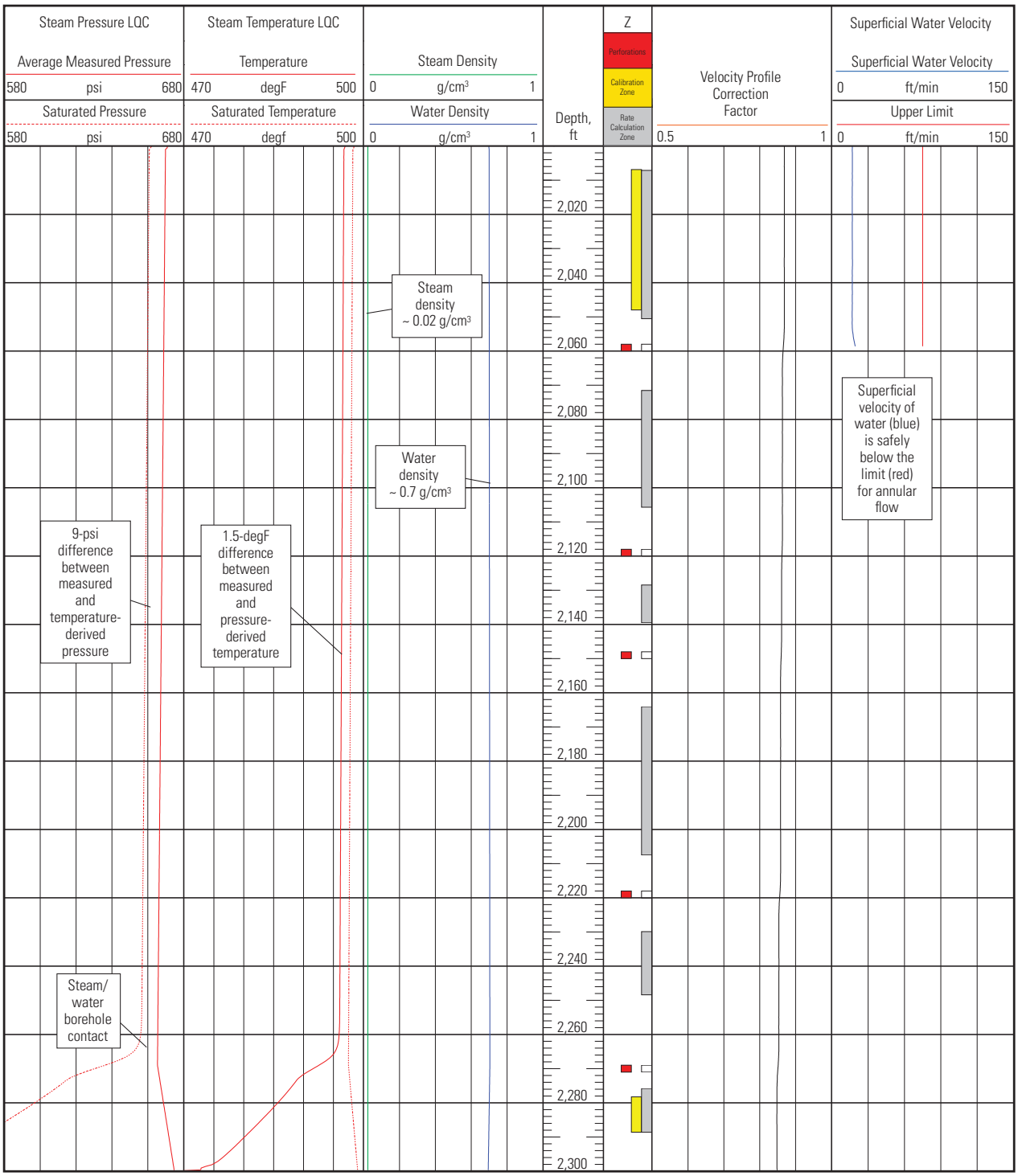

Figure 15-4. Steam injection log quality control (LQC) curves from a vertical well at 495 degF.

Figure 15-5 is the final answer, with the mass flow rate of steam in Track 1.

Track 2 shows the steam quality based on an external measurement of mass flow rate to the well and the mass flow rate of steam. In this well the steam quality is 48%. Assuming a steam quality of 100% at the steam generation plant, taking into account the condensed water enthalpy, and using a reservoir pressure and temperature of 1,015 psi and 212 degF, respectively, the reservoir is receiving 64% of the generated heat.

Track 5 has the conventional volumetric injection profile; Track 6 has the zonal volumetric injection rates into each perforation.

This technique is disclosed in a US patent application publication (Whittaker and Hammond, 2011).

References

Barnea, D., Shoham, O., and Taitel, Y.: "Flow Pattern Transition for Vertical Downward Two Phase Flow," *Chemical Engineering Science* (1982) 37, 741–744.

Wagner, W., and Kretzschmar, H.-J.: *International Steam Tables: Properties of Water and Steam Based on the Industrial Formulation* IAPWS-IF97, 2nd ed., Berlin: Springer (2008).

Whittaker, A.C., and Hammond, P.S.: "Apparatus and Method for Generating Steam Quality Delivered to a Reservoir," US Patent Application Publication No. 20120160011 (December 4, 2011).

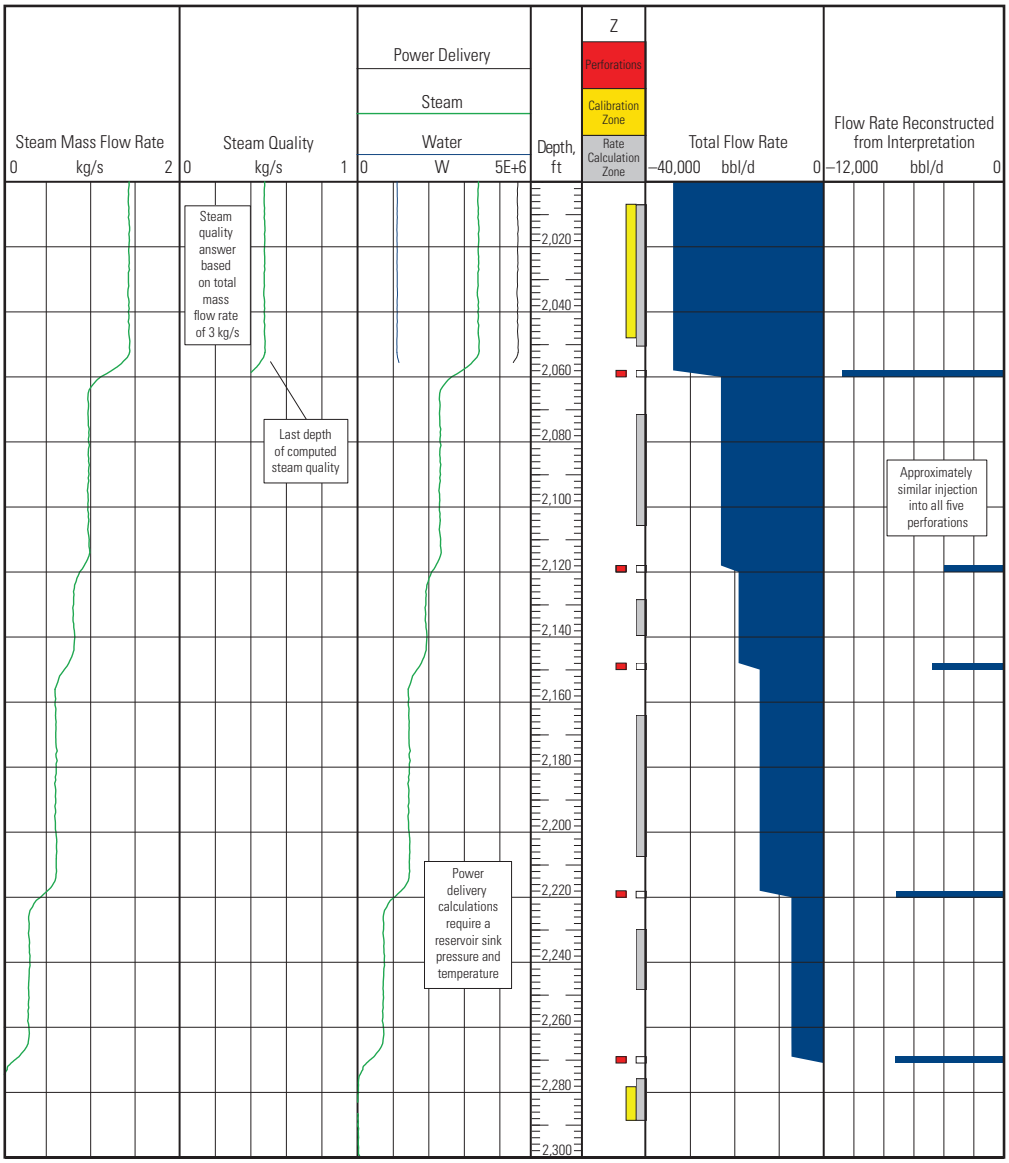

Figure 15-5. Steam injection answer product from a vertical well at 495 degF.

16 Job Planning

Ideally, this chapter should be read after all the other chapters in this book. However, some will wish to jump straight into the task of planning a production log; therefore, the previous chapters on production logging sensors are repeated in an abbreviated form.

Even the best production logging tools run in the wrong well or in the wrong way or with the wrong logging program usually produce disappointing results. To successfully plan a production log the best approach is to find a production log analyst who has been repeatedly disappointed with the datasets that he or she has tried to interpret and ask this person for recommendations. In the absence of advice from a gray-haired log analyst trained in the school of hard knocks, the alternative is to try to anticipate the problems and plan around them. This chapter on planning uses the second approach.

The downhole environment

The first planning step is to build a model of the downhole environment.

The production rates from the well (or the expected surface rates in the case of an exploration well) are sourced. The surface rates are then converted to downhole rates. For the purposes of planning, the water shrinkage factor (B_w) can be approximated to 1.0, the oil shrinkage factor (B_o) can be approximated to 1.3 or 1.4 except for the lightest of light oils or condensate, and only the surface gas rate (after subtraction of the solution gas) needs the flowing bottomhole pressure and temperature to compute the approximate gas shrinkage factor (B_g). For planning purposes the z factor (for departures from the ideal gas law) can be ignored and B_g calculated as

$$B_g = \frac{p_{sc}\, T_{dh}}{p_{dh}\, T_{sc}}, \tag{16-1}$$

where

p_{sc} = absolute reference pressure at standard conditions
T_{dh} = absolute downhole temperature
p_{dh} = absolute downhole pressure
T_{sc} = absolute reference temperature at standard conditions.

Therefore,

$$q_{o_{dh}} = q_{o_{sc}} \times B_o = q_{o_{sc}} \times 1.3, \tag{16-2}$$

$$q_{w_{dh}} = q_{w_{sc}} \times B_w = q_{w_{sc}} \times 1.0, \tag{16-3}$$

$$q_{g_{dh}} = \left(q_{g_{sc}} - q_{o_{sc}} \times R_{so}\right) \times B_g, \tag{16-4}$$

where

q = flow rate
B = shrinkage factor
R_{so} = solution gas/oil ratio

with the subscripts o, w, and g for oil, water, and gas, respectively, and dh and sc indicating downhole and standard conditions, respectively.

Care must be taken when using oilfield units that the switch from surface gas in cubic feet per day (ft^3/d) to downhole gas in barrels per day (bbl/d) is successfully accomplished.

In the absence of any guidance to the contrary, the inflow profile is normally assumed to vary linearly over the producing interval(s).

To convert the flow rates to velocities the completion internal diameter (d_{pipe}) over the producing interval is required. The deviation over the producing interval is also needed to drive the chosen slip correlation.

Historically, the next step of calculating the phase holdups and velocities was performed slowly and manually; however, in recent years the suppliers of production logging global solvers have made available tool response models and slip correlations for the purposes of job planning. Figure 16-1 shows a horizontal gas-water well with a uniform inflow profile and the predicted holdups and phase velocities.

The total flow in Track 1 shows the assumed downhole flow profile. The water holdup in Track 4 shows the computed Y_w. The phase velocities of water and gas are shown in Track 5 in blue and red, respectively. The TVD holdup track plots the water holdup inside a simulated borehole that follows the variations in the well's TVD. The red zones in the Z track show the location of the producing interval. Finally, the labels in the total flow track indicate the predicted flow regime from the gas-liquid slip correlation, in this case Petalas and Aziz (1996).

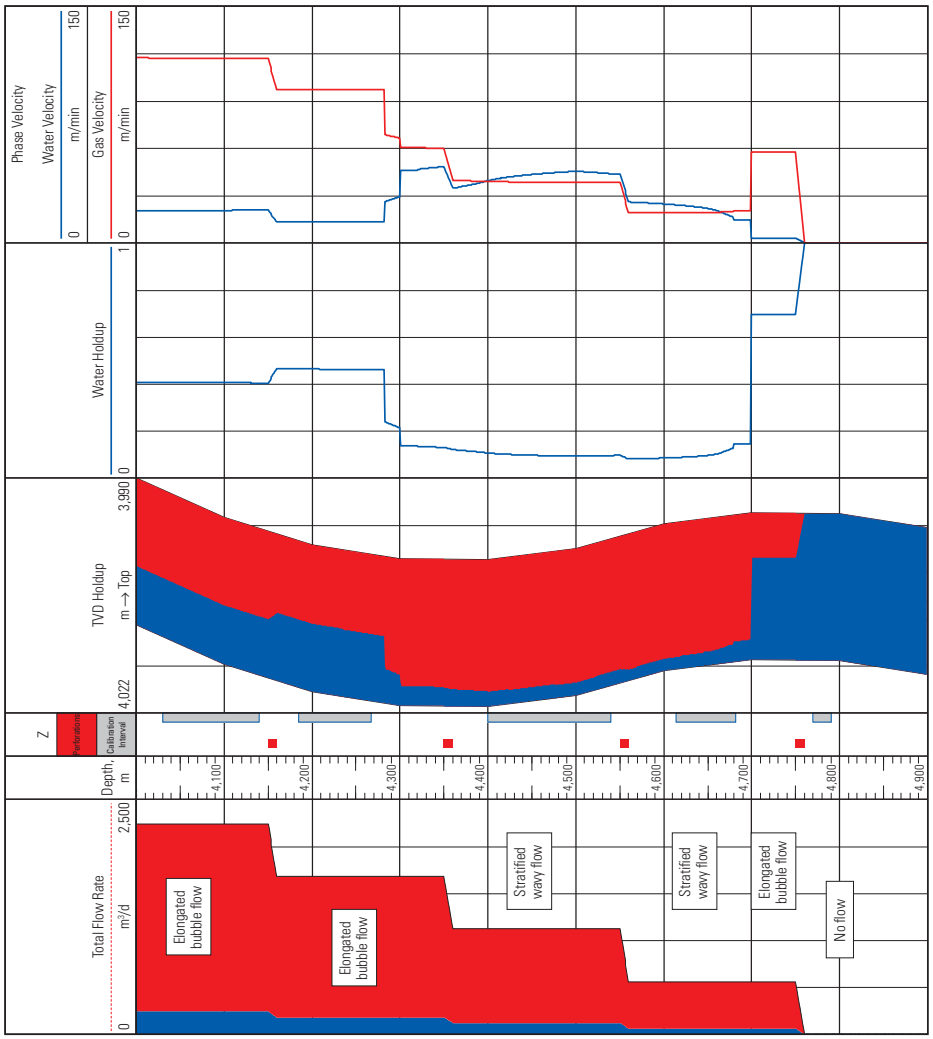

Figure 16-1. Downhole simulation of gas and water flow.

The objectives

Just as in school, where it is important to read and understand the question before answering, it is important to know why the production log is being run. If the designers of the production logging program assume that they know the objective of the logging operation, then there is ample scope for disappointment when the interpretation report is eventually delivered. It is therefore important that meaningful objectives are provided. In this respect the common phrase "The objective is to record a production log" is not particularly helpful. What is required is the use to which the production interpretation report will be put. The production logging planner appreciates objectives such as

- identify water entry points for setting a water isolation plug
- compute layer pressures from a multirate production log
- identify zones of bypassed oil for reperforation.

The objectives may not all be realizable and may even be mutually incompatible, but it is always good to agree on what can be delivered before the data has been acquired.

One common objective that is difficult to realize is the source of a small amount of water production in a gas well. The example in Figs. 16-2 and 16-3 is a 5½-in casing completion at 25° deviation flowing 2.5 MMft^3/d of gas and 20 bbl/d of water. The flowing bottomhole pressure and temperature are 3,000 psi and 250 degF, respectively. The well is producing through three sets of perforations with a roughly equal gas rate from each. The Petalas and Aziz (1996) slip correlation was used.

The simulation in Fig. 16-2 shows the holdup and density log responses for all of the water entering at the deepest perforation set. The simulation in Fig. 16-3 assumes that 19 bbl/d of water has entered at the top perforation set and just 1 bbl/d is entering at the deepest perforations to keep the borehole topped up with water.

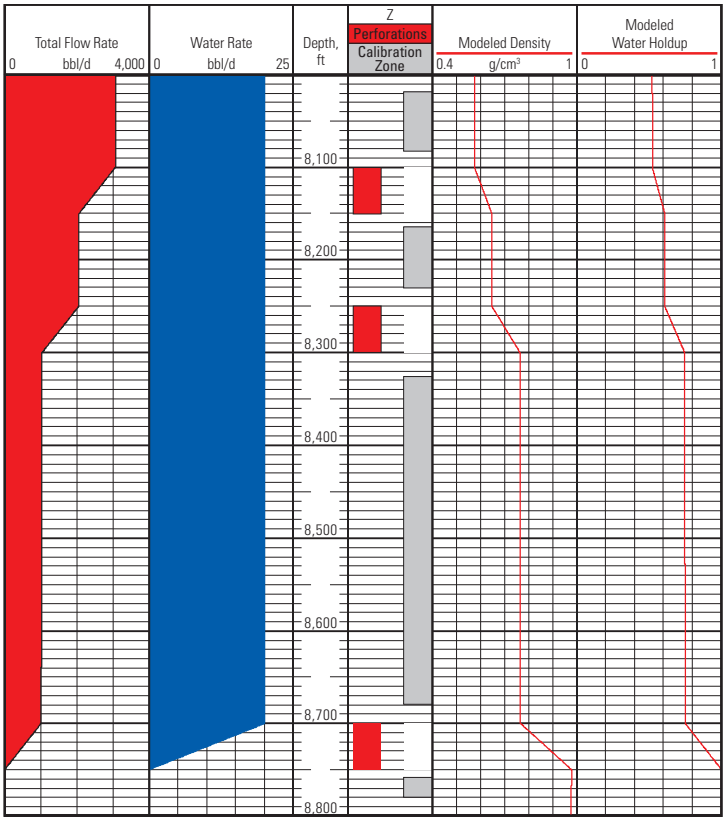

Figure 16-2. Low water entry.

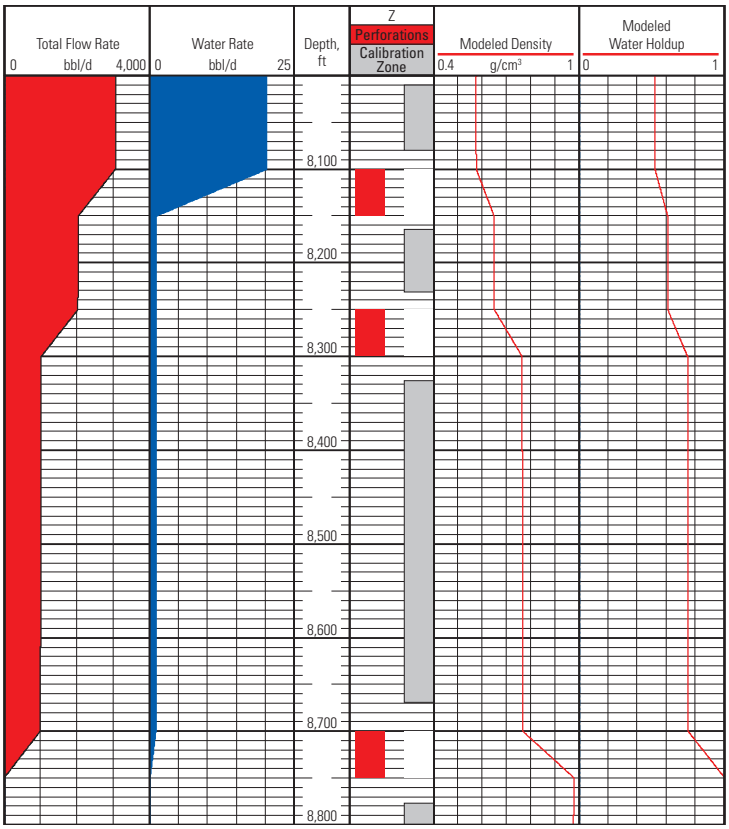

Figure 16-3. High water entry.

The holdup responses are indistinguishable from each other, which means that the holdup measurements cannot identify the source of the water. In fact, the situation is much worse because changing from Petalas and Aziz (1996) to another correlation gives very different values of holdup and density owing to the different slip velocities they calculate. This means that interpretation of the log data from this type of well assigns the source of the water production based on the slip correlation used.

Experienced log analysts know that sometimes the temperature or even the gamma ray log can suggest the source of the water production in this type of well, but the possibly ambiguous nature of the data that is likely to be acquired should be indicated and documented before the well is logged.

Finding small water entries in oil wells is a little easier but can still be very challenging.

Other constraints

A common constraint on offshore platforms is the requirement to rig up under the rig floor. The limited space available for both pressure control equipment and the production logging toolstring leads to either a very short toolstring or the use of pressure deployment bars. The choice must be made between running fewer sensors and having a more difficult (or impossible) interpretation or having a much longer duration job at the wellsite because the deployment bars are connected and pressure tested during both rig-up and rig-down. If time permits, these two scenarios should be explored and presented as alternative options to the operator.

Memory tools may be required because a lightweight, small-footprint slickline winch must be used or because the coiled tubing for a horizontal well is not electrically wired. Memory mode reduces the number of sensors that can be run because certain logging tools either need more power than a battery can provide or need a continuous stream of surface commands.

In horizontal wells the use of a conventional wireline tractor means that surface-readout logging tools are turned off while tractoring in the hole and can be powered up and logged only while pulling out of the hole. This has implications for spinner surveys and probe-based holdup measurements.

Occasionally a production log is required on a well completed with a subsea Christmas tree. This calls for either a semisubmersible rig with a riser run down from surface to the Christmas tree or a dynamically positioned light intervention vessel with a subsea pressure lubricator. The cost of either option is so large that there is little point in trying to economize on the production logging sensors being run except that an excessively long collection of logging tools compromises the system reliability and may lead to expensive lost time.

Annulus flow

Successful production logging is easier when the flow enters through perforations or screens and then moves exclusively up the borehole of the well. However, there are occasions when there is significant casing/tubing annulus flow.

In a perforate-stimulate-isolate (PSI) completion the logging tools are always inside a tubing. Fluid entries arriving through a casing perforation travel up (or down) an annulus before arriving inside the tubing via a sliding sleeve (SSD). The annulus velocity and holdup do not match the tubing velocity and holdup, and nuclear measurements that “average” the tubing and annulus responses are not representative.

Wire-wrapped screen completions may or may not be gravel packed. If the screen is not gravel packed, then there may be a flowing annulus depending on whether the formation has collapsed around the screen. Fortunately, observation of the last few feet at the top of many screen completions has rarely shown an unusual increase in the spinner velocity. This indicates that significant annular flow around a wire-wrapped screen is not normal and can be neglected for planning purposes. However, the possibility of annulus flow and its effects on the interpretation results should be considered.

Where the formation is more mechanically stable and the cost of completing a long horizontal well demands some economies, cemented and perforated completions and wire-wrapped screens are commonly replaced by slotted liners. The slotted liner annulus is open and fluid is free to travel in both the borehole and annulus. The flowing cross-sectional areas of the slotted liner ID and annulus are often similar and the common absence of centralizers places the slotted liner in the water-filled low side of the well. If the well also includes annular isolation devices such as cement-filled external casing packers (ECPs) or swell packers, then these divert the annular flow into the borehole and provide an interval of a few meters where all the flow can be measured by a production logging tool. In the absence of any annular isolation devices, a combination of nuclear measurements that average the borehole and annulus flows and of local measurements that record only the flow inside the liner is the best that can be run, although an inferior interpretation will now be delivered.

Production logging sensors

Once the downhole environment has been modeled and the objectives understood, the possible logging sensors can be evaluated for use in the well. The sensors discussed in this section are in no particular order.

Temperature

The primary use of the production logging temperature log is to drive the PVT models. Because of this a temperature log is run on every production logging toolstring.

In vertical and deviated wells the recorded temperature can be compared with the geothermal temperature (or an estimate of the geothermal temperature). Warming entries normally indicate that a liquid entry has undergone a near-wellbore pressure drop whereas cooling entries indicate either an entry at geothermal temperature or subgeothermal temperature owing to Joule-Thomson cooling. However, quantitative analysis of a production logging temperature log normally indicates the primary planned measurements are not available and the log analyst is following a backup plan.

In a horizontal well, geothermal gradients range from very small to zero. Therefore, the mentioned warming and cooling effects become more pronounced.

Hot spots on the production logging tool housing sometimes leave an anomalous heat signature in regions of stagnant flow.

Pressure

Like the temperature log, the pressure log is also used to drive the PVT models. Pressure can also be used to determine whether the well drawdown is changing and therefore whether the well is stable enough to log and then to interpret. Because of these two critical applications, a pressure sensor accompanies every production logging tool.

In addition, the pressure gradient can be converted into an accurate fluid density curve (albeit with poor depth resolution) in wells of less than 70° deviation. In high-velocity horizontal wells with monophasic flow, it is sometimes possible to use the frictional pressure drop to estimate the fluid velocity, but as with the temperature log, this would be a backup approach.

Sidebar 16A. Stability criteria

Logging programs that request that the well is stable before logging commences should provide a stability criteria. Usually a 10% change in the flow rate from the beginning to the end of the production logging survey is the maximum that can be tolerated. If the logging passes and stations are predicted to take 3 h, then the drawdown should be changing by less than 10% in the 3 h before logging commences. For a 500-psi drawdown this becomes <(500 psi × 10%)/3 h = 17 psi/h.

Before this stability requirement is realized, it is quite common to record a couple of "insurance" passes so that at least some data has been acquired if the job is subsequently cancelled or the logging tool fails.

Spinner or turbine

The assumption that a spinner averages the velocities (or momentums) of the phases present works well in vertical wells, begins to struggle in low-velocity deviated wells, and usually fails in a horizontal well. Knowing at what mixture velocities the spinner velocity becomes uninterpretable because of recirculation (countercurrent) effects relies more on experience than on mathematical modeling. In horizontal wells the extreme phase segregation and large slip velocities mean a conventional spinner interpretation is usually impossible. Sometimes in a horizontal well a centered spinner is totally immersed in just one phase. Under these conditions the spinner velocity may correspond to a phase velocity, but this again is a backup scenario.

Spinners can have an upper revolution speed that is either mechanical (from the bearings) or electronic. Fullbore flowmeters can collapse in high-velocity wells depending on the flow direction; the 2½-in PFCS collapses in water injectors at rates above approximately 800 ft/min [240 m/min].

The newer tools with multiple minispinners are designed to exploit the opportunities for single-phase logging in stratified horizontal flow conditions. The small diameter of the minispinner delivers a very small torque and requires specialized blade profiles, bearings, and rotation sensing technology to keep the minispinner threshold velocity down to a useable level and deliver an interpretable velocity array.

Gradiomanometer differential pressure sensor

Density-based holdup measurement relies on known or fixed phase densities. Typically tuning of the PVT model, small measurement offsets to match the observed phase densities under shut-in conditions, or both are needed. The upper deviation limit for the Gradiomanometer sensor is in the range 60° to 70° depending on the density contrast between the phases present. The Gradiomanometer sensor struggles with liquid velocities above 10 ft/s [3 m/s] because of friction corrections.

Probe holdup measurements

There are probe holdup measurements based on electrical conductivity, electrical capacitance, and optical reflectance. Because these are essentially point measurements, a single probe is unlikely to deliver a representative holdup in all but the most vertical of oil-water wells. As the deviation increases, the density contrast between the phases causes phase segregation. To compensate, more spatially separated probes are needed to calculate the average holdup. Logging tools that are free to rotate need more probes whereas tools designed to orient themselves to the vertical axis through the pipe cross section need fewer probes. Up to 45° deviation, 4 circumferentially distributed probes are sufficient. From 45° to 70°, a high-velocity well still needs only 4 probes, but if the velocity is low then a second tool for a total of 8 probes is needed, the same as in a horizontal well. Multiple logging passes can be combined to improve the probe coverage (e.g., three passes of a 4-probe tool equate to a single pass with a 12-probe tool), but only if the logging tool does not follow the same orientation on each pass. Unfortunately, logging tools decoupled from the cable torque with a swivel very often follow the exact same path on each logging pass. Circumferentially distributed probes necessarily acquire duplicate holdup measurements from either side of the pipe's vertical axis; therefore, 6 vertically oriented probes provide a superior holdup measurement to 8 circumferentially mounted probes.

The twin aims of ruggedness and accuracy cannot easily be satisfied with a probe holdup measurement. Larger, stronger probes suffer more from preferential wetting or blinding whereas smaller probes can easily be broken in a barefoot completion. For electrical probes the choice of conductor, insulator, and excitation frequency also affects the quality of the holdup measurement. High-permeability streaks in high-rate producers have been known to separate a probe from the logging tool. If this situation is suspected, then average pipe density or nuclear measurements are preferred.

Most probe-based holdup measurements provide better results when logged down against the flow or when logged up in a high-velocity well. This means that in a low-velocity horizontal well, a conventional tractor (with no log-down capabilities) would not be expected to deliver good probe holdup data.

Probe holdup measurements also suffer from bubble shearing in very turbulent flow, rendering the discontinuous-phase bubbles too small to be recorded. Smaller probes can accommodate more bubble shearing than larger probes.

Asphaltenes can be encountered in a well when injection gas breakthrough occurs. Asphaltene blinds most electrical and optical probes by covering them with a thin insulating and optically opaque skin. Dielectric probes may be more tolerant of asphaltenes.

Nuclear fluid density

Nuclear gamma ray density uses a chemical gamma ray source and a gamma ray detector separated either by a window open to the well fluids or a tungsten block to minimize direct coupling. A high gamma ray count rate means that a low-density fluid is present whereas a low gamma ray count means that there is a high-density fluid.

The window- or attenuation-based technique delivers only a pipe centerline density that works well in high-velocity, well-mixed liquid flows or vertical wells flowing just oil and water. High-velocity gas-liquid wells typically create annular flow conditions, with most of the liquid traveling invisibly up the pipe wall.

The tungsten block–based scattering approach needs a stronger source and usually measures beyond the casing to supply completion and formation information mixed in with the fluid density. The nuclear scattering technique is mainly used in very high-velocity wells, where the difference between the shut-in and flowing nuclear density is used to create a delta signal that is added to the more easily and conventionally measured shut-in density.

Neither nuclear density approach delivers quantitative holdup information for a horizontal interpretation.

Oxygen activation

High-energy neutrons are used to activate any oxygen in the vicinity of the neutron source. Activated oxygen decays back to ordinary oxygen by the emission of gamma rays and with a half-life of 7.2 s. Flowing water therefore carries a gamma ray signature that decays with time from the neutron activation. Either a pulsed neutron source and a single gamma ray detector or a continuous neutron flux and two gamma ray detectors are used in determining the velocity of the water. This is a

very powerful technique for use in horizontal production logging, and in the case of the pulsed neutron source, the resulting water velocity carries a very high confidence.

In the case of slotted liners and to a lesser extent screens, the oxygen activation log detects both completion flow and annulus flow. Sometimes the two can be confused or interfere with each other.

Oxygen-activation water flow logs do not have any obvious application in deviated or vertical wells, except for leak detection and verifying flow behind pipe. Water flow logs are most effective in horizontal stratified flow.

Markers

The case of oxygen activation is merely a special case of the use of markers. Markers can be radioactive or nonradioactive. Although water-soluble radioactive markers are relatively simple to engineer, it is much more difficult to create an oil-soluble radioactive marker that works at downhole temperatures. To date there are no markers that can be used for measuring a downhole methane gas velocity although radioactive krypton gas is used as a marker for injection wells.

Pulsed neutron holdup

The carbon/oxygen technique used for formation saturation logging can be adapted for wellbore holdup logging. In this application the carbon/oxygen signal is driven primarily by the carbon in the wellbore oil and gas while the oxygen responds to the water. Gas is usually detected by the inelastic gamma ray ratio between a near and far detector.

Key to understanding whether a particular logging tool is delivering calibrated answers is the

- ability of the tool to extract spectral yields
- existence of a tool characterization database that includes the same casing size, same casing weight, and, to a lesser extent, same lithology and porosity.

If these two conditions cannot be satisfied, then the log interpreter only has curves that respond to changes in holdup.

In the case of a slotted liner completion, this measurement sees into the annulus, albeit with a reduced sensitivity and accuracy.

Pulsed neutron carbon/oxygen-derived holdup is a very powerful measurement for horizontal production logging. High-velocity vertical and deviated wells where excessive bubble shear and friction corrections are present can also be logged in this way, as long as the production logging tool is not lifted out of the well by the high velocity. However, a pulsed neutron carbon/oxygen tool is quite expensive and quite easily doubles the cost of making a basic production log.

Flow-through dielectric holdup

Dielectric holdup measurements have a poorly defined nonlinear response to changes in the water holdup. In addition, a flow-through dielectric measurement samples only the pipe axis and ignores high-side and low-side holdup variations. In most wells it is very difficult to use the dielectric capacitance quantitatively in anything other than shut-in conditions with gravity-segregated phases.

Flow-through density and viscosity

A vibrating sensor can be used to measure the density and viscosity of the fluid surrounding it. This technique is successfully used by some formation testers. However, when applied to production logging, this kind of sensor suffers from pipe centerline sampling, preferential wettability by oil or water, and a sensitivity to vortex shedding created by upsets on the logging tool body in high-velocity flows. It is difficult to find a production logging application for this sensor.

Slip models

Although not a measurement, a slip model provides an extra velocity for the interpretation and therefore replaces the need for an extra measurement. Unfortunately slip models seem to work best under vertical conditions. They begin to struggle under deviated conditions before becoming very approximate in horizontal wells. Oil-water slip models tend to be more reliable and accurate than gas-liquid slip models. The Schlumberger Stratflo model for stratified oil and water is one of the few horizontal slip models that matches downhole measurements made on stratified flow. Horizontal gas-liquid slip models seem to need tuning for the large-diameter pipes and high-pressure conditions that occur in wells but cannot be reproduced in flow loops.

Sensor evaluation and selection

With so many different measurement techniques it is impractical to run everything in every well. There has to be some sensor selection based on information theory. At a minimum the toolstring sensors should satisfy the following requirements.

- To log a single-phase well there is no need for holdup information and just one velocity is required.
- To log a two-phase well there is a need for one holdup measurement and two velocities (although one velocity can be replaced by a slip model).

- To log a three-phase well there is a need for two holdup measurements and three velocities (although two velocities can be replaced by slip models).

Alternatively, production logging requirements can be expressed as "To log an n-phase flow requires n velocity measurements and $(n - 1)$ holdup measurements."

Taking the case of a simple horizontal gas-water well, Table 16-1 shows the surface flow rates converted to a downhole mixture velocity and water and gas holdups. Assuming a uniform inflow profile, the velocities and holdups are again estimated at 50% and 10% of the total flow. Because the well path is undulating, the deviation varies from interval to interval and the flow regime is changing from plug (PL) or slug (SL) flow to stratified (SS) or wavy stratified (SW) flow. The percentages assigned to the different sensors give the reliability of the measurement when used in a quantitative interpretation.

Velocity measurements from centered spinners are considered and would probably work acceptably at 100% of the flow in the high mixture velocities in the heel of the well; however, by the time stratified flow is reached in the toe, these spinners are very unlikely to furnish a meaningful mixture velocity.

The oxygen-activation water flow log should deliver a good water velocity at all three simulation depths, but that requires a slip model to provide the gas velocity, and gas-liquid slip correlations are not very accurate under these conditions.

The Flow Scanner minispinner array should manage to measure both the gas and water velocities.

Just one holdup measurement is needed, and it can come from eight electrical probes, eight optical probes, a vertical array of optical and electrical probes, or a pulsed neutron carbon/oxygen-based holdup. The use of just four probes in a horizontal well cannot provide sufficient holdup accuracy and resolution.

Two obvious solutions to logging this well therefore present themselves:

- pulsed neutron tool providing both holdup and water velocity in combination with a gas-liquid slip model
- vertical array of minispinners and holdup probes.

The first solution is probably more rugged whereas the second solution is probably more accurate.

The logging program

For a conventional vertical or deviated well it is normal to wait for the well to stabilize (see preceding "Pressure" section) and then record three passes, up and down, at 30, 60, and 90 ft/min [10, 20, and 30 m/min, respectively]. Although one down pass is all that is required to acquire the pressure, temperature, density, probe holdups, gamma ray, and casing collar locator data, the extra passes are logged to perform an in situ calibration of the

Table 16-1. Sensor Comparison

	Top 100% Flow	Middle 50% Flow	Bottom 10% Flow	Measurement
Depth, m	4,100	4,500	4,750	
Mixture velocity, m/s	1.61	0.80	0.16	
Water holdup (Y_w), %	40	15	10	
Gas holdup (Y_g), %	60	85	90	
Flow regime	PL, SL	SS, SW	SS, SW	
Deviation, °	87.6	91.0	90.2	
Velocity				
2½-in fullbore spinner	80%	50%	20%	Mixture velocity
2⅛-in tubing spinner	80%	45%	15%	Mixture velocity
Oxygen-activation log	90%	90%	90%	Water velocity
Petalas and Aziz (1996)	40%	40%	40%	Gas-liquid slip model
Vertical minispinner array	80%	90%	90%	Water and gas velocity
Holdup				
Four optical probes	50%	50%	50%	Gas holdup
Eight optical probes	80%	80%	80%	Gas holdup
Four electrical probes	50%	50%	40%	Water holdup
Eight electrical probes	80%	80%	80%	Water holdup
Pulsed neutron holdup	70%	70%	70%	Three-phase holdup
Vertical array of optical probes	90%	90%	90%	Gas holdup
Vertical array of electrical probes	90%	90%	90%	Water holdup

spinner. If the interval to be logged is very long, then the speeds can be increased and one of the passes dropped (e.g., 60 and 120 ft/min [20 and 40 m/min]).

Are shut-in passes required? Certainly not for the purpose of calibrating the spinner. The spinner is calibrated in situ at the flow rate and holdup to be interpreted. If the PVT properties are uncertain, then it would be nice to shut in the well, let the phases segregate, and then tune the PVT model to match the observed densities. However, the main reason for logging the well while shut in is to detect and quantify crossflow and subsequently compute layer pressures using a selective inflow performance (SIP) plot (Reservoir Evaluation, 1979; Noik, 1981).

Reduced flow rates are normally logged to complement the shut-in data in the SIP plot.

In a horizontal well there are typically much longer logging intervals than in vertical or deviated wells. In addition there are wireline tractors or coiled tubing and probably the presence of special sensors with special logging requirements. The horizontal logging program needs to eliminate redundant logging passes and where possible increase logging speeds while also including the stations for special tools. When specifying depths for the oxygen-activation water flow log stations, any ambiguity between tool zero and the depth of the oxygen activation should be removed by stating that the requested depth refers to the pulsed neutron source or Minitron device—normally all depths are with respect to the bottom of the toolstring.

If a log-down tractor is not used, then the time spent waiting for the well to stabilize can be used to tractor in the hole to the bottom log interval.

If the rig-up requires pressure deployment bars, coiled tubing, or both, then the possibility of tool failures leading to excessive lost time and even a cancelled logging job may require conducting the flowing survey at the start of the data acquisition.

Sample logging programs

This section presents logging program outlines. Actually executed programs tend to be much, much longer, but these outlines are the key steps in terms of data acquisition.

Fullbore spinner, Gradiomanometer sensor, holdup probes, pressure, and temperature

With the well shut in:

1. Run in hole (RIH) at the maximum safe speed and slow for all nipples, gas lift mandrels, subsurface safety valves, etc.
2. At 30 m above the top perforation at 2,500 m, stop and correlate the depth.
3. Log down at 10 m/min.
4. Stop 30 m below the bottom perforation at 2,800 m or 5 m above TD, whichever is shallower.
5. Log up at 10 m/min.
6. Stop at 2,500 m.
7. Repeat at 20 m/min and 30 m/min.
8. If tool lift is a serious concern then RIH to 2,800 m or 5 m above TD, whichever is shallower; otherwise remain at 2,500 m.
9. Direct well to the test separator.
10. Slowly open well to full rate (taking at least 5 min).
11. If the tool is at 2,800 m, then return to 2,500 m once the initial flow surge has passed.
12. Check the depth correlation.
13. Wait until drawdown is changing by less than 5% per hour or the surface separator rates are changing by less than 5% per hour or both.
14. Log down at 10 m/min.
15. Stop 30 m below the bottom perforation at 2,800 m or 5 m above TD, whichever is shallower.
16. Log up at 10 m/min.
17. Stop at 2,500 m.
18. Repeat at 20 m/min and 30 m/min.
19. Position the tool at 2,500 m.
20. If a pressure transient is to be recorded, start recording data versus time.
21. Shut in the well.
22. Record the pressure buildup (as required).
23. Pull out of hole (POOH), slowing for the wireline entry guide, nipples, gas lift mandrels, subsurface safety valves, etc.

Fullbore spinner, holdup probes, pulsed neutron holdup, oxygen-activation water flow log, pressure, temperature, and basic tractor (logging up only) in a horizontal monobore completion

With the well shut in:

1. RIH at the maximum safe speed and slow for all nipples, gas lift mandrels, subsurface safety valves, etc.
2. When below the safe depth for powering up, power up the pulsed neutron tool and verify that neutrons can be generated.
3. Continue to RIH to 50° to 60° deviation and stop.

4. Perform spinner calibration at 30, 60, and 90 ft/min.
5. Continue to RIH and position the production logging tool's pressure gauge opposite the permanent downhole gauge (PDG).
6. Record a 5-min station log.
7. Direct the well to the test separator.
8. Slowly open the well (taking at least 5 min) to the full flow rate.
9. Continue to RIH until the tool stands up.
10. Power down the production logging tool and power up the tractor.
11. Tractor in hole to 100 ft below the bottom perforation, pausing for pull tests every 500 ft.
12. Power down the tractor and power up the production logging tool in pulsed neutron holdup mode.
13. Check for well stability. The downhole drawdown and surface separator rates must be changing by less than 1.5% per hour unless otherwise advised by the wellsite witness.
14. Log up at 10 ft/min (or the speed appropriate for this well). Check the depth offset required and record it.
15. Pause the depth log at A,AAA ft of the pulsed neutron or Minitron depth and record an oxygen-activation water flow log station.
16. Continue logging up at 10 ft/min, pausing the log for additional oxygen-activation water flow log stations at B,BBB ft, C,CCC ft, D,DDD ft, etc.
17. Stop the log 100 ft above the top perforation.
18. Tractor in hole to 100 ft below the bottom perforation.
19. Power down the tractor and power up the production logging tool in sigma logging mode.
20. Log up at 30 ft/min. Check the depth offset required and record it.
21. Stop the log 100 ft above the top perforation.
22. Shut in the well and POOH.

Flow Scanner minispinners on MaxTRAC downhole well tractor system in a horizontal openhole oil-water well

With the well shut in:

1. RIH at the maximum safe speed and slow for all nipples, gas lift mandrels, subsurface safety valves, etc.
2. When the tool stands up, power up the MaxTRAC* tractor and tractor in hole at a convenient speed to 30 m above the casing shoe.
3. Direct the well to the test separator.
4. Slowly open the well (taking at least 5 min) to the full flow rate.
5. Check for well stability. The downhole drawdown and surface separator rates must be changing by less than 2.0% per hour unless otherwise advised by the wellsite witness.
6. Tractor in hole at 10 m/min while recording all Flow Scanner sensors.
7. Stop 30 m from TD.
8. Log up at 10 m/min while recording all Flow Scanner sensors.
9. Inspect the data quality.
10. If the log analyst requests more passes, then repeat the down and up passes at significantly different speeds (to improve the spinner calibration). Consultation with the MaxTRAC technician is recommended when choosing a second tractoring speed.
11. Shut in the well and POOH.

References

Noik, S.P., "SIP (Selective Inflow Performance): Informations sur Chaque Intervalle et sur L'ensemble d'un Puits Producteur," Society of Professional Well Log Analysts Paris (SAID), *Actes du Quatrième Colloque Annuel de Diagraphies*, Paris, France (October 21–23, 1981), paper 31.

Petalas, N., and Aziz, K.: "Development and Testing of a New Mechanistic Model for Multiphase Flow in Pipes," *ASME Fluids Engineering Division Second International Symposium on Numerical Methods for Multiphase Flows*, San Diego, California, USA (July 7–11, 1996).

"Reservoir Evaluation," *Schlumberger Well Evaluation Conference (WEC) Algeria*, Paris, France, Services Techniques Schlumberger (1979.)

Appendix

Schlumberger Spinner Data

This listing is for use only as a guide. It is preferable to determine slopes and thresholds with a downhole calibration.

Oilfield Customary Units

Flow-Caliper Imaging Sonde (PFCS) spinners

Blade Diameter, in	Casing, in	Slope,† rps/(ft/min)	1/Slope, (ft/min)/rps	Pitch,† in/rev	Threshold, ft/min	Start, ft/min	Minimum Diameter (skids/rollers), in
2.5	4–5	0.089	11.20	2.24	6.55	12	3.5/3.66
3.5	7–9⅝	0.096	10.40	2.08	4.98	7	4.88/5.03
4.5	9⅝	0.091	10.95	2.19	2.96	7	6.08/6.24
1.3125	Turbine	0.064	15.70	3.14	6.85	14	1.98/2.37

†1/(5 × slope) = pitch

PS Platform Inline Spinner (PILS)

Blade Diameter, in	Casing, in	Slope,† rps/(ft/min)	1/Slope, (ft/min)/rps	Pitch,† in/rev	Threshold, ft/min	Start, ft/min	Minimum Diameter (skids/rollers), in
1.10	Min.: 2⅜	0.108	9.25	1.85	17.5	20	1.7
1.10	Min: 2⅜	0.030	33.75	6.75	8.5	30	1.7

†1/(5 × slope) = pitch

Flow Scanner minispinners

Blade Diameter, in	Slope,† rps/(ft/min)	1/Slope, (ft/min)/rps	Pitch,† in/rev	Threshold for Water, ft/min	Threshold for Oil, ft/min	Threshold for Gas, ft/min
1.0	0.056	17.7	3.54	3.94	6.89	31.52

†1/(5 × slope) = pitch

Fullbore Spinner Flowmeter Sonde (FBS-B)

Blade Diameter, in	Cage Size, in	Slope,† rps/(ft/min)	1/Slope, (ft/min)/rps	Pitch,† in/rev	Threshold, ft/min
2.50	4.00	0.052	19.23	3.85	2.50
3.50	5.00	0.043	23.26	4.65	0.80
5.00	6.00	0.072	13.89	2.78	3.24
7.00	8.00	0.057	17.54	3.51	9.00

†1/(5 × slope) = pitch

Continuous Flowmeter Sonde (CFS) spinners

Blade Diameter, in	Tool Diameter, in	Slope,† rps/(ft/min)	1/Slope, (ft/min)/rps	Pitch,† in/rev	Threshold, ft/min
1.22	Two blades: 1.69	0.111	9.01	1.80	10.30
1.22	Four blades: 1.69	0.040	25.00	5.00	4.70
1.65	Two blades: 2.13	0.119	8.40	1.68	10.90
1.65	Four blades: 2.13	0.045	22.22	4.44	3.50
2.40	Two blades: 2.88	0.112	8.93	1.79	2.70
2.40	Four blades: 2.88	0.046	21.74	4.35	1.00

†1/(5 × slope) = pitch

Additional PFCS spinner information

Blade Diameter, in	Fluid	Slope,† rps/(ft/min)	1/Slope, (ft/min)/rps	Pitch,† in/rev
2.50	Water	0.0910	10.989	2.198
2.50	Oil	0.0872	11.468	2.294
3.50	Water	0.1014	9.862	1.972
3.50	Oil	0.0912	10.961	2.192
4.50	Water	0.0910	10.989	2.198
4.50	Oil	0.0915	10.929	2.186
1.3125	Water	0.0630	15.873	3.175
1.3125	Oil	0.0643	15.552	3.110

†1/(5 × slope) = pitch

SI Units

Flow-Caliper Imaging Sonde (PFCS) spinners

Blade Diameter, cm	Casing, in	Slope,† rps/(m/min)	1/Slope, (m/min)/rps	Pitch,† cm/rev	Threshold, m/min	Start, m/min	Minimum Diameter (skids/rollers), cm
6.35	4–5	0.293	3.414	5.69	1.996	3.7	8.9/9.3
8.89	7–9⅝	0.315	3.170	5.28	1.518	2.1	12.4/12.8
11.43	9⅝	0.300	3.338	5.56	0.902	2.1	15.4/15.8
3.33	Turbine	0.209	4.785	7.98	2.088	4.3	5.0/6.0

†1/(0.6 × slope) = pitch

PS Platform Inline Spinner (PILS)

Blade Diameter, cm	Casing, in	Slope,† rps/(m/min)	1/Slope, (m/min)/rps	Pitch,† cm/rev	Threshold, m/min	Start, m/min	Minimum Diameter (skids/rollers), cm
2.79	Min.: 2⅜	0.355	2.819	4.70	5.334	6.1	4.32
2.79	Min: 2⅜	0.097	10.287	17.14	2.591	9.1	4.32

†1/(0.6 × slope) = pitch

Flow Scanner minispinners

Blade Diameter, cm	Slope,† rps/(m/min)	1/Slope, (m/min)/rps	Pitch,† cm/rev	Threshold for Water, m/min	Threshold for Oil, m/min	Threshold for Gas, m/min
2.54	0.185	5.39	9.0	1.2	2.1	9.6

†1/(0.6 × slope) = pitch

Fullbore Spinner Flowmeter Sonde (FBS-B)

Blade Diameter, cm	Cage Size, cm	Slope,† rps/(m/min)	1/Slope, (m/min)/rps	Pitch,† cm/rev	Threshold, m/min
6.35	10.16	0.171	5.86	9.77	0.762
8.89	12.70	0.141	7.09	11.81	0.244
12.70	15.24	0.236	4.23	7.06	0.988
17.78	20.32	0.187	5.35	8.91	2.743

†1/(0.6 × slope) = pitch

Continuous Flowmeter Sonde (CFS) spinners

Blade Diameter, cm	Tool Diameter, cm	Slope,† rps/(m/min)	1/Slope, (m/min)/rps	Pitch,† cm/rev	Threshold, m/min
3.10	Two blades: 4.29	0.364	2.75	4.58	3.139
3.10	Four blades: 4.29	0.131	7.62	12.70	1.433
4.20	Two blades: 5.41	0.390	2.56	4.27	3.322
4.20	Four blades: 5.41	0.148	6.77	11.29	1.067
6.10	Two blades: 7.32	0.367	2.72	4.54	0.823
6.10	Four blades: 7.32	0.151	6.63	11.04	0.305

†1/(0.6 × slope) = pitch

Additional PFCS spinner information

Blade Diameter, cm	Fluid	Slope,† rps/(m/min)	1/Slope, (m/min)/rps	Pitch,† cm/rev
6.35	Water	0.299	3.349	5.58
6.35	Oil	0.286	3.495	5.83
8.89	Water	0.333	3.006	5.01
8.89	Oil	0.299	3.341	5.57
11.43	Water	0.299	3.349	5.58
11.43	Oil	0.300	3.331	5.55
3.33	Water	0.207	4.838	8.06
3.33	Oil	0.211	4.740	7.90

†1/(0.6 × slope) = pitch

Symbols

Roman symbols

A	pipe cross-sectional area
A'	flowing cross-sectional area around the density or holdup measurement
$A_{annular}$	pipe-tool annular area
A_h	area of the center hub of the spinner that does not contribute to the velocity measurement
A_s	swept area of the minispinner disc
B_g	gas shrinkage factor
B_o	oil shrinkage factor
B_w	water shrinkage factor, also water formation volume factor
c_o	oil compressibility
C	sensor capacitance
C	thermal capacity
C_f	carbon yield from the far detector
C_g	thermal heat capacity of gas
$C_{g_{ae}}$	thermal heat capacity of gas above the entry
$C_{g_{be}}$	thermal heat capacity of gas below the entry
$C_{g_{oe}}$	thermal heat capacity of gas of the entry
C_n	carbon yield from the near detector
C_o	thermal heat capacity of oil
$C_{o_{ae}}$	thermal heat capacity of oil above the entry
$C_{o_{be}}$	thermal heat capacity of oil below the entry
$C_{o_{oe}}$	thermal heat capacity of oil of the entry
C_p	thermal heat capacity of one unit of mass of the gas
C_t	inherent tool capacitance
C_w	thermal heat capacity of water
$C_{w_{ae}}$	thermal heat capacity of water above the entry
$C_{w_{be}}$	thermal heat capacity of water below the entry
$C_{w_{oe}}$	thermal heat capacity of water of the entry
d	inner or pipe diameter
d	hydraulic diameter
$d_{annulus}$	annulus diameter
d_b	average diameter of bubbles
$d_{Flow\_Scanner\_max}$	maximum opening diameter of the Flow Scanner caliper
d_{local}	spinner diameter
d_{pipe}	pipe ID
$d_{pipe_{external}}$	external pipe diameter
$d_{pipe_{internal}}$	internal pipe diameter
d_{sa}	stand-alone bubble size
d_t	Gradiomanometer outside diameter
d_{tool}	tool OD
dL	length between the two Gradiomanometer pressure ports
dp/dZ	pressure gradient
$dp_{friction}$	frictional pressure drop
dz/dT	rate of change of z factor with temperature
e	pipe surface roughness
e_t	surface roughness of the tool
E	energy
E	error
E_{global}	global error
E_n	error at interval n
f	frequency
f	Moody friction factor
f_p	pipe Moody friction factor

f_t	tool Moody friction factor
F_{vpc}	spinner correction factor; also VPCF (velocity profile correction factor)
g	gravitational acceleration
h	separation of the two Gradiomanometer pressure ports
h'_{100}	enthalpy of water at 100 degC
h'_{200}	enthalpy of water at 200 degC
h''_{200}	enthalpy of steam vapor at 200 degC
h_{ae}	enthalpy above the entry
h_{be}	enthalpy below the entry
h_{oe}	enthalpy of the entry
k	permeability
L	length
L_a	depth-smoothing interval
m	mass
m	turbulence exponent
m_i	tool measurement
m_{liquid}	mass of liquid water
m_{vapor}	mass of water vapor
M_i	modeled tool response
$M(x_i,y_i)$	modeled value of holdup, velocity, or average pipe property for local coordinates x_i and y_i
n	number of moles
n	high-energy neutron
n_b	number of bubbles
N_{bc}	bubble count frequency
N_{Fr}	Froude number
N_{Re}	Reynolds number
$N_{\text{Re\_local}}$	local Reynolds number
$N_{\text{Re\_pseudo}}$	pseudo Reynolds number
$N_{\text{WFL\_cycles}}$	number of WFL cycles
O_f	oxygen yield from the far detector
O_n	oxygen yield from the near detector
p	pressure
p	proton
p_{bp}	bubblepoint pressure
p_{cn}	critical pressure of gas component n
p_{leak}	pressure drop across a leak
p_{pc}	pseudo-critical pressure
p_{pr}	pseudo-reduced pressure
p_{wb}	wellbore pressure
p_{wf}	bottomhole flowing pressure
P	power
q	flow rate
q_b	bubble flow rate
q_{dh}	downhole flow rate
q_g	gas flow rate
$q_{g_{ae}}$	downhole flow rate of gas above the entry
$q_{g_{be}}$	downhole flow rate of gas below the entry
$q_{g_{dh}}$	downhole flow rate of gas
$q_{g_{oe}}$	downhole flow rate of gas of the entry
$q_{g_{sc}}$	gas flow rate at standard conditions
q_{hp}	heavy-phase flow rate
q_l	liquid flow rate
q_{leak}	pressure drop across a leak
q_{liquid}	flow rate of liquid water
q_{lp}	light-phase flow rate
q_n	flow rate of phase n
q_o	oil flow rate
$q_{o_{ae}}$	downhole flow rate of oil above the entry
$q_{o_{be}}$	downhole flow rate of oil below the entry
$q_{o_{dh}}$	downhole flow rate of oil
$q_{o_{oe}}$	downhole flow rate of oil of the entry
$q_{o_{sc}}$	oil flow rate at standard conditions
$q_{sg_{ae}}$	solution gas flow rate at standard conditions
$q_{t\_\text{monophasic}}$	single-phase pipe flow rate
$q_{t\_\text{multiphase}}$	multiphase pipe flow rate
q_w	water flow rate
$q_{w_{ae}}$	downhole flow rate of water above the entry

$q_{w_{be}}$	downhole flow rate of water below the entry
$q_{w_{dh}}$	water downhole flow rate
$q_{w_{oe}}$	downhole flow rate of water of the entry
$q_{w_{sc}}$	water flow rate at standard conditions
Q	steam quality
r	radius
R	pipe internal radius
R	universal gas constant
R_1, R_2	spinner blades internal, external radii
R_{so}	solution gas ratio
R_{sw}	solution gas ratio in water
R_t	resistance within the oscillator
S	surface
S	wetted perimeter
S_o	formation oil saturation
t	time
$t_{½}$	half-life
t_b	presence time of the bubble on the probe tip
$t_{\text{neutron\_off-time}}$	neutron off-time
$t_{\text{neutron\_on-time}}$	neutron on-time
t_{peak}	time of signal peak
t_{station}	WFL station time
$t(x)$	effective tool width across the vertical pipe area
T	temperature
T_{ae}	absolute temperature above the entry
T_{be}	absolute temperature below the entry
T_{cn}	critical temperature of gas component n
T_{oe}	absolute temperature of the entry
T_{pc}	pseudo-critical temperature
T_{pr}	pseudo-reduced temperature
T_r	reservoir temperature
v	velocity
$v_{+\text{threshold}}$	spinner threshold for positive spinner readings
$\text{v}_{-\text{threshold}}$	spinner threshold for negative spinner readings
v_{app}	apparent spinner velocity
v_{ave}	average pipe velocity
$v_{\text{ave\_spinner}}$	average velocity in spinner swept area
v_b	bubble velocity
$v_{\text{difference}}$	velocity difference
v_{cable}	cable (or tool) velocity
v_g	gas velocity
v_{gsup}	superficial gas velocity
v_{hp}	heavy-phase velocity
v_l	liquid velocity
v_{liquid}	velocity of liquid water
v_{local}	velocity difference between the mixture velocity and the tool velocity
v_{logging}	logging speed
v_{lp}	light-phase velocity
v_m	average volumetric mixture velocity
v_{max}	centerline velocity
v_o	oil-phase velocity
v_{osup}	superficial oil velocity
v_s	slip velocity
$v_{\text{s\_deviated}}$	deviated-pipe slip velocity
$v_{s_{gl}}$	gas-liquid slip velocity
$v_{s_{ow}}$	oil-water slip velocity
v_{spinner}	spinner velocity
$v_{\text{sup\_liquid}}$	superficial velocity of liquid water
v_t	relative velocity between the tool and flow
v_{tool}	logging speed
v_{vapor}	velocity of water vapor
v_w	water-phase velocity
v_{WFL}	reported WFL velocity
v_{wsup}	superficial water velocity

$v(r)$	axial velocity at radius r
$v(x)$	local mixture velocity up the vertical pipe axis
V	volume
V_b	volume of balloon
V_m	volume of one unit of mass of the gas
V_{sh}	shale volume
w_i	weighting factor
w_{liquid}	mass flow rate of liquid water
w_{vapor}	mass flow rate of water vapor
X_n	carbon characterization coefficient
Y_b	bubble holdup
Y_g	gas holdup
Y_{hp}	heavy-phase holdup
Y_l	liquid holdup
Y_{liquid}	holdup of liquid water
Y_{lp}	light-phase holdup
Y_n	holdup of phase n
Y_n	oxygen characterization coefficient
Y_o	oil holdup
Y_{vapor}	holdup water vapor
Y_w	water holdup
z	gas compressibility factor
z	substitution term based on radii
Z_n	gas characterization coefficient

Greek

β	beta (electron) particle
γ	gamma ray
γ_{negative}	negative slope for negative spinner readings
γ_o	specific gravity of oil
γ_{positive}	spinner slope for positive spinner readings
δ	deviation
Δp	pressure difference
ΔT	temperature difference
$\Delta\rho$	density difference
θ	well deviation
μ	dynamic viscosity
μ_m	mixture viscosity
μ_o	oil viscosity
μ_w	water viscosity
ρ	fluid density
ρ_{corr}	deviation- and friction-corrected density
$\rho_{\text{dev\_corr}}$	density corrected for deviation
ρ_{flowing}	corrected density from a flowing well
ρ_g	gas density
$\rho_{g_{ae}}$	downhole density of gas above the entry
$\rho_{g_{be}}$	downhole density of gas below the entry
$\rho_{g_{oe}}$	downhole density of gas of the entry
ρ_h	heavy-phase density
ρ_l	light-phase density
ρ_l	liquid density
ρ_{liquid}	liquid water density
ρ_m	mixture density
ρ_{measured}	tool density reading
$\rho_{\text{nuclear\_flowing}}$	nuclear density from the flowing well
$\rho_{\text{nuclear\_shutin}}$	nuclear density from the shut-in well
ρ_o	oil density
$\rho_{o_{ae}}$	downhole density of oil above the entry
$\rho_{o_{be}}$	downhole density of oil below the entry
$\rho_{o_{oe}}$	downhole density of oil of the entry
ρ_{shutin}	independently measured shut-in density
ρ_{so}	density of silicone oil at pressure and temperature
ρ_{vapor}	water vapor density
ρ_w	water density
$\rho_{w_{ae}}$	downhole density of water above the entry
$\rho_{w_{be}}$	downhole density of water below the entry
$\rho_{w_{oe}}$	downhole density of water of the entry

Σ_n	sum of n values
Σt_g	total time that the probe is in gas during time t
Σt_w	total time that the probe is in water during time t
τ	wall/interface stress
τS	wall/interface shear
υ	kinematic viscosity
φ	formation porosity
$\omega_{spinner}$	spinner reading

Nomenclature

BorFlow*	production logging tool analytical software package
cps	cycle per second
DEFT	Digital Entry and Fluid Imaging Tool
DLIS	Digital Log Information Standard
DPDZ	pressure gradient curve
DTS	distributed temperature sensing
DV	density-viscosity
Emeraude	production logging tool data interpretation software
EOS	equation of state
FCOR	far carbon/oxygen ratio
FloView*	holdup measurement tool
Flow Scanner*	horizontal and deviated well production logging system
GeoFrame*	reservoir characterization software
GHOST*	gas holdup optical sensor tool
GMET	General-Purpose Marker Ejector Tool
GOR	gas/oil ratio
Gradiomanometer*	specific gravity profile
GSO	gadolinium orthorthosilicate
HUM	holdup meter
ICAO	International Civil Aviation Organization
ID	inside diameter
ISA	International Standard Atmosphere
IUPAC	International Union of Pure and Applied Chemistry
LED	light-emitting diode
LQC	log quality control
MapFlo*	multiphase flow mapping in deviated wells
MAXIS*	multitask acquisition and imaging system
MaxTRAC*	downhole well tractor system
MaxWell*	integrated field acquisition software
MEMS	microelectromechanical system
Minitron*	pulsed neutron generator device
MWFD	manometer well fluid density
NCOR	near carbon/oxygen ratio
NFDC	nuclear fluid density tool
NICR	near/far net inelastic count rate ratio
NIST	National Institute of Standards and Technology
NTP	normal temperature and pressure
PBMS	Platform Basic Measurement Sonde
PDG	permanent downhole gauge
PFCS	Flow-Caliper Imaging Sonde
PGMS	Gradiomanometer sonde for PS Platform system
PGMS_DEVI	deviation measured by an accelerometer in the PGMS tool
PLATO	production logging tool data interpretation software
PL Flagship*	advanced well flow diagnosis service
PLGLOB	VAX-based production logging tool data interpretation software
PLT	production logging tool
POOH	pull out of hole
PSI	perforate-stimulate-isolate
PSOI	polycrystalline silicon on insulator

PS Platform*	new-generation production services platform
PVL*	phase velocity log
PVS	phase velocity sonde
PVT	pressure, volume, temperature
RIH	run in hole
RSTPro*	reservoir saturation tool
RTD	resistance temperature detector
SATP	Standard Ambient Temperature and Pressure
S.C.	surface conditions
SIP	selective inflow performance
SPE	Society of Petroleum Engineers
SPRINT*	single-pass production log interpretation
Stratflo	horizontal slip model for stratified flow
STP	standard temperature and pressure
TET	Tracer Ejector Tool
TPHL*	three-phase fluid holdup log from pulsed neutron measurements
TVD	true vertical depth
UWFD	filtered density uncorrected for deviation
VLP	vertical lift performance
VPCF	velocity profile correction factor; also F_{vpc} (spinner correction factor)
WFDE	filtered density corrected for deviation
WFL*	water flow log

Index

Note: Page numbers in *italic type* refer to illustrations.

E

F

G

H

I

J

K

L

M

N

O

P

Q

R

S

T

U

V

W

Y

Z